Hamilton-Receptor-Mediated Self-Assembly of Merocyanine Dyes into Supramolecular Polymers

Dissertation zur Erlangung des
naturwissenschaftlichen Doktorgrades
der Julius-Maximilians-Universität Würzburg

vorgelegt von
Ralf Schmidt
aus Würzburg

Würzburg 2011

Eingereicht am 20. Januar 2011

bei der Fakultät für Chemie und Pharmazie

1. Gutachter: Prof. Dr. Frank Würthner

2. Gutachter: Prof. Dr. Dirk Kurth

der Dissertation

1. Prüfer: Prof. Dr. Frank Würthner

2. Prüfer: Prof. Dr. Dirk Kurth

3. Prüfer: PD. Dr. Reinhold Fink

des Öffentlichen Promotionskolloquiums

Tag des Öffentlichen Promotionskolloquiums: 18. April 2011

Doktorurkunde ausgehändigt am:

für Eva und Udo

Acknowledgment / Danksagung

List of Abbreviations

A	acceptor
AFM	atomic force microscopy
CT	charge transfer
D	donor
dc	direct current
DCTP	2-[(2*E*)-3-(4-*tert*-butylphenyl)-2-methylprop-2-enyliden]malononitrile
DFT	density functional theory
DIPEA	diisopropylethylamine (Hünig's base)
DMSO	dimethylsulfoxide
DOSY	diffusion ordered spectroscopy
DP	degree of polymerization
EOA	electro-optical absorption
eq	equivalent
ESI	electron spray ionization
GPC	gel permeation chromatography
HATU	2-(1*H*-7-azabenzotriazol-1-yl)-1,1,3,3-tetramethyl uronium hexafluorophosphate
HF	Hartree-Fock
HOPG	highly ordered pyrolytic graphite
HPLC	high performance liquid chromatography
HRMS	high resolution mass spectrometry
LFER	linear free energy relationship
MALDI-TOF	matrix-assisted laser desorption/ionization-time of flight
MCH	methylcyclohexane
Mp	melting point
NMR	nuclear magnetic resonance
ROESY	rotating-frame Overhauser enhancement spectroscopy
rt	room temperature
TEM	tunneling electron microscopy
THF	tetrahydrofuran
TLC	thin layer chromatography
TMS	tetramethylsilane
UV/Vis	ultraviolet/visible
VSEPR	valence shell electron pair repulsion

Table of Contents

Chapter 1

Introduction and Aim of the Thesis

Nature consummately employs noncovalent interactions between a limited set of supramolecular building blocks for precise structural control of sophisticated macromolecular architectures that provide unrivalled function.[1] Among the most fascinating examples are the natural light-harvesting systems in the chlorosomes of green and purple bacteria.[2,3] Inspired by nature, self-assembly based on weak forces was realized to offer new prospects to the fields of biology and materials science.[4]

Beside the formation of a certain topology several biological polymers are capable of undergoing structural alterations between defined species as a result of environmental changes or the presence of molecular stimuli.[1,5] Subtle variations in their structure decisively influence the functions of these molecules. Examples include helix-coil,[6] and β-sheet to coil transitions in peptides,[7] and the denaturation of proteins[8] and RNA[9]. The folding of biopolymers, as for example proteins, is known to be highly cooperative.[8,10] The capacity to change structurally was also found for synthetic polymers collapsing into globular conformations due to solvophobic effects[11] and for block copolymers spontaneously self-assembling into well-defined micelles[12]. In order to create artificial supramolecular systems, emulating the formation of defined complex architectures combined with the possibility of undergoing structural changes as found in nature, directed noncovalent interactions are needed. For this purpose, weak forces, that include van der Waals forces, π–π interactions, solvophobic effects, hydrogen bonds, and electrostatic interactions, involving charges and dipoles, have been studied in the field of supramolecular chemistry. Dipolar interactions hold a prominent place among these interactions owing to their directionality. Hydrogen bonds which are predominantly of electrostatic nature may be considered as a special case. Another exception is known for the antiparallel aggregation of merocyanine dyes, owing to strong dipole-dipole interactions. Whereas hydrogen bonds have extensively been used for the

construction complex systems (Figure 1a),[13] dipolar interactions between merocyanines only recently have been proposed as novel directional binding motifs that lead to the formation of antiparallel dimers.[14] Chromophores **3** aggregated in nonpolar solvents owing to strong Coulomb forces between these dipolar dyes (Figure 1b). Furthermore, such predictable supramolecular unit afforded discrete architectures and highly ordered supramolecular polymers.[15,16]
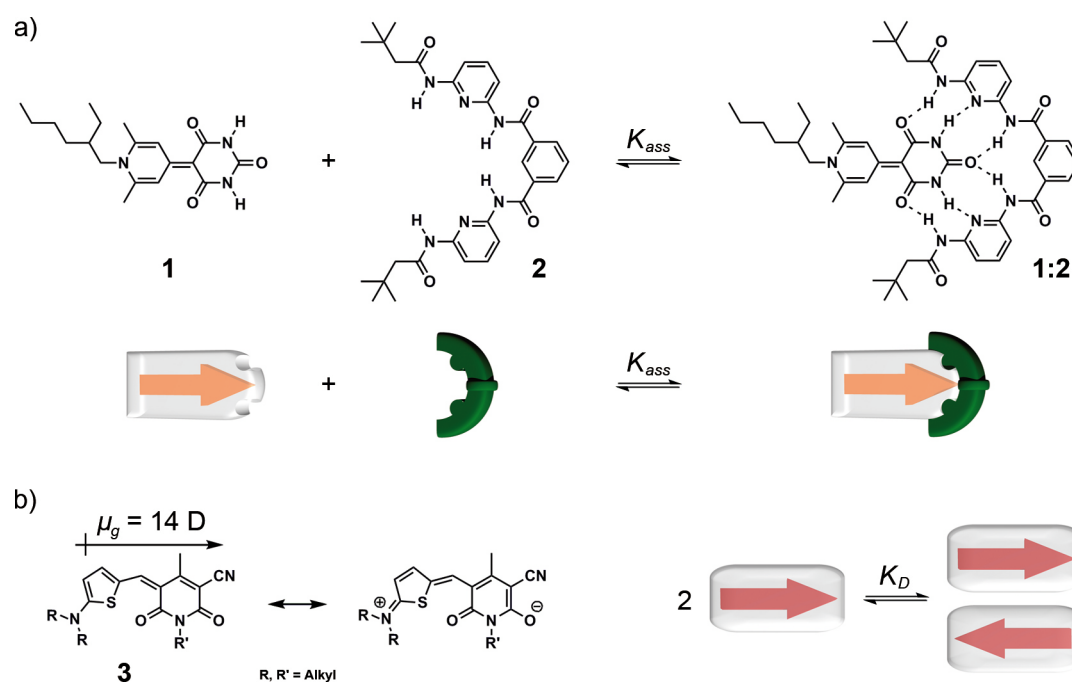
Figure 1. Molecular structure and schematic representation of the formation of the exemplary hydrogen bonded complex **1:2** (a) and of the dipolar aggregation of highly dipolar merocyanine dyes **3** into centrosymmetric dimers (b).

The orthogonal character of hydrogen bonds and dipolar interactions between merocyanine dyes might enable structurally well-defined assemblies and responsive materials. Whilst examples for defined assemblies based on such interplay of hydrogen bonding sites and dipolar merocyanine dyes have already been demonstrated,[17–19] novel functionalities such as responsiveness remain unexplored. Therefore, the aim of this thesis is to gain insight into the thermodynamics of systems, which employ a combination of these directional, orthogonal interactions. For this purpose, first of all a basic comprehension of the thermodynamics of aggregate formation is required (see Chapter 2). In the context of hydrogen bonding and antiparallel aggregation of dipolar merocyanine chromophores, a comparison of the free binding energies of such interactions may establish dipolar interactions as a feasible noncovalent force in the field of supramolecular chemistry (see Chapter 3). Special emphasis will be given to the directional character of both interactions.

Allocated to the aim of this thesis, a bis(merocyanine) dye building block, tethered by a Hamilton receptor[20] as hydrogen bonding entity (schematically depicted in Figure 2a), should represent a promising system (see Chapter 4). Antiparallel dipolar aggregation of the dyes may lead to supramolecular polymers, owing to the bifunctionality of the compound. The incorporation of an orthogonal hydrogen bonding unit would then account for the responsive character. The self-assembly will be studied by spectroscopic and microscopic techniques with particular regard to thermodynamics, revealing unexpected processes. Such thermodynamic studies are desirable since they constitute the basis for understanding the interplay between different noncovalent interactions.
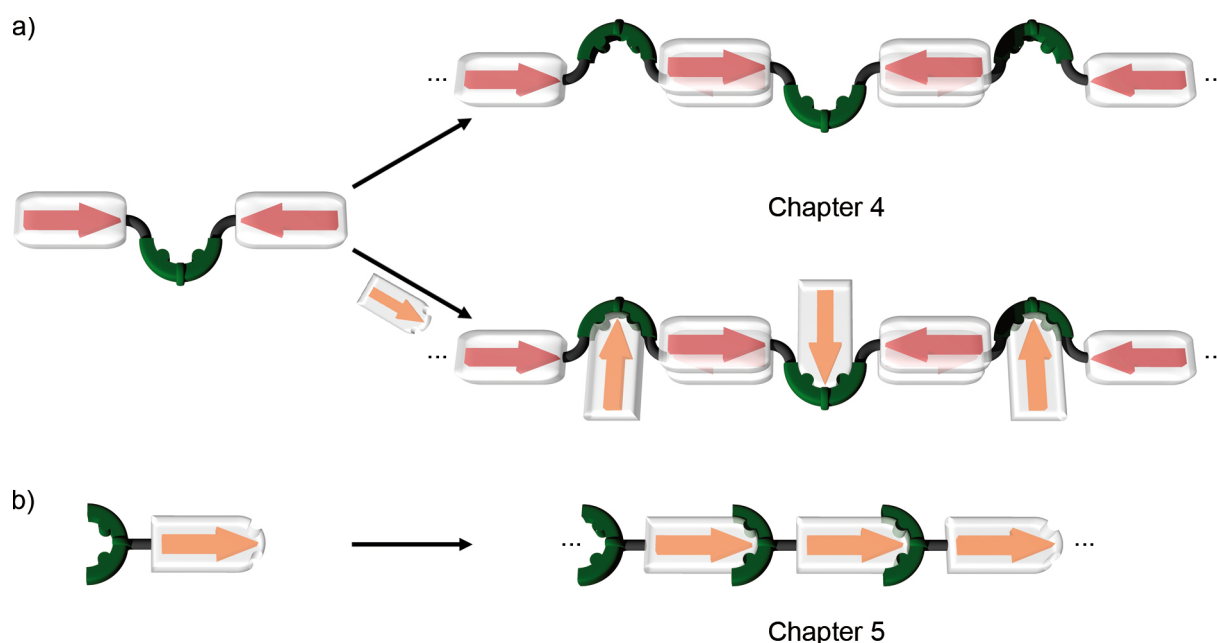
Figure 2. Schematic representation of the self-assembly of appropriately designed Hamilton-receptor-functionalized merocyanine dye building blocks into supramolecular polymers based on dipolar aggregation of the merocyanine chromophores (a) and on hydrogen bonding (b).

The fourth part of this thesis aims at the formation of hydrogen-bonded supramolecular polymers with a head-to-tail parallel arrangement of the monomer dipole moments (see Chapter 5). The formation of Hamilton-receptor-connected dimers, which result in such an arrangement, constitute the basis of this work.[18] These compounds employ a Hamilton receptor attached to the donor moiety of a merocyanine dye and a merocyanine guest, bearing a complementary barbituric acid acceptor group, to overcome the formation of antiparallel dimer aggregates. Accordingly, a self-complementary system of such type may be able to form supramolecular polymers (schematically depicted in Figure 2b). In the present studies, spectroscopic and microscopic methods will be applied to gain insight into size and thermodynamics of the formation of such aggregates.

Chapter 2

Literature Survey on Thermodynamics of Chemical Equilibria for Aggregation

Abstract: The mathematical treatment of the thermodynamics of aggregation is reviewed starting with a model to describe the formation of discrete dimers. Concentration- and temperature-dependent isodesmic models are used to characterize infinite aggregates. Furthermore, allosteric cooperativity is discussed within the approximations of concentration- and temperature-dependent nucleation–elongation models for different nuclei sizes. The formation of closed oligomeric systems is finally described employing chelate cooperativity.

2.1 Introduction

In general, finite and infinite supramolecular architectures are formed under thermodynamic conditions in solution, involving equilibria between monomeric and aggregated species. Multiple equilibria may exist in the system when more than one aggregate species is involved. For the purpose of a quantitative description of the self-assembly of various supramolecular systems several mathematical models have been developed. For early models, like the *attenuated K model*[21] and the *overall model*[22], large deviations of the calculated curves from experimental data were found. Both comprised little reasonable approximations but had the advantage of mathematical simplicity. Nowadays, more sophisticated models can be treated computationally. Such models include a simple *dimer model*, and the *isodesmic model* for infinite aggregates. In order to describe positive or negative *allosteric cooperativity* in the generation of linear chains, *nucleation–elongation models* have been introduced, allowing the formation of a nucleus prior to polymerization. If the cooperative self-assembly process is driven by differences in the strengths of inter- and intramolecular interactions, *chelate cooperativity* may lead to the formation of closed systems. This literature survey is mainly inspired by a review of Meijer et al.,[23d] which transfers conventional polymerization mechanisms of covalent polymers to their noncovalent supramolecular counterparts, and a review of Hunter and Anderson,[10] which discusses cooperative effects in the context of self-assembly.

2.2 Monomer–Dimer Model

The equilibrium between two monomers M and dimer M_2 can be written as:[23c]

$$2M \xrightleftharpoons{K_D} M_2$$

Therefore, the concentration of the dimer c_2 may be expressed as:

$$c_2 = K_D c_1^2 \tag{2.1}$$

where c_1 represents the concentration of the monomeric species and K_D the dimerization constant. With c_T as the total concentration of the molecules, equation (2) describes the molar fraction of monomer species α_{mon}, while molar fraction of aggregated species α_{agg} is given in equation (3).

$$\alpha_{mon} = \frac{c_1}{c_T} \tag{2.2}$$

$$\alpha_{agg} = 1 - \alpha_{mon} \tag{2.3}$$

Taking into account that $c_T = 2c_2 + c_1$ and equation (2.1), the following expressions for c_1, α_{mon}, and α_{agg} as functions of K_D and c_T can be found:

$$c_1 = \frac{\sqrt{8K_D c_T + 1} - 1}{4K_D} \tag{2.4}$$

$$\alpha_{mon} = \frac{\sqrt{8K_D c_T + 1} - 1}{4K_D c_T} \tag{2.5}$$

$$\alpha_{agg} = \frac{4K_D c_T + 1 - \sqrt{8K_D c_T + 1}}{4K_D c_T} \tag{2.6}$$

The relation of this model (and that of the other models described in this chapter) to absorption spectra is given in the Appendix.

Constituting the simplest description for the aggregation of dye molecules, the monomer–dimer model has successfully been applied to the description of the aggregation of cyanine[24] and phthalocyanine dyes,[25] and more recently to dipolar merocyanine dyes,[14] and perylene bisimides.[26] It was reported in the literature that the monomer–dimer model fails to describe more complicated systems as was evident from deviations of the experimental data from the model. Therefore, upon going from dimers to higher aggregates, more sophisticated models are necessary to properly describe these systems.

2.3 Isodesmic Model

Extended dye aggregates may be described within the approximations of the isodesmic model (also called equal K model).[23] This simple model assumes that aggregates are of one-dimensional, noncyclic character. The reversible formation of noncovalent bonds is identical for all binding events implying that the reactivity of the end groups does not change during the supramolecular aggregation process. Thus, the equilibrium constants and Gibbs free energy changes are equal for each step of the growing aggregate.

2.3.1 Concentration-Dependent Isodesmic Model

Within the isodesmic model the aggregation process can be written by means of consecutive addition steps as stated below:

$$M + M \rightleftharpoons M_2 \qquad\qquad c_2 = K_2 c_1^2$$

$$M_2 + M \rightleftharpoons M_3 \qquad\qquad c_3 = K_3 c_2 c_1 = K_2 K_3 c_1^3$$

$$\ldots$$

$$M_{n-1} + M \rightleftharpoons M_n \qquad\qquad c_n = K_n c_{n-1} c_1 = K_2 K_3 \ldots K_{n-1} K_n c_1^n$$
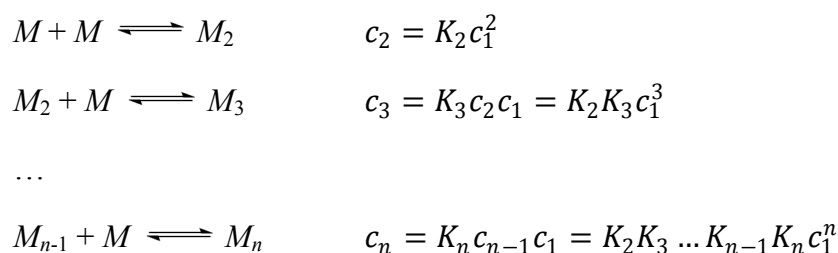
where c_1, c_2, c_3, …, c_n constitute the molar concentrations of monomer, dimer, trimer, and n-mer species, respectively, and K_2, K_3, …, K_n are the equilibrium constants for the addition of monomer to another monomer, to a dimer, and to a $(n-1)$-mer, respectively. As already mentioned all K are equal in the approximation of the isodesmic model:

$$K = K_2 = K_3 = … = K_n$$

The concentration of n-mer c_n and the total concentration of molecules in solution c_T, respectively, may be expressed according to equations (2.7) and (2.8):

$$c_n = K^{n-1} c_1^n \tag{2.7}$$

$$c_T = (c_1 + 2Kc_1^2 + 3K^2c_1^3 + \cdots + nK^{n-1}c_1^n) \tag{2.8}$$

Equation (2.8) can be simplified to equation (2.9) by taking into account the series expansion $1 + 2x + 3x^2 + … + nx^{n-1} = 1/(1-x)^2$ valid for $0 < x < 1$. This expression can subsequently be solved for c_1, leading to equation (2.10):

$$c_T = c_1/(1 - Kc_1)^2 \tag{2.9}$$

$$c_1 = \frac{2Kc_T + 1 - \sqrt{4Kc_T + 1}}{2K^2 c_T} \tag{2.10}$$

Setting $\alpha_{mon} = c_1/c_T$, where α_{mon} is the mole fraction of monomer species, leads to the fraction of aggregated molecules α_{agg}, similarily to the procedure for the dimer model:

$$\alpha_{agg} = 1 - \frac{2Kc_T + 1 - \sqrt{4Kc_T + 1}}{2K^2 c_T^2} \tag{2.11}$$

Figure 1 depicts the molar fractions of aggregated species α_{agg} plotted as a function of Kc_T. As can be seen from the calculated curves, the increase of α_{agg} for the isodesmic model is more pronounced compared to that of the dimer model. Both functions show maximum values of 1.
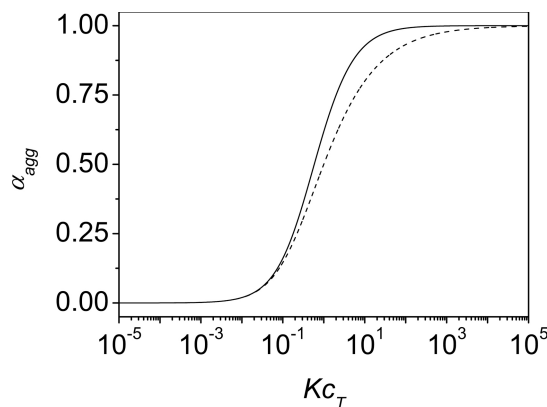
Figure 1. Molar fraction of aggregated molecules α_{agg} plotted against the dimensionless concentration Kc_T for isodesmic and dimer model according to equations (2.11) (solid line, α_{agg} calculated with the isodesmic model), and (2.6) (dashed line, α_{agg} calculated with the dimer model).[23c]

The mean number of monomers per aggregate or the number-averaged degree of polymerization DP_N may be calculated with equation (2.12):

$$DP_N = \frac{\sum_{n=1}^{\infty} nc_n}{\sum_{n=1}^{\infty} c_n} = \frac{c_T}{c_N} = \frac{c_1 + 2c_2 + 3c_3 + \cdots + nc_n}{c_1 + c_2 + c_3 + \cdots + c_n} \tag{2.12}$$

with c_N being the concentration of all species, including monomers, dimers, trimers, and n-mers. Employing equation (2.7) the following expression for c_N can be obtained:

$$c_N = c_1 + Kc_1^2 + K^2c_1^3 + \cdots + K^{n-1}c_1^n$$
$$= c_1(1 + Kc_1 + K^2c_1^2 + \cdots + K^{n-1}c_1^{n-1}) \tag{2.13}$$

Considering the series expansion $1 + x + x^2 + x^3 + \ldots + x^n = 1/(1-x)$, c_N may be expressed as:

$$c_N = c_1/(1 - Kc_1) \tag{2.14}$$

Taking into account equations (2.9) and (2.10) for c_T and c_1, respectively, and equation (2.14) for c_N, the number-averaged degree of polymerization DP_N can be calculated to:

$$DP_N = \frac{c_T}{c_N} = \frac{c_T(1 - Kc_1)}{c_1} = \frac{1 + \sqrt{4Kc_T + 1}}{2} \tag{2.15}$$

In combination with equation (2.11) a simple relationship between DP_N and α_{agg} can be found:[27]

$$DP_N^{-2} = 1 - \alpha_{agg} \tag{2.16}$$

Moreover, the weight-averaged degree of polymerization can be calculated for isodesmic aggregate formation:[23b]

$$DP_W = \frac{\sum_{n=1}^{\infty} n^2 c_n}{\sum_{n=1}^{\infty} nc_n} = \frac{c_1 + 4c_2 + 9c_3 + \cdots + n^2 c_n}{c_1 + 2c_2 + 3c_3 + \cdots + nc_n} \tag{2.17}$$

By applying the series expansion $c_1 = c_1 + 4Kc_1^2 + K^2c_1^3 + \cdots + n^2K^{n-1}c_1^n = c_1(1 + 4Kc_1 + 9K^2c_1^2 + \cdots + n^2K^{n-1}c_1^{n-1}) = c_1(1 + Kc_1)/(1 - Kc_1)^3$, DP_W can be expressed as a function of Kc_T:

$$DP_W = \frac{1 + Kc_1}{1 - Kc_1} = \sqrt{4Kc_T + 1} \tag{2.18}$$

DP_N and DP_W may be plotted as a function of c_T based on equations (2.15) and (2.18) with distinct K values as depicted in Figure 2.
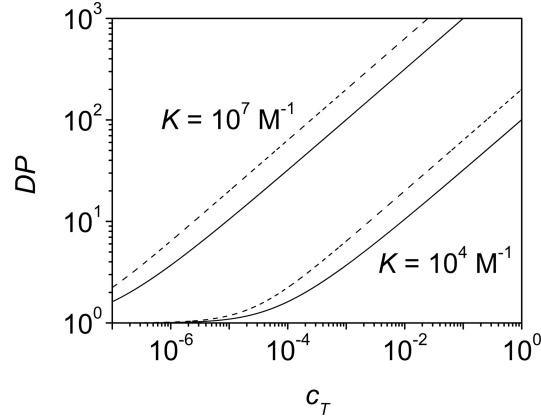
Figure 2. Number-averaged degree of polymerization DP_N (solid lines) and weight-averaged degree of polymerization DP_W (dashed lines) plotted as a function of the total concentration c_T according to the isodesmic model with $K = 10^7$ M^{-1} and 10^4 M^{-1}.[23c]

2.3.2 Temperature-Dependent Isodesmic Model

Only recently, is has been stated in literature that for a fast and unambiguous determination of the self-assembly mechanism and its thermodynamic parameters, temperature-dependent measurements are more appropriate than concentration-dependent ones, owing to the possibility to rapidly obtain large data sets.[28] Therefore, a brief introduction to the temperature-dependent isodesmic model will be given.

Assuming a two-state equilibrium, the degree of polymerization or the molar fraction of aggregated species $\alpha_{agg}(T)$ is related to temperature by means of a sigmoidal relation. This can be rationalized by taking into account that still up to high values of $\alpha_{agg}(T)$ only short oligomers are present. Equation (2.19) constitutes a general sigmoidal relation for $\alpha_{agg}(T)$, with values between 0 and 1. The temperature for $\alpha_{agg}(T) = 0.5$ is denoted the melting temperature of the aggregate T_m and is defined as:[28]

$$\alpha_{agg}(T) \cong \frac{1}{1 + e^{\frac{T-T_m}{T^*}}} \tag{2.19}$$

where T^* is a characteristic temperature that is related to the slope of the function at $T = T_m$. The slope at T_m is related to the enthalpy release ΔH via:[27,28]

$$\left. \frac{\delta \alpha_{agg}(T)}{\delta T} \right|_{T=T_m} = \frac{-1}{4T^*} \approx \frac{\left(\frac{\sqrt{2}-1}{2\sqrt{2}-1}\right)\Delta H}{RT_m^2} \tag{2.20}$$

with R as the Boltzmann constant times the Avogadro constant. From this expression T^* can be written as a function of ΔH and T_m:

$$T^* \cong \frac{-RT_m^2}{0.908\Delta H} \tag{2.21}$$

Combination of equations (2.19) and (2.21) yields the expression for the molar fraction of aggregated species $\alpha_{agg}(T)$ as a function of the temperature T:

$$\alpha_{agg}(T) \cong \frac{1}{1 + e^{-0.908\Delta H \frac{T-T_m}{RT_m^2}}} \tag{2.22}$$

Figure 3 shows the degree of aggregation $\alpha_{agg}(T)$ according to the temperature-dependent isodesmic model as a function of the dimensionless temperature T/T_m for various values of the temperature-independent aggregation enthalpy ΔH (in kJ mol^{-1}).
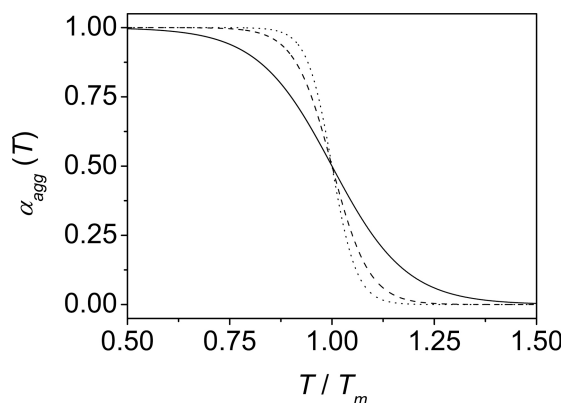
Figure 3. Molar fraction of aggregated molecules $\alpha_{agg}(T)$ plotted against the dimensionless temperature T/T_m for various values of the temperature-independent enthalpy of aggregation ΔH (−30 (solid line), −60 (dashed line), and −90 kJ mol^{-1} (dotted line)) according to the temperature-dependent isodesmic model.[23d]

The number-averaged degree of polymerization $DP_N(T)$ can be calculated from $\alpha_{agg}(T)$:

$$DP_N(T) = \frac{1}{\sqrt{1 - \alpha_{agg}(T)}} \tag{2.23}$$

Taking into account equation (2.11), this expression can be related to the equilibrium constant K and the total concentration of molecules c_T via:

$$DP_N(T) = \frac{1}{2} + \frac{1}{2}\sqrt{4K(T)c_T + 1} \tag{2.24}$$

This is equal to equation (2.15). Based on equation (2.24) the number-averaged degree of polymerization can be calculated as a function of T/T_m for various values of ΔH. The resulting curves are depicted in Figure 4. A higher enthalpy release corresponds to a higher equilibrium constant and therefore leads to higher DP_N values.
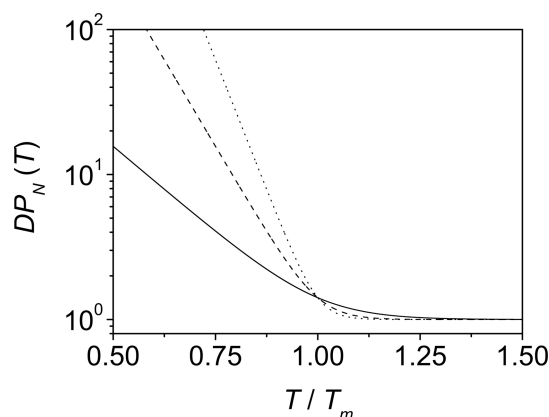
Figure 4. Number-averaged degree of polymerization $DP_N(T)$ plotted against the dimensionless temperature T/T_m for various values of the temperature-independent enthalpy of polymerization ΔH (−30 (solid line), −60 (dashed line), and −90 kJ mol^{-1} (dotted line)) according to the temperature-dependent isodesmic model. [23d]

Amongst others, the isodesmic model was successfully applied to aggregate formation of perylene bisimides,[29] phenylene ethynylene macrocycles,[30] hexa-*peri*-hexabenzocoronenes,[31] acylated 3,3'-diamino-2,2'-bipyridines,[23d] as well as to bifunctional ureido-pyrimidones,[32] stoichiometric mixtures of ditopic Hamilton-receptors and ditopic cyanurate wedges,[33] ditopic calix[4]arene tetraureas,[34] and 2-(guanidiniocarbonyl)-pyrrole-4-carboxylates.[35]

2.4 Nucleation–Elongation Models

From early investigations of polypeptide aggregates, it was evident that the aggregation process deviated from the predictions of the isodesmic model. A critical concentration was found after which the aggregation to enlarged species took place with a significant amount of monomer species remaining in solution. Furthermore, an increase of the total concentration resulted in an increase of the aggregate concentration while the monomer concentration remained constant.[36] In order to obtain better fitting with experimental data the isodesmic model was modified. The following sections will give a brief summary of nucleation–elongation models and the required alterations made to the isodesmic model.[23] These models describing nonisodesmic supramolecular polymerization incorporate the formation of a nucleus of size s with an association constant K_s in a first step. Up to the formation of this nucleus, each addition of a monomer is in accordance with the isodesmic model. Owing to (anti)cooperative effects the subsequent addition of monomers occurs, however, with an association constant K differing from K_s. The supramolecular polymerization process of the elongation phase then follows again the isodesmic model but with a different association constant than for the nucleus formation. This kind of cooperativity was designated as *allosteric* since is can be described by similar parameters as cooperative ligand binding.[10]

12

2.4.1 K_2–K Model

Implying that coordination of one of the binding sites influences the equilibrium constant on the other side of a ditopic molecule, the simplest modification of the isodesmic model is to assume, that the dimerization constant K_2 differs from the K values for higher aggregation. Thus, a nucleus with size $s = 2$ is formed, resulting in:[23,37]

$$2M \; \overset{K_2}{\rightleftharpoons} \; M_2 \; \overset{K}{\rightleftharpoons} \; \overset{K}{\rightleftharpoons} \; \ldots \; \overset{K}{\rightleftharpoons} \; M_n$$
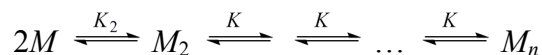
$$K_2 \neq K_3 = \ldots = K_n = K$$

By defining $\sigma = K_2/K$ the concentration of n-mer c_n and the total concentration c_T, respectively, can be obtained as displayed in equations (2.25) and (2.26):

$$c_n = K_2 K^{n-2} c_1^n = \sigma K^{n-1} c_1^n \tag{2.25}$$

$$c_T = c_1 + \sum_{n=2}^{\infty} n \sigma K^{-1} (K c_1)^n = (1 - \sigma) c_1 + \frac{\sigma c_1}{(1 - K c_1)^2} \tag{2.26}$$

with c_1 reflecting the concentration of the monomer species and σ reflecting the ratio of the two equilibrium constants K_2 and K, *i.e.* the more difficult or easier the formation of dimer species is in comparison to the stepwise growth of already aggregated species. Since it is depletive to solve equation (2.26) for general cases, Kc_T is calculated as a function of Kc_1 for given values of σ. Subsequently, α_{agg} can be obtained from this relation.

$$Kc_T = (1 - \sigma) Kc_1 + \frac{\sigma Kc_1}{(1 - Kc_1)^2} \tag{2.27}$$

$$\alpha_{agg} = 1 - \alpha_{mon} = 1 - \frac{Kc_1}{Kc_T} \tag{2.28}$$

Figure 5 depicts the fraction of aggregated molecules α_{agg} plotted as a function of the dimensionless concentration Kc_T for different values of σ. For $\sigma \gg 1$ the dimerization constant is much larger than that for further aggregation, *i.e.* the aggregation process is of anticooperative nature. The transition to extended aggregated species is smooth with a limiting case of $\sigma \to \infty$, implying that $K \approx 0$ which corresponds to the monomer-dimer equilibrium. For $\sigma = 1$ (noncooperative process) equation (2.26) equals that for the isodesmic model (Figure 5, dashed line). For $\sigma \ll 1$ aggregate formation follows a cooperative process with the great majority of the molecules being present as monomers as long as $c_T < K^{-1}$. A sharp increase of α_{agg} at the critical concentration K^{-1} and almost instantaneous the formation of extended aggregates can be observed.
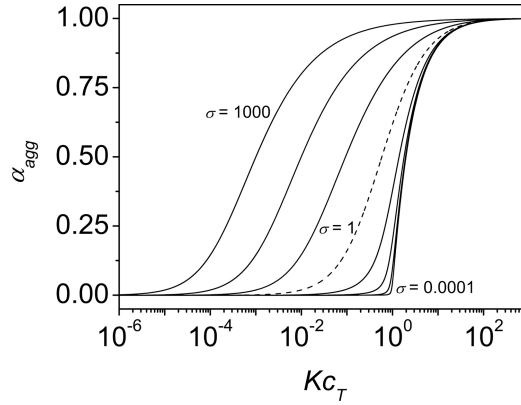
Figure 5. Fraction of aggregated molecules α_{agg} plotted against the dimensionless concentration Kc_T for various values of σ (for the curves from left to right $\sigma = 10^3$, 10^2, 10, 1, 10^{-1}, 10^{-2}, and 10^{-3}) according to the concentration-dependent K_2–K model. The curve for $\sigma = 1$ corresponds to the isodesmic model (dashed line). [23c]

The number- and weight-averaged degrees of polymerization (= aggregation) may be derived according to equations (2.29) and (2.30):

$$DP_N = \frac{\sum_{n=1}^{\infty} nc_n}{\sum_{n=1}^{\infty} c_n} = \frac{c_1 + 2c_2 + 3c_3 + \cdots + nc_n}{c_1 + c_2 + c_3 + \cdots + c_n}$$

$$= \frac{\sigma + (1-\sigma)(1-Kc_1)^2}{\sigma(1-Kc_1) + (1-\sigma)(1-Kc_1)^2} \qquad (2.29)$$

$$DP_W = \frac{\sum_{n=1}^{\infty} n^2 c_n}{\sum_{n=1}^{\infty} nc_n} = \frac{c_1 + 4c_2 + 9c_3 + \cdots + n^2 c_n}{c_1 + 2c_2 + 3c_3 + \cdots + nc_n}$$

$$= \frac{\sigma(1+Kc_1) + (1-\sigma)(1-Kc_1)^3}{\sigma(1-Kc_1) + (1-\sigma)(1-Kc_1)^3} \qquad (2.30)$$

Combining equation (2.27) with equations (2.29) and (2.30), DP_N and DP_W can be plotted as a function of Kc_T (Figure 6). These results illustrate nicely the existence of a critical concentration. When $\sigma \ll 1$ barely any larger species exist below the critical concentration K^{-1}, but both number- and weight-averaged degree of polymerization promptly increase with c_T exceeding K^{-1}. The lower the value of σ the higher the cooperativity is and the higher the DP_N that can be achieved at a particular concentration with a nucleated supramolecular polymerization process is in comparison to isodesmic aggregate formation. Assuming K to remain constant, a decrease of σ corresponds to lower values for K_2. Thus, the number of nuclei, from which extended aggregate formation takes place, decreases, resulting in fewer but larger aggregates.
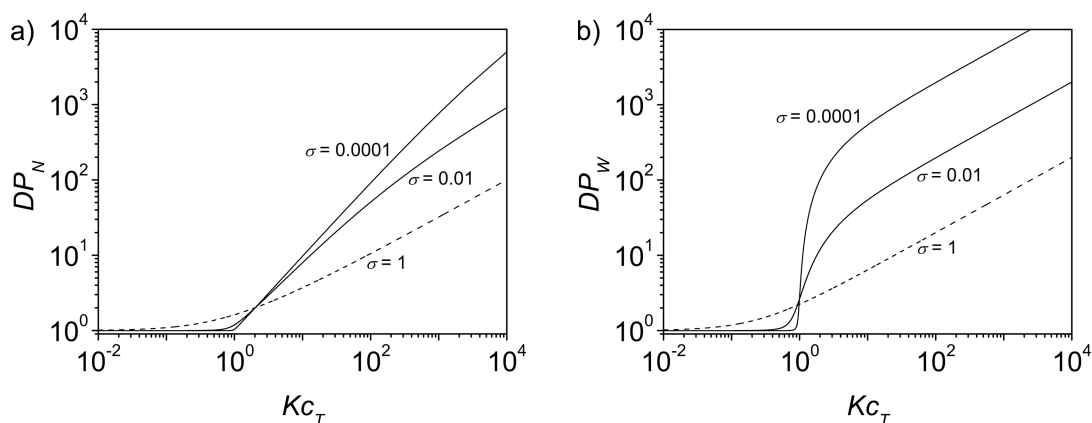
Figure 6. Number-averaged degree of polymerization DP_N (a) and weight-averaged degree of polymerization DP_W (b) plotted as a function of the dimensionless concentration Kc_T according to the concentration-dependent K_2–K model for various values of σ. The curves for $\sigma = 1$ correspond to the isodesmic model (dashed lines). [23d]

2.4.2 Temperature-Dependent Cooperative Growth

The temperature-dependent properties of cooperative supramolecular polymerizations can be treated by means of the model for *thermally activated equilibrium polymers*.[28,38,39] This corresponds to a nucleation–elongation model, with a highly active state being in equilibrium with a weakly active state. The inactive state needs to undergo activation (i.e. nucleation) and the (dimensionless) equilibrium constant describing the transition from inactive to active state is given by K_a. K_a is presumed to be small so that the activated state becomes highly unfavorable. Elongation subsequent to activation involves isodesmic supramolecular polymerization steps governed by (dimensionless) equilibrium constants K_e ($K_e = Kc_T$). The temperature T_e at which activation occurs separates two aggregation regimes. At temperatures higher than T_e the systems is in the nucleation regime, while it is in the elongation regime for temperatures smaller than T_e. The elongation enthalpy ΔH_e is negative for supramolecular polymers that aggregate upon cooling.

$$M \xrightleftharpoons{K_a} M^*$$

$$2M^* \xrightleftharpoons{K} M_2^* \xrightleftharpoons{K} \xrightleftharpoons{K} \ldots \xrightleftharpoons{K} M_n^*$$
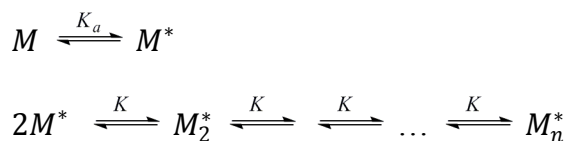
For a given concentration the dimensionless equilibrium constant K_e can be written as:[28b]

$$K_e = e^{\frac{-\Delta H_e}{RT_e^2}(T-T_e)} = 1 - DP_N(T)^{-1} + K_a DP_N(T)(DP_N(T) - 1) \tag{2.31}$$

The fraction of aggregated species $\alpha_{agg}(T)$ is related to the equilibrium constants K_a and K_e and the number-averaged degree of polymerization $DP_N(T)$, averaged over all active species, via:[28b]

$$\alpha_{agg}(T) = \frac{K_a}{K_e} DP_N(T)(DP_N(T) - 1) \tag{2.32}$$

Combination of equations (2.31) and (2.32) yields $\alpha_{agg}(T)$ in the elongation regime ($T < T_e$, equation (2.33)) and in the nucleation regime ($T > T_e$, equation (2.34)), respectively.

$$\alpha_{agg}(T) = 1 - e^{\frac{-\Delta H_e}{RT_e^2}(T - T_e)} \tag{2.33}$$

$$\alpha_{agg}(T) = \sqrt[3]{K_a}\, e^{\left(\frac{2}{3\sqrt[3]{K_a}} - 1\right)\frac{\Delta H_e}{RT_e^2}(T - T_e)} \tag{2.34}$$

The equivalence of the K_2–K model and the thermally activated self-assembly model is shown in the Appendix. Comparison of the two models reveals, that the dimensionless activation constant K_a in the latter model has the same role as the cooperativity parameter σ in the K_2–K model.

The aggregation characteristics of the thermally activated self-assembly model are similar to those of the of the K_2–K model. Low K_a values imply low concentrations of the activated species and in consequence, barely any extended aggregate species are present at temperatures above T_e. Below the critical temperature T_e the fraction of aggregated species increases promptly and the transition becomes sharper with decreasing K_a (Figure 7a). Higher ΔH_e values lead to higher equilibrium constants for the elongation K_e favoring the increase of $\alpha_{agg}(T)$ (Figure 7b).
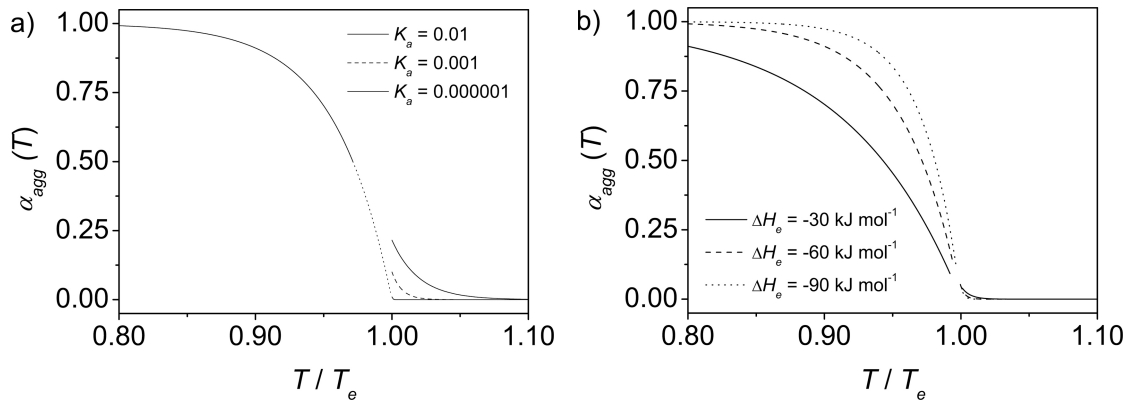
Figure 7. Molar fraction of aggregated molecules $\alpha_{agg}(T)$ plotted against the dimensionless temperature T/T_e for different values of K_a (10^{-2} (solid line), 10^{-3} (dashed line), and 10^{-6} (dotted line) with $\Delta H_e = -60$ kJ mol^{-1} (a), and various values of the temperature-independent enthalpy of aggregation ΔH_e (-30 (solid line), -60 (dashed line), and -90 kJ mol^{-1} (dotted line)) with $K_a = 10^{-4}$ (b) according to the temperature-dependent cooperative supramolecular polymerization model pursuant to van der Schoot.[23d]

Taking into account equations (2.33) to (2.34) the number-averaged degree of polymerization $DP_N(T)$, averaged over all active species, is given by equation (2.35) for the elongation regime and by equation (2.36) at the elongation temperature:[28b,39]

$$DP_N(T) = \frac{1}{\sqrt{K_a}} \frac{\alpha_{agg}}{1 - \alpha_{agg}} = \frac{1}{\sqrt{K_a}} \frac{1 - e^{\frac{-\Delta H_e}{RT_e^2}(T-T_e)}}{e^{\frac{-\Delta H_e}{RT_e^2}(T-T_e)}} \tag{2.35}$$

$$DP_N(T_e) = \frac{1}{\sqrt[3]{K_a}} \tag{2.36}$$

Supramolecular polymers with high $DP_N(T)$ are formed upon elongation of the small fraction of activated monomers below the critical elongation temperature. With increasing cooperativity, higher $DP_N(T)$ values can be reached, similar to the K_2–K model (Figure 8a). Chain growth is prompted by higher elongation enthalpy releases, corresponding to higher equilibrium constants K_e. Therefore, more negative ΔH_e leads to higher $DP_N(T)$ values (Figure 8b). At the critical temperature the number-averaged degree of polymerization is proportional to $K_a^{-1/3}$.
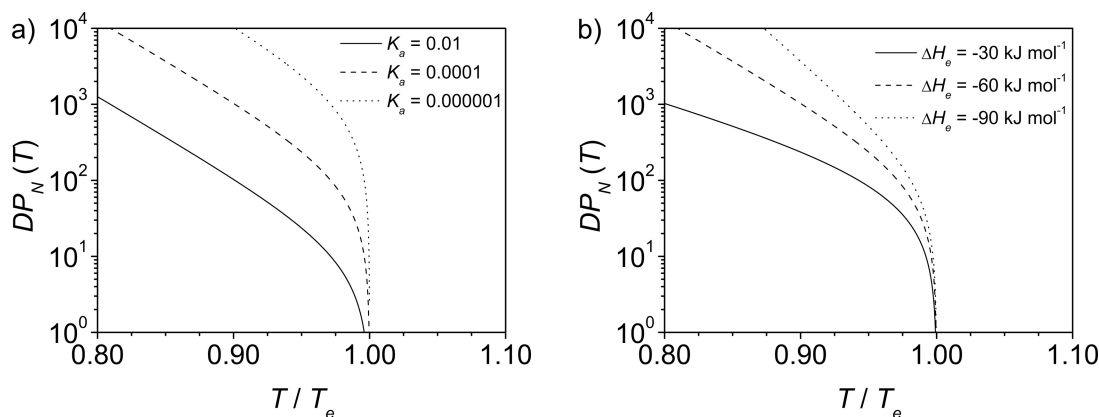
Figure 8. Number-averaged degree of polymerization $DP_N(T)$ as a function of the dimensionless temperature T/T_e for different values of K_a (10^{-2} (solid line), 10^{-4} (dashed line), and 10^{-6} (dotted line) with $\Delta H_e = -60$ kJ mol^{-1} (a), and various values of the temperature-independent enthalpy of aggregation ΔH_e (-30 (solid line), -60 (dashed line), and -90 kJ mol^{-1} (dotted line)) with $K_a = 10^{-4}$ (b) according to the temperature-dependent cooperative supramolecular polymerization model pursuant to van der Schoot.[23d]

2.4.3 General Nucleation–Elongation Model

The nucleation process can become considerably more complex than described by a simple dimer nucleus formation requiring modifications to the K_2–K model described above. The K_2–K model was generalized by Goldstein and Stryer for cooperative aggregation processes taking into account a variable nucleus size.[23d,40] According to this model a nucleus of size s is formed following the isodesmic model with a first equilibrium constant K_s. With the size of the supramolecular polymer reaching s further isodesmic association steps show equilibrium constants of K.

$$2M \underset{K_s}{\overset{K_s}{\rightleftarrows}} M_2 \underset{K_s}{\overset{K_s}{\rightleftarrows}} \ldots \underset{K_s}{\overset{K_s}{\rightleftarrows}} M_s \underset{K}{\overset{K}{\rightleftarrows}} \overset{K}{\rightleftarrows} \ldots \overset{K}{\rightleftarrows} M_n$$

17
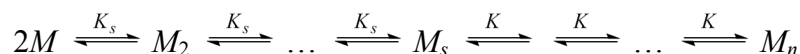
The mass balance equation for a nucleation–elongation supramolecular polymerization process can be expressed as in equation (2.37) giving a relation between the equilibrium monomer concentration c_1 and the total concentration of molecules c_T:[38]

$$Kc_T = \sum_{n=1}^{s} n\sigma^{n-1}(Kc_1)^n + \sum_{n=s+1}^{\infty} n\sigma^{s-1}(Kc_1)^n$$

$$= \frac{s(Kc_1)^s\sigma^{s-1}}{1-Kc_1} + \frac{(Kc_1)^{s+1}\sigma^{s-1}}{(1-Kc_1)^2} + \frac{Kc_1(s(\sigma Kc_1)^{s-1}-1)}{\sigma Kc_1 - 1} \qquad (2.37)$$

$$- \frac{\sigma(Kc_1)^2((\sigma Kc_1)^{s-1}-1)}{(\sigma Kc_1 - 1)^2}$$

where σ reflects again the parameter for the cooperativity defined as K_s/K, and s is the size of the nucleus. Since it is not possible to determine σ alone but only in combination with s, a *cumulative cooperativity* was defined as $\omega = \sigma^{s-1}$.

Similar to the case of the K_2–K model, the fraction of aggregated molecules α_{agg} can be calculated from the relation of Kc_T and Kc_1 using equation (2.37) in combination with equation (2.28). The resulting plots of α_{agg} as a function of the dimensionless concentration Kc_T are depicted in Figure 9. Panel a shows α_{agg} for various values of σ and s but for equal ω. Curves of equal ω show coalescence when the total concentration exceeds the critical concentration, *i.e.* $Kc_T > 1$. In addition, for large nuclei sizes a significant amount of molecules is already polymerized before reaching the critical concentration. α_{agg} for a nucleus size of 4 but for different values of ω is depicted in Figure 9b, with the curves showing less quick coalescence with increasing concentration compared to the situation for fixed ω.
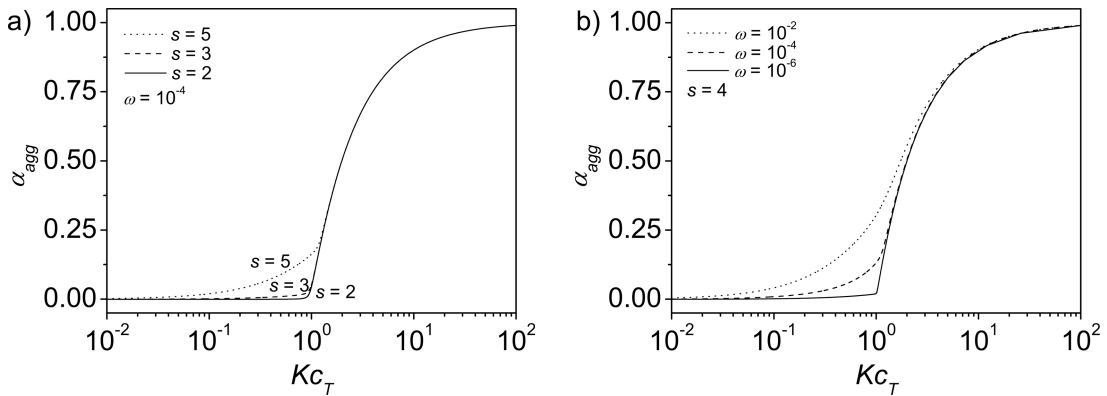
Figure 9. Molar fraction of aggregated molecules α_{agg} plotted against the dimensionless concentration Kc_T according to the general nucleation–elongation model proposed by Goldstein and Stryer: a) α_{agg} for nucleus sizes of 2, 3, and 5 and a cumulative cooperativity of $\omega = 10^{-4}$. b) α_{agg} for a constant nucleus size of 4 and various values of the cumulative cooperativity ($\omega = 10^{-2}$, 10^{-4}, and 10^{-6}).[23d]

Definition of the number-averaged degree of polymerization DP_N applied to the general nucleation–elongation model gives equation (2.38), which can subsequently be transformed to equation (2.39) comprising standard expressions for infinite converging series:[23d]

$$DP_N = \frac{\sum_{n=1}^{\infty} n c_n}{\sum_{n=1}^{\infty} c_n} = \frac{Kc_T}{\sum_{n=1}^{\infty} Kc_n} = \frac{Kc_T}{\sum_{n=1}^{s} \sigma^{n-1}(Kc_1)^n + \sum_{n=s+1}^{\infty} \sigma^{s-1}(Kc_1)^n} \qquad (2.38)$$

$$DP_N = \frac{Kc_T}{\dfrac{(\sigma Kc_1)^{s+1}}{\sigma(\sigma Kc_1 - 1)} - \dfrac{Kc_1}{\sigma Kc_1 - 1} - \dfrac{\sigma^{s-1}(Kc_1)^{s+1}}{Kc_1 - 1}} \qquad (2.39)$$

The weight-averaged degree of polymerization DP_W may be calculated according to equations (2.40) and (2.41), once more making use of standard expressions for infinite converging series:[23d]

$$DP_W = \frac{\sum_{n=1}^{\infty} n^2 c_n}{\sum_{n=1}^{\infty} n c_n} = \frac{\sum_{n=1}^{\infty} n^2 Kc_n}{Kc_T} = \frac{\sum_{n=1}^{\infty} n^2 \sigma^{n-1}(Kc_1)^n + \sum_{n=s+1}^{\infty} n^2 \sigma^{s-1}(Kc_1)^n}{Kc_T} \qquad (2.40)$$

$$DP_W = (\sigma Kc_1)^{s+1}\left(\frac{\dfrac{-2(s+1)\sigma^2(Kc_1)^2 + 2(s+1)\sigma Kc_1 + \sigma^2(Kc_1)^2 + \sigma Kc_1}{\sigma(\sigma Kc_1 - 1)^3}}{Kc_T} \right.$$
$$\left. + \frac{\dfrac{(s+1)^2\sigma^2(Kc_1)^2 - 2(s+1)^2\sigma Kc_1 + (s+1)^2}{\sigma(\sigma Kc_1 - 1)^3}}{Kc_T} \right) - \frac{\dfrac{Kc_1(\sigma Kc_1 + 1)}{(\sigma Kc_1 - 1)^3}}{Kc_T}$$
$$- \frac{\dfrac{\sigma^{s-1}(Kc_1)^{s+1}((Kc_1 - 1)^2 s^2 + (2 - 2Kc_1)s + 1 + Kc_1)}{(Kc_1 - 1)^3}}{Kc_T} \qquad (2.41)$$

Figure 10 shows DP_W plotted as a function of the dimensionless concentration Kc_T. DP_W for various values of σ and s, but for equal cumulative cooperativities ω is depicted in panel a. Although a significant amount of molecules are aggregated below the critical concentration for large nuclei sizes as shown in Figure 9a and 10a it is obvious from the values of DP_W that the system can mainly be allocated to monomers and dimers. As evident from Figure 10b, lower values of ω lead to an instantaneous formation of higher molecular weight species at the critical concentration. By comparing panels a and b in Figure 10 it is evident that the degree of polymerization at higher concentrations is exclusively determined by ω.
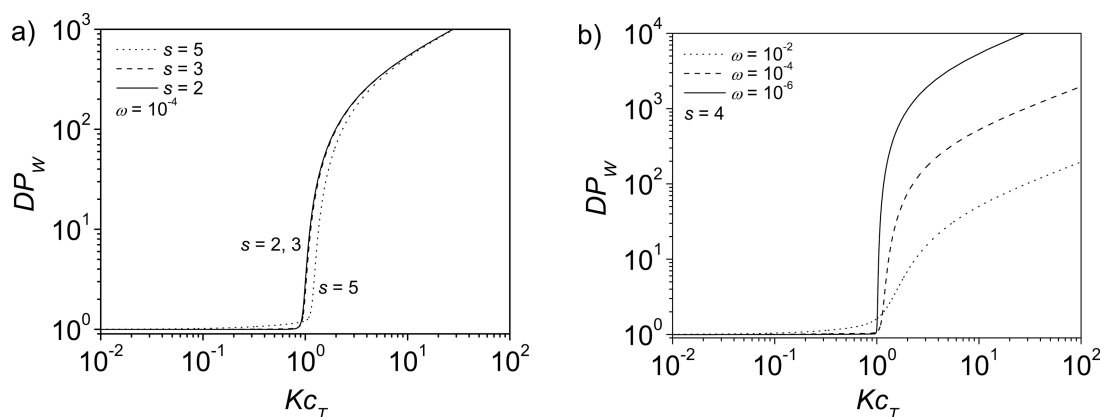
Figure 10. Weight-averaged degree of polymerization DP_W plotted as a function of the dimensionless concentration Kc_T according to the general nucleation–elongation model proposed by Goldstein and Stryer: a) DP_W for nucleus sizes of 2, 3, and 5 and a cumulative cooperativity of $\omega = 10^{-4}$. b) DP_W for a constant nucleus size of 4 and various values of the cumulative cooperativity ($\omega = 10^{-2}$, 10^{-4}, and 10^{-6}).[23d]

Examples for the successful application of nucleation–elongation models include bis-urea-based supramolecular polymers,[41] oligo(*p*-phenylene-vinylenes) equipped with self-complementary ureidotriazine hydrogen bonding units,[38] trialkylbenzene-1,3,5-tricarboxamides,[39] gelators based on aliphatic diamines with lysine units attached to each end,[42] *L,L* dendritic dipeptides,[43] *m*-diethynylbenzene macrocycles in specific solvents,[44] and to perylene bisimide J-aggregates formed by hydrogen-bond-directed π-π stacking.[45]

2.5 Self-Assembly of Closed Oligomeric Systems

A different kind of cooperativity can be observed in systems that allow for intramolecular binding processes. These self-assembly processes are driven by different strengths of intra- and intermolecular interactions. Since such kind of cooperativity is a function of the molecular architecture, this phenomenon was termed *chelate cooperativity*.[10]

The formation of closed oligomeric assemblies of a self-complementary system may be regarded as a special case of the oligomerization to polydisperse open-chain aggregates as discussed in Sections 2.3 and 2.4. In contrast, now one particular oligomer gains additional stabilization owing to the intramolecular interaction, leading to the formation of a closed system. Scheme 1 depicts the formation of a linear chain with no allosteric cooperativity from a self-complementary molecule with one specific oligomer being in equilibrium with its cyclic counterpart. *K* denotes the equilibrium constant for the formation of the linear chain.

$$AB \; \overset{K}{\rightleftharpoons} \; (AB)_2 \; \overset{K}{\rightleftharpoons} \; \cdots \; (AB)_N \; \overset{K}{\rightleftharpoons} \; (AB)_{N+1} \cdots$$

$$\Big\Updownarrow K_c$$

$$c\text{-}(AB)_N$$
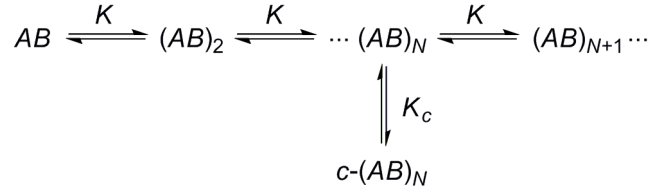
Scheme 1. Self-assembly of oligomers, of which one can form a closed structure, from self-complementary monomers ($\sigma = 1$).[10]

The properties of such a system are governed by the intramolecular equilibrium constant K_c. This interaction can be described in terms of the effective molarity EM:[10]

$$EM = N \frac{K_c}{K} \tag{2.42}$$

This concentration-independent ratio is the molecular parameter, which accounts for the cooperativity of the system. For $K \cdot EM \ll 1$ the closed system is not populated and the system behaves as described in the models above. In the case of $K \cdot EM \gg 1$ the intramolecular equilibrium constant is higher than the one for the chain elongation and the closed species dominates over a wide concentration range.

The formation of the open-chain linear oligomers can be described by the same equations as discussed in Section 2.3:

$$c_n = \sigma K^{n-1} c_1^n \tag{2.43}$$

where σ represents the parameter for the allosteric cooperativity as defined in Section 2.3.1. Taking into account equation (2.43), the concentration of bound A sites can be expressed by equation (2.44) after simplification as Taylor series expansion:

$$c_{bound \; A \; sites} = \sum_{n=2}^{\infty} (n-1)c_n = \sigma \sum_{n=2}^{\infty} (n-1)K^{n-1} c_1^n = \sigma c_1 \sum_{n=1}^{\infty} n(Kc_1)^n$$

$$\approx \frac{\sigma K c_1^2}{(1 - Kc_1)^2} \tag{2.44}$$

Similarly, the concentration of unbound A sites can be derived:

$$c_{unbound \; A \; sites} = \sum_{n=2}^{\infty} c_n = \sigma \sum_{n=2}^{\infty} K^{n-1} c_1^n = \sigma c_1 \sum_{n=1}^{\infty} (Kc_1)^n \approx \frac{\sigma K c_1^2}{(1 - Kc_1)} \tag{2.45}$$

In addition, the formation of the closed system needs to be considered. The concentration of the closed oligomer c_{cN} can be written as:

$$c_{cN} = \frac{1}{N} K^N \cdot EM c_1^N \tag{2.46}$$

where N is the number of molecules in the oligomer that is stabilized by an additional intramolecular interaction. Employing equations (2.44)–(2.46), the total concentration c_T may be expressed by equation (2.47):

$$c_T = c_1 + c_{bound\ A\ sites} + c_{unbound\ A\ sites} + Nc_{cN}$$
$$= \frac{c_1\{\sigma^{-1}(1 - Kc_1)^2 + Kc_1(2 - Kc_1)\}}{\sigma^{-1}(1 - Kc_1)^2} + K^N \cdot EMc_1{}^N \quad (2.47)$$

Combination of equations (2.44), (2.46), and (2.47) yields the molar fraction of aggregated species α_{agg}:

$$\alpha_{agg} = \frac{c_{bound\ A\ sites} + Nc_{cN}}{c_T}$$
$$= \frac{\sigma^{-1}(1 - Kc_1)^2 K \cdot EM(Kc_1)^{N-1} + Kc_1}{\sigma^{-1}(1 - Kc_1)^2\{1 + K \cdot EM(Kc_1)^{N-1}\} + Kc_1(2 - Kc_1)} \quad (2.48)$$

The molar fraction of aggregated species α_{agg} as a function of the normalized dimensionless concentration $\log K'c_T$ ($K' = 1/c_{50}$, where c_{50} corresponds to the concentration at which $\alpha_{agg} = 0.5$) is depicted in Figure 11. The curves were calculated assuming no allosteric cooperativity ($\sigma = 1$). In the regime of strong chelate cooperativity ($K \cdot EM \gg N$), a sharp increase of α_{agg} can be observed for high values of N. At high concentrations, the shape of the curves for different N values is similar, while it shows significant deviations below $\log K'c_T = 0$.
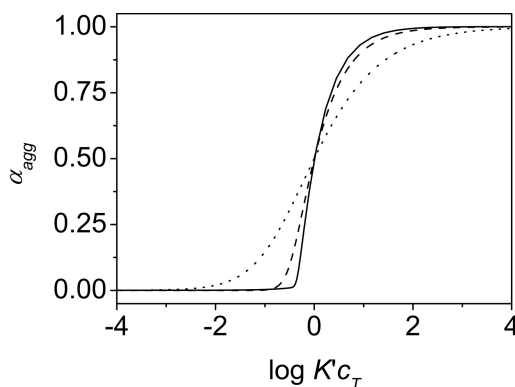
Figure 11. Fraction of aggregated molecules α_{agg} plotted against the normalized dimensionless concentration $\log K'c_T$ for various values of N ($N = 2$ (dotted line), 5 (dashed line), and 20 (solid line)) for the self-assembly of oligomers of which one can form a closed system.[10] The binding isotherms are in the regime of strong chelate cooperativity ($K \cdot EM \gg N$) and K is set to 10^5 M^{-1}. No allosteric cooperativity is assumed ($\sigma = 1$). The abscissa is calculated taking into account $K' = \frac{1}{2} (K^N \cdot EM)^{1/N-1} = 1/c_{50}$, where c_{50} corresponds to the concentration at which $\alpha_{agg} = 0.5$.

2.6 Other Models

According to Meijer et al., three main growth mechanisms for supramolecular polymers can be distinguished.[23d] Up to now, two of these mechanisms were discussed in sections 2.3 and 2.4, namely, *isodesmic* and *cooperative* processes. An example for the covalent counterpart for isodesmic processes is the step-by-step reversible polycondensation of polyesters.[46] Cooperative covalent polymer formation can be found for the acid-initiated polymerization of isocyanides to helical polymers.[47] A special case of the third major aggregation mechanism, i.e. ring–chain equilibria, was covered in section 2.5. Generally, *ring–chain supramolecular polymerizations* represent the reversible aggregation of ditopic monomers with each linear aggregate being in equilibrium with its cyclic counterpart. Presuming that the linker, which separates the two binding units, incorporates flexibility, most step growth aggregation processes contain macrocyclic byproducts. Theoretical description of linear supramolecular oligomers and polymers being in thermodynamic equilibrium with their cyclic equivalents was allocated and existence of a critical concentration below which the system is only composed of cyclic products was shown.[48] The assumptions of this theory, including the conformational requirements of the spacer, were recently summarized.[49] Covalent counterparts for this growth mechanism include the formation of macrocyclic oligomers of ω-hydroxy-*n*-alkyl carboxylic acids.[50]

2.7 Conclusions

Progresses in supramolecular chemistry enabled the construction of a multitude of finite and infinite architectures that are reversibly formed by noncovalent interactions. Proper analysis of such systems in terms of their thermodynamics plays a crucial role to derive design criteria for the purposeful construction of new assemblies. The current compilation provided models for the interpretation of experimental data for dimeric, oligomeric, and polymeric aggregates. Mechanisms for supramolecular polymerization include the concentration- and temperature-dependent isodesmic and cooperative formation of linear polymers. In contrast to the allosteric cooperativity which may be present in the formation of polydisperse open oligomers and polymers, the formation of closed systems involves chelate cooperativity, arising from differences between intra- and intermolecular equilibrium constants. Thus, this chapter adds to a basic understanding of the thermodynamics of chemical equilibria for aggregation and to the thorough investigation of noncovalent systems.

Chapter 3

Dipolar Interactions as Directional Noncovalent Forces in Supramolecular Chemistry

Abstract: In this Chapter, hydrogen bonding and dipole-dipole interactions between dipolar merocyanine dyes are discussed as special cases of dipolar interactions and are compared in terms of their respective binding strength. Special emphasis is given on the directionality of these two types of interactions. Experimental data for more than 130 different systems in chloroform solution, including single and multiple hydrogen bonding entities with various donor acceptor arrays, and dipolar interactions between single bonds and highly dipolar merocyanine dyes, are compiled to compare the free interaction energies. Comparison based on the ratio of the free energy and the area of the respective interaction gives further insight into the relative strengths of these different types of dipolar interactions. Such comparison establishes that dipolar interactions of merocyanine dyes are most suitable noncovalent forces in supramolecular chemistry.

3.1 Introduction

Intermolecular forces may roughly be divided into three categories.[52] The first category incloses the interactions between charges, permanent dipoles and further multipoles that are purely of electrostatic nature. They can be described by Coulomb forces between charges. The second category comprises static polarization forces which originate from induced dipole moments, including interactions between permanent and induced dipole moments (Debye interactions), as well as dynamic polarization between instantaneously induced multipole moments arising from quantum mechanical electron correlation between two interacting molecules (dispersion interaction). Third, orbital interactions give rise to forces that are quantum mechanical in origin, involving charge transfer and exchange interactions. Because of their particular importance some interactions that combine different contributions of electrostatic, polarization, and orbital interactions have been given special denotations. The free energies for the angle averaged dipole-dipole interaction of rotating permanent dipoles (Keesom interaction), Debye interaction, and dispersion interaction contribute to the van der Waals interaction.[52] Hydrophobic or more general solvophobic effects are one of the major driving forces for aggregation of π systems in appropriate solvents,[53] that are strongly affected by entropic effects. Dispersion interactions exhibit the major contribution to the magnitude of π–π interactions, while electrostatic interactions account for the geometry.[54] Although hydrogen bonds involve different contributions, they are strongly governed by electrostatics.[55]

Electrostatic interactions, especially those between dipolar molecules or dipolar groups, are of particular significance for the arrangement of molecules in supramolecular assemblies owing to their directional character. However, dipole-dipole interactions usually do not provide the largest contribution to the overall interaction energy. The latter is often dominated by dispersion forces. Hydrogen bonds represent an exception due to the proximity of the involved groups. The extraordinary situation of eminently small distances emerges from the small size of the proton. Owing to the r^{-3} distance dependence between two dipoles, a strong interaction results from the law of electrostatic attraction.

In the present chapter, data will be discussed that establish a second exception which is found for merocyanine dyes with large dipole moments. The large dipole moments of these chromophores are a consequence of their, to some extent, zwitterionic character (Scheme 1). In analogy to hydrogen bonds, electrostatic interactions in merocyanine dye aggregates are capable of accounting for the largest contribution to the overall intermolecular interaction.
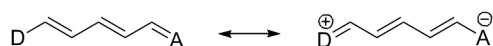
Scheme 1. Mesomeric structures for merocyanines that can be classified as polyene-type (left structure dominates), betaine-type (right structure dominates) and cyanine-type (or polymethine-type with equal contributions of the two structures).[56]

3.2 General Aspects of Dipole-Dipole Interactions

3.2.1 Definition

Upon placing one dipole in the field of another dipole, an interaction occurs that arises from the attraction between partially positively and partially negatively charged termini. If two dipolar bonds or molecules are in close proximity they will experience a dipole-dipole interaction. The permanent dipole moment of a molecule may be estimated by summation of the bond moment vectors. Simple electrostatic theory can be employed to calculate the interaction between two geometrically fixed dipoles.[52]

3.2.2 Geometrical Considerations

The electrostatic nature of the interaction accounts for the directionality and leads to a preferential orientation of the dipoles in which positively charged ends interact with negatively charged ends. The energy for two point dipoles μ_g in a fixed geometry can be calculated according to equation (3.1):[52]

$$E = -\frac{\mu_g^2}{4\pi\varepsilon_0\varepsilon_r r^3}(2\cos\alpha_1\cos\alpha_2 - \sin\alpha_1\sin\alpha_2\cos\beta) \tag{3.1}$$

where ε_0 the permittivity of free space, ε_r the relative permittivity of the solvent, and r the distance between the centers of the dipoles. Angles α and β are defined in Scheme 2. According to equation (3.1) the attractive force is maximized for the two dipoles in a linear parallel arrangement ($\alpha_1 = \alpha_2 = \beta = 0°$), while half of this value is obtained for an antiparallel geometry ($\alpha_1 = \alpha_2 = 90°$, $\beta = 180°$), given that the value for r remains constant.

The linear arrangement can be found for hydrogen bonds, due to the small dimension of the proton. Therefore, hydrogen bonds are often governed by electrostatics. A second exceptional case, which is dominated by dipole-dipole interactions, was found for highly dipolar merocyanine dyes.[14] Owing to their anisotropic dimensions (long molecules with the possibility for a rather short π-π distance) the largest possible dipolar interaction of these dyes is given in an antiparallel arrangement.[14] These two exceptions are discussed in the following and compared with each other.
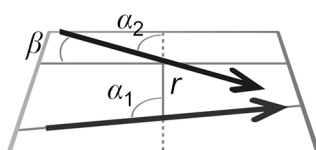
Scheme 2. Schematic representation of two dipoles in fixed geometries. r is the distance between the centers of the dipoles, angles α_1 and α_2 depict the in-plane rotation and β shows the out-of-plane rotation.

3.3 Hydrogen Bonds

3.3.1 Definition

Hydrogen bonds that connect two atoms which have electronegativities larger than that of hydrogen involve close contact of a donor (D) bearing an available hydrogen and an acceptor (A) providing a lone pair of electrons.[13c] Hydrogen bonds can also involve interactions between partially positively charged hydrogen atoms and π systems.[57]

Numerous theoretical approaches to characterize hydrogen bonds can be found in the literature. Early descriptions of hydrogen bonds suggested interactions purely based on electrostatics, arguing that hydrogen can only form one covalent bond.[58] Therefore the second interaction was supposed to arise from electrostatic forces between the partially positive hydrogen and a lone pair of an adjacent acceptor. Even though electrostatic models were quite successful to rationalize certain aspects of hydrogen bonds, there are convincing arguments against such simplified descriptions. Nowadays, more sophisticated theoretical models indicate a complex interplay of several contributions involving electrostatic or Coulomb energy, charge-transfer energy, polarization energy, dispersion forces, and exchange repulsion.[55,59] Nevertheless, electrostatic interactions are dominant in the majority of cases. The theory developed by Bader (Atoms in Molecules, AIM) has extensively been used in the past decade to study hydrogen bonds based on electron density distributions.[60]

3.3.2 Geometrical Considerations

Imparting the directional character, the optimal geometry of the hydrogen bond is collinear with respect to the three atoms involved (Scheme 3), although deviations can be accepted. Such arrangement results from the angle dependence of the law of electrostatic attraction (equation (3.1)) and the exceptionally small size of the proton. The preference for a linear geometry was demonstrated for intramolecular hydrogen bonding in a homologous series of diamides.[61] Furthermore, as evidenced by analysis of gas phase dimers, organic crystals, and of a multitude of amide bonds in proteins, the D–H bond axis of the donor bearing the hydrogen atom commonly coincides with the imaginary axis of a nonbonded electron pair of the acceptor.[62] If there are no lone pairs present in the acceptor but π bonds, the D–H axis intersects the bond connecting the two atoms that form the π bond and is perpendicular to the plane of symmetry of the π bond. A linear geometry is expected for acceptors bearing only one lone pair. Since the polarization energy, dispersion forces, and exchange repulsion are effectively angle insensitive, the ideal geometry arises from a compromise between the optimal angle for the electrostatic interaction and the charge-transfer energy.[55] The valence shell electron pair repulsion (VSEPR) theory[63] can be consulted to rationalize the observed

angles with two electron lone pairs. The equilibrium angle in the HF–H_2O dimer is close to the expected tetrahedral arrangement (Scheme 3). The hydrogen bond should be in one plane and at an angle of approximately 60° for carbonyl compounds with the angle defined in Scheme 3. In accordance with these considerations, thorough analysis of crystallographic data and rotational spectra in the gas phase revealed a distribution with a maximum at 55°.[62,64] However, since for many hydrogen bonds electrostatic interactions dominate, there is only a slight preference towards the direction of the acceptor electron lone pairs.[62a] Deviations for hydrogen bonds between amide groups in proteins were ascribed to the demands for repetitions in helical structures.[65]
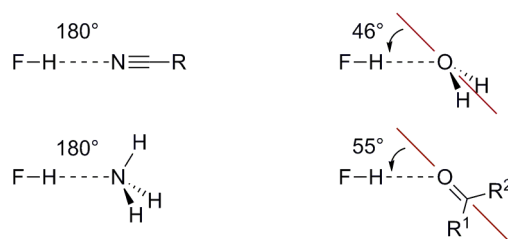
Scheme 3. Some examples of experimentally determined hydrogen bond geometries.[62,66]
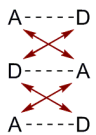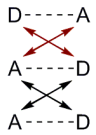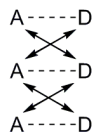
3.3.3 Interaction Energy

In the gas phase, binding energies of hydrogen bonds are usually around 5–100 kJ mol^{-1}, which is in between covalent bonds and dispersion forces.[67] These values can significantly increase if the involved species become charged. Individual hydrogen bonds are very sensitive to the nature of the donor and the acceptor. Owing to their high electronegativities, the strongest hydrogen bonds are formed of acceptor atoms N, O, and the donor HF, indicating that in many cases a simple electrostatic model sufficiently describes such interactions. In this context, three types of hydrogen bonds can be distinguished. Most hydrogen bonds are weak, showing a double-well potential with a significant energy barrier between the distinct zero-point energies of the hydrogen attached to either donor or acceptor. If the distance between the heteroatoms is shortened and the zero-point energies assimilate, the energy barrier is decreased leading to strong low-barrier and no-barrier hydrogen bonds. While the latter type of hydrogen bond involves some extent of covalent bonding, the first two types are dominated by electrostatic interactions.[55] Since for strong hydrogen bonds the zero-point energies are similar their pK_a values are nearly equal. Therefore, the primary hydrogen bond strength for strong hydrogen bonds and for hydrogen atoms attached to the same kind of heteroatom depends on the acidity of the donor site and the basicity of the acceptor site.[66,68] It is generally not possible to sort out the relative contributions of individual contacts in complicated complexes such as DNA base pairs. However, it is possible to order

the stability of structurally similar complexes on measured pK_a values or expected relative acidities or basicities.

Owing to the limited strength of single hydrogen bonds, cooperativity is required in order to create defined and stable architectures.[13a,c] This can be achieved by combining hydrogen bonds with other noncovalent interactions or with themselves to multiple hydrogen bonding entities. Cooperativity may be regarded as an entropic effect since the first hydrogen bonds overcome most of the entropic deficit, while the enthalpy gain linearly increases with the number of hydrogen bonds.[69]

Beside the number of hydrogen bonds, the arrangement of donor and acceptor groups affects to a large extent the free binding energy as recognized for experiments on the association of linear triple hydrogen bonding entities (Scheme 4). Jorgensen computationally confirmed experimental results for different triply hydrogen-bonded complexes displaying K_a values that span several orders of magnitude.[70] These observations were attributed to secondary electrostatic interactions that vary for different donor-acceptor arrays. Owing to their close spatial proximity, adjacent donor and acceptor groups contribute significantly to the stability of the complex. The number of attractive secondary interactions is maximized for the DDD:AAA motif, while for ADA:DAD arrays the number of repulsive interactions is developed for the maximum. To predict free binding energies for different complexes Schneider postulated a linear relationship based on empirical increments.[71] Each primary hydrogen bond contributes 7.9 kJ mol^{-1} to the total complexation energy and each attractive or repulsive secondary interaction adds $\pm$ 2.9 kJ mol^{-1}.

	Experimental data	Calculated values (Schneider's rule)
A-----D D-----A A-----D	$K_a = 10^1 - 10^3$ M^{-1} $-\triangle G° = 4 - 17$ kJ mol^{-1}	$-\triangle G° = 12$ kJ mol^{-1}
D-----A A-----D A-----D	$K_a = 10^4 - 10^5$ M^{-1} $-\triangle G° = 23 - 29$ kJ mol^{-1}	$-\triangle G° = 24$ kJ mol^{-1}
A-----D A-----D A-----D	$K_a > 10^5$ M^{-1} $-\triangle G° > 30$ kJ mol^{-1}	$-\triangle G° = 35$ kJ mol^{-1}

\------ primary hydrogen bond

$\longleftrightarrow$ attractive secondary interaction $\longleftrightarrow$ repulsive secondary interaction

Scheme 4. Thermodynamic stability of triple hydrogen bonding entities with different donor-acceptor arrays. A denotes a hydrogen bonding acceptor site and D a hydrogen bonding donor site.[13d]

Among the many other factors, influencing the free binding energy of hydrogen bonds, are additional electrostatic effects that differ to those originating from primary and secondary contacts. Generally, hydrogen bonds are stronger if donor or acceptor or both are charged.[72] Resonance and polarization enhanced hydrogen bonds also benefit from increased electrostatic interactions.[73,74]

Different tautomeric forms of molecules bearing hydrogen bonding motifs can affect the free binding energy of the complex and its specificity. This was suggested for DNA base pairs[75] and studied for synthetic biomimetic systems like diaminohydropyridines,[76] and ureidopyrimidones[77].

Structurally related complexes, varying in their degree of preorganization, show different binding constants. The relatively higher stability of the dimers build up from certain acylated diaminotriazines and diaminopyrimidines was attributed to intramolecular hydrogen bonds.[78] Discrepancies in the free binding energies of complexes of several ethoxynaphthyridines and guanin were ascribed to conformational effects.[79]

In addition, the solvent influences to a great extent the strength of hydrogen bonds. While the interaction appears to be stronger in nonpolar solvents, it is considerably decreased in polar solvents.[80] Various polar solvents are competitive and have the ability to form hydrogen bonds themselves, making the solvent an important parameter in the determination of the hydrogen bond strength. Several solvent scales correlate with the solvents capability to form hydrogen bonds.[18b,81,82]

3.4 Dipole-Dipole Interactions Between Highly Dipolar Merocyanine Dyes

3.4.1 Definition

The formation of centrosymmetric dimer aggregates already in rather dilute solutions, arising predominantly from dipole-dipole interactions of the dipolar merocyanine chromophores, has been demonstrated by Würthner and coworkers.[14] Directing such antiparallel dimerization, the exceedingly high ground state dipole moments of merocyanine dyes with cyanine-type or betaine-type ground state electron configuration (Scheme 1) were ascribed to a major contribution of zwitterionic resonance structures which benefit from a gain of aromaticity in the two heterocyclic subunits (Scheme 5).[83]
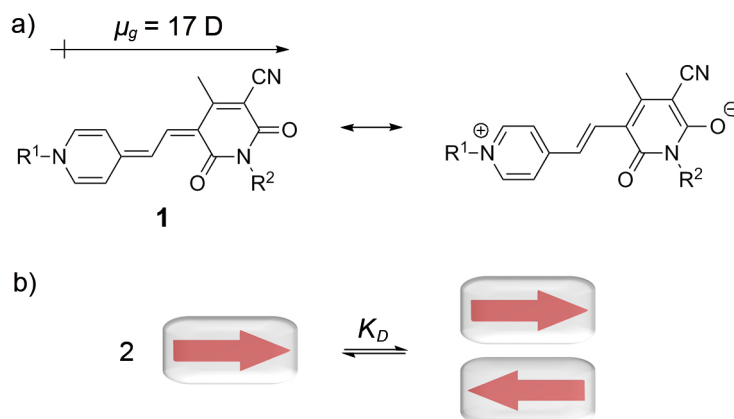
Scheme 5. a) Resonance structures of highly dipolar merocyanine dyes **1**. b) Schematic representation of the dipolar aggregation of highly dipolar merocyanine dyes into centrosymmetric dimers.

3.4.2 Geometrical Considerations

As pointed out before, for the same values of r the linear parallel geometry is energetically more favorable than the antiparallel one (equation (3.1)). Most dipolar molecules are, however, not spherical but anisotropic, with the dipole moment directed along the long axis of the molecule. Therefore, merocyanine dyes can spatially approach each other considerably closer in an antiparallel arrangement, favoring this geometry. The energy for an antiparallel orientation with a translational offset, as schematically depicted in Scheme 6, can be obtained from equation (3.2).

$$\Delta G^0 = -\frac{N_A \mu_g^2}{4\pi\varepsilon_0\varepsilon_r r^3}(3\cos^2\gamma - 1) \tag{3.2}$$

For an angle γ of ~54.7°, the interaction vanishes since the $3\cos^2\gamma - 1$ term becomes zero. Such antiparallel arrangements with γ close to 90° were proven to be predominant for anisotropic dipolar merocyanine dyes without steric constraints in solution (Figure 1).[14]
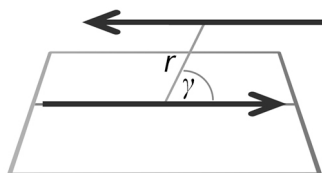
Scheme 6. Schematic representation of two dipoles in fixed geometries. r is the distance between the centers of the dipoles and γ the slip angle, resulting from the translational offset.
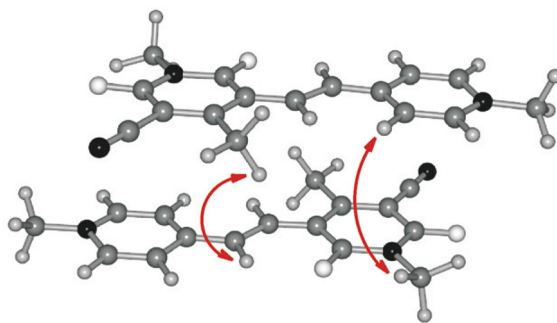
Figure 1. Structural model for the dimeric unit of a merocyanine dye in solution based on NMR studies and AM1 geometry-optimized molecules. The curved arrows indicate spatial proximities as evidenced by ROESY NMR cross coupling peaks. All alkyl substituents were replaced by methyl for simplicity.[14]

3.4.3 Interaction Energy

Beside the relative orientation, dipole-dipole interactions decisively depend on the magnitude of the dipole moments involved and on their relative distance. The interaction energy drops off with inverse third power of the interspace. Hence, at distances in the order of molecular separations, interactions between small bond dipoles account for the organization of some crystal lattices,[84] but were found to only play a minor role in solution. This situation changes for very dipolar molecules like merocyanine dyes. The dipole moments of such molecules decisively depend on the strength of the donor and the acceptor entities and the length of the methine bridge.[85] Design strategies for the optimization of the dipole moment by proper variation of the donor and the acceptor moieties have been established by Würthner and coworkers.[14,86] A variety of merocyanine dyes with different dipole moments has been synthesized and their dimerization has been studied (Figure 2). Many mono- and dimethine dyes beyond the cyanine limit were found to interact strongly with each other in solution and an electrostatic model could be applied for the free interaction energy.[14] One of the major contributions to the interaction energy arises from the interaction of the monomer dipole moments and has been described employing equation (3.2). A linear relationship between $\Delta G°$ and μ_g^2 has been found for sterically noncrowded merocyanines supporting the expectation that the dimerization energy is a function of the dipole moment (see equation (3.3) (vide infra) and Figure 2b).[14b]

However, DFT calculations with dispersion correction (further denoted as DFT-D) revealed that, beside the major electrostatic part, a considerable fraction of the total interaction energy is due to dispersion interactions.[87] The major contributions to the overall interaction energy were found to arise from electrostatic interactions between the dipolar dyes, exchange repulsion, and dispersion interactions. These results could be confirmed by computing dimers of a series of merocyanines on RI-DFT-D (B97-d/TZV(P)) level and subsequently performing
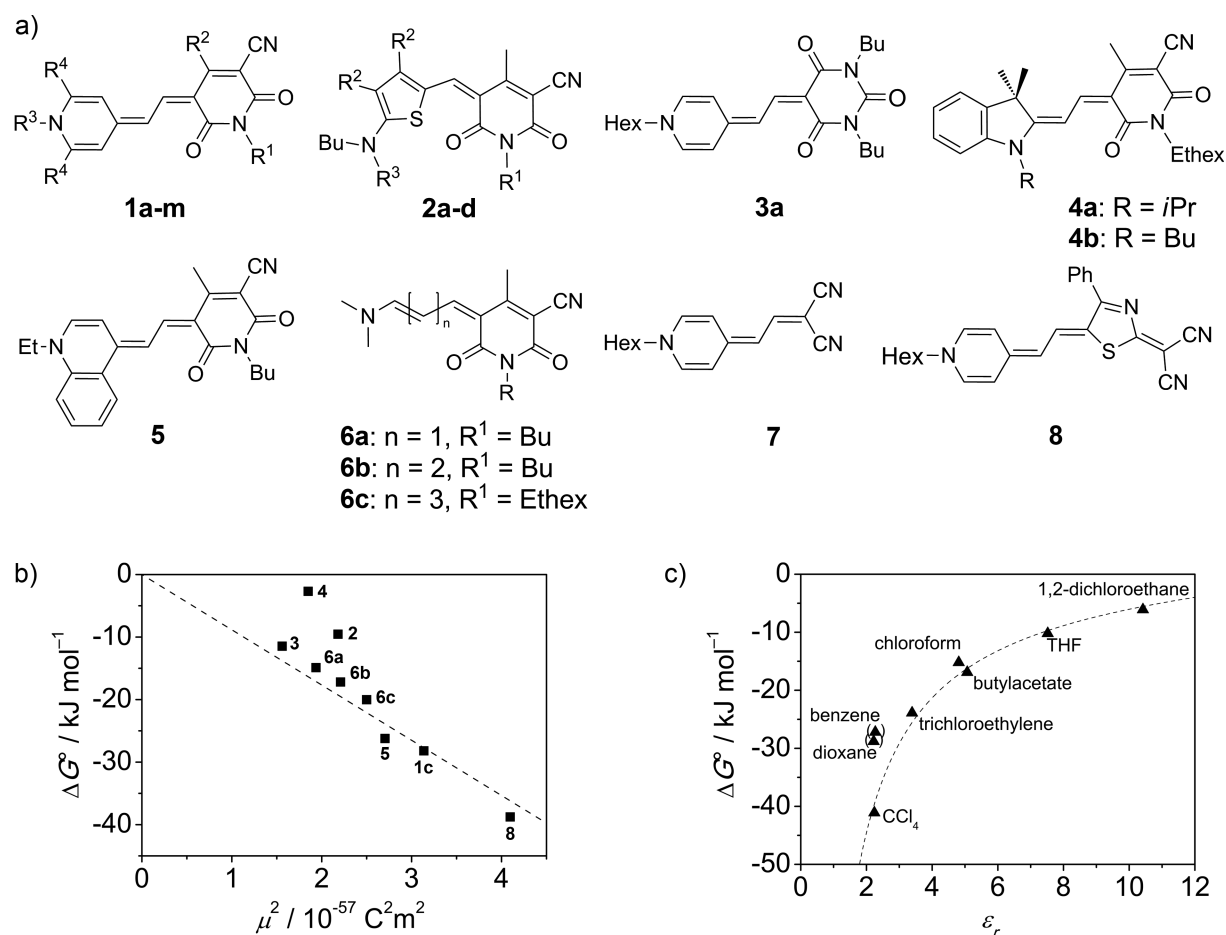
Figure 2. a) Structures of merocyanine dyes with different dipole moments and aggregation properties. b) Dependence of the Gibbs dimerization energies measured in 1,4-dioxane on the ground state dipole moments of the dyes and linear regression analysis. The deviation of dye **2** is a result of the bent-shaped chromophore unit while the deviation of dye **4** can be attributed to the strong sterical effect of the 3,3-dimethylmethylene group.[14] c) Dependence of the Gibbs dimerization energy of dye **1a** (R^1, R^3 = 1-dodecyl, R^2 = methyl, R^4 = H) on the solvent permittivity and nonlinear regression analysis according to equation (3.3). The data for benzene and 1,4-dioxane were neglected.[14]

an energy decomposition analysis (EDA).[88,i] The computational details for such calculations are given in the Appendix. Merocyanine dyes **1–4**, **9**, and **10** show varying dipole moments owing to substitution with donor and acceptor functionalities of different strengths (Figure 3, Table 1). Antiparallel dimers without translational offset are formed from dyes **1–3** (Figure 3a), while dyes **4**, **9**, and **10** are arranged in geometries with noticeable slip angles (Figure 3b). Table 1 summarizes the results obtained from the EDA. Both, the absolute value of the electrostatic interaction as well as the ratio of the electrostatic and the dispersion interaction decrease with decreasing dipole moment of the monomer within the respective series. The total interaction energy also decreases with decreasing dipole moment, justifying that the simple electrostatic model given above yields correct trends. Calculated electrostatic

---

[i] Energy decomposition analysis was carried out in collaboration with PD Dr. Reinhold Fink.
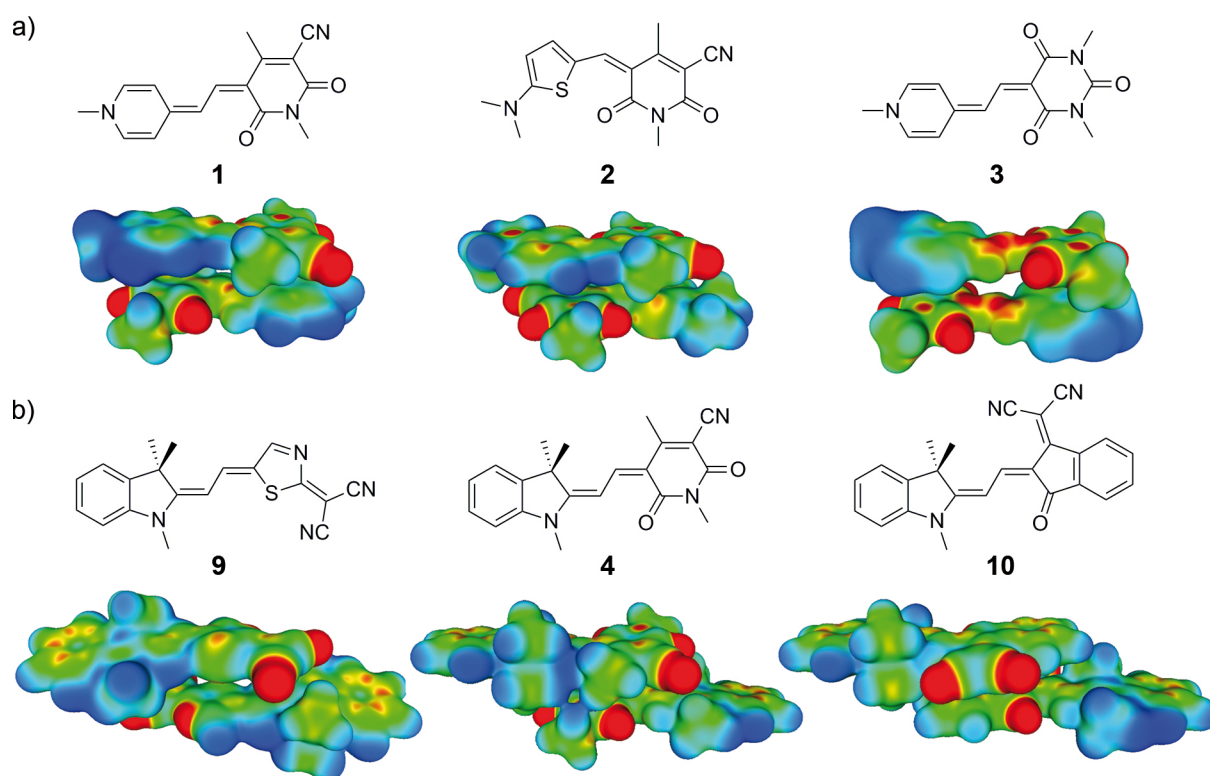
Figure 3. Structures of merocyanine dyes **1–4**, **9**, and **10** and electrostatic potential maps for the respective dimer from RI-DFT-D (B97-d/TZV(P)) calculations generated at an isodensity of 0.05 a.u.. Electron-deficient and electron-rich areas are indicated in blue and red, respectively.

Table 1. Monomer ground state dipole moments μ_g (D)^a of dyes **1–4**, **9**, and **10** calculated on RI-DFT-D (B97-d/TZV(P)) level and results of the EDA for the respective dimer. The electrostatic interaction energy E_{es}, the exchange repulsion energy E_{exr}, the relaxation energy E_{rel}, the dispersion interaction energy E_{disp}, and the total interaction energy E_{tot} are given in kcal mol^{-1}.

dye	$\mu_g{}^a$	E_{es}	E_{exr}	E_{rel}	E_{disp}	E_{tot}	E_{el}/E_{disp}
1	19.8	−115.5	116.7	−16.9	−41.6	−57.3	2.78
2	14.8	−95.2	103.6	−11.6	−40.5	−43.7	2.35
3	12.2	−35.1	37.8	−4.9	−25.8	−28.1	1.25
9	17.5	−73.6	75.5	−9.9	−29.1	−37.2	2.53
4	13.9	−75.6	84.1	−10.1	−33.7	−35.3	2.24
10	8.6	−55.9	73.2	−4.7	−31.4	−18.8	1.78

^{a} Calculated for the geometry-optimized monomers.

potential maps of the dimers further substantiate these results, showing decreasing zwitterionic character with decreasing dipole moment of the monomer (Figure 3).

Experimental binding studies furthermore show that the Gibbs free binding energies exhibit a pronounced solvent dependency. Polar solvents interact with the dipole moment of the molecule, lowering the energy of the monomers relative to an antiparallel dimer with vanishing dipole moment (Figure 4).[14] In contrast, nonpolar solvents strongly favor the aggregation of the dipoles to a centrosymmetric species with no resulting dipole moment.

Both contributions may be treated by electrostatic theory approximating the solvent as a dielectric continuum with permittivity ε_r.[89] By addition of the corresponding term that describes the interaction of the monomer dipole moment with the reaction field of the solvent to equation (3.2), equation (3.3) is obtained. This expression yields an excellent prediction of the dependence of the Gibbs dimerization energy on the solvent permittivity (Figure 2c).[14] In this equation, *a* corresponds to the Onsager radius of the solvent cavity. The good fit of equation (3.3) for a large variety of solvents strongly supports the appropriateness of such simple electrostatic model.

$$\Delta G^0 = -\frac{N_A \mu_g^2}{4\pi\varepsilon_0\varepsilon_r r^3}(3\cos^2\gamma - 1) + \frac{2N_A\mu_g^2}{4\pi\varepsilon_0 a^3}\frac{(\varepsilon_r - 1)(\varepsilon_r + 2)}{9\varepsilon_r} \tag{3.3}$$
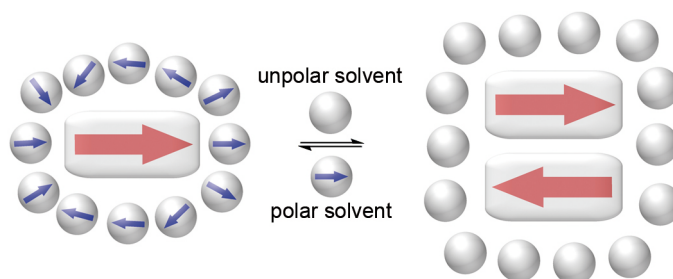
Figure 4. Schematic representation of the stabilization of the monomer in dipolar solvents and dipole-induced dimerization in nonpolar solvents.

3.5 Gibbs Free Binding Energy Comparison of Hydrogen Bonds and Dipole-Dipole Interactions Between Merocyanine Dyes

Experimental data for free binding energies in chloroform solution for selected single, double, triple, quadruple, and sextuple hydrogen binding entities[90–95] are compared with dipole-dipole interactions between single bond dipoles[96,97] and highly dipolar merocyanine dyes[14,15a] (Figure 5). The present comparison of hydrogen bonds and antiparallel dipolar aggregation of merocyanine dyes in chloroform disfavors the latter since the aggregation of such chromophores is well-known to be unfavorable in this particular solvent. Hydrogen bonds, however, are known to be rather strong in chloroform. Thus, the relative strength will change in favor of merocyanine aggregation in most other solvents.

Examples for single hydrogen bonds include the interaction between different phenol derivatives and several bases[91b] as well as pyridine and carboxylic acids.[91c] Double, triple and quadruple hydrogen bonding arrays are by far the most studied. Twofold hydrogen bonding
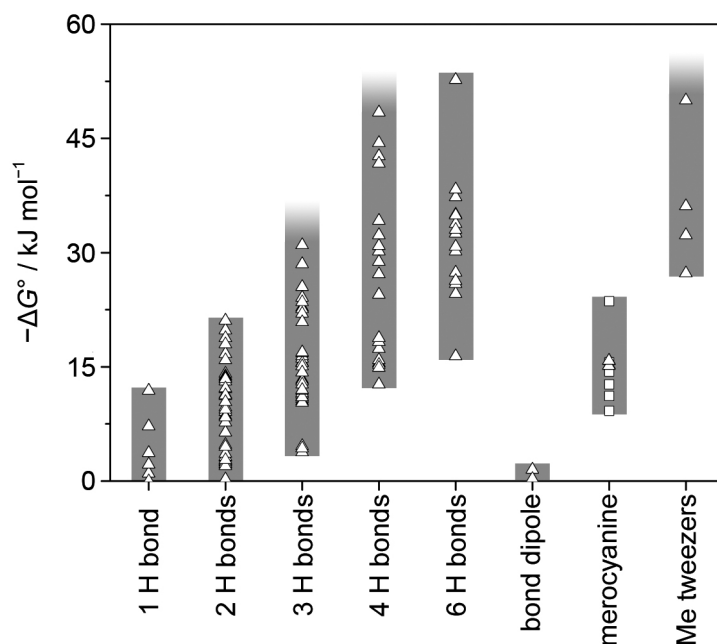
Figure 5. Free binding energies for single and multiple hydrogen bonding entities as well as for dipole-dipole interactions between single bond dipoles and highly dipolar merocyanine (Me) dyes and their tweezers in chloroform at 298 K.[14,15a,90–97] Experimental values are denoted with △, extrapolated values for chloroform with □. Color gradients indicate estimated lower limits for certain high $-\Delta G°$ values.

between *cis*- and *trans*-configured secondary amides revealed low $-\Delta G°$ values only up to 2.7 kJ mol^{-1}.[92d] Schneider et al. investigated the binding properties of nucleobases and synthetic counterparts. Free binding energies ranging from 2.2 kJ mol^{-1} for adenine dimers to 21.1 kJ mol^{-1} for an artificial AA:DD array could be found.[92g] Complexes with AA:DD hydrogen bonding patterns enforced by additional secondary hydrogen bonds were studied by Zimmerman and coworkers, showing free binding energies of maximal 19.8 kJ mol^{-1}.[92f] Diaminopyridines and diaminotriazines which form three hydrogen bonds to uracil derivatives were investigated by Meijer et al., revealing $-\Delta G°$ values of 3.8–16.9 kJ mol^{-1}.[93g] A widely used hydrogen bonding motif can be found between melamines and cyanurates. The binding properties of derivatives of these compounds were studied by Reinhoudt and coworkers.[93i] High free binding energies for triple hydrogen bonding arrays with an estimated lower limit of 28.5 kJ mol^{-1} were observed for AAA:DDD patterns, maximizing the amount of attractive secondary hydrogen bonds.[93e] Free binding energies from 12.7 to 30.2 kJ mol^{-1} could be deduced for quadruple hydrogen bonding between self-complementary ADAD arrays of acylated diaminopyrimidines and diaminotriazines.[94d] For the energetically more favorable dimerization of AADD arrays of ureidopyrimidones, $-\Delta G°$ was determined to 44.4 kJ mol^{-1}.[94g] Even higher values ($-\Delta G° = 48.4$ kJ mol^{-1}) were reported by Zimmerman et al. for ADDA:DAAD arrays composed of a tautomerically fixed guanosine derivative and 2,7-diamido-1,8-naphthyridine.[94j] Sixfold hydrogen bonding entities include artificial receptors for barbiturates as introduced by Hamilton and coworkers. Depending on the degree of

preorganization and steric hindrance, free binding energies ranging from 24.7 to 35.1 kJ mol^{-1} were found.[95a] Upon attaching such a receptor to dipolar merocyanine dyes and binding to various merocyanine guests bearing barbituric acid acceptor groups, $-\Delta G°$ values up to 38.3 kJ mol^{-1} could be measured in chloroform.[95h] Oligoamides with complementary linear ADAADA:DADDAD hydrogen bonding patterns formed very stable dimers with $-\Delta G°$ = 52.7 kJ mol^{-1}.[95d]

Dipolar interactions between single bond dipoles are hard to quantify owing to their small magnitude. Experimental attempts to quantify dipole-dipole interactions between orthogonal C–F and C=O bonds made use of the Wilcox torsion balance,[98] revealing a contribution of $-\Delta G°$ = 0.31 kJ mol^{-1} in chloroform.[86] In a similar way, the interaction energy between orthogonal C=O bond dipoles of two amide carbonyl groups was obtained ($-\Delta G°$ = 1.5 kJ mol^{-1}).[87] Highly dipolar merocyanine dyes were found to form stable dimers owing to strong antiparallel dipolar aggregation. The lowest $-\Delta G°$ values in a series of chromophores were found for molecules with small dipole moments, e.g. for derivatives of dye **3**.[14] Substitution of the barbiturate acceptor entity with hydroxypyridones yielded derivatives of **1**. As a result of the larger dipole moment, a larger free binding energy of 15.2 kJ mol^{-1} was experimentally detected for chromophore **1** in chloroform solution.[14b] The highest value in a series in 1,4-dioxane was measured for the most dipolar chromophore **8** bearing the dicyanovinylthiazole acceptor moiety.[14b] From this value, the free dimerization energy in chloroform can be extrapolated to 23.6 kJ mol^{-1} according to equation (3.3). Incorporating derivatives of dye **1** in tweezers units (Scheme 7) gave rise to higher $-\Delta G°$ values of 27.3 kJ mol^{-1}.[15a] Other merocyanine dye tweezers (see Appendix, Figure B3) showed even higher free binding energies of up to 50 kJ mol^{-1}.[15a]
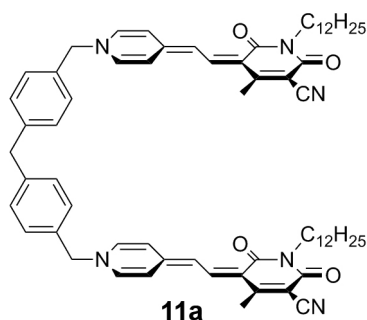
Scheme 7. Example for a bis(merocyanine) dye tweezer.

Such comparison based on Gibbs free energies demonstrates that the interaction energies between single bond dipoles are rather weak. In contrast, molecules with large dipole moments as arising in donor-acceptor-substituted π systems give rise to free binding energies that are similar in magnitude to those found for double and triple hydrogen bonding arrays.

Merocyanine dye tweezers bind even stronger and may be compared to quadruple and sextuple hydrogen bonding.

For further comparison of hydrogen bonds and antiparallel dimerization of merocyanine dyes we introduce an energy density σ parameter that provides deeper insight into the relative strength of these interactions. In analogy to the definition of the surface charge density, such a parameter may be defined according to equation (3.4) upon dividing $-\Delta G°$ by the area of the respective interaction.

$$\sigma = \frac{-\Delta G°}{A} \tag{3.4}$$

where A denotes the area in Å^2. Figure 6 depicts schematically how the areas are calculated. Details of these calculations are given in the Appendix of this chapter. Average $-\Delta G°$ values were used for the different hydrogen bonding systems (see Appendix). Table 2 summarizes the results obtained for single and multiple hydrogen bonding sites as well as for single merocyanine dyes and bis(merocyanine) tweezers. Such comparison shows that the energy density for dipolar aggregation of merocyanine chromophores is only slightly lower than that of single to triple hydrogen bonding, while tweezers thereof are approximately in between the values obtained for three and four hydrogen bonds. Quadruple hydrogen bonding shows higher values which may be ascribed to cooperativity.[13c] The latter energy densities are even exceeded by certain strongly bound bis(merocyanine) tweezers (see Table B7 in the Appendix).
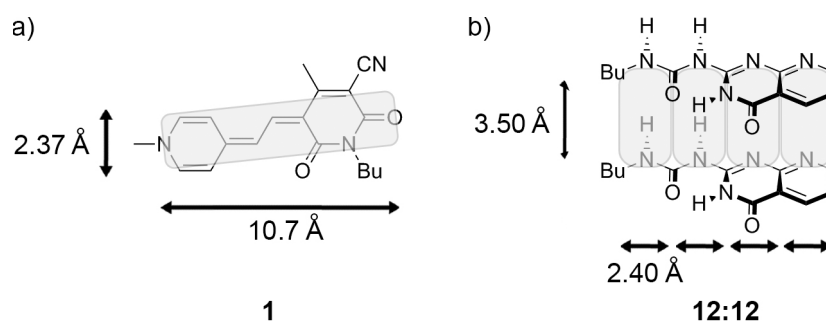
Figure 6. Schematic representation of the areas used for the calculation of the energy density for a) merocyanines and b) hydrogen bonds. The area of the π-system was used for the merocyanine dyes. To obtain the area for a single hydrogen bond, the distance between hydrogen bonds in a typical array was used in combination with the π-π distance, which constitutes the smallest displacement to an adjacent hydrogen bond.

Table 2. Energy densities σ (in kJ mol^{-1} Å^{-2}) for different hydrogen bonding systems and single merocyanine dyes as well as bis(merocyanine) dye tweezers.

system	σ
1 hydrogen bond	0.71
2 hydrogen bonds	0.70
3 hydrogen bonds	0.69
4 hydrogen bonds	0.91
merocyanine dyes	0.61
bis(merocyanine) tweezers [a]	0.77

[a] Twice the area of the monomeric dye was used for the energy density of the tweezers.

3.6 Conclusions

In general, dipole-dipole interactions differ from other noncovalent interactions, of which most are angle insensitive, in terms of directionality. In order to create more sophisticated supramolecular assemblies, strong directional noncovalent interactions are desirable. Dipolar interactions are of highly directional character but typically do not account for the predominant part of the overall interaction energy. In this Chapter, two exceptions are discussed which are governed by dipole-dipole interactions. The vast majority of hydrogen bonds is known to be dominated by electrostatics. Recent investigations have shown that the same holds true for dipolar merocyanine dyes that self-assemble into tightly bound centrosymmetric dimers. Quantum mechanical calculations of merocyanines show that the contribution of dipole-dipole interactions between such dyes can be augmented by proper variation of donor and acceptor units. Thus, the investigation of dimers consisting of chromophores with different ground state dipole moments establishes the predominantly electrostatic character of the interaction. Owing to geometrical considerations that favor certain spatial arrangements, hydrogen bonds prefer a linear geometry while for dipolar merocyanine molecules of anisotropic shape the antiparallel arrangement is most stable. Hydrogen bonding is widely used in the field of supramolecular chemistry, whereas other dipole-dipole interactions have scantly been considered. Their strength has long been regarded to be too low to significantly contribute to the overall energy. Comparison of experimental free binding energies in chloroform reveals that this is true for single bond dipoles, but highly dipolar molecules like merocyanine dyes are, by all means, able to form aggregates of high thermodynamic stability in solution. Gibbs free energy ($-\Delta G°$) values for the dimerization of merocyanine dyes in chloroform are in the same range as double and triple hydrogen bonding systems. Calculated energy densities demonstrate that the antiparallel dimerization of such chromophores may be compared to single, double, and triple hydrogen bonding. The aggregation of tweezers of these chromophores gives rise to even higher free binding energies and energy densities that partially exceed those of quadruple hydrogen bonds. Altogether, the comparison presented here establishes the use of dipole-dipole interactions as feasible noncovalent forces in supramolecular chemistry. In this context, it is surprising that experimental data for dipolar interactions other than hydrogen bonds are still scarce.

Chapter 4

Solvent- and Guest-Responsive Self-Assembly of Hamilton-Receptor-Tethered Bis(merocyanine) Dyes

Abstract: A novel supramolecular building block **8** consisting of a Hamilton receptor and two merocyanine dyes has been synthesized and the self-assembly based on orthogonal hydrogen bonding and dipolar interactions has been studied in detail. Different self-assembled species, including oligomers, polymers, and inverted micelles could be observed upon variation of the solvent polarity and the concentration. Moreover, this system is highly responsive toward molecular stimuli such as merocyanine molecules containing the barbituric acid motif that are bound by the Hamilton receptors. Detailed UV/Vis absorption studies provided insight into isodesmic or cooperative steps during the self-assembly of **8** into different species. The size of the aggregates in solution and the morphology on substrates have been explored by a combination of DLS, AFM, and TEM investigations.

4.1 Introduction

In this Chapter, studies on the self-assembly of Hamilton-receptor-tethered bis(merocyanine) dyes in the absence and presence of guest molecules are presented. Such investigations include remarkable and unexpected solvophobically driven hierarchical self-assembly processes and the formation of supramolecular polymers based on two orthogonal and directional noncovalent interactions. A brief introduction to literature known responsive natural and artificial systems as well as to combinations of merocyanine dyes and hydrogen bonds is provided in Chapter 1 and will therefore not be repeated here.

4.2 Results and Discussion

4.2.1 Synthesis

Hamilton-receptor-tethered bis(merocyanine) dye **8** was synthesized according to the route depicted in Scheme 1. Etherification of commercially available 3-hydroxyisophthalic acid methyl ester **1** with trialkoxy benzyl chloride **2**, which was prepared from gallic acid methyl ester in three steps according to literature procedures,[99] afforded diester **3** bearing a trialkoxybenzyl group in 96% yield. Amidation of this diester with monolithiated 2,6-diaminopyridine afforded diamine **4** in 44% yield. Carboxylic acid functionalized merocyanine **7** was synthesized by a Knoevenagel type condensation reaction of pyridone **6**, which was obtained according to literature procedure,[100] with the respective aldehyde **5**[101] in
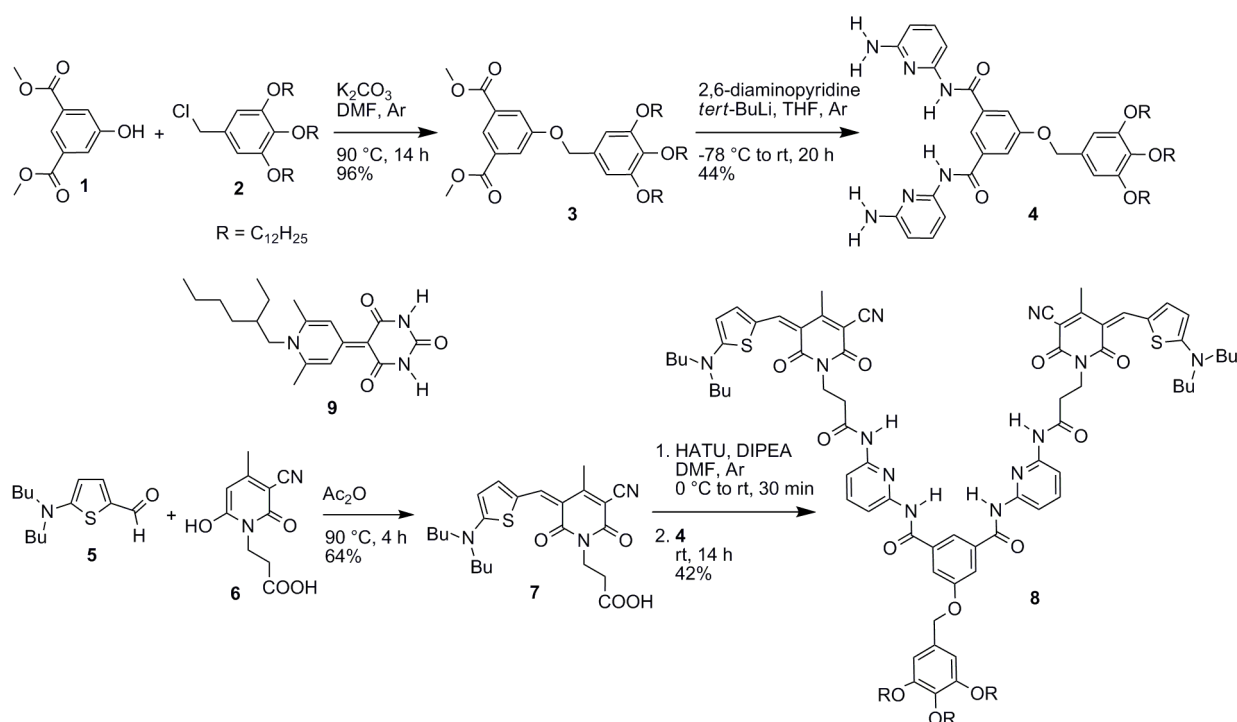
Scheme 1. Synthesis of Hamilton-receptor-tethered bis(merocyanine) **8** and chemical structure of guest **9**.

64% yield. The coupling of merocyanine **7** with diamine **4** by amidation using 2-(1*H*-7-azabenzotriazol-1-yl)-1,1,3,3-tetramethyl uronium hexafluorophosphate (HATU) and diisopropylethylamine (DIPEA) as coupling reagents in DMF afforded the desired Hamilton-receptor-ligated bis(merocyanine) **8** in 42% yield. The detailed synthetic procedures and structural characterization data for the unknown compounds **3**, **4**, **7**, and **8** are given in the Experimental Section. Merocyanine **9** bearing a barbituric acid acceptor group for the formation of six-fold hydrogen bonding to the Hamilton receptor was synthesized according to the literature and was used in molecular stimuli experiments with bis(merocyanine) **8**.[18]

4.2.2 Solvent-Induced Self-Assembly

First indication for the self-aggregation of **8** was obtained by mass spectrometry. Samples prepared by solvent evaporation from solutions of **8** in THF/MCH = 10:90 vol% (tetrahydrofuran/ methylcyclohexane, $c = 1.0 \times 10^{-4}$ M) were measured by MALDI-TOF and peaks corresponding to the protonated cationic monomer ($[M+H]^+$) and sodium adduct ($[M+Na]^+$) as well as dimer ($[M_2+H]^+$), trimer ($[M_3+H]^+$) and traces of tetramer ($[M_4+H]^+$) were observed (see Appendix, Figure C3). The self-assembly of Hamilton-receptor-tethered bis(merocyanine) **8** was further studied by UV/Vis spectroscopy in THF/MCH mixtures of different composition. The solvent polarity strongly affects the thermodynamic equilibrium between different self-assembled species observed for these dyes as shown previously by solvent-dependent UV/Vis studies for a variety of bis(merocyanine) dyes in THF/MCH mixtures.[15,16] Due to the relatively high polarity of pure THF ($\varepsilon_r = 7.52$), Hamilton-receptor-tethered bis(merocyanine) dye **8** is present predominantly in its monomeric form (further denoted as **A**) in this solvent with a characteristic narrow cyanine-type absorption band at $\lambda_{max} = 538$ nm (Figure 1).[102] Upon increasing the amount of nonpolar MCH ($\varepsilon_r = 2.02$), this chromophore aggregates owing to the increased Coulomb forces between highly dipolar dye molecules ($\mu_g = 14$ D).[14] Two distinct transitions can be recognized by quasi-isosbestic points at 517 nm and 496 nm, respectively (see Figure C4). The first transition to a species with a hypsochromically shifted band at 510 nm (further denoted as **B**) occurred upon increasing the ratio of MCH and was most pronounced in THF/MCH ≈ 40:60 vol% at a concentration of 1.0×10^{-4} M. This band could be assigned to H-type aggregated dimers of excitonically coupled chromophores,[14] which indicates the formation of a supramolecular polymer (or oligomer) owing to the bifunctionality of dye **8**. Further increase of the MCH content in solution led to the formation of a second species (further denoted as **C**) with a broader absorption band that is indicative of a high heterogeneity of the local dye-dye contacts ("amorphous" state). Similarly, broad spectra have been previously observed for the applied aminothiophene oxopyridine (ATOP) chromophores in amorphous photorefractive films.[102] The corresponding α_{50} values for the different aggregated species are summarized in the

Appendix (Table C2). Notably, the solvent ratio for the formation of different species is dependent on the total monomer concentration of **8** (see Figure C6).
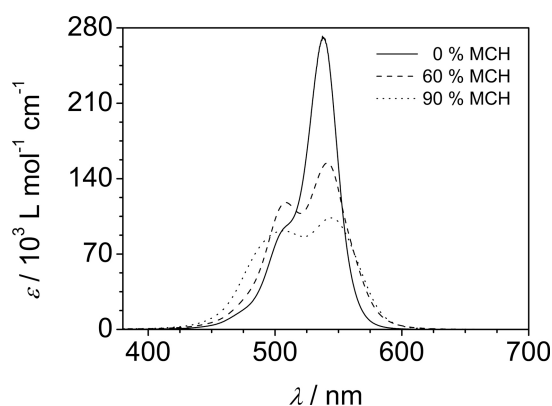
Figure 1. UV/Vis absorption spectra of monomers **A** (THF/MCH = 100:0 vol%, solid line), and self-assembled species **B** (THF/MCH = 40:60 vol%, dashed line) and **C** (THF/MCH = 10:90 vol%, dotted line) emerging from dye **8** in various THF/MCH mixtures ($c(\mathbf{8}) = 1.0 \times 10^{-4}$ M) at 298 K.

An initial screening of the aggregate sizes by means of capillary viscosity measurements revealed an unexpected behavior (Figure 2). Thus, upon increasing concentration the viscosity η_{red} first increases as expected for a growing chain of a supramolecular polymer, but then decreases once a concentration of 0.2 mg/mL (corresponds to 1.1×10^{-4} M) is exceeded. This unexpected behavior is indicative of the formation of a new species **C** with a homogeneous size, which is smaller than that of **B**.
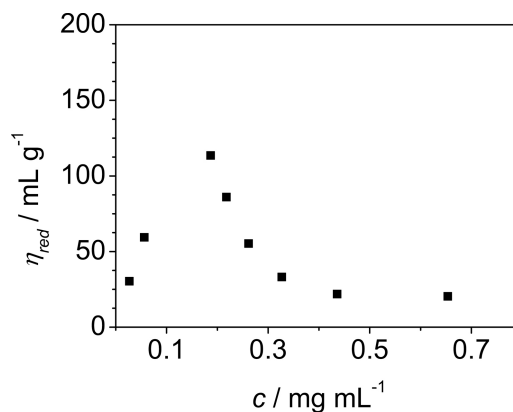
Figure 2. Reduced viscositiy η_{red} of **8** in THF/MCH = 40:60 vol% at different concentrations.

4.2.3 Self-Assembly of Supramolecular Polymers B

The self-assembly of the aggregated species **B** was initially investigated by ^{1}H NMR experiments in deuterated THF/MCH (50:50 vol%) mixtures (see Figure C7). The spectra of **B** showed broad signals in the aromatic region, indicating aggregation of the merocyanine dyes and conformational flexibility of the diacyldiaminopyridine moieties.

Concentration- and temperature-dependent UV/Vis experiments were performed to gain insight into the self-assembly processes in solution. Figure 3a shows the concentration-dependent spectral changes of bis(merocyanine) **8** at concentrations between 2.5 x 10^{-8} and 1.0 x 10^{-5} M in THF/MCH (30:70 vol%) mixtures at ambient temperature. Depletion of the absorption maximum at 538 nm is accompanied by the emergence of a weak, new hypsochromically shifted transition centered at ~510 nm, which can be ascribed to H-type supramolecular aggregates (Figure 3a).
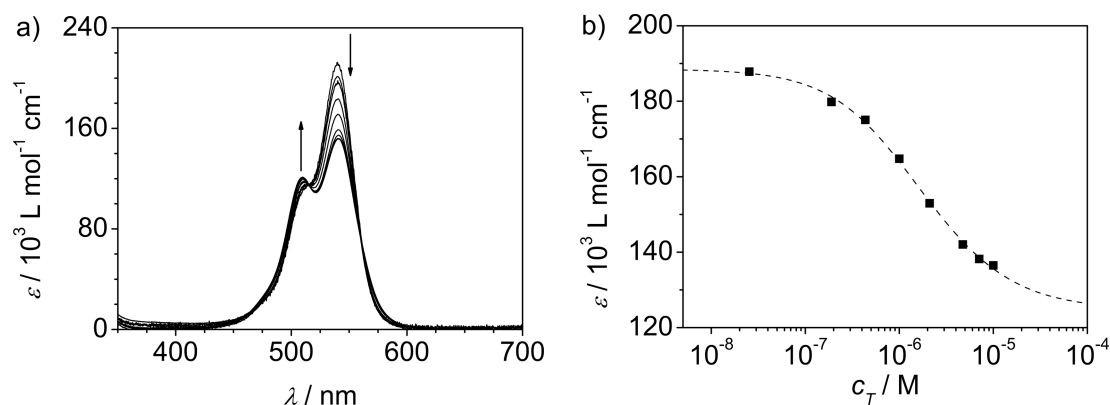
Figure 3. a) Concentration-dependent UV/Vis spectra of **8** in THF/MCH = 30:70 vol% at 298 K from c = 2.5 x10^{-8} M to 1.0 x 10^{-5} M. Arrows indicate changes upon increasing concentration. b) Apparent absorption coefficient at 533 nm plotted against c_T and the result of the nonlinear regression analysis based on the isodesmic model for the formation of **B**.

The isodesmic model (also called equal K model)[23] could successfully be applied to the transition from **A** to **B**. According to this model, the molar fraction of the self-assembled species can be expressed by equation (4.1):[23]

$$\alpha_{agg} = 1 - \alpha_{mon} = 1 - \frac{c_{mon}}{c_T} = 1 - \frac{2Kc_T + 1 - \sqrt{4Kc_T + 1}}{2K^2c_T^2} \qquad (4.1)$$

in which α_{mon} and α_{agg} are the molar fraction of the monomeric and self-assembled species, respectively, c_{mon} and c_T are the concentration of the monomeric species in solution and the total concentration of all dyes in the system, respectively, and K is the equilibrium constant. This mathematical expression can be related to the UV/Vis absorption spectra. By applying equation (4.1) in equation (4.2), equation (4.3) can be obtained:

$$\alpha_{agg} = 1 - \frac{\varepsilon(c_T) - \varepsilon_{agg}}{\varepsilon_{mon} - \varepsilon_{agg}} \tag{4.2}$$

$$\varepsilon(c_T) = \frac{2Kc_T + 1 - \sqrt{4Kc_T + 1}}{2K^2 c_T^2}\left(\varepsilon_{mon} - \varepsilon_{agg}\right) + \varepsilon_{agg} \tag{4.3}$$

where ε_{mon}, ε_{agg}, and $\varepsilon(c_T)$ denote the molar absorption coefficients of free monomers **A**, self-assembled dyes, and the apparent absorption at the concentration c_T, respectively. By fitting the data obtained from the concentration-dependent series in THF/MCH = 30:70 vol% to equation (4.3), an equilibrium constant of $K = (3.9 \pm 0.5) \times 10^5$ M^{-1} was obtained (Figure 3b). This equilibrium constant compares well to dimerization constants reported for simple merocyanine dyes bearing similar donor and acceptor subunits.[14b] The number-averaged degree of polymerization DP_N and the weight-averaged degree of polymerization DP_W according to the concentration-dependent isodesmic model could be calculated to 7 and 13, respectively, for a 1.0×10^{-4} M concentration of **8** (see Table C3).

Temperature-dependent UV/Vis studies were subsequently performed to get further insight into the self-assembly processes. A more sophisticated analysis[28] of temperature-dependent UV/Vis absorption spectra confirms the isodesmic self-assembly mechanism (Figures C11 and C13) and provides the melting temperature of the aggregate $T_m = 301$ K and the thermodynamic parameters of molar enthalpy of aggregate formation $\Delta H = -88.6$ kJ mol^{-1} and change in entropy $\Delta S = -203$ J mol^{-1} K^{-1}. Details concerning data evaluation are given in the Appendix and the applied equations are derived in Chapter 2. Comparison of the enthalpy and entropy contributions to the Gibbs free energy changes for aggregation leads to the conclusion that the self-assembly process is enthalpy-driven, whereas it is entropically disfavored.

The size of supramolecular species **B** was determined by dynamic light scattering (DLS) experiments. A relatively broad distribution of particle sizes, ranging from ~80 to 350 nm with a maximum at 147 nm was found (Figure 4), which is in accordance with our structural assignment of supramolecular polymers. This comparatively high degree of polydispersity can be expected for supramolecular polymers in which a rapid dynamic equilibrium between free and associated species takes place.
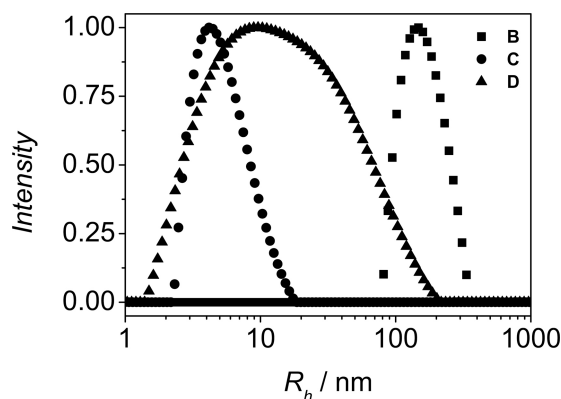
Figure 4. Hydrodynamic radius R_h distributions obtained from DLS experiments on **B** ($c(\mathbf{8})$ = 1.0 x 10^{-3} M, THF/MCH = 50:50 vol%), **C** ($c(\mathbf{8})$ = 1.0 x 10^{-3} M, THF/MCH = 10:90 vol%), and **D** ($c(\mathbf{8})$ = 1.0 x 10^{-3} M, THF/MCH = 20:80 vol%).

Convincing evidence for the formation of linear supramolecular aggregates was obtained by atomic force microscopy (AFM)[i] and transmission electron microscopy (TEM)[ii] investigations. A solution of **8** (1.0 x 10^{-5} M) in THF/MCH (30:70 vol%) was drop-cast on highly ordered pyrolytic graphite (HOPG) and tapping-mode AFM images were recorded at room temperature under ambient conditions (Figure 5a). The images disclosed the formation of long fibrils with lengths between 80 and 300 nm with a maximum at 143 nm (see Figure C24a). These dimensions are in accordance with those determined by DLS experiments. Cross-section analysis revealed an average distance between two fibrils of 5.5 ± 0.5 nm, while the rather small height of 0.29 ± 0.04 nm of these structures can be attributed to the presence of simple supramolecular chains. TEM images of **B** (Figure 5b)
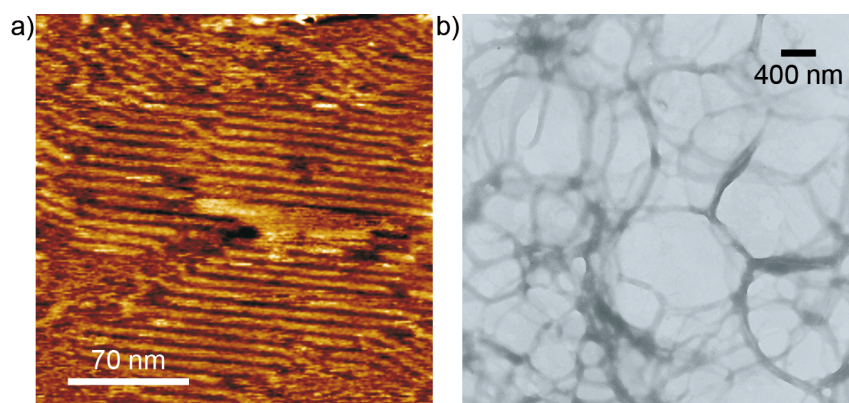
Figure 5. a) AFM height image of spin-coated samples of **B** (4000 rpm, $c(\mathbf{8})$ = 1.0 x 10^{-5} M, THF/MCH = 30:70 vol%, 298 K) onto HOPG. b) Transmission electron micrograph of **B** after evaporation of the solvent ($c(\mathbf{8})$ = 1.0 x 10^{-4} M, THF/MCH = 40:60 vol%) on a carbon-coated copper grid.

---

[i] AFM studies were performed by Dr. Shinobu Uemura.
[ii] TEM studies were conducted by Dr. Xin Zhang.

performed onto carbon-coated copper grids showed larger network-like structures with strands up to several micrometers in length. Apparently, further aggregation takes place during the evaporation process, leading to merging individual fibrils. Structural models that explain the organization of these supramolecular polymers on HOPG by the peripheral alkyl chains were derived by molecular modeling (Figure C25a). Dye aggregation leads to the formation of polymeric chains while the alkyl moieties are directed perpendicular to the propagation direction. The distance between two chains suggests interpenetration of the alkyl chains, leading to adhesive linear structures.

The above described results indicate that species **B** consists of supramolecular polymers based on antiparallel aggregation of the merocyanine dye units of ditopic monomer **8** with high equilibrium constants in solution.

4.2.4 Self-Assembly of Inverted Micelles C

Similarly to the polymeric structure **B**, the next level of structural hierarchy, i.e. the self-assembly of species **C** was thoroughly investigated in solution and on substrates by a number of techniques. Upon increasing the MCH ratio, the peak broadening of the ^{1}H NMR spectra was even more pronounced for **C** in comparison with polymeric species **B**, suggesting that a distinctly new species is forming (see Figure C7). Concentration-dependent UV/Vis experiments were initially performed to evaluate in detail the self-assembly processes. Experiments in THF/MCH = 20:80 vol% in a concentration range of $c = 1.3 \times 10^{-6}$ M to 1.3×10^{-4} M revealed a transition from **B** to **C** (Figure 6a). The isodesmic model was not applicable to this transition as evidenced by a sharp decrease of the apparent absorption at 507 nm upon reaching a certain concentration (Figure 6b, dashed curve). Such abrupt changes indicate a cooperative process. Application of the K_2–K model[23] and the more general model of Goldstein and Stryer[40] yielded good fits. However, it seems scientifically more appropriate to use a model that explicitly comprises the formation of a closed system from an oligomeric species since further investigations by DLS, NMR, and AFM suggest the formation of a discrete species (*vide infra*). Therefore, a model was used that includes the possibility to describe the formation of closed systems.[10] Such a model is described in detail in Chapter 2. The self-assembly of complementary oligomers, of which one can form a closed structure is schematically depicted in Scheme 2.

$$AB \underset{}{\overset{K}{\rightleftharpoons}} (AB)_2 \underset{}{\overset{K}{\rightleftharpoons}} \cdots (AB)_N \underset{}{\overset{K}{\rightleftharpoons}} (AB)_{N+1} \cdots$$
$$\Big\Vert K_c$$
$$c\text{-}(AB)_N$$

Scheme 2. Self-assembly of complementary oligomers, of which one can form a closed structure ($\sigma = 1$).[10]

Figure 6. a) Concentration-dependent UV/Vis spectra of **8** in THF/MCH = 20:80 vol% at 298 K from $c = 1.3 \times 10^{-6}$ M to 1.3×10^{-4} M. b) Fraction of aggregated molecules α_{agg} plotted as a function of log $K'c_T$ according to the isodesmic model (dashed curve) and to the self-assembly of a closed oligomer (solid curve) and plot of the experimental data at 507 nm for the formation of **C** after manual fit of the line shape. The exact parameter values used to calculate the solid curve in Figure 6b are given in the Appendix (see Figure C15).

The total concentration c_T may be expressed as a function of the monomer concentration c_1, the equilibrium constant K of the linear chain formation, the effective molarity EM as defined in equation (4.4), the parameter for allosteric cooperativity σ, and the number of molecules N in the oligomer that forms the closed structure:[10]

$$EM = N \frac{K_c}{K} \tag{4.4}$$

$$c_T = \frac{c_1[\sigma^{-1}(1 - Kc_1)^2 + Kc_1(2 - Kc_1)]}{\sigma^{-1}(1 - Kc_1)^2} + K^N EM c_1^N \tag{4.5}$$

The molar fraction of aggregated species α_{agg} can subsequently be described by equation (4.6):[10]

$$\alpha_{agg} = \frac{\sigma^{-1}(1 - Kc_1)^2 KEM(Kc_1)^{N-1} + Kc_1}{\sigma^{-1}(1 - Kc_1)^2[1 + KEM(Kc_1)^{N-1}] + Kc_1(2 - Kc_1)} \tag{4.6}$$

Since it is exhaustive to solve equation (4.5) for c_1 and insert the result into equation (4.6), curves for different combinations of K, EM, σ and N were calculated and plotted against the normalized concentration scale log $K'c_T$ for better comparison. Here, $K' = 1/c_{50}$ and c_{50} corresponds to the concentration at which $\alpha_{agg} = 0.5$. A relation of the experimental data points to the ordinate can be established by taking into account the equation (4.7):

$$\alpha_{agg} = 1 - \frac{\varepsilon(c_T) - \varepsilon_{agg\ \mathbf{C}}}{\varepsilon_{agg\ \mathbf{B}} - \varepsilon_{agg\ \mathbf{C}}} \tag{4.7}$$

where $\varepsilon_{agg\ \mathbf{B}}$, $\varepsilon_{agg\ \mathbf{C}}$, and $\varepsilon(c_T)$ denote the molar absorption coefficients of species **B**, species **C**, and the apparent absorption at the concentration c_T, respectively.

The calculated curves were fitted manually for the best match to a plot of the experimental data points for α_{agg} against $\log K'c_T$ (Figure 6b). The abrupt changes in the absorption spectra suggest high values for *EM* and *N*. Because of the large number of parameters and manual fitting of the data, it would not make much sense to give the exact values for *K*, *EM*, σ and *N*. Instead, a qualitative discussion of the results based on the order of magnitude of the respective parameter is provided. Best fit was obtained for *K* values in the order of $10^5 \, M^{-1}$, which is in accordance with the equilibrium constant observed for the formation of **B** from monomers **A**. High values for *EM*, likewise in the order of $10^5 \, M$, could be estimated. Such high effective molarities strongly favor the formation of the closed species rather than further growth of the chain. Almost no allosteric cooperativity seems to be present ($\sigma \approx 1$). The number of molecules in the oligomer that tends to form the closed structure was found to be in the order of 20. Thus, taking into account equation (4.4) the equilibrium constant K_c for the formation of **C** can be roughly estimated to be 5×10^8.

The aggregate size of species **C** in solution could be determined by DLS performed on $1.0 \times 10^{-3} \, M$ solutions of **8** in THF/MCH = 10:90 vol%. Surprisingly, a remarkably narrow distribution of particles, ranging from 2 nm (monomer) to ~10 nm with a maximum at 4.2 nm was observed (Figure 4), which clearly supports the formation of aggregates with discrete size. Similar particle sizes were found by diffusion ordered spectroscopy (DOSY) NMR experiments at the same concentration and solvent composition (see Figure C8).

The morphology of aggregates **C** formed on substrates was investigated by AFM imaging on HOPG. The images revealed discrete globular objects with diameters of 9.0 ± 2.0 nm and heights of 2.8 ± 0.3 nm (Figure 7) in accordance with the values determined by DLS and DOSY experiments. Notably, the size of the aggregates did not change upon changing the substrate, in particular HOPG vs. Si-wafer (Figure C22).
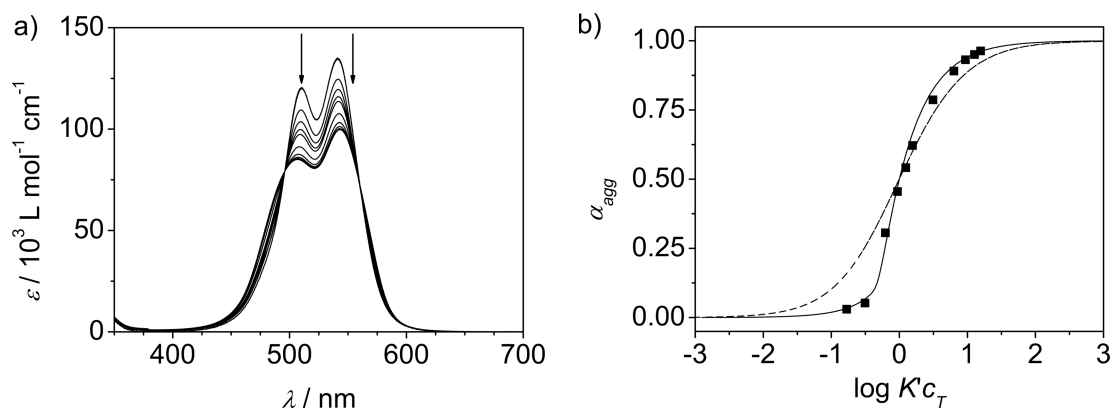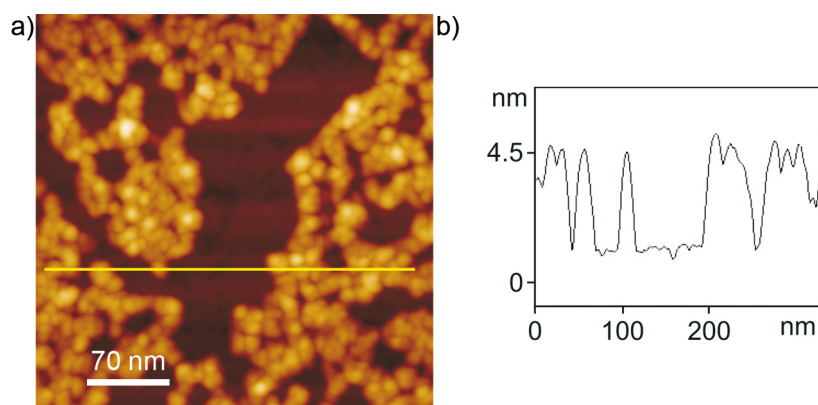

Figure 7. a) AFM height image of spin-coated samples of **C** (4000 rpm, $c(\mathbf{8}) = 1.0 \times 10^{-5}$ M, THF/MCH = 5:95 vol%, 298 K) onto HOPG. b) Cross-section along the yellow line in panel a.

The overall results suggest that aggregate **C** is formed as a result of a solvent-induced collapse of **B** as soon as the oligomers reach a certain size and the polarity of the applied solvent is low. The cooperative self-assembly, the size in solution, and the morphology on substrates suggest the formation of inverted micelles in which all polar dyes are encapsulated and shielded from the nonpolar solvent by the aliphatic tails of the molecules.

4.2.5 Guest-Induced Self-Assembly

The capability of the Hamilton-receptor-tethered bis(merocyanine) dye **8** to host appropriate barbiturate guest molecules through a pattern of six hydrogen bonds has been explored to evaluate the influence of guest binding in the stability of the above described supramolecular structures. Constant host UV/Vis titration experiments[103,104] with guest molecule **9** were performed to gain insight into the receptor properties of **8**, revealing a binding constant of K_{ass} = 5.2 x 10^6 M^{-1} in $CHCl_3$ (Figure 8). For practical reasons (detection of spectral changes in the visible region), the role of the host and guest were reversed in these experiments. From this K_{ass} value a binding constant of approximately 1.2 x 10^{13} M^{-1} can be estimated in pure MCH by assuming a linear free energy relationship with related Hamilton receptor host-guest systems.[18] Therefore, almost complete complex formation can be safely assumed in mixtures with high MCH ratios even under dilute conditions.
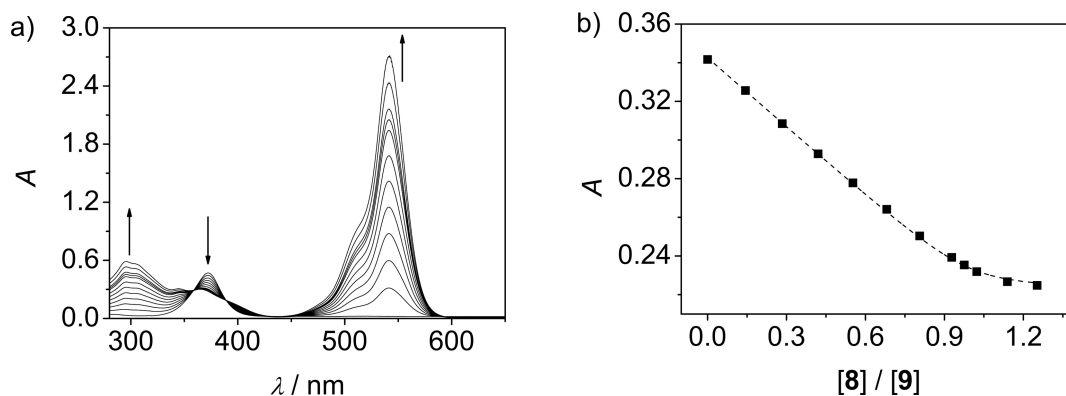
Figure 8. a) UV/Vis titration of barbiturate dye **9** (as host at a constant concentration of c = 1.0 x 10^{-5} M) with increasing amounts of bis(merocyanine) **8** as guest in chloroform at 298 K. b) Titration isotherm for a 1:1 complex model at a wavelength of 381 nm.

Subsequent to the formation of a stoichiometric host-guest complex between **8** and **9**, the aggregation of **AG** (**AG** denotes the monomeric complex **8:9**) could again be studied by concentration-dependent UV/Vis spectroscopy which revealed a clear transition between two species with a defined isosbestic point at 510 nm (Figure 9). Upon increasing the concentration, the band of the monomeric dye at 538 nm decreased at the expense of a hypsochromically shifted aggregate band at λ_{max} = 500 nm that is characteristic for an antiparallel π-stacked arrangement of ATOP chromophores in a dimeric unit as reported

previously.[14] Accordingly, due to the bifunctionality of **AG** a supramolecular polymer (denoted as **D**) has formed. It is noteworthy that barely any spectral changes could be observed within the band at 365 nm which corresponds to the guest dye, indicating that the self-assembly is driven by the dipolar aggregation of **8**. The isodesmic model could be applied with very high accuracy to the formation of this supramolecular polymer **D** from complex **AG** (Figure 9b). By fitting the data obtained from the concentration-dependent series, an equilibrium constant of $(2.8 \pm 0.1) \times 10^3$ M^{-1} was obtained, which is significantly lower than that for the formation of **B**. This might be ascribed to steric hindrance for the dipolar interaction evoked by the binding of a guest molecule and small attractive dipole-dipole interactions between the dipolar guest and the dyes covalently linked to the Hamilton receptor. Temperature-dependent measurements revealed similar changes as observed for the concentration-dependent series and almost identical equilibrium constants were calculated (see Figures C12, C14, and Table C4).
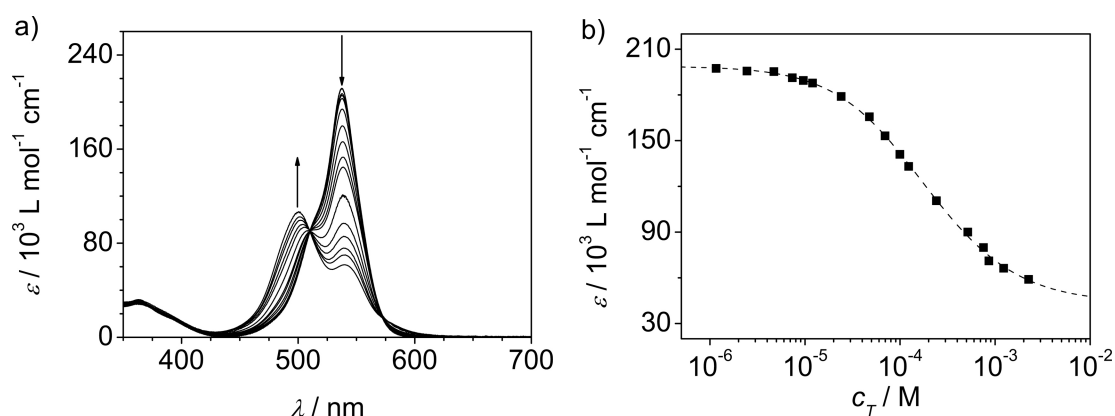
Figure 9. a) Concentration-dependent UV/Vis spectra of **AG** in THF/MCH = 20:80 vol% at 298 K from $c = 1.2 \times 10^{-6}$ M to 2.3×10^{-3} M. Arrows indicate changes upon increasing concentration. b) Apparent absorption coefficient at 533 nm plotted against c_T and the result of the nonlinear regression analysis based on the isodesmic model for the formation of **D**.

The size of **D** in solution for a 1.0×10^{-3} M solution of complex **AG** in THF/MCH = 20:80 vol% was determined by DLS. Larger average particle sizes of 12 nm were obtained for species **D** and they show a broad size distribution (Figure 4). Particles with sizes ranging from 2 nm (monomer) up to 200 nm were found. Such dissemination is indicative for the formation of supramolecular oligomers or polymers rather than discrete objects.

Similarly to species **B**, AFM images of **D** on HOPG under air showed long fibrils with kinks (Figure 10a). With an average distance between two fibrils of 5.0 ± 0.4 nm and a height of 0.36 ± 0.05 nm, cross-section analysis revealed almost identical results for the two polymeric aggregates. The chain lengths of **D** were found to be smaller than those observed for **B**. In accordance with the DLS studies, fibrils with average lengths between 10 and 130 nm were obtained with a maximum at 40 nm (see Figure C24b). Kinks in supramolecular

structures indicate the formation of polymers. TEM images of **D** also revealed network-like structures with lengths of the strands up to micrometers but the width being much smaller than that for **B** (Figure 10b). A structural model, explaining the organization of **D** on HOPG, was obtained by molecular modeling (Figure C25b) and suggests a similar binding motif as for **B**. Chain propagation is a result of the aggregation of the dyes of ditopic host **8**, while interaction between the chains on HOPG may be ascribed to interdigitation of alkyl chains.
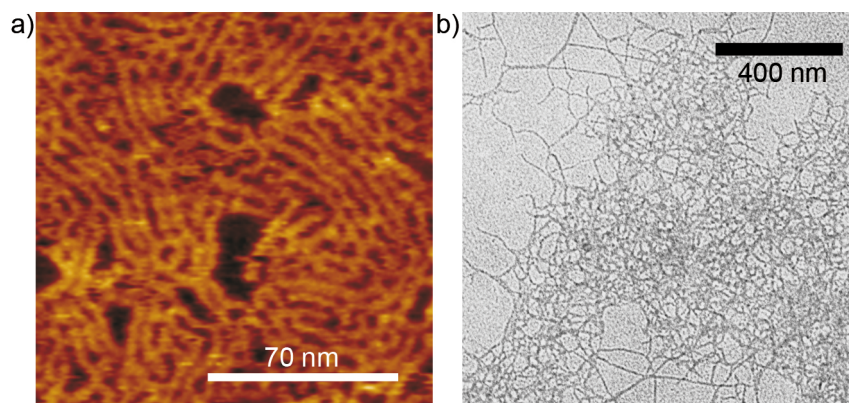
Figure 10. a) AFM height image of spin-coated samples of **D** (4000 rpm, $c(\mathbf{8}) = 1.0 \times 10^{-5}$ M with 1 eq. of guest **9**, THF/MCH = 5:95 vol%, 298 K) onto HOPG. b) Transmission electron micrograph of **D** after evaporation of the solvent (THF/MCH = 20:80 vol%, $c(\mathbf{8}) = 4.0 \times 10^{-4}$ M) on a carbon-coated copper grid.

Species **D** could also be obtained from inverted micelles **C**, thereby demonstrating the responsiveness of these supramolecular systems to the presence of guest molecules. Addition of one equivalent of **9** to aggregates **C** (relating to the total concentration of **8**) in THF/MCH = 5:95 vol% afforded **D** after a period of several hours as revealed by UV/Vis spectroscopy and AFM studies (see Figures C17 and C18).

Noteworthy, addition of guest **9** to polymers **B** entailed the formation of mainly monomeric complex **AG** as could be shown by UV/Vis and NMR spectroscopy (see Figures C19 and C20). Such behavior confirms the considerably lower equilibrium constant for the formation **D** compared to **B**.

4.3 Summary of the Self-Assembly Processes

The incorporation of a hydrogen-bonding site as spacer unit between two dipolar merocyanine dyes offered a new tool to switch between different supramolecular architectures. The self-assembly processes of Hamilton-receptor-tethered bis(merocyanine) dye **8** explored by different methods as described above are summarized in Figure 11. Starting from monomeric bis(merocyanine) dye in pure THF (**A**), the linear, polymeric species **B** was reversibly formed upon decreasing the solvent polarity, using 30–50 vol% MCH, depending on the total monomer concentration. The formation of **B** was studied by concentration- and temperature-dependent UV/Vis measurements and properly agreed with the isodesmic model. Further decreasing the solvent polarity by increasing the ratio of MCH to 90–95 vol%, again depending on the concentration, led to the solvent-induced collapse of **B** to inverted micelles **C**. Concentration-dependent UV/Vis studies revealed a cooperative self-assembly mechanism from species **B** to **C**.

Upon offering a complementary guest **9** to **A**, complex **AG** was formed. Analog to the formation of **B** from **A**, the linear oligomeric species **D** could be formed from **AG** upon decreasing the solvent polarity. Investigations on the self-assembly of this complex revealed an isodesmic self-assembly mechanism, which ended up with supramolecular oligomers. Addition of guest molecules to inverted micelles **C** led to the transformation to supramolecular polymers **D**, thus emphasizing the responsiveness of the present system.
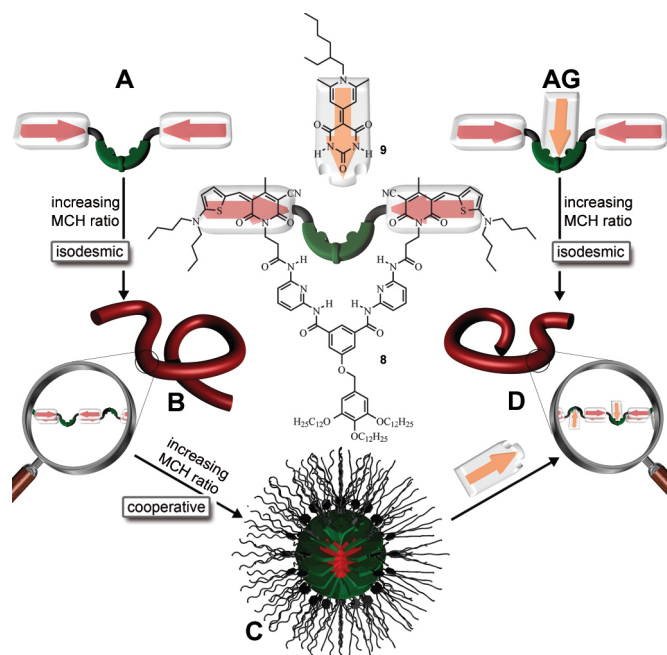
Figure 11. Schematic representation of the solvent- and guest-dependent self-assembly of Hamilton-receptor-tethered bis(merocyanine) dyes **8**. Starting with the monomer (**A**) in pure THF, supramolecular polymers (**B**) were formed upon addition of MCH which collapse into globular inverted micelles (**C**) in highly nonpolar environment. Addition of guest **9** switched the inverted micelles back to a supramolecular polymer (**D**), which was also formed by self-assembly of complex **AG**.

4.4 Conclusion

Hamilton-receptor-tethered bis(merocyanine) dye **8** is a remarkably adaptive supramolecular building block. Depending on assessable parameters such as solvent polarity, concentration and the presence of guest molecules, formation of different supramolecular species can be triggered. Lowering the solvent polarity yielded in the isodesmic formation of supramolecular polymers composed of well-defined dimeric dye entities. Upon further increasing of the ratio of nonpolar MCH, these polymers "collapsed" into inverted micelles, whose absorption spectra resembled those of amorphous films of these chromophores.[108] This reorganization process was proven to be cooperative similar as observed for protein folding.[8,10] A cooperative model that describes the formation of a closed species from a particular oligomer was successfully applied to concentration-dependent UV/Vis spectra. More intricate supramolecular polymers were formed by the addition of guest **9** to the inverted micelles. These polymers, incorporating merocyanine chromophore guest molecules, could also be built up from complex **8:9** following the isodesmic self-assembly model. This unique combination of two orthogonal directional noncovalent interactions allowed adjustable organization upon environmental changes and molecular stimuli. It is noteworthy that the observed self-encapsulation of the dyes in inverted micelles **C** enables high dye concentrations in nonpolar media and, at the same time, low viscosities which are both highly attractive features for the coloration of low polarity commodity plastics like polyethylene and polypropylene.[105]

4.5 Experimental Section

Materials and Methods: Solvents and reagents were obtained from commercial suppliers and used without further purification, unless otherwise stated. Trialkoxybenzyl chloride **2**, thiophene **5**, and pyridone **6** were synthesized according to literature procedures.[99–101] Column chromatography was performed on silica gel (Merck Silica 60, particle size 0.04–0.063 nm) and thin layer chromatography (TLC) was conducted on silica gel plates (60 F_{254} Merck, Darmstadt). High performance liquid chromatography (HPLC) was carried out on a PU 2080 PLUS system (JASCO) with a UV/Vis detector (UV 2077 PLUS) using a semi-preparative SP 250/21 Nucleodur 100-7 C18 ec column (Macherey-Nagel) and purity-grade "pa" solvents. Melting points were determined on a Büchi Melting Point B545 heating stage and are uncorrected. Solvents for UV/Vis absorption and AFM studies were of spectroscopic grade and used as purchased. ^{1}H NMR spectra were recorded on a Bruker Advance 400 spectrometer at 293 K, unless otherwise stated, with TMS or residual non-deuterated solvent as internal standard. High resolution ESI-TOF mass spectrometry was carried out on a

microTOF focus instrument (Bruker Daltronik GmbH) in positive mode with CH_3CN or $CHCl_3$ as solvent, unless otherwise stated.

Self-Assembly and Titration Experiments: Solutions for the self-assembly experiments in THF/MCH mixtures were prepared from stock solutions of **8** in tetrahydrofuran (THF). Aggregation into the different species was initiated by addition of the low polarity solvent methylcyclohexane (MCH) to the respective THF monomer solution. Samples for aggregation studies of **D** were prepared from concentrated stock solutions of appropriate amounts of **8** and **9**, respectively, in THF and subsequent addition of MCH ending up with the desired solvent ratio. These concentrated solutions were further diluted for the respective measurements. For practical reasons (detection of more pronounced spectral changes for **9** upon complex formation), the role of the host and guest were reversed in the constant host titration experiments. Thus, to the solution of host merocyanine dye **9** ($c = 1.0 \times 10^{-5}$ M) aliquots of solution of a guest receptor (**8**, $c = 1.0 \times 10^{-4}$ M) in the same host solution were added and UV/Vis spectra at 298 K were recorded after each addition. Analysis of the data was made by nonlinear regression analysis at different wavelength and averaging over the obtained K_{ass} values. Further titration experiments were performed by addition of appropriate amounts of guest molecules **9** to the already self-assembled solutions of **8**.

UV/Vis Experiments: UV/Vis absorption spectra were measured on a Perkin Elmer Lambda 950 UV/Vis spectrophotometer with a spectral bandwidth of 0.20 nm and a scan rate of 141 nm/min using conventional quartz cells of 0.1–50 mm path length to cover a suitable concentration range. Temperature was controlled by a PTP-1 Peltier element (Perkin Elmer).

Viscosity Measurements: Solution viscosities were recorded in purity-grad "pa" solvents at 25 °C with a capillary viscosimeter using the automated viscosity measuring device AVS 360 (Schott Geräte GmbH) in order to obtain reproducible run times. The effective capillary diameter was 0.64 mm. The setup was mounted in a thermostat, which was controlled by circulating water. The measurements were performed from concentrated to diluted solutions. Dilution was achieved by using an automated Titronic *universal* unit (Schott Geräte GmbH). The reduced viscositiy η_{red} was obtained from equation (4.8):

$$\eta_{red} = \frac{t - t_0}{t_0}\frac{1}{c} \tag{4.8}$$

where t and t_0 represent the run times of the dye solution and the pure solvent, respectively, while c corresponds to the concentration of the dye solution in g L^{-1}.

Dynamic Light Scattering (DLS): DLS measurements were carried out at $\theta = 90°$ and 25 °C on an ALV CGS-3 goniometer using a HeNe laser ($\lambda = 632.8$ nm) and an ALV LSE-5004 correlator. Sample solutions ($c(\mathbf{8}) = 1.0 \times 10^{-3}$ M for **B**, **C**, or **D**) were filtrated into a

dust-free vial through a 0.45 μm hydrophobic PTFE filter. The correlation curve was fitted in a data point interval of 10–150 using the default DLS exponential $g2(t)$ fit function with a target *PROB1* parameter of 0.5.

Transmission Electron Microscopy (TEM): TEM measurements were performed on a Siemens Elmiskop 101 Electron Microscope, operating at an acceleration voltage of 80 kV. For the observation of aggregates, a drop of sample solutions (1.0 x 10^{-4} M solution of **8** in THF/MCH = 40:60 vol% and 4.0 x 10^{-4} M solution of **8** in THF/MCH = 20:80 vol% with one equivalent of **9**) was placed on 100-mesh formvar copper grids coated with carbon.

Atomic Force Microscopy (AFM): AFM measurements were carried out under ambient conditions by using a Veeco MultiMode™ Nanoscope IV system operating in tapping mode under air. Silicon cantilevers (Olympus, OMCLAC160TS) with a resonance frequency of ~ 300 kHz were used. The 512 x 512 pixel images were collected at a rate of 2 scan lines per second. Large scale images were recorded at a scan rate of 1 Hz. Solutions of bis(merocyanine) dyes **8** in the respective THF/MCH mixture and with and without barbiturate guest **9** were spin-coated onto highly oriented pyrolytic graphite (HOPG, NanoTechnology Instruments, Netherlands).

Synthesis and Characterization of Compounds 3, 4, 7, and 8:

5-[3,4,5-Tris(dodecyloxy)]-benzylether-1,3-isophthalic acid dimethyl ester (3): 5-Hydroxyisophthalic acid dimethylester (130 mg, 0.619 mmol) and K_2CO_3 (102 mg, 0.736 mmol) were suspended in dry DMF (1.5 mL) under argon atmosphere and 3,4,5-tris(dodecyloxy)benzyl chloride **2** (0.50 g, 0.736 mmol) was added. The resulting mixture was heated to 90 °C for 14 h. After removal of the solvent under reduced pressure the crude product was purified by column chromatography using silica and CH_2Cl_2/MeOH = 70:1 vol% as eluent to give pure **3** as a white solid. Yield: 507 mg (0.594 mmol, 96%). Mp 41 °C. ^{1}H NMR (400 MHz, $CDCl_3$): δ 8.29 (s, 1 H, H$_{isophthalic\ acid\ ester}$), 7.84 (s, 2 H, H$_{isophthalic\ acid\ ester}$), 6.63 (s, 2 H, ArH), 5.03 (s, 2 H, OCH$_2$Ar), 4.01 – 3.94 (m, 6 H, OCH$_2$), 3.94 (s, 6 H, OCH$_3$), 1.83 – 1.71 (m, 6 H, CH$_2$), 1.52 – 1.39 (m, 6 H, CH$_2$), 1.38 – 1.19 (m, 52 H, CH$_2$), 0.88 (t, ^3J = 6.9 Hz, 9 H, CH$_3$). HRMS (ESI, pos. mode, CH_3CN/$CHCl_3$ = 1:1 vol%): calc. m/z $C_{53}H_{89}O_8$ ([M+H]$^+$) 854.2894; found 854.2887.

N^1,N^3-**Bis(6-aminopyridin-2-yl)-5-(3,4,5-tris(dodecyloxy)benzyloxy)isophthalamide (4)**: 2,6-Diaminopyridine (320 mg, 2.93 mmol) was dissolved in dry THF (5 mL) under argon atmosphere and cooled to −78 °C (acetone/dry ice). Then *tert*-butyllithium (1.95 mL of a 1.5 M solution in pentane, 2.93 mmol) followed by diester **3** (500 mg, 0.586 mmol) in dry THF (7 mL) were added dropwise. The resulting solution was stirred for 4 h at −78 °C and additional 16 h at room temperature. After addition of aqueous $NaHCO_3$ (8 mL) and $CHCl_3$

(6 mL), the aqueous phase was extracted with $CHCl_3$ (3 x 5 mL). The combined organic layers were dried over $MgSO_4$ and the solvent was removed under reduced pressure. The crude product was purified by column chromatography using silica and CH_2Cl_2/MeOH = 80:1 vol% as eluent to give pure **4** as a beige solid. Yield: 257 mg (0.256 mmol, 44%). Mp 114 °C. ^{1}H NMR (400 MHz, $CDCl_3$): δ 8.79 (s, 4 H, NH_2), 8.07 (s, 1 H, ArH), 7.73 (s, 2 H, ArH), 7.67 (d, ^3J = 7.6 Hz, 2 H, $H_{pyridine}$), 7.53 (t, ^3J = 7.9 Hz, 2 H, $H_{pyridine}$), 6.65 (s, 2 H, ArH), 6.32 (d, ^3J = 8.1 Hz, 2 H, $H_{pyridine}$), 5.07 (s, 2 H, OCH_2Ar), 3.98 (t, ^3J = 7.3 Hz, 4 H, OCH_2), 3.96 (t, ^3J = 7.4 Hz, 2 H, OCH_2), 1.84 – 1.71 (m, 6 H, CH_2), 1.52 – 1.42 (m, 6 H, CH_2), 1.40 – 1.17 (m, 52 H, CH_2), 0.88 (t, ^3J = 6.9 Hz, 9 H, CH_3). HRMS (ESI, pos. mode, CH_3CN/$CHCl_3$ = 1:1 vol%): calc. m/z $C_{61}H_{95}N_6O_6$ ([M+H]$^+$) 1006.4915; found 1006.4904.

3-(3-Cyano-5-((5-(dibutylamino)thiophen-2-yl)methylene)-4-methyl-2,6-dioxo-5,6-dihydropyridin-1(2H)-yl)propanoic acid (7): Carboxylic-acid-functionalized pyridone **6** (1.11 g, 5.0 mmol) and 2-dibutylamino-5-formylthiophene **5** (1.20 g, 5.0 mmol) in Ac_2O (5 mL) were stirred at 90 °C for 2 h. After cooling down to room temperature the solvent was removed under reduced pressure. The resulting solid was recrystallized two times from MeOH to give pure **7** as a red crystalline solid. Yield: 1.41 g (3.18 mmol, 64%). Mp > 350 °C. ^{1}H NMR (DMSO-d_6): δ 8.06 (1 H, d, ^3J = 5.4, $H_{thiophene}$), 7.88 (1 H, s, $H_{methine}$), 6.89 (1 H, d, ^3J = 5.2, $H_{thiophene}$), 4.05 (2 H, t, ^3J = 7.8, NCH_2CH_2COOH), 3.62 (4 H, t, ^3J = 7.7, NCH_2), 2.46 (3 H, s, CH_3), 2.43 (2 H, t, ^3J = 7.8, NCH_2CH_2COOH), 1.75 – 1.61 (4 H, m, CH_2), 1.43 – 1.20 (4 H, m, CH_2), 0.94 (6 H, t, ^3J = 7.5, CH_3). HRMS (ESI, pos. mode, CH_3CN/$CHCl_3$ = 1:1 vol%): calc. m/z $C_{23}H_{29}N_3O_4S$ ([M]$^+$) 443.18733; found 443.18728.

N^1,N^3-Bis(6-(3-(3-cyano-5-((5-(dibutylamino)thiophen-2-yl)methylene)-4-methyl-2,6-dioxo-5,6-dihydropyridin-1(2H)-yl)propanamido)pyridin-2-yl)-5-(3,4,5-tris(dodecyloxy) benzyloxy)isophthalamide (8): Carboxylic-acid-functionalized merocyanine **7** (433 mg, 0.976 mmol), HATU (407 mg, 1.07 mmol) and DIPEA (202 mg, 265 mL, 1.56 mmol) in dry DMF (2 mL) under argon atmosphere were stirred for 20 min at room temperature. Diamine **4** (49.1 mg, 0.0488 mmol) in dry DMF (0.5 mL) was added dropwise and the resulting mixture was stirred for 15 h at room temperature. The solvent was removed under reduced pressure and the residue was purified by column chromatography using silica gel with CH_2Cl_2/MeOH = 98.5:1.5 vol% as eluent to give pure **8**. Yield: 38.0 mg (20.5 μmol, 42%) and 11.9 mg (8.30 μmol, 17%) of monoacylated product. The purity (> 99 %) of product **8** was confirmed by HPLC (reversed phase, MeOH/CH_2Cl_2 = 7:3 vol%). Mp 216 °C. ^{1}H NMR (400 MHz, CD_2Cl_2/MeOH-d_4 = 4:1 vol%): δ 8.10 (s, 1 H, ArH), 7.94 – 7.92 (m, 2 H, $H_{pyridine}$), 7.75 (s, 2 H, ArH), 7.67 – 7.63 (m, 4 H, $H_{pyridine}$), 7.61 (d, ^3J = 5.6 Hz, 2 H, $H_{thiophene}$), 7.54 (s, 2 H, ArH), 6.63 (s, 2 H, $H_{methine}$), 6.45 (d, ^3J =5.2 Hz, 2 H, $H_{thiophene}$), 5.06 (s, 2 H, OCH_2), 4.23 (t, ^3J = 7.6 Hz, 4 H, NCH_2CH_2CON), 3.91 (t, ^3J = 6.44, 4 H, OCH_2),

3.86 (t, ^3J = 6.6 Hz, 2 H, OCH$_2$), 3.45 (t, ^3J = 7.7 Hz, 8 H, NCH$_2$), 2.67 (t, ^3J = 7.3 Hz, 4 H, NCH$_2$CH_2CON), 2.37 (s, 6 H, CH$_3$), 1.74 – 1.58 (m, 14 H, CH$_2$), 1.57 – 1.34 (m, 6 H, CH$_2$), 1.33 – 1.12 (m, 64 H, CH$_2$), 0.87 (t, ^3J = 7.3 Hz, 12 H, CH$_3$), 0.78 (t, ^3J = 9.8 Hz, 9 H, CH$_3$). UV/Vis (THF): λ_{max}/nm (ε_{max}/L mol^{-1} cm^{-1}) = 538 (272 x 10^3). HRMS (ESI, pos. mode, THF): calc. *m/z* C$_{107}$H$_{149}$N$_{12}$O$_{12}$S$_2$Na ([M+Na]$^+$) 1857.07486; found 1857.07811.

Chapter 5

Supramolecular Polymers from Self-Complementary Hamilton-Receptor-Functionalized Merocyanine Dyes

Abstract: A self-complementary Hamilton-receptor-functionalized merocyanine dye has been synthesized by incorporating a hydrogen bonding receptor site to the donor moiety of a merocyanine chromophore that bears a barbituric acid acceptor unit. The optical and electro-optical properties of monomeric dyes have been studied by UV/Vis, fluorescence, and electro-optical absorption (EOA) spectroscopy in polar solvents or solvents with hydrogen bond acceptor ability under dilute condition. The self-assembly properties of this self-complementary merocyanine in solution have been investigated by concentration- and temperature-dependent UV/Vis and one- and two-dimensional NMR spectroscopy. These studies revealed that the present functionalized merocyanine dye self-assembles in a head-to-tail fashion by forming six hydrogen bonds. The aggregate size in solution was determined by DLS and DOSY NMR investigations. In nonpolar solvent mixtures at high concentrations this merocyanine dye forms appreciably fluorescent gels while the monomeric dye and self-assemblies in solution are only weakly fluorescent.

5.1 Introduction

For anisotropic dipolar molecules such as merocyanines, usually the mutual antiparallel orientation in dimeric aggregates is favored by electrostatic interactions (see Chapter 3). This characteristic property of merocyanine dyes has been used to create supramolecular polymers by tethering two dyes via a spacer unit.[16] The Hamilton receptor that was used to connect the merocyanine units in Chapter 4 provides the opportunity to modify the self-assembly by offering a competing hydrogen bonding site.[106] Hydrogen bonding interactions, in turn, have been extensively used for creating supramolecular polymers and several reviews have been published on this topic.[107] Hamilton receptors have been employed in various systems for molecular recognition,[20] complexes enabling photoinduced electron-transfer studies,[108] supramolecular polymers,[109] supramolecular dendrimers,[110] foldamers,[111] noncovalently cross-linked block copolymers,[112] and binding of barbiturates to surfaces.[113] Structurally related systems based on melamines were used to arrange merocyanine dyes via hydrogen bonds and afforded a variety of complex architectures.[19] Formation of supramolecular sheet aggregates from self-complementary bis(acylaminopyridines) was also reported.[114]

The question arises whether antiparallel orientation of merocyanine dyes can be circumvented and supramolecular polymers of such dipolar dyes can be achieved by their head-to-tail orientation through hydrogen bonding. Recently, Würthner and coworkers have shown that the antiparallel arrangement of merocyanines can be overcome in hydrogen-bonded bimolecular complexes of Hamilton-receptor-functionalized merocyanines containing a *N*-alkyl-substituted barbiturate acceptor moiety and complementary merocyanines bearing a barbituric acid unit.[18] Two methyl substituents at the *ortho* positions of the dihydropyridone heterocycles of the merocyanine dye enforce an almost perpendicular orientation of the two planes of the Hamilton receptor and the chromophore. Thereby, the antiparallel aggregation of the even more dipolar bimolecular complex is impeded.[18] Based on this concept it appears feasible that self-complementary, hydrogen-bonding receptor containing merocyanines would lead to supramolecular polymers by head-to-tail orientation of the dipolar dyes. Therefore, we have constructed the self-complementary merocyanine dye **1** that consists of a Hamilton receptor and a merocyanine chromophore bearing a barbituric acid acceptor group, and studied the self-assembly properties of dye **1** (Scheme 1).

Highly directional noncovalent interactions such as hydrogen bonding are known to facilitate the formation of organogels.[115] It has been shown previously that organogels could be prepared from bis(merocyanine) dyes. However, such gels show no emission owing to antiparallel aggregation of the highly dipolar chromophores.[16] Strong quenching of the fluorescence is well-known for many H-type dimer aggregates,[116] and theoretical interpretations for such quenching have been discussed in the literature.[117] Nevertheless, some

exceptions are known.[118] Organogels based on hydrogen-bond-mediated merocyanine dye assemblies with head-to-tail arrangement of the chromophores may show favorable emission properties owing to the modified binding motif. Therefore, we have also investigated the gelation properties of Hamilton-receptor-functionalized merocyanine dye **1** and found that this newly designed merocyanine forms remarkably fluorescent gels in nonpolar solvent mixtures at high concentrations.
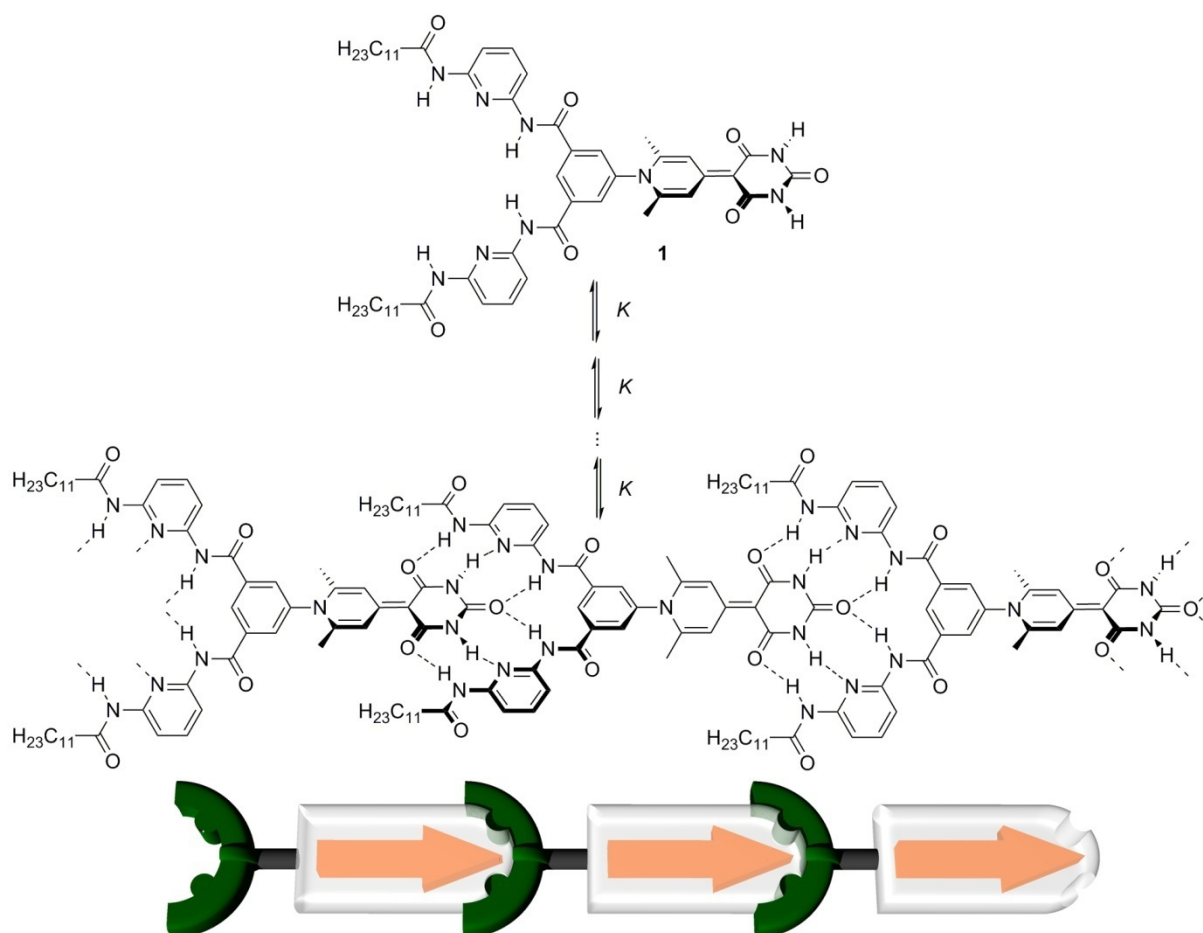
Scheme 1. Concept for the hydrogen-bond-directed formation of supramolecular polymers consisting of self-complementary merocyanine dyes **1** arranged in a head-to-tail fashion and schematic representation of the enhancement of the dipole moment upon self-assembly.

5.2 Results and Discussion

5.2.1 Synthesis

The Hamilton-receptor-functionalized merocyanine dye **1** was synthesized according to the route outlined in Scheme 2. Diamide **7** was prepared according to the literature, starting with the reaction of 5-aminoisophthalic acid **2** and dehydroacetic acid **3** to pyridone hydrochloride

4.[18] Esterification of the latter resulted in diethyl ester derivative **5**, which could be transformed to diamide **7** with monolithiated 2,6-diaminopyridine.[18] Subsequent acylation of **7** with dodecanoyl chloride afforded the precursor **8** for the target compound **1** in 42% yield. The Knoevenagel condensation reaction of **8** with CH-acidic barbituric acid **9** yielded the desired Hamilton-receptor-functionalized merocyanine dye **1** in 4%. The low yield of the last step can partially be attributed to the demanding purification process, comprising successive column chromatography, gel permeation chromatography (GPC), and recrystallization. Merocyanine dye guest molecule **10** equipped with a barbituric acid acceptor group, reference Hamilton receptor **11** and Hamilton-receptor-functionalized merocyanine **12** with *n*-butyl substituents in imide positions were prepared according to the literature (structures are shown in Scheme 3).[18,119] Merocyanine **12** is a valuable reference system as it is, in contrast to newly synthesized merocyanine **1**, not self-complementary. The precursor **8** and the target compound merocyanine **1** were characterized by NMR spectroscopy and high resolution mass spectrometry (HRMS). For the detailed structural assignment of monomeric dye **1** by 1- and 2-D NMR spectroscopy, see section 5.2.4.
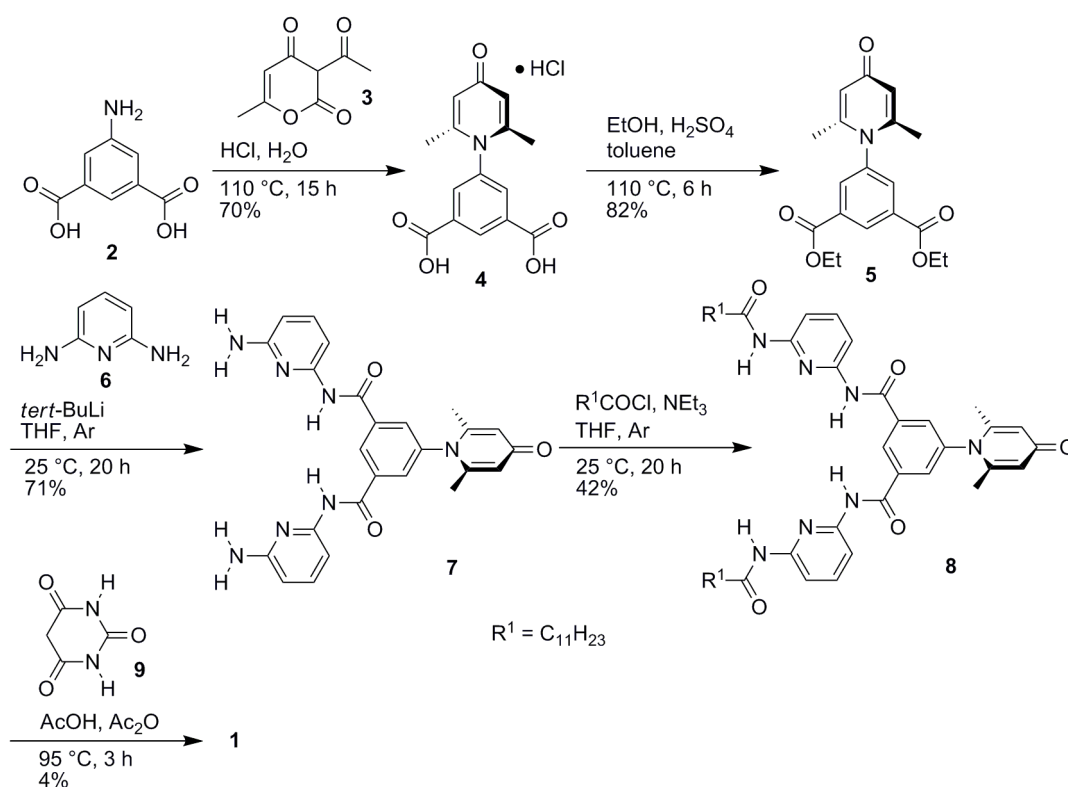
Scheme 2. Synthesis of self-complementary Hamilton-receptor-functionalized merocyanine dye **1**.
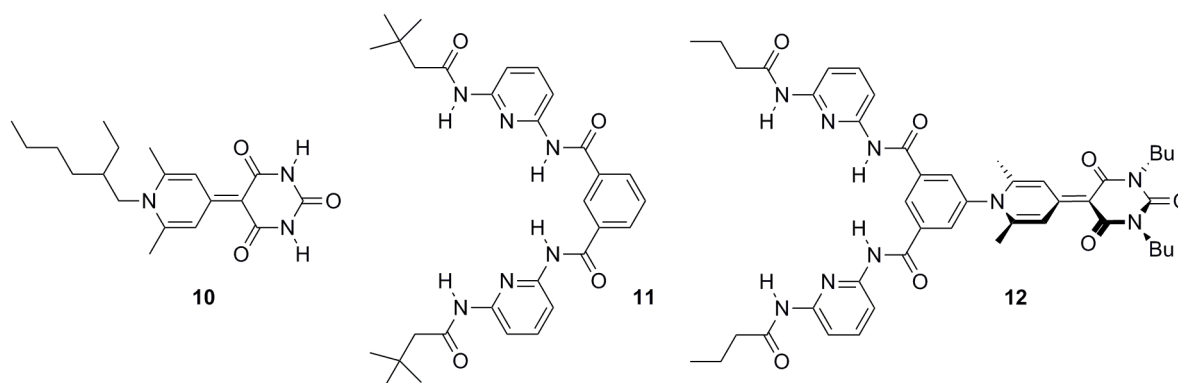
Scheme 3. Structures of merocyanine dye guest molecule **10** bearing a barbituric acid acceptor group, reference Hamilton receptor **11** and Hamilton-receptor-functionalized merocyanine **12**.

5.2.2 Spectroscopic Studies of Merocyanine 1 Monomers

In order to investigate the optical and electro-optical properties of monomers of merocyanine dye **1**, solvents of high polarity like dimethylsulfoxide (DMSO, $\varepsilon_r = 46.5$) and solvents of strong hydrogen bond acceptor capability like 1,4-dioxane ($\varepsilon_r = 2.25$) were used. The investigation of monomers of **1** in nonpolar solvents is hampered by self-assembly of this self-complementary system. The presence of monomers in deuterated DMSO was confirmed by ^{1}H NMR spectroscopy (for details, see section 5.2.4). Highly dilute solutions were employed to ensure the presence of monomers in 1,4-dioxane ($c = 5.3 \times 10^{-7}$ M)[120] and CHCl$_3$ ($c = 1.4 \times 10^{-7}$ M, $T = 328$ K). Merocyanine **1** is existent as monomer in highly diluted CHCl$_3$ solution at elevated temperature as was attested by temperature-dependent fluorescence experiments (for details, see section 5.2.3). The UV/Vis spectra of **1** in 1,4-dioxane, CHCl$_3$, and DMSO exhibit typical absorption properties of monomeric merocyanine dyes. The intense charge transfer (CT) absorption band shows negative solvatochromism as this band is hypsochromically shifted with increasing solvent polarity (λ_{max}(1,4-dioxane) = 396 nm, λ_{max}(CHCl$_3$) = 392 nm, λ_{max}(DMSO) = 389 nm) and the absorption coefficient ε is decreased in more polar solvent (Figure 1). This solvatochromism may be attributed to differences in the stabilization of the ground and excited states by the solvent, and hence to the change of the dipole moment difference $\Delta\mu = \mu_e - \mu_g$ (μ_e and μ_g denote the excited and ground state dipole moments, respectively) upon optical excitation in solvents of different polarity.[81,121]

Dipole moments of the ground state μ_g and the dipole moment differences $\Delta\mu$ of merocyanine dye **1**, and the reference compounds **10** and **12** in dilute 1,4-dioxane solution were determined by electro-optical absorption (EOA) spectroscopy.[122,i] A quantitative evaluation of the optical and electro-optical data of these chromophores provides the dipole

---

[i] EOA experiments were carried out by Dr. Matthias Stolte.
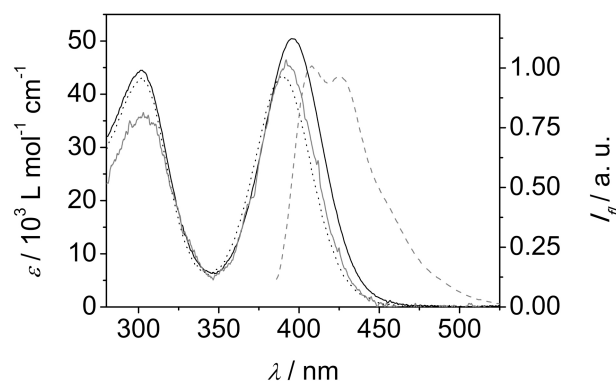
Figure 1. UV/Vis absorption spectra of monomeric **1** in 1,4-dioxane (black solid line, 298 K), CHCl$_3$ (grey solid line, 328 K), and DMSO (black dotted line, 298 K) and normalized fluorescence spectrum in CHCl$_3$ (grey dashed line, 328 K, λ_{ex} = 370 nm).

moments μ_g, transition dipole moment μ_{eg}, and $\Delta\mu$ (Table 1). Only minor optical changes of the CT absorption bands of merocyanine dyes **1**, **10**, and **12** could be observed (see also Figure D6 in the Appendix). The data shown in Table 1 reveal that the covalent attachment of a Hamilton receptor to the donor moiety of the merocyanine chromophore leads to a bathochromic shift of the absorption maximum (λ_{max}) and an increase of absorbance (ε_{max}) and transition dipole moment (μ_{eg}). The dipolar character of the merocyanine decreases upon functionalization with the receptor owing to the unfavorable orientations of the partial dipole moments of the Hamilton receptor rotamers with respect to the direction of μ_g of the merocyanine dye.[123] However, the dipole difference $\Delta\mu$ remains almost unaffected. The negative $\Delta\mu$ values of these merocyanines are in accordance with the observation of negative solvatochromism.[18] Recent EOA investigations of bimolecular complex **10:12** have revealed the formation of hydrogen-bond-mediated highly dipolar structures.[18,123] Thus, self-complementary Hamilton-receptor-functionalized merocyanine dye **1** constitutes a promising building block for the creation of self-assembled, highly dipolar linear polymers.

Fluorescence studies have revealed that dye **1** monomers are very weakly emissive in CHCl$_3$ (ϕ_{fl} = 0.03). This may be attributed to rapid nonradiative deactivation pathways

Table 1. Dipole moments and optical data of **1**, **10**, and **12** determined by UV/Vis and EOA spectroscopy in 1,4-dioxane at 298 K. Values for compounds **10** and **12** are taken from reference 18a.

	λ_{max} (nm)	ε_{max} (M^{-1} cm^{-1})	μ_{eg} (D)	$\mu_g{}^a$ (D)	$\Delta\mu{}^a$ (D)
10	379	50600	6.5	10.1 ± 0.1	-3.9 ± 0.1
12	391	56000	7.2	7.7 ± 0.1	-3.7 ± 0.1
1	396	50800	6.9	7.9 ± 0.2	-4.3 ± 0.4

^{a} "Gas phase" dipole moments were calculated by a solvent correction within the approximations of Onsager's continuum model.[89] (1 D = 3.336 x 10^{-30} C m)

through a bond-twisting mechanism and constitutes a common feature of merocyanine and cyanine dyes in solution.[124] The maximum of the emission band λ_{em} was observed at 408 nm (Figure 1). Emission of the monomer in $CHCl_3$ was determined at low concentrations and elevated temperature (c = 1.4 x 10^{-7} M, 328 K). Similarly, weak emission has also been found for the reference compound **12** in toluene.[125]

5.2.3 Self-Assembly Studies

First indication for the self-assembly of Hamilton-receptor-functionalized merocyanine dyes **1** in the gas phase was obtained by mass spectrometry. Mass peaks observed in MALDI-TOF spectra of dye **1** correspond to monomeric (m/z 944.2 ($[M]^+$); calc. 943.5) and dimeric (m/z 1888.1 ($[M_2]^+$); calc. 1888.3) species (see Figure D5 in the Appendix). To gain insight into the self-assembly properties of self-complementary merocyanine dye **1** in solution, concentration- and temperature-dependent UV/Vis spectroscopic studies were performed. Owing to the low solubility of **1** in 1,4-dioxane, no solutions of high concentration could be prepared. Therefore, tetrahydrofuran (THF) was chosen for self-assembly studies since it has been previously shown that for the formation of the structurally related bimolecular complex **10:12** similar binding constants were found in 1,4-dioxane and THF.[18] The concentration-dependent measurements in THF at 298 K reveal a hypsochromic shift of the absorption maximum upon increasing the concentration (Figure 2a). The observation of an isosbestic point indicates an equilibrium between free and bound dye molecules **1**. Monomeric and self-assembled species may be distinguished on the basis of their absorption maxima at λ_{max} = 396 nm and 382 nm, respectively. The absorption maxima of free and bound species were extrapolated using equations (5.1) and (5.2) (vide infra). A hypsochromic shift was observed
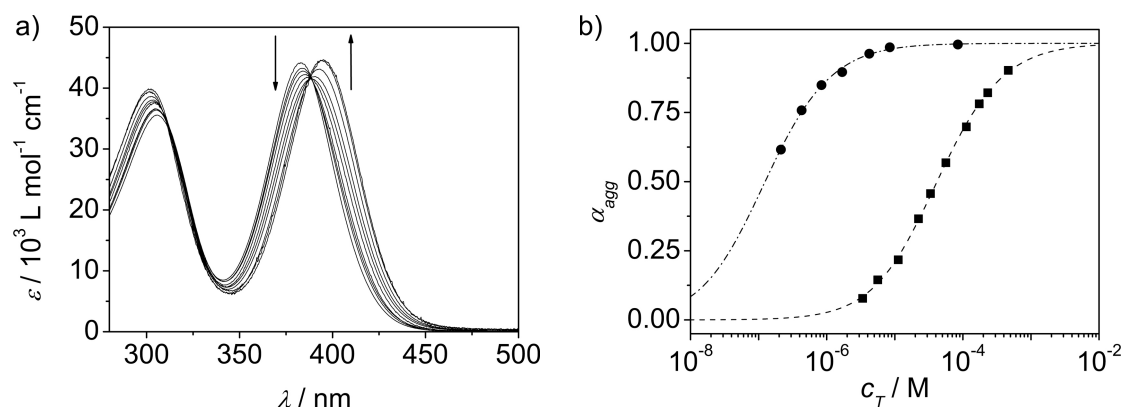
Figure 2. a) Concentration-dependent UV/Vis spectra of **1** in THF at 298 K at the concentration range from c = 4.7 x 10^{-4} M to 3.4 x 10^{-6} M. Arrows indicate spectral changes upon dilution. b) α_{agg} in THF (■, calculated from the apparent absorption coefficient ε at 370 nm) and $CHCl_3$ (●, calculated from the apparent absorption coefficient at 375 nm) plotted against c_T and the fitting curves obtained by the nonlinear regression analysis based on the isodesmic model.

upon self-assembly at high concentrations that can be ascribed to an effect exerted by the receptor which is similar to that of solvents of different polarity on a solvatochromic dye.[18b,81,121] Similar absorption spectral changes have been observed for the formation of bimolecular complexes between reference compounds **10** and **11**.[18]

The isodesmic model[23] could be applied to the formation of supramolecular polymers from self-complementary dyes **1**. According to this model, the molar fraction of aggregated species α_{agg} can be expressed as a function of the total concentration c_T and the equilibrium constant K (see Chapter 2):[23]

$$\alpha_{agg} = 1 - \frac{2Kc_T + 1 - \sqrt{4Kc_T + 1}}{2K^2 c_T^2} \tag{5.1}$$

α_{agg} can be calculated from the apparent absorption coefficient of the solution $\varepsilon(c_T)$ and the absorption coefficients of monomer ε_{mon} and aggregate ε_{agg}:

$$\alpha_{agg} \approx \frac{\varepsilon(c_T) - \varepsilon_{mon}}{\varepsilon_{agg} - \varepsilon_{mon}} \tag{5.2}$$

The equilibrium constant K is defined according to:

$$\mathbf{1}_n + \mathbf{1} \rightleftharpoons \mathbf{1}_{n+1} \; ; \qquad K = \frac{[\mathbf{1}_{n+1}]}{[\mathbf{1}_n][\mathbf{1}]} \tag{5.3}$$

Nonlinear regression analysis of the data obtained from the concentration-dependent UV/Vis measurements in THF at certain wavelengths by employing equation (5.1) yielded an equilibrium constant of $K = (1.6 \pm 0.3) \times 10^4 \, M^{-1}$ (Figure 2b). The equilibrium constant was averaged over the values deduced at four different wavelengths (see Figure D7).

Similar concentration-dependent UV/Vis experiments in CHCl$_3$ at 298 K revealed a more pronounced driving force of **1** towards self-assembly (Figure 2b, for more details see Figures D8 and D9). Hence, it was not possible to cover the whole binding isotherm with data points. Nevertheless, the equilibrium constant in CHCl$_3$ could be roughly estimated to $6.2 \times 10^6 \, M^{-1}$. This value is in good agreement with that for the formation of bimolecular complex **10:12** from reference merocyanines **10** and **12** in CHCl$_3$. For this complex, an equilibrium constant of $K_{dim} > 10^6 \, M^{-1}$ was obtained from ^{1}H NMR titration experiments at a constant host concentration and 298 K.[18]

Temperature-dependent UV/Vis measurements in THF revealed spectral changes that are in good accordance with the concentration-dependent series. The self-assembly of **1** was probed upon variation of temperature from 10 °C to 60 °C in steps of 5 °C at a concentration of $c = 3.5 \times 10^{-5} \, M$ (Figure 3a). A decrease of the temperature resulted in a hypsochromic shift of the absorption maximum, suggesting self-complexation of **1**. The equilibrium between free

and bound species is indicated by an isosbestic point. Since, in comparison to the concentration-dependent series, a smaller part of the fitting curve can be covered within the accessible temperature range (Figure 3b), the extrapolation of the absorption maxima of free and bound species according to equations (5.4) and (5.5) (vide infra) is less precise. However, the maximum values for monomeric and self-assembled compound at λ_{max} = 396 nm and 385 nm, respectively, are in reasonable agreement.

The isodesmic self-assembly process was confirmed by an excellent fit of the temperature-dependent isodesmic model[28] (Figure 3b). This model expresses the molar fraction of aggregated species $\alpha_{agg}(T)$ as a function of temperature (see Chapter 2):[28]

$$\alpha_{agg}(T) = \frac{1}{1 + e^{-0.908\Delta H \frac{T-T_m}{RT_m^2}}} \tag{5.4}$$

where T_m denotes the melting temperature of the aggregate and ΔH the molar enthalpy of aggregate formation. $\alpha_{agg}(T)$ can be obtained from absorption spectra using the following equation:

$$\alpha_{agg}(T) \approx \frac{\varepsilon(T) - \varepsilon_{mon}}{\varepsilon_{agg} - \varepsilon_{mon}} \tag{5.5}$$

Application of this model to the apparent absorption coefficients $\varepsilon(T)$ at 395 nm provided T_m = 316 K, the molar Gibbs free energy $\Delta G° = -26.6$ kJ mol^{-1}, and the molar enthalpy of aggregate formation $\Delta H° = -46.2$ kJ mol^{-1} as well as the change of entropy $\Delta S° = -65.8$ J mol^{-1} K^{-1}. A more detailed description of the equations used to compute the respective values is given in the Appendix and in Chapter 2. Comparison of the enthalpy and entropy contributions to the total Gibbs free energy changes for aggregation reveals that the self-assembly process is entropically disfavored but enthalpically driven. The equilibrium
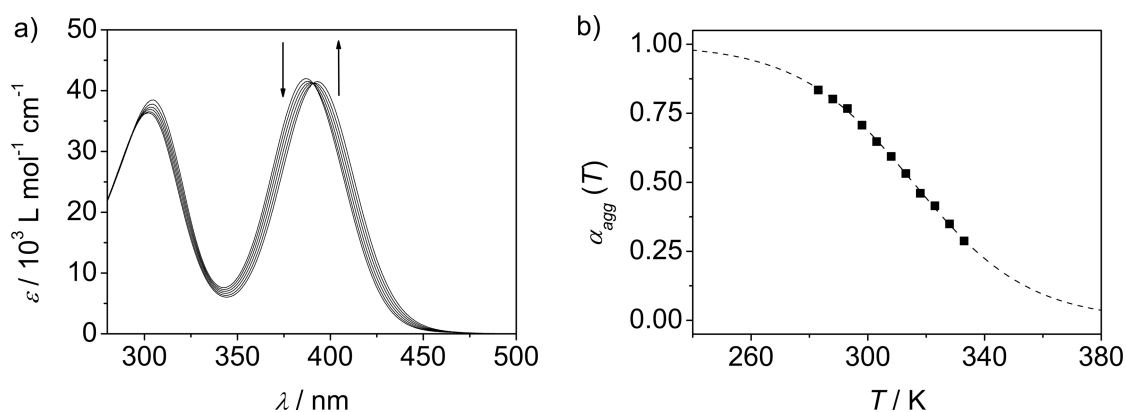
Figure 3. a) Temperature-dependent UV/Vis spectra of **1** in THF (c = 3.5 x 10^{-5} M) from 10 °C to 60 °C in steps of 10 °C. Arrows indicate spectral changes upon increasing temperature. b) Temperature-dependent degree of aggregation $\alpha_{agg}(T)$ calculated from the apparent absorption coefficient at 395 nm plotted against the temperature and fitting curve obtained by the nonlinear regression analysis based on the isodesmic model.

constant as a function of the temperature was calculated to $K = 4.5 \times 10^4 \, M^{-1}$ at 298 K (see Figure D10c in the Appendix). It is noteworthy that, in order to investigate the hydrogen-bond-directed association process by UV/Vis spectroscopy, conditions were applied where only monomers up to small oligomers are present.

The average of the two equilibrium constants determined from concentration- and temperature-dependent UV/Vis experiments in THF was calculated to $K = 3.1 \times 10^4 \, M^{-1}$, and this value is in very good agreement with the dimerization constant of reference merocyanines **10** and **12** ($K_{dim} = 3.6 \times 10^4 \, M^{-1}$).[18b] Linear free energy relationships (LFERs) were previously used to estimate the equilibrium constant in solvents of low polarity.[81,82] With such LFER analysis, a K value in the order of $10^{15} \, M^{-1}$ was estimated for the self-assembly of dye **1** in pure *n*-hexane (see Figure D11, Table D3).

The emission property of **1** is markedly affected by the self-assembly. Concentrated solution of **1** in CHCl$_3$ ($c = 0.7 \times 10^{-4}$ M, $\alpha_{agg} = 1$) showed increased emission ($\phi_{fl} = 0.07$)[126] at $\lambda_{em} = 489$ nm (Figure 4) in comparison to that of monomers ($\phi_{fl} = 0.03$). Excitation spectra revealed that the emission originates from the self-assembled species (see Figure D12). The increase of the emission might be ascribed to the loss of radiationless deactivation pathways upon self-assembly owing to the rigidification of the molecules upon self-assembly. Several polymethine dyes have been reported to exhibit enhanced emission intensities after being physically or chemically rigidified.[127]
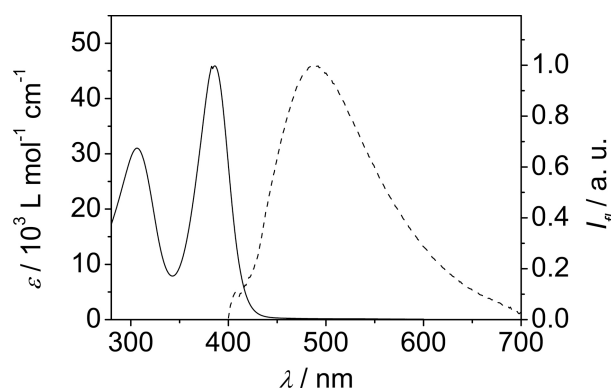
Figure 4. UV/Vis absorption and fluorescence spectra of assemblies of merocyanine dye **1** in CHCl$_3$ ($c = 0.7 \times 10^{-4}$ M, 298 K, $\lambda_{ex} = 370$ nm).

Temperature-dependent fluorescence spectra of merocyanine **1** at low concentration ($c = 1.4 \times 10^{-7}$ M, $\alpha_{agg} \approx 0.5$) in CHCl$_3$ revealed an increase of the emission with decreasing temperature (Figure 5a). The fluorescence quantum yield increases from $\phi_{fl} = 0.03$ to 0.07 upon decreasing the temperature from 55 °C to 10 °C. This increase of fluorescence may be attributed to a transformation of monomers at high temperatures to self-assemblies at low temperatures. The temperature-dependent isodesmic model (vide supra) was applied to a plot of the molar fractions of self-assembled species α_{agg} against the temperature (Figure 5b).

From this plot the thermodynamic parameters T_m, K, $\Delta G°$, $\Delta H°$, and $\Delta S°$ for the self-assembly of merocyanine **1** could be obtained (Table 2). α_{agg} was calculated with equation (5.2) using the integrated fluorescence intensity instead of absorption. With a value of 7.3 x 10^6 M^{-1}, the equilibrium constant is in very good agreement with the value obtained from concentration-dependent UV/Vis experiments (K = 6.2 x 10^6 M^{-1}).
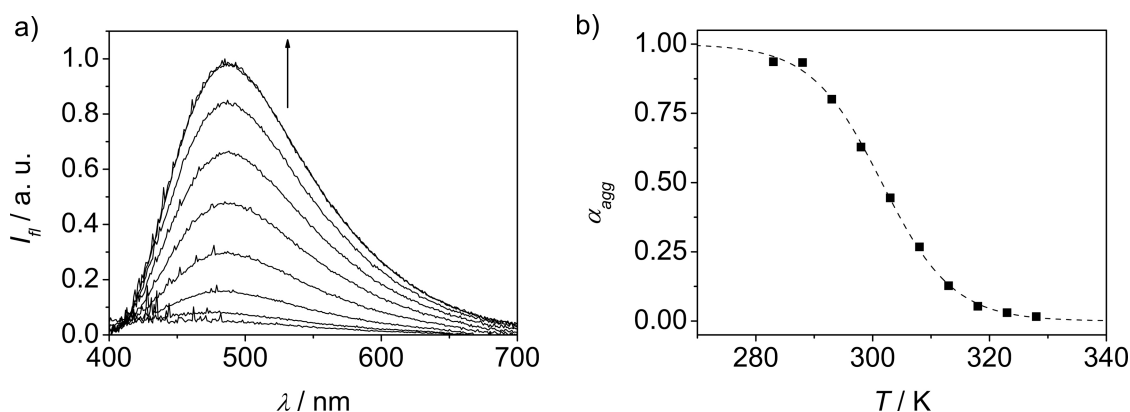
Figure 5. a) Temperature-dependent fluorescence spectra of **1** in CHCl$_3$ (c = 1.4 x 10^{-7} M , λ_{ex} = 370 nm) from 10 °C to 55 °C in steps of 5 °C. The arrow indicates changes upon decreasing temperature. b) Plot of the temperature-dependent molar fractions of self-assembled species α_{agg} calculated from the integrated fluorescence intensity and fitting curve obtained by nonlinear regression analysis based on the isodesmic model.

Table 2. Thermodynamic parameters T_m (K), $\Delta G°$ (kJ mol^{-1}), $\Delta H°$ (kJ mol^{-1}), $\Delta S°$ (J mol^{-1} K^{-1}), and K (M^{-1}) obtained from the temperature-dependent self-assembly of **1** (c = 1.4 x 10^{-7} M, CHCl$_3$) based on the isodesmic model.

T_m	$\Delta G°$	$\Delta H°$	$\Delta S°$	K [a]
302	−39.2	−137	−131	7.3 x 10^6

[a] Value determined at 298 K.

5.2.4 Structural Elucidation of Monomeric and Self-Assembled Dye 1 by NMR Spectroscopy

The structural binding motif of assemblies of **1** was studied in detail by NMR spectroscopy at concentrations of 0.5 mmol L^{-1}. In ^{1}H NMR spectrum of **1** in deuterated dimethylsulfoxide (DMSO-d_6), a simple pattern of sharp signals was observed, indicating that dye **1** is monomerically dissolved in this polar solvent. Upon changing the solvent to CDCl$_3$, significant changes compared to the spectrum in DMSO-d_6 were observed, apparently due to self-assembly. Structural features of the self-assembled species were elucidated by (^{1}H,^{1}H)-COSY, (^{1}H,^{13}C)-HSQC, and (^{1}H,^{13}C)-HMBC NMR experiments. For comparison, similar NMR experiments were performed for the reference Hamilton-receptor-functionalized merocyanine **12** in CDCl$_3$ which cannot form self-assemblies owing to *N*-alkyl substituents of

the barbiturate acceptor moiety. The assignment of the significant ^{1}H NMR signals is shown in Table 3 and complete data are given in Table D1 in the Appendix.

Monomers of **1** in DMSO-d_6 showed a single set of nicely resolved ^{1}H NMR signals (Figure 6a, Table 3). The protons marked with and without prime (see structures in Table 3) are chemically equivalent, which is in accordance with an overall C_{2v}-symmetry of monomeric **1**. The different conformers of the receptor in solution are usually not observable due to fast interconversion on the NMR time scale.[111c] Apart from solvent-induced shifts of signals, a similar pattern was obtained for monomeric reference compound **12** in CDCl$_3$ (Table 3).

A considerably more complex spectrum was obtained for supramolecular polymers of **1** in CDCl$_3$. The signals are broader and split into intricate patterns compared to those of monomeric **1** in DMSO-d_6. The splitting for selected proton signals in CDCl$_3$ is highlighted in Figure 6 by dots of the same color (see also Table 3). Upon complex formation with a barbituric acid the Hamilton receptor becomes fixed in a specific conformation that deviates from planarity by about 46°.[123] Self-assembly into extended oligomers and the loss of symmetry due to deviation from planarity lead to signal splitting and broadening. Beside significant splitting and peak broadening, pronounced changes of the chemical shifts for
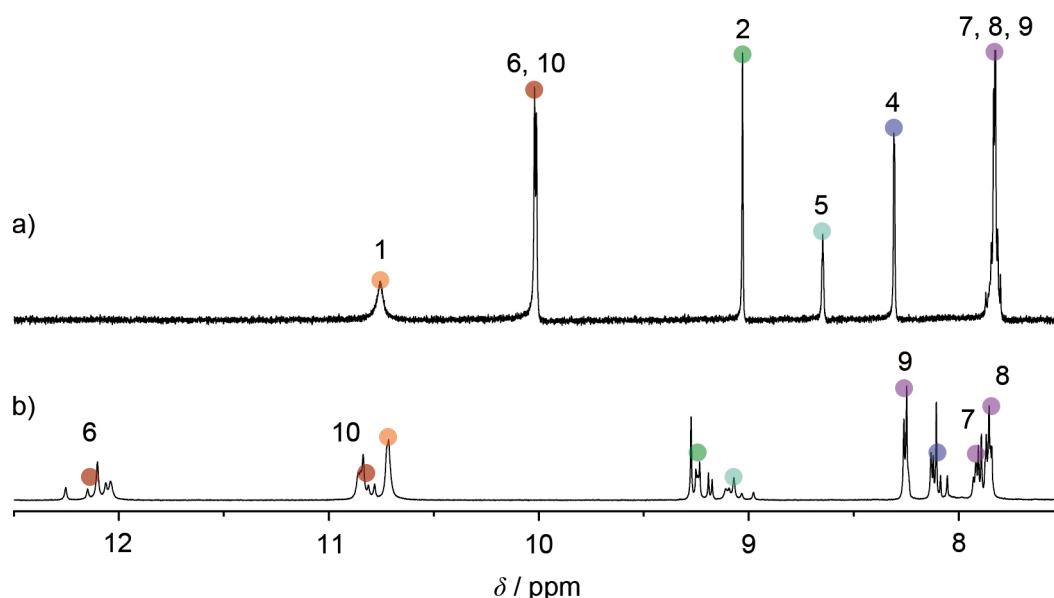
Figure 6. Sections of the ^{1}H NMR spectra of **1** in a) DMSO-d_6 (c = 5.0 x 10^{-4} M, 400 MHz) and b) CDCl$_3$ (c = 5.0 x 10^{-4} M, 600 MHz) at 293 K. The colored dots highlight the splitting of selected monomer signals upon self-assembly.

Table 3. Assignment of significant proton signals of Hamilton-receptor-functionalized merocyanine dyes **1** and **12** in CDCl$_3$ (600 MHz) and DMSO-d_6 (400 MHz).
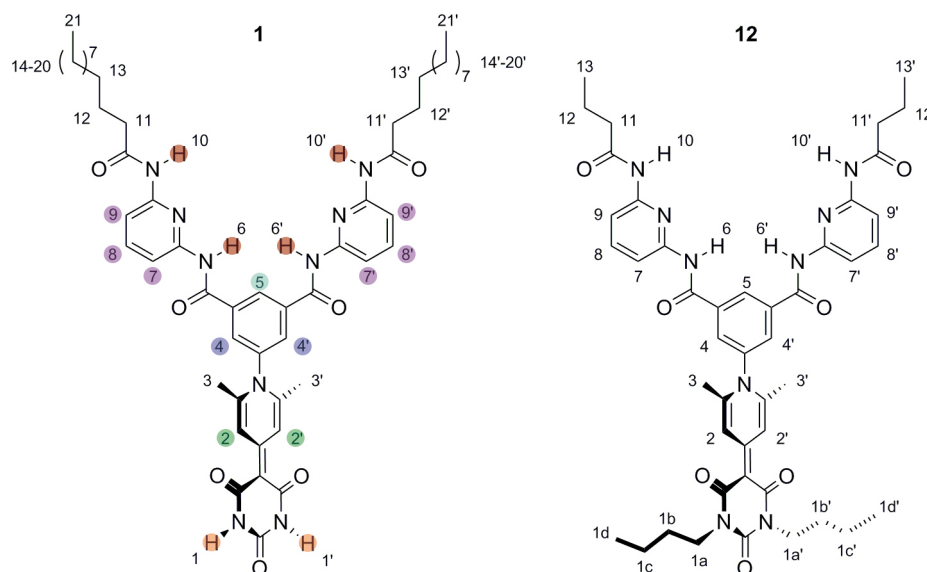
position of protons	12	1		
	CDCl$_3$	DMSO	CDCl$_3$	
	δ_H (J / Hz)	δ_H (J / Hz)	δ_H (J / Hz)	$\Delta\delta_H$ [b,c]
1, 1'	-	10.75 (s, 2H)	10.78 (s, 2H)	-
2, 2'	9.17 (s, 2H)	9.03 (s, 2H)	9.23 [a] (m, 2H)	0.06
3, 3'	2.19 (s, 6H)	2.22 (s, 6H)	2.30 (br s, 6H)	0.11
4, 4'	8.02 (s, 2H)	8.31 (s, 2H)	8.10 [a] (m, 2H)	0.08
5	8.69 (s, 1H)	8.65 (s, 1H)	9.08 [a] (m, 1H)	0.39
6, 6'	8.52 (s, 2H)	10.02 (s, 2H)	12.12 [a] (m, 2H)	3.60
7, 7'	8.00 (d, 8.1, 2H)	7.83 (m, 2H)	7.92 (d, 9.0, 1H)	−0.08
			7.90 (d, 7.8, 1H)	−0.10
8, 8'	7.83 (t, 8.1, 2H)	7.83 (m, 2H)	7.86 (t, 8.1, 2H)	0.03
9, 9'	8.05 (d, 8.0, 2H)	7.83 (m, 2H)	8.25 (d, 7.8, 2H)	0.20
10, 10'	7.60 (s, 2H)	10.02 (s, 2H)	10.82 [a] (m, 2H)	3.22
11, 11'	2.39 (t, 7.4, 4H)	2.39 (t, 7.4, 4H)	2.62 (br, 4H)	0.23

[a] Estimated value due to partial overlap or broadening of signals. [b] Chemical shift difference $\Delta\delta_H$ of the respective protons of **1** and **12** in CDCl$_3$ (c = 5.0 x 10^{-4} M). [c] The centers of the multiplets for certain protons of **1** were used to calculate the shift.

protons at positions 5 (0.39 ppm) and 11 (0.23 ppm), and even more for the amide protons 6 (3.60 ppm) and 10 (3.22 ppm), upon self-assembly of **1** could be observed by comparing the ^{1}H NMR data of **1** and **12** in CDCl$_3$ (see Table 3). Similar shifts have recently been reported for bimolecular complexes of merocyanine **10** with reference Hamilton receptor **11** and merocyanine **12**, respectively,[18] which indicates the formation of self-assemblies of **1** in CDCl$_3$.[ii]

   The close proximity of protons of two molecules should result in through-space coupling, which can be investigated by rotating-frame Overhauser enhancement spectroscopy (ROESY) NMR. Thus, ROESY experiments were performed with merocyanine **1** and reference compound **12** in CDCl$_3$ at a concentration of 5.0 x 10^{-4} M. Through-space couplings between the protons of **1** at positions 1 and 6, 1 and 10, 2 and 11, and between 3 and 11 are observed and highlighted by red circles in Figure 7a. They are in accordance with the geometry-optimized dimer structure (AM1, HyperChem 8.05[128]) of **1** shown in Figure 8, and thus provide evidence for the Hamilton-receptor-mediated self-assembly of **1** in CDCl$_3$. The intermolecular distances between the pairs of protons which show cross-peaks in the ROESY spectrum of **1** are in the range of 2.2–3.0 Å based on a calculated dimer of **1** (Figure 8). Such distances are well within the range of ROESY experiments, while the respective intramolecular displacements are far beyond the sensitivity of this technique. Intramolecular NOE signals for Hamilton-receptor systems between protons at positions 4 and 6, and 5 and 6, owing to conformational flexibility around the bond connecting the amides to the isophthaloyl moiety, have been reported in the literature.[111c] While for **12** a similar pattern can be observed, the absence of the cross-coupling peak between the protons at positions 4 and 6 for **1** in CDCl$_3$ underlines the conformational fixation of the receptor moiety upon binding a guest molecule (Figure 7, blue circles). In contrast to the observation of further intermolecular cross-peaks for **1**, e.g. between proton 3 with protons 12, 13, and 14, only signals corresponding to intramolecular couplings are observed for reference compound **12**. Signals between protons 2 and 3, 3 and 4, 7 to 9, and the protons within the respective alkyl chain can be observed for **12** (Figure 7b).

[ii] It is to note that, since the electronic structure of merocyanine dyes, and with it the chemical shift, strongly depends on the solvent polarity,[121] comparison of the NMR data of **1** with those of structurally akin reference compound **12** in CDCl$_3$ seems more appropriate than comparison of data of **1** in CDCl$_3$ and DMSO-d_6 as solvent effects in the latter case cannot be excluded.
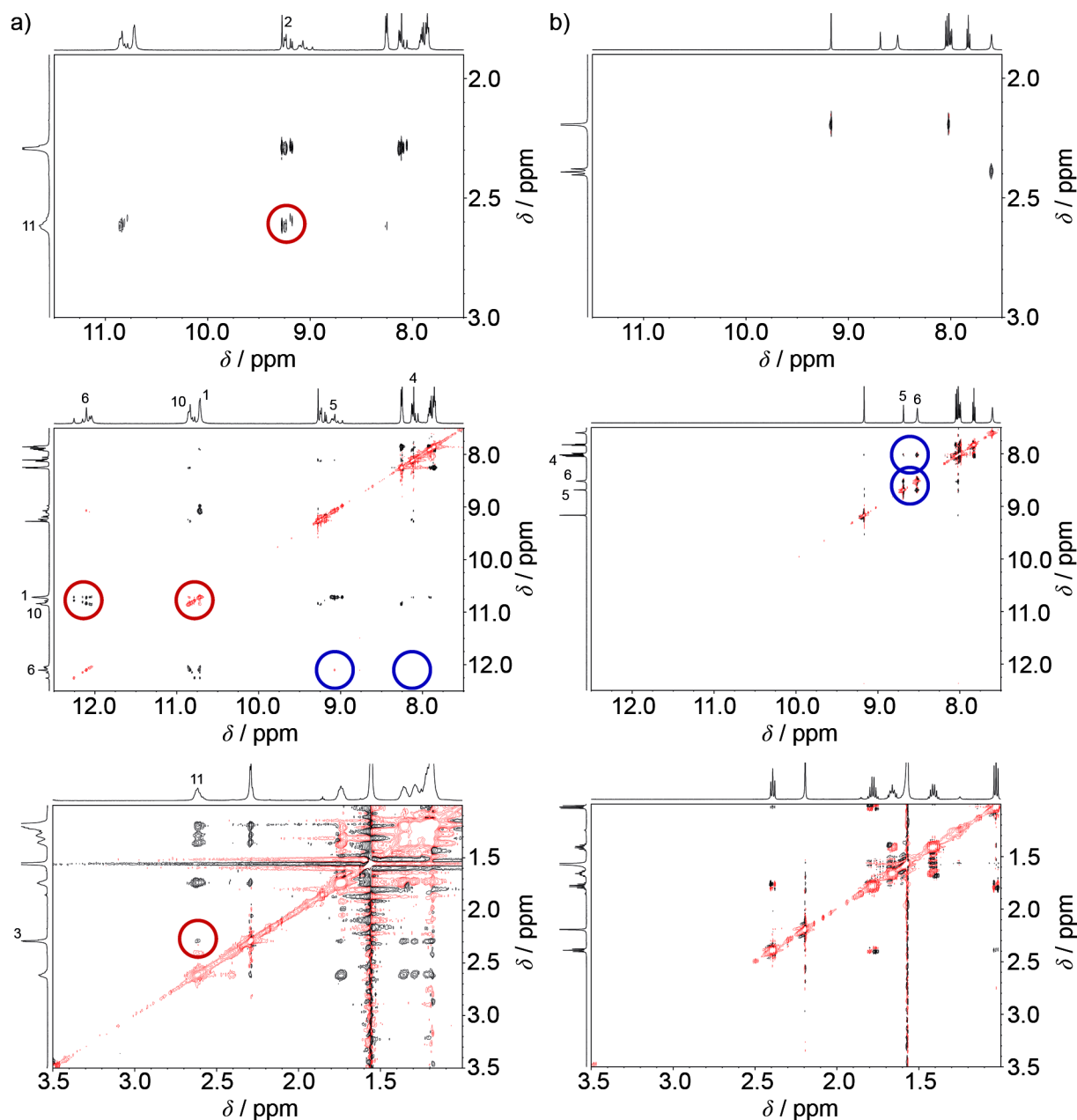
Figure 7. Sections of the 600 MHz ROESY NMR spectra of dyes **1** (a) and **12** (b) in CDCl$_3$ (c = 5.0 x 10^{-4} M) at 293 K and 250 ms mixing time. Positive and negative signals are represented by black and red lines, respectively. Red and blue circles highlight selected inter- and intramolecular cross-coupling peaks.
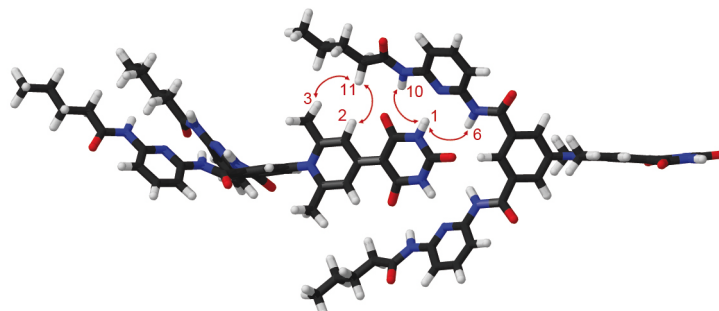
Figure 8. Structural model for a dimer of **1** based on NMR studies and molecular modeling on semiempirical level (AM1, HyperChem 8.05[128]). The long alkyl chains in the Hamilton receptor are replaced by butyl groups for simplicity. The arrows indicate ROESY cross-coupling signals, which provide evidence for spatial proximities between these protons. The corresponding signals are highlighted by red circles in Figure 7.

5.2.5 Size of the Self-Assemblies in Solution

   Dynamic light scattering (DLS) experiments were performed to determine the size of the self-assemblies of Hamilton-receptor-functionalized merocyanine dyes **1** in solution. Measurements of a 4.5 x 10^{-4} M solution of **1** in CHCl$_3$ at 293 K revealed average particle sizes from 53 nm to 516 nm, depending on the scattering angle (Figure 9a). The corresponding autocorrelation functions are shown in the Appendix (Figure D13). The dependence of the particle size on the scattering angle provides strong evidence for the nonspherical nature of the assemblies. The relatively broad distribution of particle sizes from ~13 to 1606 nm supports the formation of supramolecular polymers. Addition of merocyanine dye **10** and or receptor **11** to a solution of **1** in CHCl$_3$ should result in oligomeric self-assemblies of smaller size because these molecules act as chain stoppers. Indeed, DLS of a mixture of **10**, **1**, and **11** in a ratio 1:3:1 in CHCl$_3$ (c(**1**) = 1.0 x 10^{-4} M) at 293 K revealed an average particle size of only 4.3 nm (Figure 9b). Molecular modeling of complex **10:1$_3$:11** on semi-empirical level (AM1, HyperChem 8.05[128]) revealed a bended structure with a length of 5.3 nm (Figure 10), which is in good accordance with the value estimated by DLS investigations. The observed narrow size distribution is indicative for the formation of a well-defined oligomeric complex instead of supramolecular polymers.
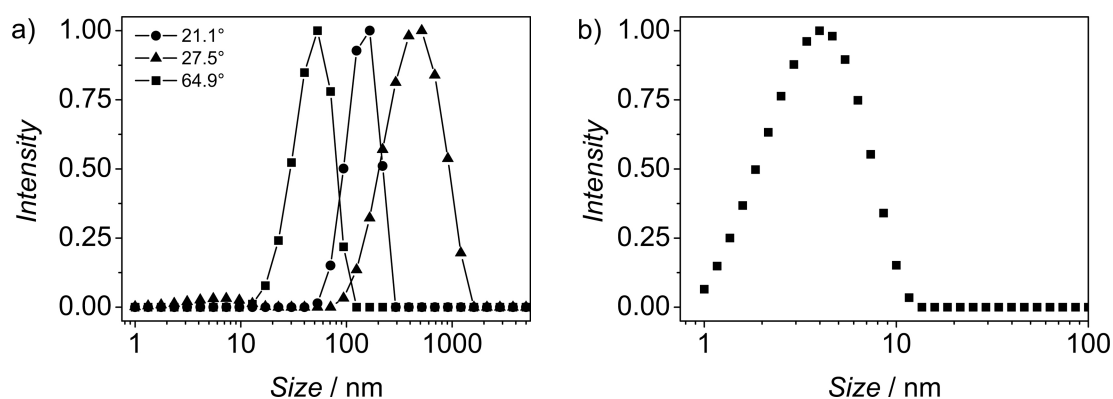
Figure 9. a) Size distribution of self-assembled **1** at 293 K in CHCl$_3$ (c = 4.5 x 10^{-4} M) obtained from DLS at different scattering angles indicated in the inset (no evaluable autocorrelation function was obtained for 90°). b) Size distribution for a mixture of **10**, **1**, and **11** in the ratio of 1:3:1 (c(**1**) = 9.5 x 10^{-4} M, 293 K) measured at 90°.

5.3 nm
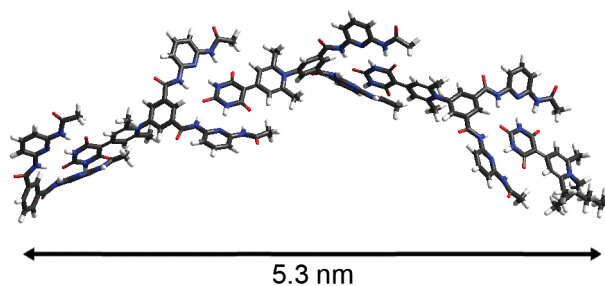
Figure 10. Geometry-optimized (AM1, HyperChem 8.05[128]) structure of complex **10:1$_3$:11**. Long alkyl chains were replaced by methyl groups.

To further substantiate the formation of extended assemblies of **1** in solution, diffusion ordered spectroscopy (DOSY) NMR experiments were performed. According to the Stokes-Einstein relation (equation (5.6)), the diffusion coefficient of a molecular species is inversely proportional to the hydrodynamic radius R of a molecule. Therefore, the size of two species may be compared based on their diffusion coefficients D, assuming that the other parameters being identical.

$$D = \frac{k_B T}{6\pi\eta R}$$

(5.6)

where T denotes the temperature, k_B the Boltzmann constant, and η the dynamic viscosity of the solvent. Reference compound **12**, which has similar size and molecular weight ($MW(\mathbf{12}) = 832$ g mol^{-1}, $MW(\mathbf{1}) = 944$ g mol^{-1}) as dye **1** and cannot form self-assemblies was used for comparison of the diffusion coefficients. The diffusion coefficients for **1** and **12** were measured in CDCl$_3$ at a concentration of 5.0 x 10^{-4} M and 293 K (Figure 11). DOSY NMR investigations revealed a diffusion coefficient of $D = 1.93$ x 10^{-10} m^2 s^{-1} for **1**, while for **12** a D value of 5.33 x 10^{-10} m^2 s^{-1} was obtained. The large difference in D values of **1** and **12** indicates considerably different hydrodynamic radii. Thus, DOSY NMR studies also confirm the formation of extended assemblies of **1**. Further information can be obtained by taking into account that the cube root of the molecular weight being proportional to D^{-1}.[129] The average size of the self-assembled species of **1** can therefore be estimated to $DP(\mathrm{DOSY}) \approx (D(\mathbf{12}) / D(\mathbf{1}))^3 = 21$ at the given concentration. Although the average degree of polymerization (DP) derived from such comparison is just a rough approximation because the polymers are assumed to be hydrodynamically spherical, the obtained value is in reasonable agreement with the number-averaged degree of polymerization calculated from the equilibrium constant obtained by UV/Vis spectroscopy ($DP_N = 56$).
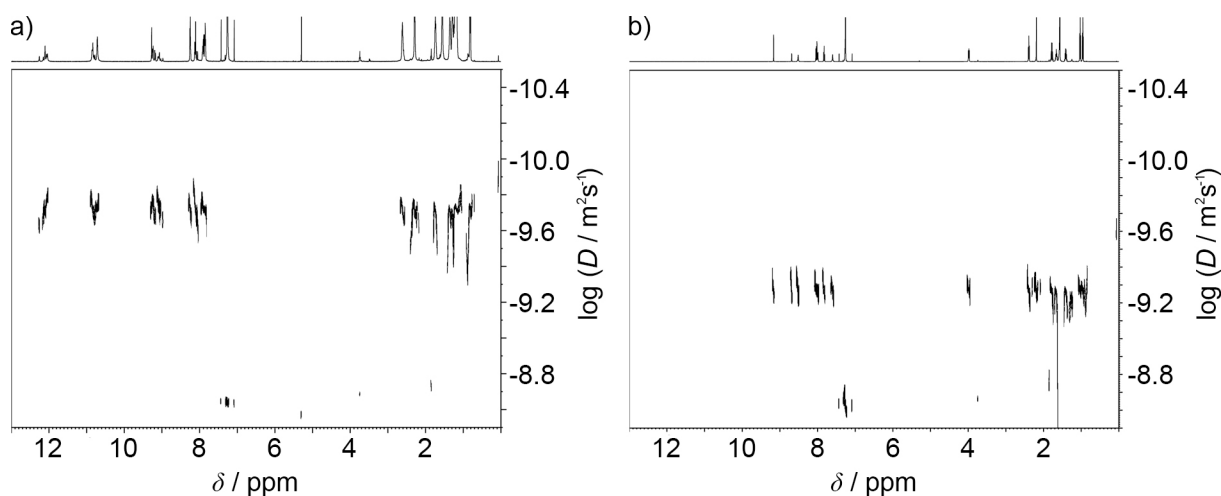
Figure 11. DOSY NMR spectra of self-complementary dye **1** (a) and reference compound **12** (b) at 293 K in CDCl$_3$ ($c = 5.0$ x 10^{-4} M). The logarithmic diffusion coefficients D are plotted against the chemical shift δ.

5.2.6 Gelation and Morphology Study

The ability of dye **1** to form gels was assessed in CHCl$_3$/*n*-hexane (40:60 vol%) at 88 mM concentration. A yellow opaque gel was formed at room temperature within 30 min after addition of appropriate amounts of *n*-hexane to a stock solution of **1** in CHCl$_3$ (Figure 12, inset). The critical gel concentration was found to be 8 wt%. The gel showed a remarkable increase of the fluorescence emission (ϕ_{fl} = 0.17, λ_{em} = 496 nm; Figure 12). In comparison to the monomeric and self-assembled species, the fluorescence of the gel is shifted to longer wavelengths and is ever significantly stronger than that of monomeric (ϕ_{fl} = 0.03 in CHCl$_3$) and self-assembled merocyanine dyes **1** (ϕ_{fl} = 0.07 in CHCl$_3$), which may be attributed to further rigidification of the molecules upon gel formation.[127]

Furthermore, gelation tests were conducted in different organic solvents and solvent mixtures. In CHCl$_3$/*n*-hexane mixtures with more than 70 vol% of CHCl$_3$ the compound remained dissolved and in solvent mixtures with less than 40 vol% CHCl$_3$ precipitation was observed. No gel formation could be observed in polar solvents with hydrogen bond acceptor ability like DMSO and THF. In nonpolar aromatic solvent like toluene, precipitation was observed upon cooling the solution to room temperature, while this dye is not soluble in aliphatic solvents like *n*-hexane, even at elevated temperature.
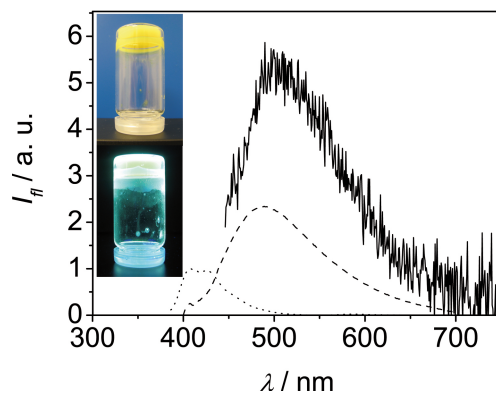
Figure 12. Fluorescence spectrum of a gel prepared from merocyanine **1** in CHCl$_3$/*n*-hexane (40:60 vol%, *c* = 88 mM, λ_{ex} = 370 nm, solid line) and of monomeric (*c* = 1.4 x 10^{-7} M, 328 K, λ_{ex} = 370 nm, dotted line) and self-assembled (*c* = 0.7 x 10^{-4} M, λ_{ex} = 370 nm, dashed line) dye **1** in CHCl$_3$. The inset shows a photograph of the gel and the fluorescence upon excitation (λ_{ex} = 366 nm).

Once the self-assembly of Hamilton-receptor-functionalized merocyanine dye **1** in solution and its gelation in nonpolar solvent mixtures at high concentrations have been confirmed, the morphology of the assemblies was investigated by transmission electron microscopy (TEM).[iii] TEM micrographs show long strands which extend over several micrometers (Figure 13). Their average diameter being ~14–18 nm is much larger than expected for single fibrils from

---

iii TEM measurements were performed by Dr. Xin Zhang.

molecular modeling (see Figure D14), indicating that individual fibrils of self-assembled molecules **1** merge to strands which further form entangled networks.
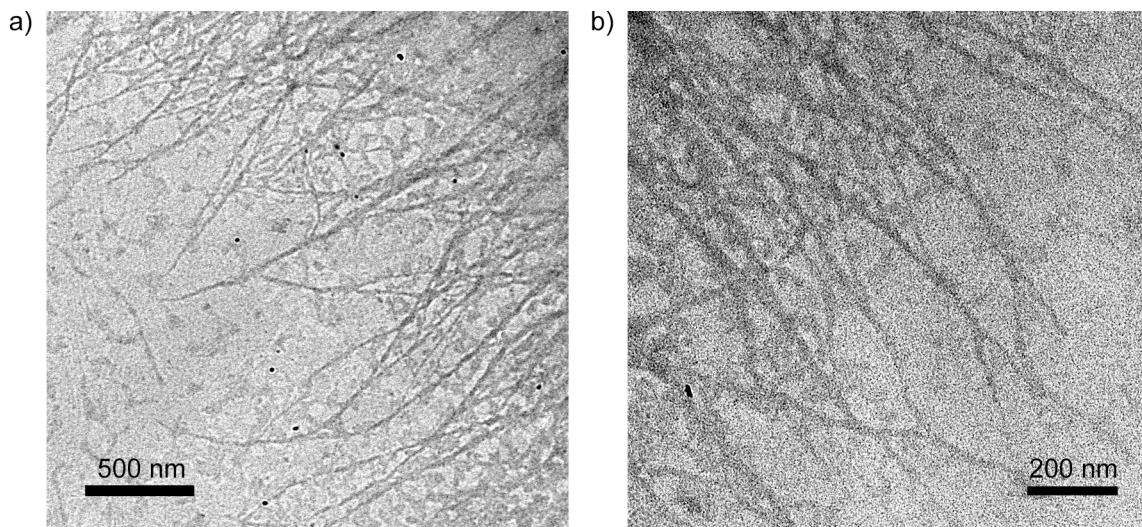
Figure 13. Transmission electron micrographs of self-assembled **1** (c = 2.3 x 10^{-4} M, CHCl$_3$) after evaporation of the solvent on a carbon-coated copper grid.

5.3 Conclusions

The synthesis of a self-complementary Hamilton-receptor-functionalized merocyanine dye enabled to outwit the most common antiparallel aggregation of the dipolar merocyanine dyes, and hence to achieve the highly desirable head-to-tail orientation of such dyes by six-fold hydrogen bonding, leading to supramolecular polymers. Evaluation of concentration- and temperature-dependent UV/Vis experiments of merocyanine dye **1** in THF and CHCl$_3$ by employing the isodesmic model revealed high equilibrium constants for the self-assembly of **1** that gave rise to high degree of polymerization even in dilute solutions. In accordance with these observations, DLS and DOSY NMR studies provided evidence for the formation of large assemblies. Fluorescent organogels were formed in concentrated solutions of merocyanine **1** in nonpolar solvent mixtures. The enhanced emission properties of the supramolecular polymers and gel phase in comparison to the nearly nonemissive monomer might be of interest for photonic and sensing applications.

5.4 Experimental Section

Materials and Methods: Solvents and reagents were acquired from commercial suppliers and used without further purification, unless otherwise stated. THF was dried according to literature.[130] Column chromatography was performed, using silica gel (Merck Silica 60, particle size 0.04–0.063 nm). Thin layer chromatography (TLC) was performed on silica gel plates (60 F_{254} Merck, Darmstadt). Gel permeation chromatography (GPC) was carried out on a recycling preparative LC-9105 system (Japan Analytical Industries Co., Ltd.) with a UV/Vis (UV-3702, 380 nm) and a refractive index detector (RI-7s) using a preparative JAIGEL-1H+2H column and solvents of purity grad "pa". Determination of the melting points (uncorrected) was conducted on a Büchi Melting Point B545 heating stage. Solvents for UV/Vis absorption and AFM studies were of spectroscopic grade and used as received. Unless otherwise stated, ^{1}H NMR spectra were recorded on a Bruker Advance 400 spectrometer at 293 K with TMS or residual undeuterated solvent as internal standard. MALDI-TOF mass spectrometry was performed on an autoflex II instrument (Bruker Daltronik GmbH) in positive mode with a DCTB matrix. A microTOF focus instrument (Bruker Daltronik GmbH) was used to perform high resolution ESI-TOF mass spectrometry in positive mode with CH_3CN and $CHCl_3$ or THF and $CHCl_3$ as solvent.

UV/Vis Experiments: UV/Vis absorption spectra were recorded on a Perkin Elmer Lambda 950 UV/Vis spectrophotometer with a spectral bandwidth of 0.20 nm and a scan rate of 141 nm/min. Conventional quartz cells of 0.1–50 mm path length were used to cover a suitable concentration range. Temperature control was achieved with a PTP-1 Peltier element (Perkin Elmer).

Electro-Optical Absorption (EOA) Measurements: The difference of absorption of a solution with ($\varepsilon^E(\varphi, \tilde{v})$) and without ($\varepsilon(\tilde{v})$) an externally applied electric field **E** with light parallel ($\varphi = 0°$) and perpendicularly ($\varphi = 90°$) polarized to the direction of **E** is measured by EOA spectroscopy.[122] For uniaxial phases, induced in a solution by both an alternating and a constant electric field of about 3 x 10^6 V m^{-1}, the dichroism $\varepsilon^E(\varphi, \tilde{v}) - \varepsilon(\tilde{v})$ depends on the orientational order of the molecules due to their ground state dipole moments μ_g, the shifts of the absorption bands, which are proportional to the dipole moment differences $\Delta\mu$, and on the electric field dependence of the electric transition dipole moments $\mu_{eg}(\mathbf{E})$. UV/Vis spectra that are required for the evaluation of the integral absorption (μ_{eg}^2) and the multi-linear analysis of the EOA spectra were recorded with a Perkin-Elmer Lambda 900 spectrophotometer in 1,4-dioxane at 298 K.

Fluorescence Measurements: The steady state fluorescence spectra in solution were recorded under ambient conditions on a PTI QM4/2003 spectrofluorometer. A front-face

setup was used for the self-assembled solution in $CHCl_3$ owing to the high optical density of the sample. All fluorescence spectra were corrected. Due to the overlap of the excitation peak with the emission, the excitation peak was removed by measuring a reference sample with pure solvent. The fluorescence quantum yields were determined using the optical dilution method with diphenylantracene (ϕ_{fl} = 0.67 in benzene[131]) as standard.[132] The given quantum yields are averaged over the values obtained at three different excitation wavelengths. Absolute quantum yields of the gel were measured under ambient conditions on an absolute photoluminescence quantum yield measurement system C9920-02 (Hamamatsu).

NMR Experiments: Two-dimensional (2D) NMR measurements for compounds **1** and **12** were performed at 293 K in standard 5 mm NMR tubes on a Bruker DMX 600 spectrometer equipped with a 5 mm $^{13}C/^1H$ cryoprobe with z axis gradient coil capable of producing pulsed magnetic field gradients of 55 G cm^{-1}. Prior to 2D-NMR measurements, the samples were degassed by bubbling with dry argon gas for at least 30 min. For both samples of **1** and **12** in $CDCl_3$ a set of ^1H as well as two-dimensional ($^1H,^1H$)-COSY, ($^1H,^1H$)-ROESY and ^1H-DOSY spectra were measured using the ^1H solvent signal as internal standard (7.26 ppm). Alternating-phase 180° pulses were applied during the mixing time of 250 ms in the ROESY spectra to suppress the unwanted TOCSY contributions.[133] In the DOSY experiments, the suppression of flow effects due to temperature gradients in the coil of the cryoprobe was achieved by two different methods: (i) using the stimulated echo BPP-LED pulse sequence[134] (longitudinal eddy current delay sequence with bipolar gradient pulse pairs for diffusion and additional spoil gradients after the second and fourth 90° pulse) in which convection in the z direction was suppressed by sample rotation[135] and (ii) by the corresponding double stimulated echo pulse sequence[136] (without sample rotation and with additional spoil gradients after the second, fourth and sixth 90° pulse) in which the *double* stimulated echo results in a compensation of the flow effects. The following acquisition parameters were used for both methods: duration σ of a bipolar gradient pulse: 10 ms (2 × 5 ms) for the sample of **1** and 6 ms (2 × 3 ms) for the sample of **12**, diffusion time Δ: 50 ms, eddy current delay: 5 ms. The diffusion time Δ was kept constant in each DOSY experiment whereas the sinusoidal diffusion gradients were incremented from 2% to 95% of maximum gradient strength in 32 linear steps. For the sample of **1** additional standard ($^1H,^{13}C$)-HSQC, ($^1H,^{13}C$)-HMBC and ($^1H,^1H$)-NOESY spectra (mixing times 75 ms and 300 ms) were recorded.

Dynamic Light Scattering (DLS): DLS experiments were carried out using a commercial N5 Submicron Particle Size Analyzer (Beckman Coulter, Inc.) laser light scattering spectrometer equipped with a 25 mW Helium-Neon laser operating at 632.8 nm. Sample solutions ($c(\mathbf{1})$ = 1.0 x 10^{-4} M) were filtrated into a dust-free vial through a 0.45 μm teflon filter. The size distribution profile deconvolution algorithm is based on the CONTIN program.

Gelation Tests: The measured amount of organogelator (merocyanine **1**) was dissolved in the respective amount of CHCl₃ in a screw-capped sample vial. Gels were formed upon addition of appropriate amounts of *n*-hexane to the stock solution. The formation of the gel was tested by the "stable-to-inversion of a vial" method[137] after leaving the sample for 1 h at ambient conditions.

Transmission Electron Microscopy (TEM): Transmission electron micrographs were recorded on a Siemens Elmiskop 101 Electron Microscope operating at an acceleration voltage of 80 kV. For the monitoring of aggregates, a drop of sample solution ($c(\mathbf{1})$ = 2.3 x 10^{-4} M, CHCl₃) was placed on 300-mesh formvar copper grids coated with carbon. About 1 min after the deposition, the grid was tapped with filter paper to remove surface solvents.

Synthesis and Characterization of Intermediates 4, 5, and 7:[18]

1-(3,5-Dicarboxy)phenyl-2,6-dimethyl-4-pyridone hydrochloride (4): An aqueous solution of HCl (37%, 100 mL) was added to a suspension of 5-aminoisophthalic acid **2** (28.1 g, 155 mmol) and dehydroacetic acid **3** (26.1 g, 155 mmol) in H₂O (160 mL) and the resulting mixture was heated to 110 °C for 15 h. After cooling down to 0 °C, the precipitated grey solid was separated by filtration. Recrystallization from MeOH gave pure **4** as a white crystalline solid (35.1 g, 109 mmol, 70%). Mp 249 °C (decomposition). ^{1}H NMR (400 MHz, MeOH-d_4): δ 8.89 (t, ^{4}J = 1.6 Hz, 1H), 8.35 (d, ^{4}J = 1.5 Hz, 2H), 7.18 (s, 2H), 2.26 (s, 6H).

1-(3,5-Dicarbethoxy)phenyl-2,6-dimethyl-4-pyridone (5): Ethanol (190 mL) and conc. H₂SO₄ (5.5 mL) were added to a suspension of pyridone hydrochloride **4** (30.5 g, 94.2 mmol) in toluene (470 mL) and the mixture was heated to reflux at 110 °C by using a water separator. After 1.5 h of heating hydrochloride **4** was dissolved, and ethanol/toluene 1:2 (20 mL) was added to replace the separated amount of toluene/H₂O. While heating for further 20 h, the reaction volume was continually kept constant by replacing the separated amount of toluene/H₂O with ethanol/toluene 1:2 mixture. After being cooled down to room temperature, the solution was poured into water (140 mL). The resultant solid was separated by filtration, dissolved in chloroform (100 mL), and made basic (pH 9–10) by adding saturated aqueous Na₂CO₃ solution. Subsequent to the separation of the organic layer, the aqueous layer was extracted with chloroform (3 x 40 mL). The combined organic layers were washed with water (3 x 70 mL) and dried over Na₂SO₄. After evaporation of the solvent, the residue was recrystallized from cyclohexane/EtOAc (1:2 vol%) to give pure **5** as a white crystalline solid (26.5 g, 77.2 mmol, 82%). Mp 217–220 °C. ^{1}H NMR (400 MHz, CDCl₃): δ 8.81 (t, ^{4}J = 1.5 Hz, 1H), 8.06 (d, ^{4}J = 1.6 Hz, 2H), 6.33 (s, 2H), 4.45 (q, ^{3}J = 7.1 Hz, 4H), 1.90 (s, 6H), 1.44 (t, ^{3}J = 7.1 Hz, 6H).

1-[3,5-Bis-(6-aminopyridine-2-yl)carbamoyl]phenyl-2,6-dimethyl-4-pyridone (7): 2,6-Diaminopyridine **6** (9.56 g, 87.6 mmol) was dissolved in dry THF (150 mL) under an argon atmosphere and cooled to −78 °C. At this temperature, *tert*-butyllithium (1.9 M in *n*-pentane, 46.1 mL, 87.6 mmol) was added dropwise. Afterwards, a solution of pyridone **5** (6.00 g, 17.5 mmol) in dry THF (200 mL) was added dropwise and the reaction mixture was stirred for 4 h at −78 °C and additional 16 h at room temperature. The resultant suspension was poured into a saturated aqueous solution of $NaHCO_3$ (200 mL, pH 8–10). The precipitate was separated by filtration and kept for further purification. After extracting the aqueous layer with $CHCl_3$ (3 x 150 mL), the combined organic layers were dried over $MgSO_4$. The solvent was removed under reduced pressure and the remainder was combined with the filter residue. Recrystallization from MeOH gave pure **7** (5.82 g, 12.4 mmol, 71%). Mp 319 °C (decomposition). ^1H NMR (400 MHz, DMSO-d_6): δ 10.55 (br s, 2H), 8.56 (t, ^4J = 1.6 Hz, 1H), 8.12 (d, ^4J = 1.7 Hz, 2H), 7.45 (t, ^3J = 7.8 Hz, 2H), 7.38 (dd, ^3J = 7.7 Hz, ^4J = 0.8 Hz, 2H), 6.28 (dd, ^3J = 7.9 Hz, ^4J = 0.9 Hz, 2H), 6.12 (s, 2H), 5.78 (s, 4H), 1.93 (s, 6H).

Synthesis and Characterization of Precursor 8 and the Target Compound 1:

1-{3,5-Bis[(6-dodecyrylamino)pyridine-2-yl]carbamoyl}phenyl-2,6-dimethyl-4-pyridone (8): Diamine **7** (2.22 g, 4.72 mmol) was dissolved in dry THF (140 mL) under an argon atmosphere and cooled to 0 °C. At this temperature, dodecanoyl chloride (2.38 g, 2.59 mL, 10.9 mmol) was added dropwise. Afterwards, the reaction mixture was stirred for 16 h at room temperature. The resultant suspension was poured into a saturated aqueous solution of $NaHCO_3$ (200 mL, pH 8–10). After extracting the aqueous layer with $CHCl_3$ (4 x 50 mL), the combined organic layers were dried over $MgSO_4$. The solvent was removed under reduced pressure and the residue was purified by column chromatography using silica with EtOAc/EtOH = 10:1 vol% as eluent to give pure **8** (1.65 g, 1.98 mmol, 42%): ^1H NMR (400 MHz, $CDCl_3$): δ 9.92 (br s, 4 H, NH), 8.86 (s, 1 H, ArH), 8.25 (s, 2 H, ArH), 8.06 (d, ^3J = 7.2 Hz, 2 H, $CH_{pyridine}$), 8.01 (d, ^3J = 5.9 Hz, 2 H, $CH_{pyridine}$), 7.77 (t, ^3J = 7.4 Hz, 2 H, $CH_{pyridine}$), 2.33 (t, ^3J = 7.2 Hz, 4 H, $COCH_2$), 1.77 (s, 6 H, CH_3), 1.67 (m, 4 H, CH_2), 1.23 (m, 32 H, CH_2), 0.86 (t, ^3J = 6.8 Hz, 6 H, CH_3). ^{13}C NMR (400 MHz, $CDCl_3$): δ 172.59, 163.18, 150.64, 149.78, 140.87, 139.49, 136.93, 130.29, 117.53, 117.07, 116.93, 116.88, 110.66, 110.31, 37.63, 34.46, 32.03, 29.34, 25.50, 25.10, 21.83, 14.23. HRMS (ESI, pos. mode, $CH_3CN/CHCl_3$ = 1:1 vol%): calc. *m/z* $C_{49}H_{68}N_7O_5$ ([M+H]$^+$) 834.52819; found 834.52764.

5-{1-[3,5-Bis[(6-dodecyrylamino)pyridine-2-yl]carbamoyl]phenyl-2,6-dimethyl-pyridine-4-ylidene}-pyrdimidine-2,4,6-trione (1): A catalytic amount of concentrated HOAc was added to a solution of pyridone **8** (1.77 g, 2.12 mmol) and barbituric acid **9** (272 mg, 2.12 mmol) in Ac_2O (3.80 mL). The resultant reaction mixture was heated to 90 °C for 3 h. Afterwards the solvent was removed under reduced pressure. In a first purification step, the

crude product was purified by column chromatography using silica and $CH_2Cl_2/MeOH$ = 98.5:1.5 vol%. Subsequent purification by GPC ($CHCl_3$) and repeated reprecipitation from $CHCl_3/n$-hexane yielded pure **1** (80.1 mg, 84.8 μmol, 4%). Mp 325–327 °C (decomposition). UV/Vis (1,4-dioxane): λ_{max}/nm (ε_{max}/L mol^{-1} cm^{-1}) = 396 (50.8 x 10^3). ^{1}H NMR (400 MHz, 293 K, DMSO-d_6): δ 10.75 (s, 2 H, NH), 10.02 (s, 4 H, NH), 9.03 (s, 2 H, CH), 8.65 (s, 1 H, ArH), 8.31 (s, 2 H, ArH), 7.83 (m, 6 H, CH$_{pyridine}$), 2.39 (t, ^3J = 7.7 Hz, 4 H, COCH$_2$), 2.22 (s, 6 H, CH$_3$), 1.58 (m, 4 H, CH$_2$), 1.24 (m, 32 H, CH$_2$), 0.85 (t, ^3J = 6.8 Hz, 6 H, CH$_3$). ^{13}C NMR (600 MHz, 313 K, DMSO-d_6): δ 172.00, 170.57, 170.39, 165.12, 165.09, 163.77, 150.43, 150.03, 149.98, 139.83, 136.18, 129.94, 129.49, 123.46, 113.54, 110.03, 109.99, 36.02, 31.10, 30.76, 24.47, 24.83, 21.90, 21.88, 21.86, 13.72. HRMS (ESI, pos. mode, $CHCl_3/THF$ = 1:1 vol%): calc. *m/z* $C_{53}H_{70}N_9O_7$ ([M+H]$^+$) 944.53927; found 944.53850.

Chapter 6

Summary

The prediction and control of the mutual spatial arrangement of functional dyes in solution, on substrates, and in the solid state is of decisive importance for the development of functional supramolecular systems and organic electronics. Thus, the precise examination of directional noncovalent interactions and the transfer to novel architectures may lead to improved device performances in the future. In this context, the objective of this thesis was the construction and investigation of well-defined merocyanine dye assemblies based on the interplay of antiparallel dipolar aggregation of the chromophores and hydrogen bonding. Owing to their directional character, hydrogen bonds and dipolar aggregation of merocyanine dyes hold a prominent place in supramolecular chemistry. Both forces may approximately be described on the basis of dipole-dipole interactions. For this purpose, appropriate molecular systems were synthesized and their self-assembly was studied by various techniques. A summary of the content of this thesis is given below:

In *Chapter 2* a short review on the mathematical treatment of the thermodynamics of aggregate formation was given, starting with a model to describe the formation of discrete dimers. In the following, infinite one-dimensional aggregates were discussed within the approximations of the isodesmic model. Subsequently, allosteric cooperativity in such systems was treated with regard to nucleation–elongation models. Finally, a mathematical approach to the formation of closed systems from oligomers was dealt with in terms of chelate cooperativity.

Chapter 3 gave a comparison of hydrogen bonding and antiparallel aggregation of dipolar merocyanine dyes. Both interactions were discussed as special cases of dipole-dipole interactions. Their directionality was deduced from basic equations, describing the interaction of two dipoles as a function of their mutual distance and angles. Quantum mechanical calculations were employed to identify dipolar interactions as the major contribution to the

overall interaction energy between two merocyanine dyes in an antiparallel arrangement. An extensive literature survey on the Gibbs free energies for various systems in chloroform solution and energy densities derived from them, together with the directional character, establishes the dipole-driven antiparallel aggregation of merocyanines as a valuable tool in supramolecular chemistry.

The following chapters comprise studies on the construction of well-defined assemblies, including supramolecular polymers as well as discrete, globular species on the basis of dipolar aggregation of ditopic bis(merocyanine) dyes and on hydrogen bonding. The underlying concept was based on the attachment of merocyanine dyes at different positions of a hydrogen bonding receptor unit. The self-assembly of such systems depends on the interplay of two orthogonal, highly directional, noncovalent interactions.

In ***Chapter 4*** a novel class of tethered bis(merocyanine) dyes was described. Two chromophores are covalently connected via a Hamilton receptor. These molecules self-assemble into supramolecular polymers upon decreasing the solvent polarity (Figure 1). Concentration- and temperature-dependent UV/Vis studies revealed an isodesmic self-assembly process. The polymeric nature was proven by viscosity, DLS, TEM, and AFM experiments. Further decrease of the solvent polarity led to the collapse of the supramolecular polymers into inverted micelles. This process was shown by UV/Vis measurements to be cooperative and could be described by a model that includes the formation of a closed species from a particular oligomer. The formation of discrete, globular nanoparticles was evidenced by viscosity experiments and DLS, DOSY NMR, and AFM studies. The addition of merocyanine dye guest molecules bearing barbituric acid units, which are complementary to the Hamilton receptor, to the inverted micelles yielded more intricate supramolecular polymers, incorporating the guest. Thus, these aggregates are responsive to molecular stimuli.
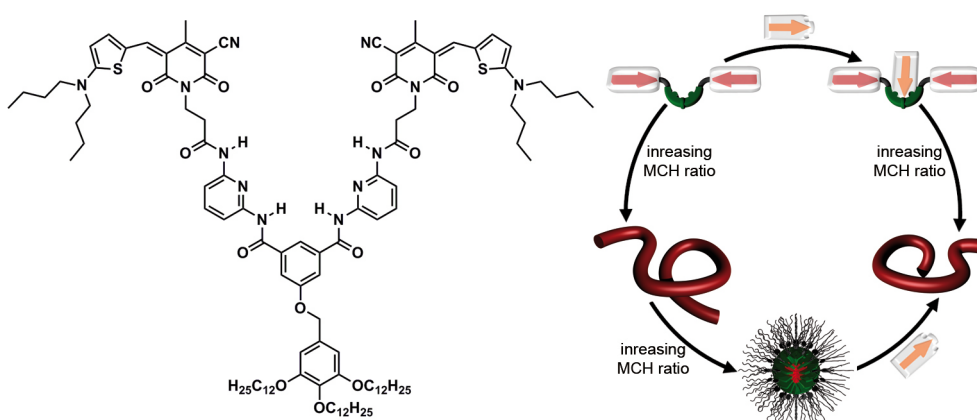
Figure 1. Structure of a Hamilton-receptor-tethered bis(merocyanine) dye and schematic representation of the solvent- and guest-dependent self-assembly.

The latter supramolecular polymers could also be built up from the previously formed monomeric complex of the chromophore guest molecules with the host. Similarly to the supramolecular polymers without guests, UV/Vis studies disclosed the self-assembly process to be isodesmic.

A detailed study of the self-assembly properties of Hamilton-receptor-connected merocyanine dyes is presented in ***Chapter 5***. The self-complementary compound was achieved by attaching a Hamilton receptor to the donor moiety of a merocyanine chromophore which bears a barbituric acid acceptor group (Figure 2). Thereby, the otherwise unavoidable antiparallel orientation of the dipolar dyes was overcome by sixfold hydrogen bonding, leading to a head-to-tail arrangement. Concentration- and temperature-dependent UV/Vis studies suggested an isodesmic self-assembly process with high equilibrium constants. The desired binding motif was confirmed by two-dimensional ROESY NMR experiments. The aggregate size in solution was determined by DOSY NMR and DLS measurements and denotes the formation supramolecular polymers. Further aggregation at high concentrations in unpolar solvent mixtures led to the formation of organogels with strongly enhanced fluorescence as a result of the modified binding motif and rigidification.
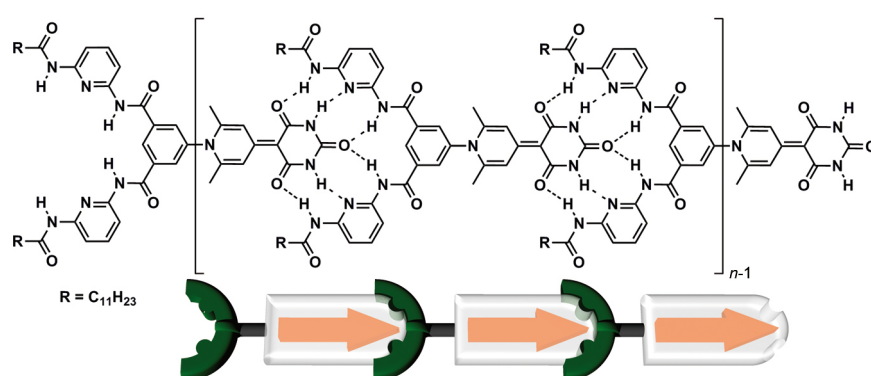
Figure 2. Concept for the formation of supramolecular polymers with head-to-tail arrangement of Hamilton-receptor-functionalized merocyanine dyes.

In conclusion, the present thesis gives insights into the complex interplay of dipolar aggregation of merocyanine dyes and hydrogen bonding as directional noncovalent interactions in supramolecular chemistry. The combination of dipole-driven antiparallel aggregation and hydrogen bonding provides novel building blocks that were responsive to molecular stimuli owing to two orthogonal interactions. Furthermore, hydrogen bonds constituted the basis for the formation of linear supramolecular polymers in a head-to-tail arrangement by overcoming the otherwise preferred antiparallel dimer aggregates with vanishing dipole moments.

Zusammenfassung

Die Vorhersage und Kontrolle der gegenseitigen räumlichen Anordnung von funktionellen Farbstoffen in Lösung, auf Substraten und im Festkörper ist von entscheidender Bedeutung für die Entwicklung funktionaler supramolekularer Systeme und von organischen Elektronikmaterialien. Die genaue Untersuchung von gerichteten, nichtkovalenten Wechselwirkungen und der Transfer auf neue Architekturen könnten daher in Zukunft zu leistungsfähigeren Bauteilen führen. In diesem Zusammenhang war die Konstruktion und Untersuchung von wohldefinierten Merocyaninfarbstoffanordnungen - basierend auf einem Zusammenspiel von antiparalleler, dipolarer Aggregation der Chromophore und Wasserstoffbrückenbindungen - das Ziel dieser Arbeit. Wasserstoffbrückenbindungen und dipolare Aggregation von Merocyaninfarbstoffen haben aufgrund ihrer Richtungsabhängigkeit eine Sonderstellung in der supramolekularen Chemie. Beide Wechselwirkungen können näherungsweise auf Basis von Dipol-Dipol-Wechselwirkungen beschrieben werden. Zu diesem Zweck wurden geeignete molekulare Systeme synthetisiert und ihre Selbstorganisation mit verschiedenen Techniken studiert. Die Ergebnisse dieser Dissertation sind im Folgenden zusammengefasst:

In *Kapitel 2* wurde eine kurze Literaturübersicht über die mathematische Behandlung der Thermodynamik der Aggregatbildung gegeben. Begonnen wurde mit einem Modell zur Beschreibung von diskreten Dimeren. Unendliche, eindimensionale Aggregate werden anschließend innerhalb der Näherungen des isodesmischen Models diskutiert. Weiterhin wirde allosterische Kooperativität in solchen Systemen in Hinblick auf Nukleations−Wachstums−Modelle behandelt. Schließlich wurde ein mathematischer Ansatz zur Bildung von geschlossenen Systemen aus Oligomeren hinsichtlich chelatbedingter Kooperativität besprochen.

Kapitel 3 bot einen Vergleich zwischen Wasserstoffbrückenbindungen und antiparalleler, dipolarer Aggregation von Merocyaninfarbstoffen. Beide Wechselwirkungen wurden als Spezialfälle von Dipol-Dipol-Wechselwirkungen diskutiert. Ihre Richtungsabhängigkeit wurde aus fundamentalen Gleichungen abgeleitet, die die Wechselwirkung zweier Dipole als Funktion ihres gegenseitigen Abstands und ihrer Winkel zueinander beschreiben. Quantenmechanische Berechnungen wurden verwendet, um dipolare Wechselwirkungen als Hauptanteil der Gesamtwechselwirkungsenergie zwischen zwei Merocyaninen in einer antiparallelen Anordnung zu identifizieren. Ein ausführlicher Überblick über die Literatur von freien Gibbs Energien für verschiedene Systeme in Chloroformlösung und daraus abgeleitete

Energiedichten etablieren, zusammen mit dem gerichteten Charakter, die Dipol-getriebene, antiparallele Aggregation von Merocyaninen als wertvolles Instrument in der supramolekularen Chemie.

Die folgenden Kapitel beinhalten Studien über die Konstruktion wohldefinierter Anordnungen, einschließlich supramolekularer Polymere sowie diskreter, kugelförmiger Spezies auf Basis von dipolarer Aggregation ditoper Bis(merocyanine) und Wasserstoffbrücken. Die Anfügung von Merocyaninfarbstoffen an verschiedenen Stellen einer Wasserstoffbrückenbindungsrezeptoreinheit bildet das zugrunde liegende Konzept. Die Selbstorganisation beruht auf dem Zusammenspiel zweier orthogonaler, hoch gerichteter, nichtkovalenter Wechselwirkungen.

In *Kapitel 4* wurde eine neue Art von verbrückten Bis(merocyanin)farbstoffen beschrieben. Zwei Chromophore sind kovalent über einen Hamilton Rezeptor verbunden. Mit abnehmender Lösungsmittelpolarität ordnen sich diese Moleküle zu supramolekularen Polymeren an (Abbildung 1). Konzentrations- und temperaturabhängige UV/Vis-Studien offenbaren einen isodesmischen Selbstorganisationsprozess. Die polymere Natur wurde durch Viskositäts-, DLS-, TEM- und AFM-Experimente nachgewiesen. Weiter abfallende Lösungsmittelpolarität führt zum Kollabieren der supramolekularen Polymere zu invertierten Mizellen. Mittels UV/Vis-Experimenten konnte gezeigt werden, dass dieser Prozess kooperativ ist und mit einem Model beschrieben werden kann, das die Bildung einer geschlossenen Spezies aus einem bestimmen Oligomer mit einschließt. Die Ausbildung von diskreten, kugelförmigen Nanopartikeln wurde durch Viskositätsmessungen und mit DLS-, DOSY NMR- und AFM-Studien nachgewiesen. Die Zugabe von Merocyaninfarbstoff-
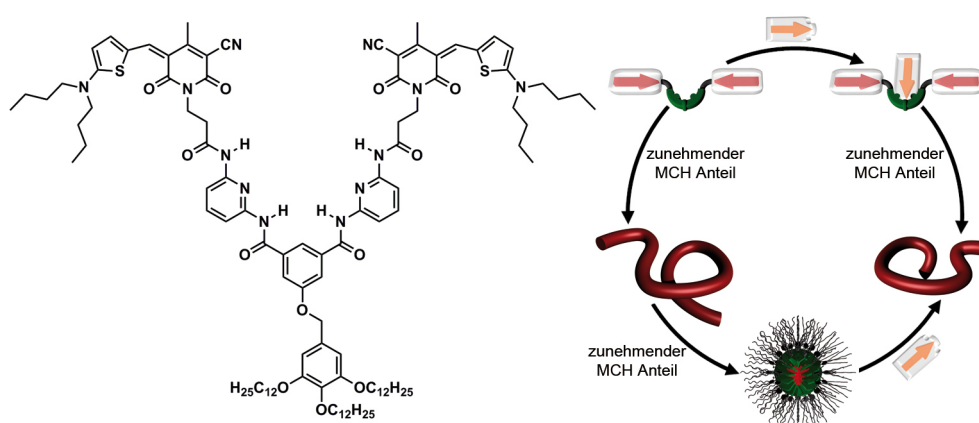
Abbildung 1. Struktur eines Hamilton-Rezeptor-verbrückten Bis(merocyanin)farbstoffs und schematische Darstellung der Lösungsmittel- und Gast-abhängigen Selbstanordnung.

Gastmolekülen mit zum Hamilton-Rezeptor komplementären Barbitursäureeinheiten zu den invertierten Mizellen ergab komplexere supramolekulare Polymere mit eingebauten Gästen.

Somit reagieren diese Aggregate auf molekulare Impulse. Letztere supramolekulare Polymere konnten auch aus dem vorher gebildeten, monomeren Komplex aus dem Gastchromophor mit dem Wirt aufgebaut werden. Ähnlich wie im Fall der supramolekularen Polymere ohne Gast enthüllten UV/Vis-Studien einen isodesmischen Selbstorganisationsprozess.

Eine detaillierte Studie der Selbstorganisationseigenschaften von Hamilton-Rezeptor-verbundenen Merocyaninfarbstoffen wird in *Kapitel 5* präsentiert. Die selbstkomplementäre Verbindung wurde durch Anbringen eines Hamilton-Rezeptors an die Donoreinheit eines Merocyaninchromophors, der eine Baribitursäureakzeptoreinheit trägt, erhalten (Abbildung 2). Dadurch wurde die ansonsten unvermeidbare antiparallele Orientierung dipolarer Farbstoffe durch die Ausbildung von sechs Wasserstoffbrückenbindungen überwunden, was zu einer „Kopf-Schwanz"-verknüpften Anordnung führt. Konzentrations- und temperaturabhängige UV/Vis-Studien deuten auf einen isodesmischen Selbstorganisationsprozess hin. Das gewünschte Bindungsmotiv wurde durch zweidimensionale ROESY NMR-Experimente bestätigt. Die Größe der Aggregate in Lösung konnte mit DOSY NMR- und DLS-Messungen bestimmt werden und zeigt die Bildung von supramolekularen Polymeren. Weitere Aggregation bei hohen Konzentrationen in unpolaren Lösungsmittelmischungen führte zur Bildung von Organogelen mit stark erhöhter Fluoreszenz als Resultat des modifizierten Bindungsmotivs und Verhärtung.
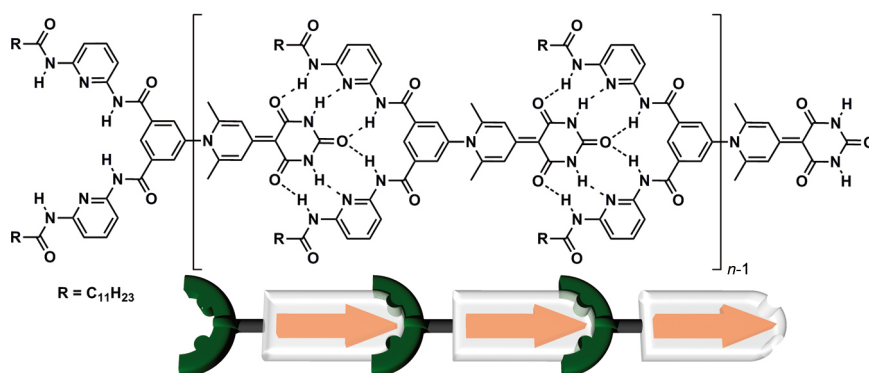
Abbildung 2. Konzept für die Bildung von supramolekularen Polymeren mit „Kopf-Schwanz"-Anordnung von Hamilton-Rezeptor-funktionalisierten Merocyaninfarbstoffen.

Insgesamt bietet die vorliegende Doktorarbeit Einblicke in das komplexe Zusammenspiel von dipolarer Aggregation von Merocyaninfarbstoffen und Wasserstoffbrückenbindungen als gerichtete, nichtkovalente Wechselwirkungen in der supramolekularen Chemie. Die Kombination von Dipol-getriebener antiparalleler Aggregation und Wasserstoffbrücken-bindungen stellt neue Bausteine bereit, welche aufgrund von zwei orthogonalen Wechselwirkungen auf molekulare Impulse reagieren. Weiterhin stellen Wasserstoff-brückenbindungen die Basis für die Ausbildung von linearen supramolekularen Polymeren in

einer „Kopf-Schwanz"-Anordnung dar, indem die ansonsten bevorzugten antiparallelen Dimeraggregate mit verschwindenden Gesamtdipolmomenten überwunden werden.

Appendix

A Supplement for Chapter 2

In order to apply the models described above, a relation to spectroscopic data like e.g. UV/Vis absorption spectra needs to be established.

A.1 Relation of Concentration-Dependent Models to Absorption Spectra

The following equations describe the relation between the mole fraction of monomeric and aggregated species, respectively, and the absorption coefficient of a solution of a given total concentration c_T:

$$\alpha_{mon} \approx \frac{\varepsilon(c_T) - \varepsilon_{agg}}{\varepsilon_{mon} - \varepsilon_{agg}} \tag{A2.1}$$

$$\alpha_{agg} \approx 1 - \frac{\varepsilon(c_T) - \varepsilon_{agg}}{\varepsilon_{mon} - \varepsilon_{agg}} = \frac{\varepsilon(c_T) - \varepsilon_{mon}}{\varepsilon_{agg} - \varepsilon_{mon}} \tag{A2.2}$$

where ε_{mon} and ε_{agg}, denote the molar absorption coefficients of free monomeric dyes and aggregated dyes, respectively, and $\varepsilon(c_T)$ denotes the apparent absorption coefficient at the concentration c_T.

Monomer–Dimer Model

To obtain a relation that can be fitted to absorption spectra, equation (2.5) is inserted into equation (A2.1). Subsequent resolution for $\varepsilon(c_T)$ gives equation (A2.3):

$$\varepsilon(c_T) = \frac{\sqrt{8K_D c_T + 1} - 1}{4K_D c_T}\left(\varepsilon_{mon} - \varepsilon_{agg}\right) + \varepsilon_{agg} \tag{A2.3}$$

Isodesmic Model

Inserting equation (2.11) into equation (A2.2) and solving for $\varepsilon(c_T)$ yields equation (A2.4) which can be used to be fitted to the experimental data:

$$\varepsilon(c_T) = \frac{2Kc_T + 1 - \sqrt{4Kc_T + 1}}{2K^2 c_T^2}\left(\varepsilon_{mon} - \varepsilon_{agg}\right) + \varepsilon_{agg} \tag{A2.4}$$

K_2–K Model

Since it is exhaustive to solve equation (2.26) for general cases, the above mentioned relation between Kc_T and Kc_1 (equation (2.27)) is used to obtain α_{agg} (equation (2.28)) for given σ values. Taking into account equation (A2.2), the ordinate can be fitted to the

experimental data. Fitting of the abscissa is performed manually by multiplying the given total concentration by K for the best match to the calculated curve. Such a procedure was recently employed to fit concentration-dependent UV/Vis data of perylene bisimides to the K_2–K model.[45]

General Nucleation–Elongation Model

In case of a variable nucleus size, additional parameters have to be taken into account. Plots of α_{agg} against Kc_T for several combinations of s and σ are calculated according to equations (2.37) and (2.28). The fitting procedure to experimental data is then similar to the one described for the K_2–K model.

A.2 Relation of Temperature-Dependent Models to Absorption Spectra

The mole fraction of the aggregated species $\alpha_{agg}(T)$ at each temperature can be estimated from absorption spectra according to equation (A2.5):

$$\alpha_{agg}(T) \approx \frac{\varepsilon(T) - \varepsilon_{mon}}{\varepsilon_{agg} - \varepsilon_{mon}} \tag{A2.5}$$

where $\varepsilon(T)$ denotes the temperature-dependent apparent absorption coefficient of the mixture and ε_{agg} and ε_{mon} the absorption coefficients of the aggregate, and the monomer, respectively.

Isodesmic Model

The combination of equations (2.22) and (A2.5) yields equation (A2.6), which can be fitted to experimentally detected, temperature-dependent absorption spectra:

$$\varepsilon(T) = \frac{1}{1 + e^{-0.908\Delta H \frac{T - T_M}{RT_M^2}}} \left(\varepsilon_{agg} - \varepsilon_{mon} \right) + \varepsilon_{mon} \tag{A2.6}$$

Thermally Activated Equilibrium Polymerization Model

Equations (A2.7) and (A2.8), which can be fitted to experimental data in the elongation regime ($T < T_e$) and in the nucleation regime ($T > T_e$), respectively, can be obtained by inserting the respective expression for $\alpha_{agg}(T)$ (equations (2.33) and (2.34)) into equation (A2.5) and solving the result for $\varepsilon(T)$:

$$\varepsilon(T) = \left(1 - e^{\frac{-\Delta H_e}{RT_e^2}(T - T_e)} \right) \left(\varepsilon_{agg} - \varepsilon_{mon} \right) + \varepsilon_{mon} \tag{A2.7}$$

$$\varepsilon(T) = K_a{}^{1/3} e^{\left(\frac{2}{3}K_a{}^{-1/3}-1\right)\frac{\Delta H_e}{RT_e^2}(T-T_e)} \left(\varepsilon_{agg} - \varepsilon_{mon}\right) + \varepsilon_{mon} \tag{A2.8}$$

A.3 Equivalence of the K_2–K Model and the Thermally Activated Self-Assembly Model

It can be shown that the thermally activated self-assembly model equals the K_2–K model.[28a,51] The equilibrium conditions described above lead to the following expressions for the concentrations of the active monomer c_1^* (equation (A2.9)) and the activated n-mer c_n^* (equation (A2.10)) as functions of the inactive monomer c_1:

$$c_1^* = K_a c_1 \tag{A2.9}$$

$$c_n^* = \frac{1}{K}(K K_a c_1)^n = \frac{K_a}{K'}(K' c_1)^n \tag{A2.10}$$

with $K' = K K_a$. This is equal to equation (2.25) describing c_n in the K_2–K model, where σ was replaced by K_a. Small deviations can be found, comparing the mass balance equations. For the K_2–K model, monomers and polymers of size n are present, leading to equation (2.26) for c_T. The thermal activation self-assembly model involves monomers, activated monomers and polymers of size n, and the corresponding mass balance equation is given by:

$$c_T = c_1 + \sum_{n=1}^{\infty} n c_n^* = c_1 + \sum_{n=1}^{\infty} n \frac{K_a}{K'}(K' c_1)^n = c_1 + \frac{K_a c_1}{(1 - K' c_1)^2} \tag{A2.11}$$

For concentrations far above the critical concentration or for systems displaying high cooperativity ($K_a = \sigma \ll 1$) the first term can be neglected and both expressions become equivalent:

$$c_T = \frac{\sigma c_1}{(1 - K' c_1)^2} \tag{A2.12}$$

Solving this expression for c_1 leads to equation (A2.13), which simplifies to equation (A2.14) for $\sigma \ll 1$ and $K' c_T \gg 1$:

$$c_1 = \frac{1}{2}\frac{2K' c_T + \sigma - \sqrt{4K' c_T + \sigma^2}}{K'^2 c_T} \tag{A2.13}$$

$$c_1 = \frac{1}{K'} \tag{A2.14}$$

Having determined the term c_1, the degree of aggregation is given by:

$$\alpha_{agg} = 1 - \alpha_{mon} = 1 - \frac{c_1}{c_T} = 1 - \frac{1}{K' c_T} \tag{A2.15}$$

The temperature-dependence of α_{agg} can be expressed, making use of the Van't Hoff equation:

$$\ln K' = -\frac{\Delta G}{RT} = -\frac{\Delta H}{RT} + \frac{\Delta S}{R} \tag{A2.16}$$

The equilibrium constant is required to be dimensionless to take the logarithm. This can be done by multiplying K' with c_T to give $K_e = K'c_T$.

$$\alpha_{agg} = 1 - \frac{1}{K_e} = 1 - \frac{1}{e^{-\frac{\Delta G_e}{RT}}} = 1 - \frac{e^{\frac{\Delta G_e}{RT}}}{1} \tag{A2.17}$$

This expression is equal to equation (2.33).

B Supplement for Chapter 3

B.1 Computational Details

The merocyanine dye monomers and dimers were calculated with the dispersion-corrected DFT-D method in combination with the B97-d functional using the parameters fitted by Grimme and coworkers.[138] The semi-empirical dispersion correction method was absolutely essential for a proper description of the dimers.[87] In all computations, the resolution-of-the-identity (RI) approximation was employed.[139] All calculations were performed with the TURBOMOLE program (version 5.10).[140] The TZVP[141] basis for C, N, O, and S atoms was combined with the TZV[140] basis for the H atom. This basis is designated as TZV(P) and was found to be an excellent compromise between accuracy and computational effort for systems of similar size.[142] Corresponding auxiliary basis sets were applied for fitting the charge density.[143] All merocyanine dye dimers were fully geometry-optimized, emanating from crystal structures in which alkyl chains and benzyl units were replaced by methyl groups.[i]

Energy decomposition analysis was performed with the wavels program[144] on Hartree-Fock (HF) level, employing also the TZV(P) basis. In this analysis, the formation of noncovalent bonding between the two fragments is divided into four contributions. The first contribution is given by the energy expectation value of the superimposed HF electron densities of the fragments in the geometry of the dimer. This is interpreted as the electrostatic interaction energy E_{es}. Subsequently, the occupied orbitals are orthogonalized and renormalized. The energy expectation value of the corresponding Slater determinant represents the sum of E_{es} and the second contribution, the exchange repulsion energy E_{exr}. In the next step, the molecular orbitals are allowed to relax to their final form, which yields the stabilizing relaxation energy E_{rel}. While these terms are evaluated at the HF level, the dispersion energy term E_{disp} is calculated as the dispersion contribution of the DFT-D approach. The total interaction energy E_{tot} is given by the equation (B3.1).

$$E_{tot} = E_{es} + E_{exr} + E_{rel} + E_{disp} \tag{B3.1}$$

E_{tot} differs from the true total interaction energy by the amount of energy which is necessary to distort the optimal monomer geometries into the structure they have in the dimer. This energy was found to be very small for a dimer of merocyanine **1** and similar systems and has therefore been neglected.[87]

---

[i] Geometry-optimization for merocyanine **3** did not converge owing to oscillation of the energy. Therefore, the structure with the lowest energy after 400 iterations was used for the EDA.

B.2 Cartesian Coordinates of the Geometry-Optimized Merocyanine Dimers

Table B1. Cartesian coordinates (in Å) of a geometry-optimized dimer of merocyanine **1** on RI-DFT-D (B97-d/TZV(P)) level.

E (Hartree)		-1866.185207	
Atom	x	y	z
C	-0.463724	2.495344	-4.383362
H	0.029338	3.123578	-5.116438
C	-0.319901	2.675107	-3.034938
H	0.297036	3.497097	-2.681884
C	-0.913501	1.783301	-2.089536
C	-1.703075	0.734642	-2.659124
H	-2.187536	-0.008198	-2.034117
C	-1.820906	0.601244	-4.016066
H	-2.374435	-0.209847	-4.476391
C	-0.639836	1.965817	-0.709782
H	0.016840	2.789459	-0.454090
C	-1.126654	1.167878	0.309812
H	-1.800408	0.368947	0.010388
C	-0.881426	1.250308	1.705381
C	-1.558364	0.372847	2.605100
C	-1.326792	0.465894	3.978008
C	-0.405100	1.441245	4.561079
C	0.111826	2.200041	2.235195
C	-1.300706	1.263566	-6.342774
H	-1.461541	0.204033	-6.546334
H	-2.122562	1.868926	-6.745707
H	-0.351291	1.555819	-6.797683
C	-2.511011	-0.673552	2.073939
H	-2.932450	-1.284783	2.875421
H	-1.996627	-1.334511	1.364935
H	-3.341613	-0.198854	1.535348
C	-1.881728	-0.460198	4.899542
C	1.170385	3.302378	4.147438
H	1.016757	3.416832	5.220590
H	1.010138	4.249127	3.625698
H	2.201076	2.979644	3.949372
N	-1.200320	1.458736	-4.884706
N	0.212496	2.307376	3.641508
N	-2.283337	-1.260994	5.647686
O	-0.144252	1.497837	5.767875
O	0.868360	2.890423	1.543218
C	0.464417	-2.495217	4.383385
H	-0.027978	-3.123828	5.116560
C	0.320253	-2.675007	3.035032

H	-0.296507	-3.497193	2.682160
C	0.913858	-1.783359	2.089500
C	1.703277	-0.734502	2.658946
H	2.187569	0.008355	2.033907
C	1.821336	-0.601039	4.015836
H	2.374721	0.210219	4.476028
C	0.640386	-1.966166	0.709745
H	-0.015906	-2.790097	0.453989
C	1.126832	-1.167929	-0.309825
H	1.800205	-0.368685	-0.010437
C	0.881518	-1.250418	-1.705381
C	1.557867	-0.372567	-2.605159
C	1.326010	-0.465647	-3.977997
C	0.404280	-1.441015	-4.560849
C	-0.111779	-2.200183	-2.234989
C	1.301618	-1.263756	6.342647
H	1.464619	-0.204470	6.546389
H	2.122301	-1.870668	6.745628
H	0.351615	-1.554212	6.797439
C	2.511221	0.673293	-2.074433
H	2.932558	1.284446	-2.876022
H	1.997563	1.334413	-1.365056
H	3.341819	0.198090	-1.536291
C	1.881110	0.460169	-4.899818
C	-1.171146	-3.302160	-4.146881
H	-1.019702	-3.414672	-5.220553
H	-1.009155	-4.249728	-3.627103
H	-2.201610	-2.980462	-3.945989
N	1.200964	-1.458578	4.884568
N	-0.212806	-2.307444	-3.641272
N	2.283024	1.260648	-5.648168
O	0.142871	-1.497165	-5.767584
O	-0.867713	-2.891064	-1.542908

Table B2. Cartesian coordinates (in Å) of a geometry-optimized dimer of merocyanine **2** on RI-DFT-D (B97-d/TZV(P)) level.

E (Hartree)		-2586.416100	
Atom	x	y	z
S	2.857837	-0.404080	1.824578
O	0.478707	0.490143	2.565217
O	-4.080996	0.333973	2.953361
N	5.570387	-0.450025	1.469812
N	-1.776944	0.352223	2.803730
N	-5.391988	-2.041385	0.698638

C	5.658452	0.661912	2.419878
H	5.429668	1.613512	1.921196
H	6.675324	0.701672	2.820090
H	4.965061	0.502317	3.253963
C	6.761058	-0.740335	0.658760
H	6.813272	-1.813086	0.444507
H	7.647474	-0.456445	1.232089
H	6.737879	-0.172553	-0.279277
C	4.373603	-0.916837	1.064992
C	4.143688	-1.829427	0.011322
H	4.924277	-2.206435	-0.637498
C	2.803944	-2.113638	-0.151709
H	2.426175	-2.782167	-0.921658
C	1.914358	-1.446601	0.723232
C	0.536135	-1.647573	0.624537
H	0.337260	-2.371536	-0.162038
C	-0.627743	-1.161956	1.247493
C	-0.570755	-0.078149	2.230907
C	-1.675266	1.437147	3.791784
H	-0.963735	1.152522	4.571989
H	-2.665043	1.610660	4.214199
H	-1.303045	2.349622	3.310667
C	-3.060071	-0.128497	2.449209
C	-3.062195	-1.195119	1.442459
C	-4.348321	-1.659384	1.052758
C	-1.904130	-1.692130	0.857872
C	-1.992119	-2.770635	-0.195180
H	-3.021649	-3.097788	-0.354982
H	-1.399181	-3.647297	0.096577
H	-1.598853	-2.393172	-1.147354
S	-2.855340	0.395249	-1.826992
O	-0.470904	-0.502387	-2.552298
O	4.086591	-0.314569	-2.950282
N	-5.570145	0.444222	-1.489942
N	1.782813	-0.346494	-2.798403
N	5.386591	2.060864	-0.690048
C	-5.652951	-0.674295	-2.432721
H	-5.431024	-1.623029	-1.925243
H	-6.666528	-0.714093	-2.841456
H	-4.952039	-0.522645	-3.261998
C	-6.766072	0.737977	-0.687814
H	-6.814431	1.810169	-0.470214
H	-7.649078	0.461026	-1.269971
H	-6.753196	0.166302	0.248118
C	-4.375451	0.911037	-1.078289

C	-4.151110	1.825729	-0.025314
H	-4.935053	2.204292	0.618584
C	-2.812030	2.109066	0.145395
H	-2.438694	2.779134	0.916132
C	-1.917694	1.439550	-0.722578
C	-0.540018	1.641073	-0.617876
H	-0.344710	2.366081	0.168656
C	0.626591	1.158350	-1.238181
C	0.575154	0.074145	-2.221296
C	1.686284	-1.429782	-3.788618
H	0.969530	-1.148935	-4.565397
H	2.675815	-1.594364	-4.215127
H	1.323250	-2.346436	-3.308459
C	3.063409	0.141037	-2.444245
C	3.060633	1.204800	-1.434571
C	4.344611	1.674882	-1.044614
C	1.900314	1.693749	-0.847333
C	1.983952	2.768896	0.209806
H	3.012571	3.097117	0.373099
H	1.390280	3.645619	-0.080438
H	1.589269	2.387233	1.159676

Table B3. Cartesian coordinates (in Å) of a geometry-optimized dimer of merocyanine **3** on RI-DFT-D (B97-d/TZV(P)) level.

E (Hartree)		-1864.3015	
Atom	x	y	z
O	-0.233209	6.134590	1.327457
O	2.317454	2.335043	1.155828
O	-2.423381	2.123440	1.838816
N	-1.330953	4.138304	1.608652
N	1.031257	4.239376	1.286730
N	0.835582	-4.467799	2.077171
C	2.218115	5.105222	1.104964
H	2.125752	5.622377	0.139364
H	3.099960	4.479549	1.121538
H	2.254700	5.852617	1.913342
C	-2.648875	4.810606	1.726432
H	-3.302180	4.467920	0.908344
H	-2.461006	5.889767	1.689620
H	-3.128310	4.538467	2.663784
C	-0.183546	4.911092	1.406694
C	-1.342512	2.708704	1.682910
C	1.187523	2.818830	1.324599
C	-0.024771	2.055094	1.558484

C	-0.018247	0.646676	1.654314
H	-1.022460	0.243433	1.821295
C	1.045274	-0.243632	1.579003
H	2.035723	0.161832	1.400178
C	0.936422	-1.651202	1.727595
C	2.107067	-2.475045	1.643279
H	3.069848	-2.025120	1.421976
C	2.033347	-3.832408	1.799094
H	2.896278	-4.482602	1.729078
C	-0.285395	-2.366524	1.976617
H	-1.232775	-1.825445	2.019860
C	-0.313362	-3.717934	2.153778
H	-1.244373	-4.263079	2.337781
C	0.799205	-5.938198	2.247159
H	0.356795	-6.426101	1.385082
H	0.195181	-6.199813	3.114910
H	1.818520	-6.298325	2.393904
O	1.795080	-2.414714	-2.046878
O	-0.646370	-6.083109	-0.740468
O	-2.777461	-2.050954	-0.684358
N	0.544561	-4.244409	-1.412473
N	-1.727604	-4.046675	-0.773162
N	0.125744	4.421786	-2.466997
C	-3.004751	-4.640420	-0.336885
H	-2.841824	-5.716340	-0.210591
H	-3.316852	-4.189189	0.608880
H	-3.792985	-4.447975	-1.079778
C	1.698330	-5.151058	-1.600836
H	2.530431	-4.573776	-1.995258
H	1.951736	-5.611078	-0.636153
H	1.428520	-5.956079	-2.308799
C	-0.631322	-4.879802	-0.993522
C	0.689086	-2.848001	-1.679710
C	-1.738161	-2.648191	-0.963976
C	-0.513226	-2.042857	-1.476962
C	-0.548581	-0.646449	-1.669142
H	-1.530697	-0.214226	-1.433850
C	0.464766	0.222863	-2.091465
H	1.450305	-0.189012	-2.299541
C	0.307267	1.613887	-2.203921
C	1.431639	2.427388	-2.568997
H	2.402849	1.963148	-2.734337
C	1.321605	3.784502	-2.677089
H	2.171039	4.415508	-2.911803
C	-0.985333	3.678246	-2.132675

H	-1.903129	4.238288	-1.982653
C	-0.927966	2.325112	-1.972999
H	-1.837521	1.809918	-1.676362
C	-0.014372	5.868646	-2.664889
H	-0.339276	6.125398	-3.693635
H	-0.740361	6.237713	-1.936130
H	0.933418	6.354654	-2.457563

Table B4. Cartesian coordinates (in Å) of a geometry-optimized dimer of merocyanine **9** on RI-DFT-D (B97-d/TZV(P)) level.

E (Hartree)		-2700.858311	
Atom	x	y	z
S	-0.071756	6.694679	8.055777
N	-3.456615	4.184877	4.801464
C	-4.528137	3.992266	3.909255
C	-5.035972	5.862246	5.284692
N	-0.740576	8.299760	10.044994
C	-1.768422	7.186977	8.239417
C	-2.316680	3.274216	4.891593
H	-2.624036	2.297163	4.515790
H	-2.025003	3.153913	5.937220
N	2.293813	9.198673	12.015266
C	-1.850996	8.047547	9.354758
C	0.324558	7.667146	9.502995
C	-2.814965	6.731701	7.435378
H	-3.787442	7.183586	7.622147
C	-6.654781	5.002246	3.384481
H	-7.416410	5.760582	3.558271
C	1.640587	7.733686	9.990304
H	-2.795985	8.479218	9.682707
H	-1.470346	3.652827	4.302453
C	-4.685016	3.009678	2.933627
H	-3.935062	2.242528	2.761280
C	-5.489915	4.980767	4.137297
C	-6.837064	4.024331	2.393112
H	-7.744082	4.026668	1.791813
C	1.982852	8.550711	11.094672
C	-5.862149	3.042727	2.175904
H	-6.020015	2.287545	1.408593
C	-4.940392	7.341514	4.860735
H	-4.248087	7.465509	4.019983
H	-4.593721	7.964837	5.692245
H	-5.931848	7.694309	4.552782
C	-6.004097	5.687324	6.478849

H	-6.999832	6.035205	6.178889
H	-5.685404	6.261925	7.351943
H	-6.077227	4.634682	6.765557
N	3.455820	6.214562	8.954837
C	2.652859	6.924493	9.420766
C	-2.685961	5.726289	6.477427
H	-1.723384	5.222548	6.432525
C	-3.657880	5.269807	5.594256
S	-2.199315	4.574585	10.794357
N	1.160529	7.077707	14.054492
C	2.222156	7.277914	14.956975
C	2.749049	5.402613	13.593094
N	-1.534700	2.971260	8.802557
C	-0.502749	4.082134	10.606877
C	0.004800	7.967371	13.952298
H	0.259342	8.925724	14.406488
H	-0.229703	8.143321	12.899299
N	-4.559110	2.061521	6.842970
C	-0.422345	3.223713	9.489789
C	-2.599088	3.601767	9.349264
C	0.543934	4.532868	11.413211
H	1.516447	4.080954	11.226830
C	4.342817	6.267213	15.510673
H	5.103477	5.505628	15.347334
C	-3.916719	3.529639	8.868621
H	0.521819	2.793495	9.158319
H	-0.863731	7.531393	14.463496
C	2.372585	8.266263	15.928351
H	1.625990	9.039593	16.086418
C	3.187105	6.288001	14.743899
C	4.515993	7.248447	16.500146
H	5.415013	7.246561	17.112295
C	-4.256245	2.711345	7.764328
C	3.541409	8.234255	16.699377
H	3.692728	8.993427	17.464161
C	2.647524	3.925199	14.022175
H	1.954578	3.807587	14.863445
H	2.297887	3.300867	13.192985
H	3.637631	3.569783	14.332946
C	3.732441	5.572896	12.410605
H	4.724158	5.225399	12.723873
H	3.422576	4.995273	11.535668
H	3.809514	6.624349	12.120187
N	-5.733163	5.040214	9.913650
C	-4.930301	4.333190	9.442983

C	0.411559	5.537201	12.372001
H	-0.549716	6.044432	12.407679
C	1.375230	5.992838	13.265231

Table B5. Cartesian coordinates (in Å) of a geometry-optimized dimer of merocyanine **4** on RI-DFT-D (B97-d/TZV(P)) level.

E (Hartree)		-2254.33208	
Atom	x	y	z
O	-0.692963	2.490644	-0.813382
O	3.302581	2.245873	1.408922
N	1.259094	2.418975	0.349575
N	3.049055	0.057415	4.143691
N	-5.252095	1.033701	-0.681405
C	-0.081016	2.021045	0.150494
C	1.769601	3.436240	-0.582066
H	2.767715	3.729433	-0.259043
H	1.093173	4.295852	-0.584794
H	1.808673	3.034297	-1.600058
C	2.119770	1.909904	1.343474
C	1.500457	0.964306	2.278868
C	2.357147	0.475706	3.303130
C	0.173427	0.569398	2.188766
C	-0.391355	-0.405896	3.194513
H	-0.746853	-1.306915	2.682829
H	-1.236866	0.040773	3.735240
H	0.356740	-0.712739	3.928092
C	-0.654167	1.078680	1.131473
C	-2.009791	0.707986	1.073317
H	-2.334786	0.056322	1.873890
C	-2.992921	1.056867	0.145528
H	-2.696597	1.657264	-0.704229
C	-4.331239	0.691894	0.261284
C	-4.945257	1.790512	-1.893878
H	-4.683566	2.824770	-1.635709
H	-5.815845	1.785396	-2.550185
H	-4.114077	1.324136	-2.425220
C	-6.548616	0.619262	-0.319869
C	-7.750561	0.782595	-1.009270
H	-7.802972	1.285521	-1.971005
C	-8.908620	0.262641	-0.416704
H	-9.861047	0.371799	-0.932007
C	-8.860055	-0.393344	0.819160
H	-9.774096	-0.789463	1.257134
C	-7.638190	-0.543708	1.494654

H	-7.597962	-1.054726	2.455476
C	-6.486056	-0.030650	0.917346
C	-5.051812	-0.036731	1.409025
C	-4.571532	-1.489837	1.612181
H	-5.248036	-1.989069	2.317153
H	-3.562123	-1.527206	2.031927
H	-4.571795	-2.034140	0.664697
C	-4.944679	0.774535	2.721776
H	-5.306782	1.799044	2.577306
H	-3.909357	0.819091	3.074743
H	-5.558557	0.294096	3.493620
O	0.696520	-2.476777	0.826004
O	-3.296892	-2.270480	-1.405633
N	-1.253752	-2.424502	-0.340800
N	-3.051178	-0.089734	-4.150241
N	5.258574	-1.055937	0.661713
C	0.083226	-2.017052	-0.141787
C	-1.759269	-3.444846	0.590560
H	-2.756163	-3.742401	0.267247
H	-1.078272	-4.300953	0.592313
H	-1.800588	-3.044888	1.609298
C	-2.116751	-1.925921	-1.339146
C	-1.501960	-0.979445	-2.277045
C	-2.360005	-0.501667	-3.305650
C	-0.176747	-0.578259	-2.188264
C	0.381965	0.400751	-3.193705
H	0.718098	1.310004	-2.682866
H	1.238565	-0.033222	-3.726997
H	-0.365201	0.691979	-3.934802
C	0.654313	-1.081553	-1.130744
C	2.008612	-0.705687	-1.074784
H	2.332512	-0.065766	-1.885037
C	2.991159	-1.043594	-0.142960
H	2.690235	-1.621282	0.720460
C	4.333037	-0.696029	-0.270210
C	4.958245	-1.827648	1.867481
H	4.384471	-2.720530	1.595131
H	5.893689	-2.135751	2.336105
H	4.380272	-1.226982	2.575325
C	6.548772	-0.612187	0.314333
C	7.746941	-0.750443	1.015566
H	7.797299	-1.240548	1.983870
C	8.900498	-0.210210	0.432918
H	9.849561	-0.298915	0.958039
C	8.850862	0.443580	-0.803947

H	9.761174	0.856138	-1.234370
C	7.631633	0.575543	-1.488070
H	7.590094	1.089340	-2.447345
C	6.483488	0.044168	-0.919459
C	5.050372	0.037361	-1.415253
C	4.561323	1.487346	-1.621116
H	5.237244	1.990481	-2.323718
H	3.553728	1.518842	-2.045381
H	4.554403	2.031725	-0.673996
C	4.952811	-0.775153	-2.728309
H	5.323735	-1.796366	-2.583415
H	3.918245	-0.828635	-3.082572
H	5.563796	-0.289259	-3.499054

Table B6. Cartesian coordinates (in Å) of a geometry-optimized dimer of merocyanine **10** on RI-DFT-D (B97-d/TZV(P)) level.

E (Hartree)	-2406.093371		
Atom	x	y	z
N	9.738726	13.303939	11.948421
O	6.653630	9.721692	11.076204
C	10.556845	14.448914	12.017215
C	11.592128	14.743456	12.905589
H	11.889478	14.058821	13.695966
N	5.684341	14.757037	7.453186
C	12.250421	15.970862	12.745132
H	13.062494	16.228041	13.423082
N	3.164656	12.063527	5.356628
C	11.880532	16.865958	11.734287
H	12.405644	17.813301	11.631250
C	10.833217	16.547295	10.853963
H	10.540417	17.244191	10.070219
C	10.176846	15.334319	11.001094
C	9.031654	14.732443	10.208170
C	8.827519	13.393087	10.930312
C	7.781207	15.633921	10.305794
H	7.477367	15.757478	11.352276
H	6.945437	15.226612	9.733766
H	8.020726	16.622386	9.895830
C	9.454574	14.525964	8.734781
H	10.341932	13.885645	8.675240
H	9.696187	15.499578	8.292285
H	8.651967	14.073716	8.146116
C	9.832762	12.161918	12.852310
H	10.684484	12.298093	13.520053

H	9.969674	11.238246	12.277261
H	8.914992	12.068585	13.446543
C	7.916660	12.380194	10.680543
H	7.930740	11.507889	11.322942
C	6.970130	12.393547	9.645798
H	6.944357	13.270031	9.013370
C	6.073204	11.371002	9.356401
C	6.009359	10.077424	10.090750
C	4.991029	9.256032	9.390875
C	4.570895	7.971100	9.705863
H	5.005634	7.451021	10.556044
C	3.572947	7.392140	8.916937
H	3.210782	6.392736	9.146173
C	3.025949	8.106396	7.842194
H	2.240355	7.650963	7.242277
C	3.450243	9.403332	7.528093
H	2.987664	9.924082	6.699620
C	4.452908	9.988151	8.313014
C	5.100458	11.325935	8.277380
C	4.778990	12.331414	7.365694
C	5.300590	13.654747	7.425857
C	3.876845	12.160856	6.275426
N	-1.807116	8.386823	7.938255
O	1.273327	11.967363	8.826119
C	-2.627498	7.243629	7.870874
C	-3.663237	6.949731	6.982949
H	-3.956860	7.631105	6.188320
N	2.234886	6.923938	12.443858
C	-4.327724	5.726413	7.148644
H	-5.141316	5.471473	6.471941
N	4.759546	9.606282	14.541603
C	-3.963810	4.834227	8.164160
H	-4.493891	3.890195	8.270953
C	-2.915593	5.151837	9.043645
H	-2.626956	4.458189	9.831859
C	-2.252826	6.360470	8.890661
C	-1.108954	6.961039	9.685660
C	-0.901327	8.299231	8.961369
C	0.140504	6.056586	9.593485
H	0.450568	5.933970	8.548884
H	0.973316	6.461503	10.171298
H	-0.103869	5.067883	10.000924
C	-1.536394	7.165647	11.157100
H	-2.421692	7.809073	11.215725
H	-1.783952	6.191612	11.596043

H	-0.734384	7.612072	11.751376
C	-1.902283	9.530887	7.037243
H	-2.750581	9.392609	6.365833
H	-2.045517	10.452385	7.615103
H	-0.983007	9.630559	6.446559
C	0.008877	9.311247	9.214259
H	-0.001369	10.184335	8.572205
C	0.951696	9.294841	10.252343
H	0.972496	8.418450	10.885036
C	1.850411	10.314737	10.543988
C	1.915809	11.609406	9.812552
C	2.932046	12.428774	10.517278
C	3.352976	13.715609	10.208664
H	2.918361	14.240417	9.360912
C	4.350084	14.291121	11.002199
H	4.710161	15.293130	10.780623
C	4.897375	13.570668	12.072550
H	5.682884	14.022440	12.674837
C	4.472661	12.272507	12.379169
H	4.935994	11.746547	13.203780
C	3.469614	11.692580	11.592517
C	2.821291	10.355989	11.624410
C	3.141929	9.348494	12.534184
C	2.619731	8.025632	12.471985
C	4.045803	9.514292	13.623839

B.3 Calculation of the Energy Density σ

The $-\Delta G°$ values used for the calculation of σ according to equation (3.4) were averaged over the high and low extreme values for each single and multiple hydrogen bonding system, single merocyanine dyes and their tweezers (see Figure 5). The associated areas were calculated from AM1 geometry-optimized structures.[128] Figure B1 exemplifies the procedure for two systems. The distances between the red and blue highlighted atoms, respectively, were measured and subsequently multiplied to obtain the area. The area resulting for the merocyanine dye corresponds to the π-surface of the molecule. For the bis(merocyanine) dye tweezers, twice the area of the single chromophore was used. For a single hydrogen bond, a fourth of the distance between the blue spots and the π-π distance (3.5 Å) was chosen to estimate the displacement to next possible hydrogen bonds.[ii] Figures B2–B4 depict the areas for the investigated systems and the AM1 geometry-optimized structures.
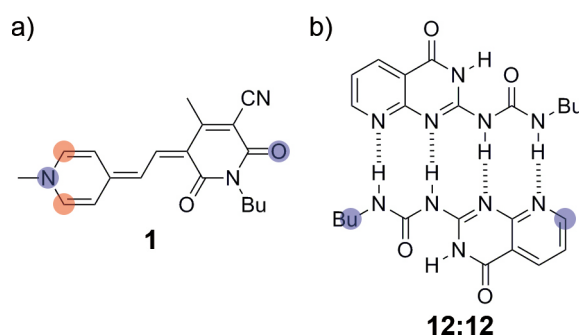
Figure B1. Merocyanine dye **1** (a) and complex **12:12** (b). The red and blue spots mark the atoms between the respective distances for the calculation of the area were measured.
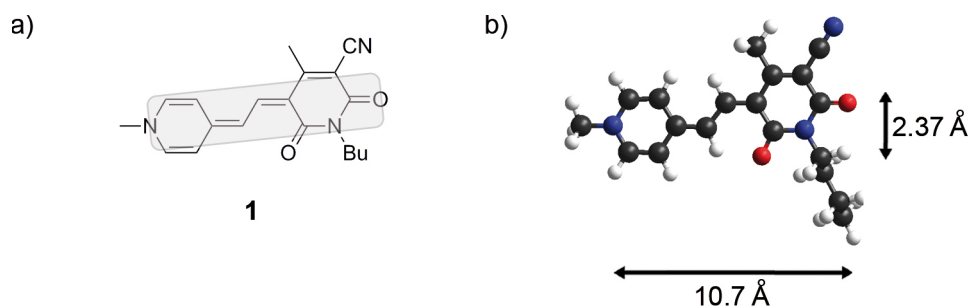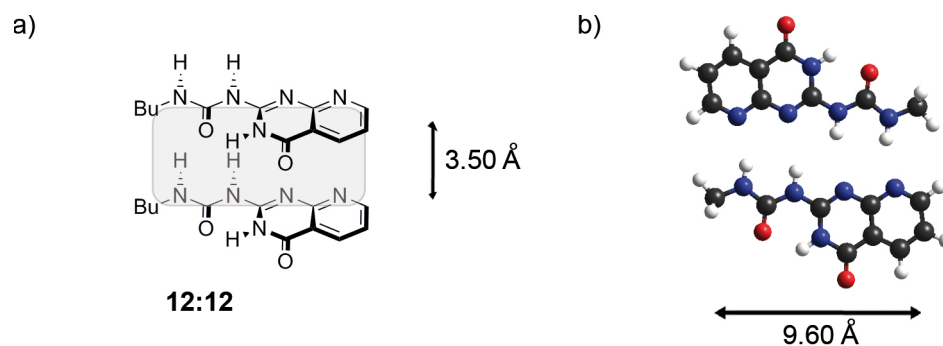

Figure B2. a) Merocyanine dye **1**. The grey shimmed domain indicates the area which was used to calculate the energy density. b) AM1 geometry-optimized structure of **1**.

[ii] In order to obtain reasonable average values for a single hydrogen bond, a system was chosen that exhibits quadruple hydrogen bonds and whose free binding energy is roughly in the middle of the two extremes for the respective multiple hydrogen bonding site. The area for the hydrogen bonding systems was calculated by multiplying the distance corresponding to the width of the single compound (blue spots in Figure B1b) with the π-π distance (3.5 Å). The resulting value was divided by four to obtain a quantity for a single hydrogen bond.
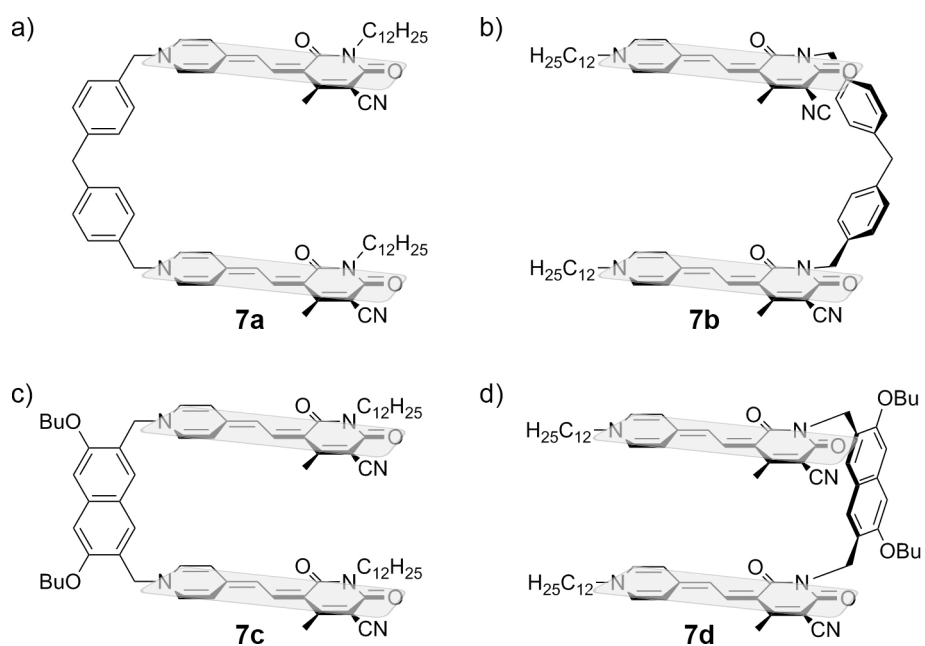
Figure B3. Bis(merocyanine) dye tweezers **7a–d**. The grey shimmed domains indicate the areas which were used to calculate the energy densities.

Figure B4. a) Complex **12:12**. The grey shimmed domain indicates the area which was used to calculate the energy density. b) AM1 geometry-optimized structure of **12:12**.

Table B7. Energy densities σ (in kJ mol^{-1} Å^{-2}) of bis(merocyanine) dye tweezers **7a–d**.

system	σ
bis(merocyanine) tweezers **7a**	0.54
bis(merocyanine) tweezers **7b**	0.64
bis(merocyanine) tweezers **7c**	0.71
bis(merocyanine) tweezers **7d**	0.99

C Supplement for Chapter 4

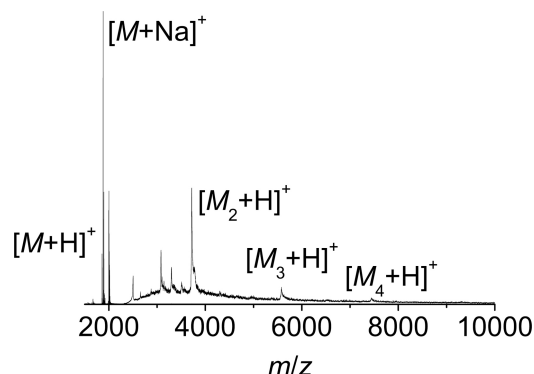## C.1 Characterization of Hamilton-Receptor-Tethered Bis(merocyanine) Dye 8
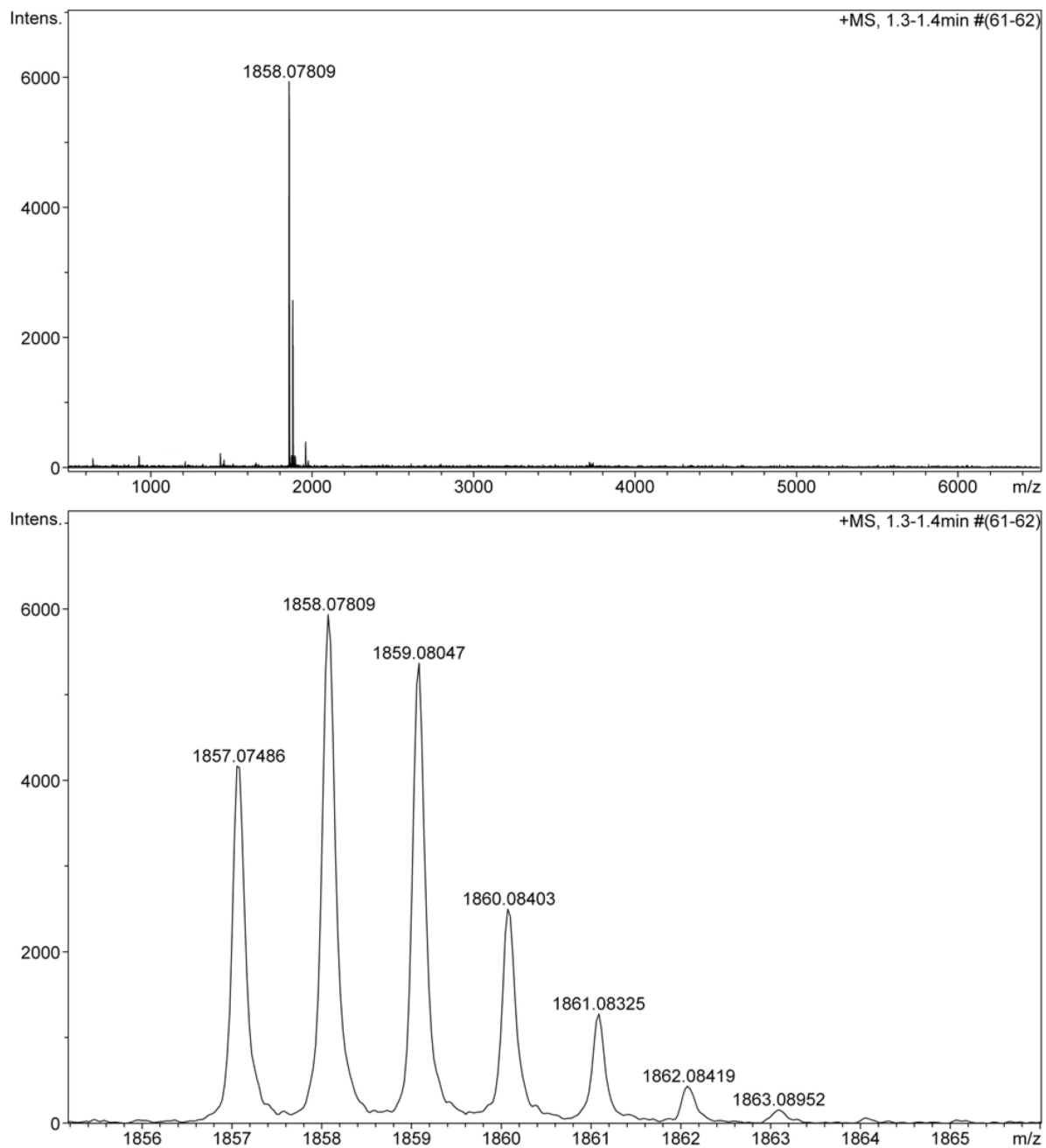
Figure C1. HRMS ESI (positive mode, THF) of **8**.

0.7655
0.7832
0.8148
0.8571
0.8754
0.8937
1.1254
1.3325
1.3454
1.4398
1.5838
1.6759
1.7454

2.3733
2.6505
2.6678
2.6898

3.2379
3.4274
3.4466
3.4659
3.8437
3.8605
3.8769
3.8965
3.9126
3.9287
4.0534
4.2118
4.2308
4.2497
5.0598
5.2672

6.4475
6.4604
6.6347

7.5401
7.6016
7.6155
7.6525
7.6657
7.7544
7.7579
7.9167
7.9274
7.9385
8.1001
8.1039
8.1074

11.104
12.931
55.246
11.868
7.0101
15.269

5.9589

3.8203

8.2120
2.2453
4.4042
4.0166

1.9442

1.9926
2.1146

1.9114
2.1022
4.1411
2.1211
2.1435
1.0000

(ppm)

Integral

Figure C2. ^{1}H NMR of Hamilton-receptor-tethered bis(merocyanine) **8** in CD$_2$Cl$_2$/MeOH-d_4 (4:1 vol%).

116

C.2 Mass Spectrometric Studies

Figure C3. MALDI-TOF spectrum of a sample prepared from a 1.0×10^{-4} M solution of Hamilton-receptor-tethered bis(merocyanine) dye **8** in THF/MCH = 10:90 vol%. The peaks, corresponding to the positively charged sodium adduct of the monomer and singly protonated dimer, trimer, and tetramer cations, are marked with $[M+\text{Na}]^+$, $[M_2+\text{H}]^+$, $[M_3+\text{H}]^+$, and $[M_4+\text{H}]^+$, respectively.

Table C1. Monoisotopic mass peaks observed in MALDI-TOF MS spectra of Hamilton-receptor-tethered bis(merocyanine) **8** that correspond to monomeric , dimeric, trimeric, and tetrameric aggregates.

calculated m/z (ion)	found
1859.531 ($[M+\text{H}]^+$)	1859.121
1880.067 ($[M+\text{Na}]^+$)	1880.126
3718.054 ($[M_2+\text{H}]^+$)	3718.034
5576.578 ($[M_3+\text{H}]^+$)	5576.525
7434.093 ($[M_4+\text{H}]^+$)	7434.195

C.3 Solvent-Dependent Degree of Aggregation

The mole fraction of aggregated dyes α_{agg} as a function of the solvent composition was calculated according to:

$$\alpha_{agg} \approx \frac{\varepsilon_{mix} - \varepsilon_{mon}}{\varepsilon_{agg} - \varepsilon_{mon}} \tag{C4.1}$$

where ε_{mix} denotes the apparent absorption coefficient of **8** in the respective THF/MCH mixture at 541 nm, and ε_{mon} the absorption coefficient of **8** in pure THF at 541 nm. ε_{agg} corresponds to the absorption coefficient of **B** at 541 nm. As can be seen from Figure C4a the first self-assembled species **B** was most pronounced in THF/MCH ≈ 40 :60 vol% for a concentration of 1.0×10^{-4} M. The sigmoidal fit (Figure C5, ■, dotted curve) has been obtained by using the Sigmoidal function as implemented in Origin 7.5,[145] leading to the critical solvent composition in which the mole fraction of the aggregate is 0.5 (α_{50}) and which can be estimated from such a plot. The transition from **B** to **C** is depicted in Figure C4b.

Likewise, α_{agg} for this process could be calculated (Figure C5, ●, solid green curve) with ε_{mix} denoting the apparent absorption coefficient of **8** in the respective THF/MCH mixture, ε_{mon} representing the absorption coefficient of **B**, and ε_{agg} corresponding to the absorption coefficient of **C** at 541 nm, respectively. These investigations showed that **C** was favored at the highest MCH content, i.e. THF/MCH = 10:90 vol%, at a concentration of 1.0×10^{-4} M. The corresponding α_{50} values are reported in Table C2. Notably, the slope for the transition from **B** to **C** is much steeper than the one from **A** to **B**, as expected for a cooperative process.
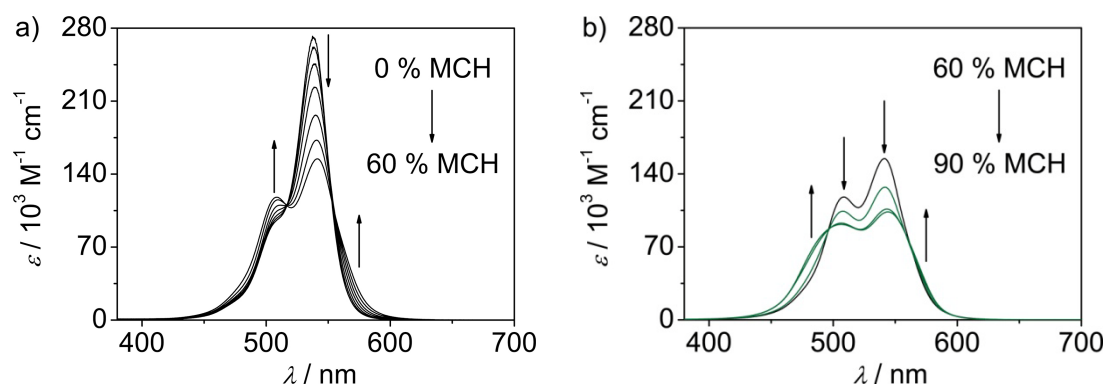
Figure C4. UV/Vis absorption spectra of 1.0×10^{-4} M solutions of dye **8** in various THF/MCH mixtures at 298 K. Arrows indicate changes upon increasing MCH ratio. The MCH content was increased in steps of 10 %. a) Process from **A** to **B** (black curves). b) Process from **B** to **C** (green curves).
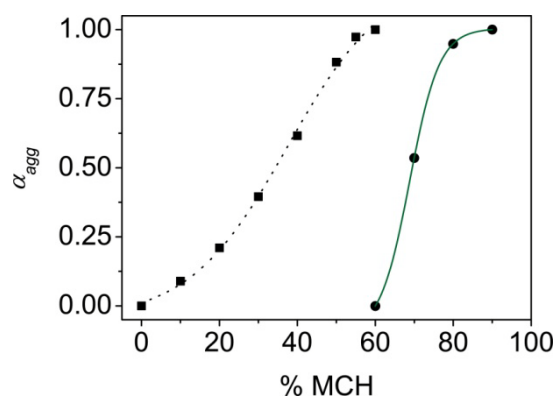
Figure C5. Plot of α_{agg} as a function of the solvent composition (THF/MCH) for a 1.0×10^{-4} M solution of Hamilton-receptor-tethered bis(merocyanine) **8** at 298 K. The sigmoidal fits for the data points were obtained by using the Sigomoidal function as implemented in Origin 7.5.[145] Transitions from **A** to **B** (■, dotted black curve), and from **B** to **C** (●, solid green curve), respectively, are shown.

Table C2. The α_{50} values (% of MCH in THF at which the α_{agg} value is 0.5, $c = 1.0 \times 10^{-4}$ M) for the formation of aggregates **B** and **C**.

	A → B	**B → C**
α_{50}	35	70

The MCH content necessary to obtain a certain self-assembled species varied with the concentration. Since various methods used for characterization of the aggregated species work at a broad concentration range, similar studies have been performed for different concentrations. Such an example is shown in Figure C6.
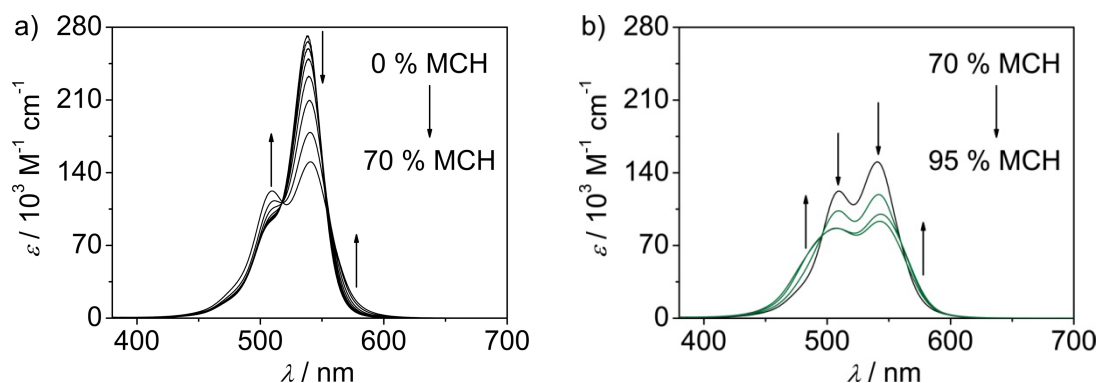

Figure C6. UV/Vis absorption spectra of 1.0×10^{-5} M solutions of dye **8** in various THF/MCH mixtures at 298 K. Arrows indicate changes upon increasing MCH ratio. The MCH content was increased in steps of 10 % from 0 % to 90 % and to 95%. a) Process from **A** to **B** (black curves). b) Process from **B** to **C** (green curves).

C.4 Supplementary NMR Spectra

^{1}H NMR spectra of **A**, **B**, and **C**, respectively, show an increasing peak broadening (Figure C7). DOSY NMR was employed to gain insight into the size of species **C** (Figure C8). The diameter was calculated from the average diffusion coefficient using the Stokes-Einstein-relation (equation (C4.2)):

$$D = \frac{k_B T}{6\pi\mu R_0}$$
(C4.2)

where D represents the diffusion coefficient in $\text{m}^2\,\text{s}^{-1}$, k_B is the Boltzmann factor, and T denotes the temperature in K, while μ corresponds to the dynamic viscosity of the solvent in $\text{kg m}^{-1}\,\text{s}^{-1}$, and R_0 to the hydrodynamic radius of the aggregate in meter. With an average diffusion coefficient of $D = 8.7 \times 10^{-11}\ \text{m}^2\,\text{s}^{-1}$, a diameter of $2R_0 = 9.0$ nm was obtained which is in good accordance with the DLS data.

THF

A

THF/MCH = 50:50 vol%

B

THF/MCH = 10:90 vol%

C

δ / ppm
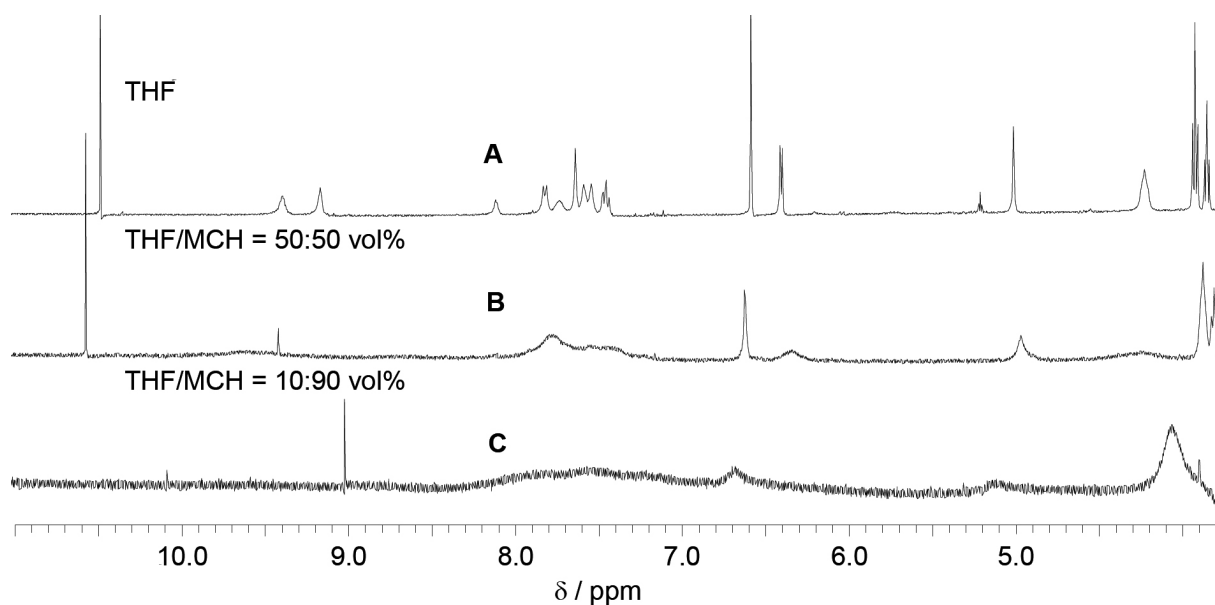
***Figure C7.*** Sections of the 400 MHz ^{1}H NMR spectra of 1.0×10^{-3} M solutions of dye **8** in different mixtures of THF-d_8/MCH-d_4 at 298 K corresponding to **A** and aggregates **B**, and **C**, respectively.


log (D / m^{2}s^{-1})

δ / ppm
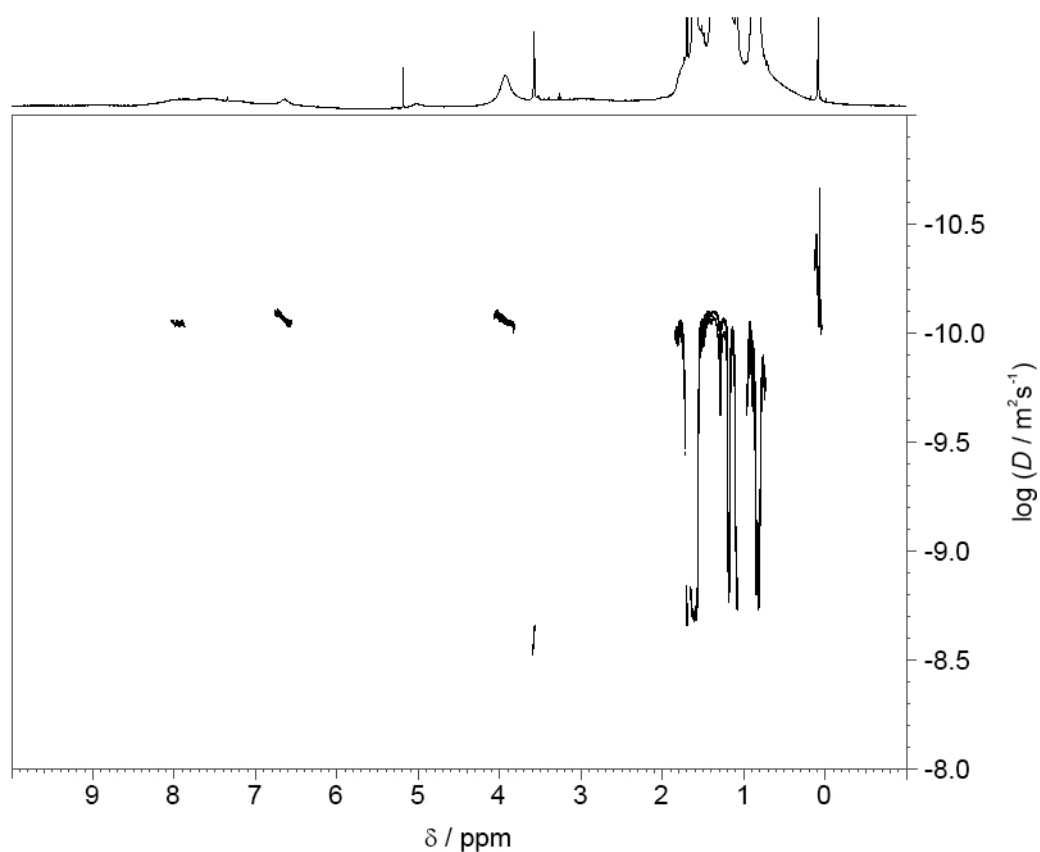
Figure C8. DOSY NMR spectra of **C** (c(**8**) = 1.0×10^{-3} M) in THF-d_8/MCH-d_{14} = 10:90 vol%. The diffusion coefficients D (m^2 s^{-1}) are plotted in a logarithmic scale against chemical shift δ (ppm).

C.5 Concentration-Dependent Formation of Supramolecular Polymers B and D
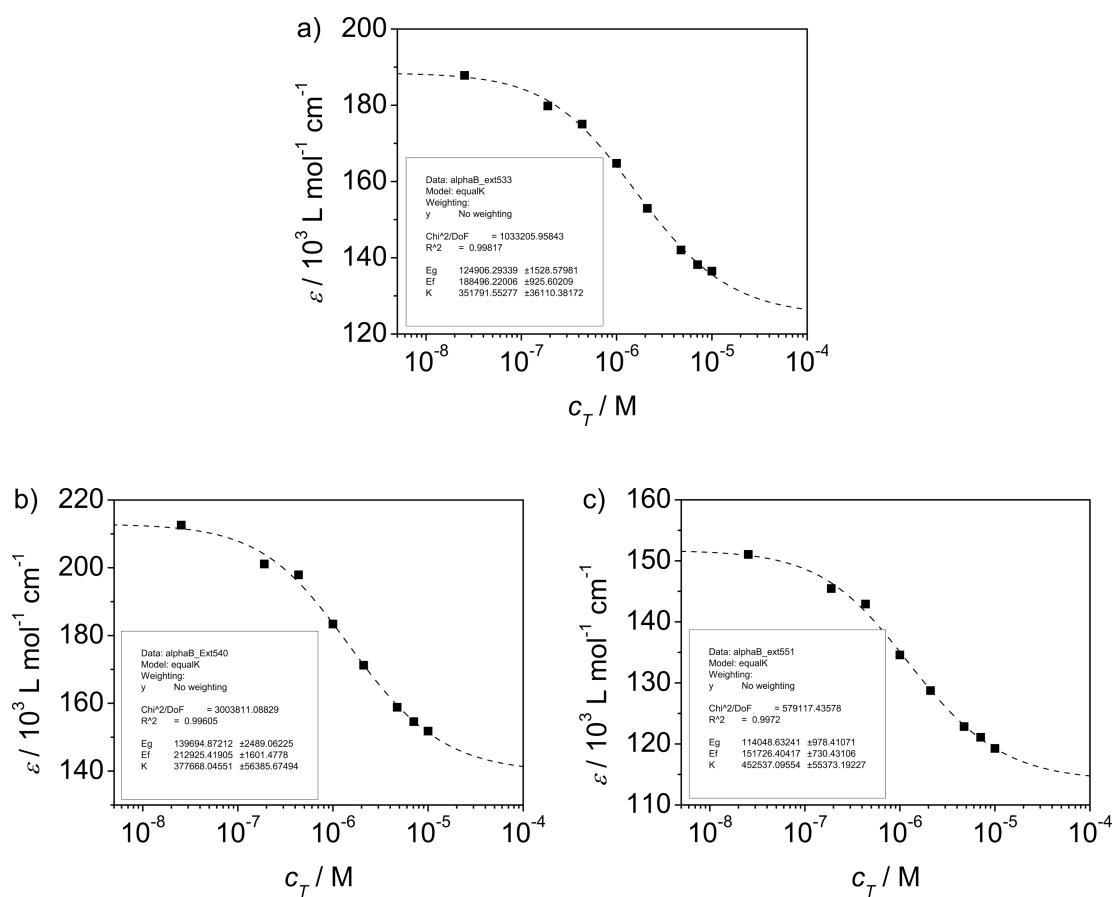
Figure C9. Apparent absorption coefficients of solutions of **8** in THF/MCH = 30:70 vol% at 533 nm (a), 540 nm (b), and 551 nm (c) plotted against c_T and the corresponding result of the nonlinear regression analysis based on the isodesmic model.
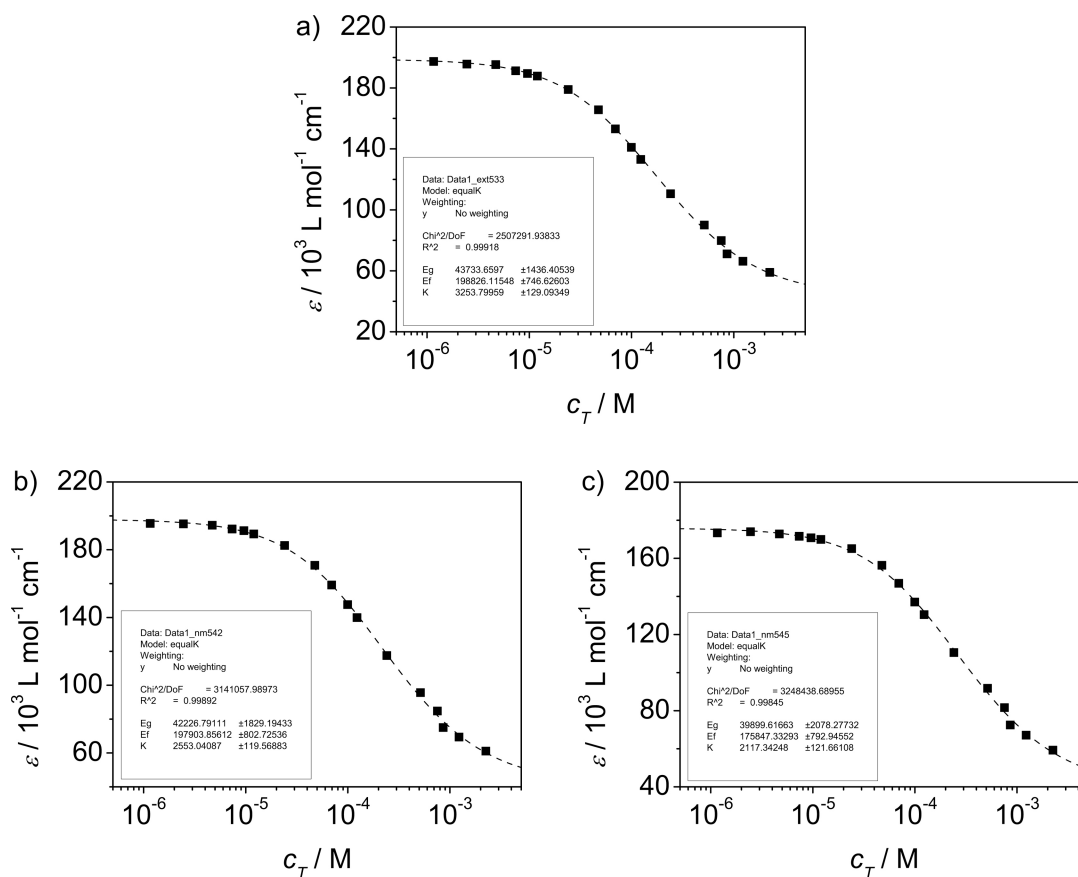
Figure C10. Apparent absorption coefficients of solutions of complex **8:9** in THF/MCH = 20:80 vol% at 533 nm (a), 542 nm (b), and 545 nm (c) plotted against c_T and the corresponding result of the nonlinear regression analysis based on the isodesmic model.

Table C3. Calculated number and weight-averaged degrees of polymerization DP_N and DP_W for species **B** (THF/MCH = 30:70 vol%) and **D** (THF/MCH = 20:80 vol%), respectively, at 298 K and different concentrations *c* in the respective THF/MCH mixture.

|	**B**		**D**	
c	DP_N	DP_W	DP_N	DP_W
10^{-5} M	2.5	4.1	1.0	1.1
10^{-4} M	6.8	13	1.2	1.5
10^{-3} M	20 [a]	40 [a]	2.3	3.5
10^{-2} M	63 [a]	125 [a]	5.8	11

[a] Hypothetical values owing to the collapse of supramolecular polymers **B** to inverted micelles **C** at high concentrations.

C.6 Temperature-Dependent Formation of Supramolecular Polymers B and D

The transitions from **A** to **B**, and from **AG** to **D**, respectively, were studied by temperature-dependent UV/Vis spectroscopy. Note that for these experiments conditions were applied where only small oligomers are present, i.e. the initial process of aggregation can be followed by UV/Vis spectroscopy. Figures C11 and C12 depict the temperature-dependent UV/Vis spectra for **B** (c = 0.9 x 10^{-5} M, THF/MCH = 30:70 vol%), and **D** (c = 2.0 x 10^{-4} M, THF/MCH = 20:80 vol%), respectively.
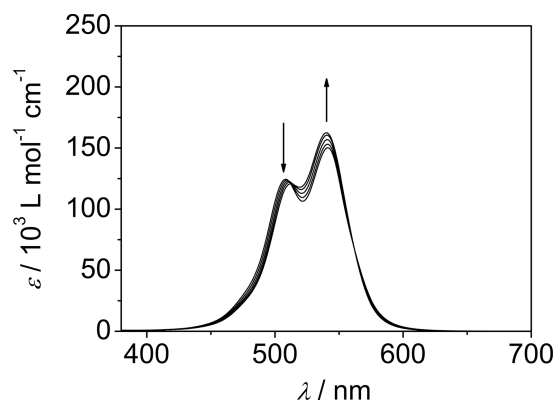
Figure C11. Temperature-dependent UV/Vis spectra of **8** in THF/MCH = 30:70 vol% (c = 0.9 x 10^{-5} M) from 10 °C to 50 °C in steps of 10 °C. Arrows indicate the spectral changes upon increasing temperature.
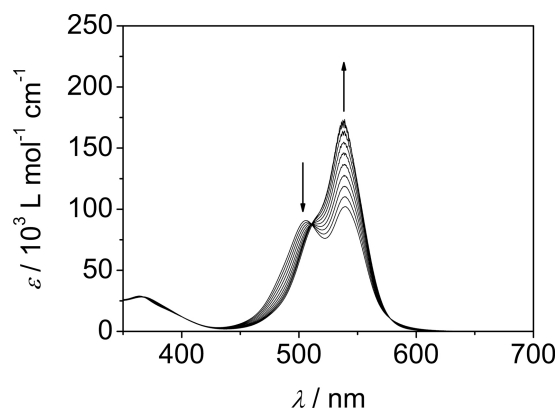
Figure C12. Temperature-dependent UV/Vis spectra of complex **8:9** (**AG**) in THF/MCH = 20:80 vol% (c = 2.0 x 10^{-4} M) from 10 °C to 55 °C in steps of 5 °C. Arrows indicate the spectral changes upon increasing temperature.

The mole fraction of the aggregated species $\alpha_{agg}(T)$ at each temperature was estimated according to equation (C4.3):

$$\alpha_{agg}(T) \approx \frac{\varepsilon(T) - \varepsilon_{mon}}{\varepsilon_{agg} - \varepsilon_{mon}} \tag{C4.3}$$

with $\alpha_{agg}(T)$ being the mole fraction of aggregate at each temperature, and $\varepsilon(T)$, ε_{agg}, and ε_{mon} being the apparent absorption coefficients of the mixture, the absorption coefficient of the aggregate, and the monomer, respectively. The absorption coefficients of pure monomer and aggregate were determined by extrapolation of the measured apparent absorption coefficients to their asymptotic values at high and low temperature. By applying the temperature-dependent isodesmic model to a plot of $\alpha_{agg}(T)$ against the temperature, the molar enthalpy of aggregate formation ΔH and T_m can be calculated:[23d,28]

$$\alpha_{agg}(T) \cong \frac{1}{1 + \exp\left(-0.908\Delta H \dfrac{T - T_m}{RT_m^2}\right)} \tag{C4.4}$$

The number-averaged degree of polymerization DP_N is related to $\alpha_{agg}(T)$ by:

$$DP_N = \frac{1}{\sqrt{1 - \alpha_{agg}(T)}} \tag{C4.5}$$

Fitting equation (C4.4) to the experimental data for **B** (Figure C13), and **D** (Figure C14), respectively, yielded ΔH and subsequently ΔS and DP_N. The values are summarized in Table C4. For a more detailed description of the equations used to calculate the respective values, see Chapter 2.
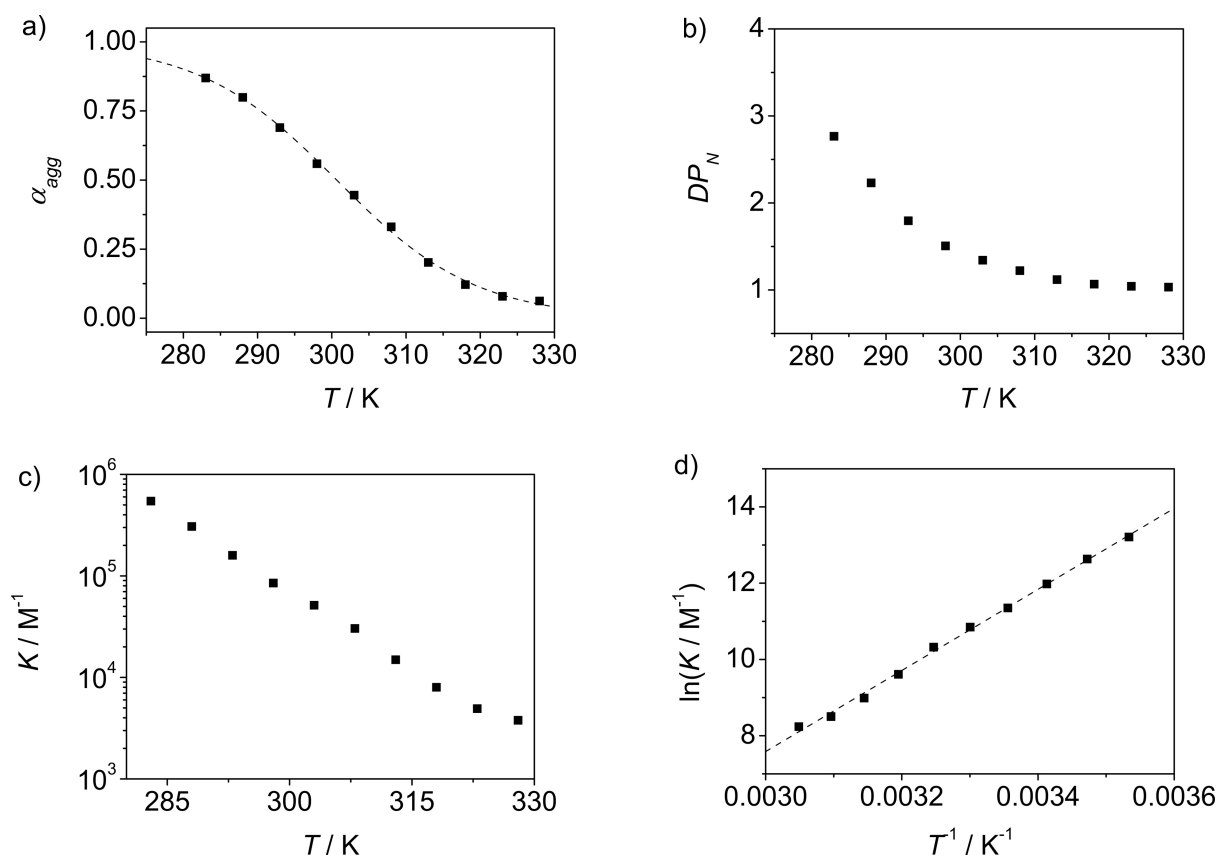
Figure C13. a) Temperature-dependent degree of aggregation $\alpha_{agg}(T)$ for the formation of **B** calculated from the apparent UV/Vis absorption coefficient at 541 nm and the corresponding fit based on the isodesmic model (dashed line). b) Number-averaged degree of polymerization (DP_N) as a function of the temperature. c) Equilibrium constant (K) as a function of the temperature. d) Van't Hoff plot for the self-assembly of **8** in THF/MCH = 30:70 vol%.
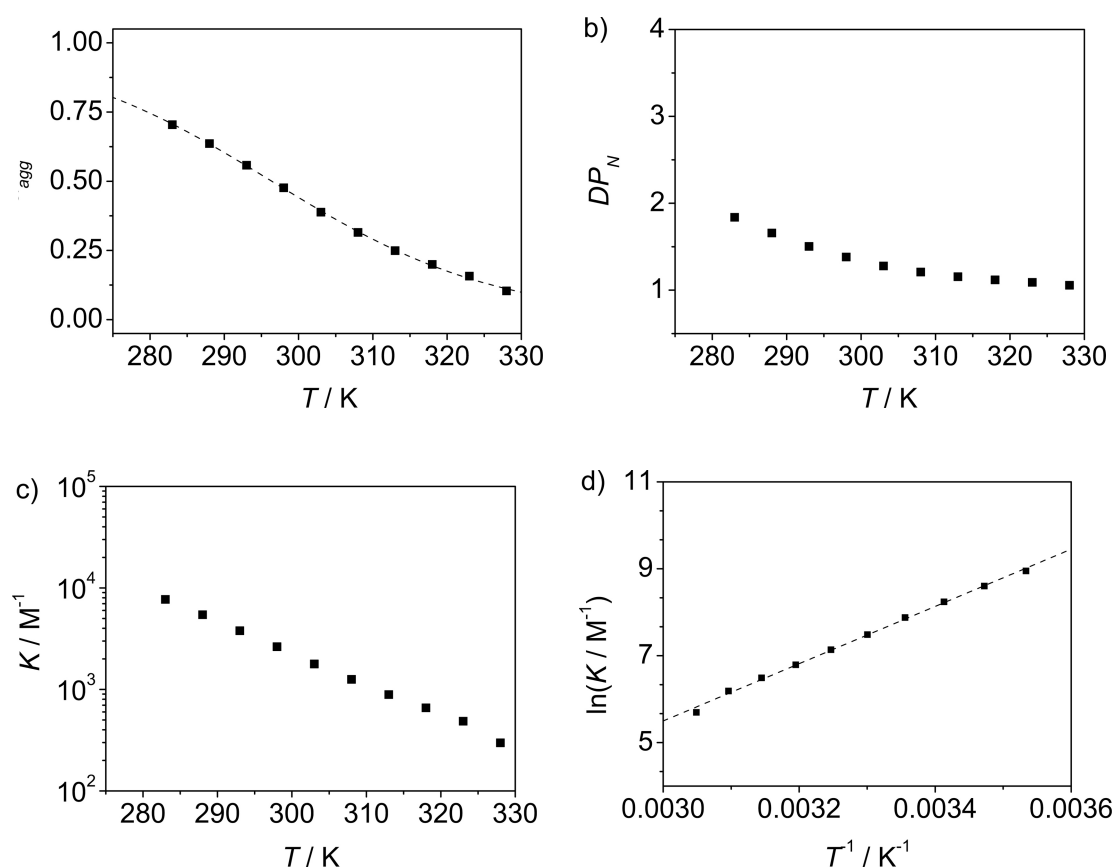
Figure C14. a) Temperature-dependent degree of aggregation (α_{agg}) for the formation of **D** calculated from the apparent UV/Vis absorptions coefficient at 500 nm and the corresponding fit based on the isodesmic model (dashed line). b) Number-averaged degree of polymerization (DP_N) as a function of the temperature. c) Equilibrium constant K as a function of the temperature. d) Van't Hoff plot for the self-assembly of **8:9** in THF/MCH = 20:80 vol%.

Table C4. Thermodynamic parameters K (M^{-1}), T_m (K), ΔH (kJ mol^{-1}), ΔS (J mol^{-1} K^{-1}), and DP_N obtained from the temperature-dependent self-assembly of **8** (c = 0.9 x 10^{-5} M, THF/MCH = 30:70 vol%), and **8:9** (c = 2.0 x 10^{-5} M, THF/MCH = 20:80 vol%), leading to **B** and **D**, respectively, based on the isodesmic model.

Aggregate	K^a	T_m	ΔH	ΔS	DP_N ^{a,b}
B	0.85 x 10^5	301	−88.6	−203	3.5
D	2.6 x 10^3	296	−52.8	−112	1.2

^{a} Values determined at 298 K. ^{b} Calculated for c = 1.0 x 10^{-4} M.

C.7 Concentration-Dependent Formation of Inverted Micelles C

The equation used for the fitting procedure of the concentration-dependent formation of **C** is given in the main text. Plots of α_{agg} against log $K'c_T$ for several combinations of σ, K, EM, and N were calculated and the experimental data in THF/MCH = 20:80 vol% was fitted manually for the best match (Figure C15). Such a procedure was employed recently to fit concentration-dependent UV/Vis data of perylene bisimides to the K_2–K model.[45]
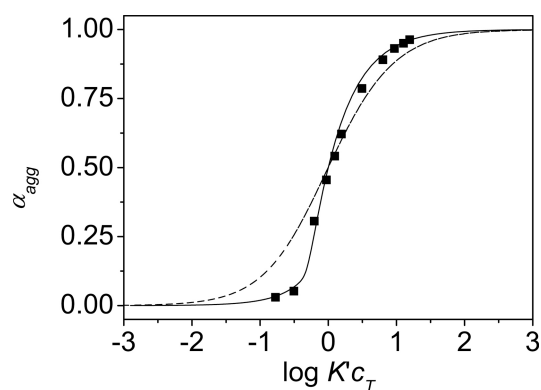
Figure C15. Fraction of aggregated molecules α_{agg} plotted as a function of log $K'c_T$ according to the isodesmic model (dashed curve) and to the self-assembly of a closed oligomer (solid curve) and plot of the experimental data at 507 nm for the formation of **C** after manual fit of the line shape. The black curve was calculated with the following parameter values: $\sigma = 0.25$, $K = 0.9 \times 10^5$ M^{-1}, $EM = 1.2 \times 10^5$ M, and $N = 21$.
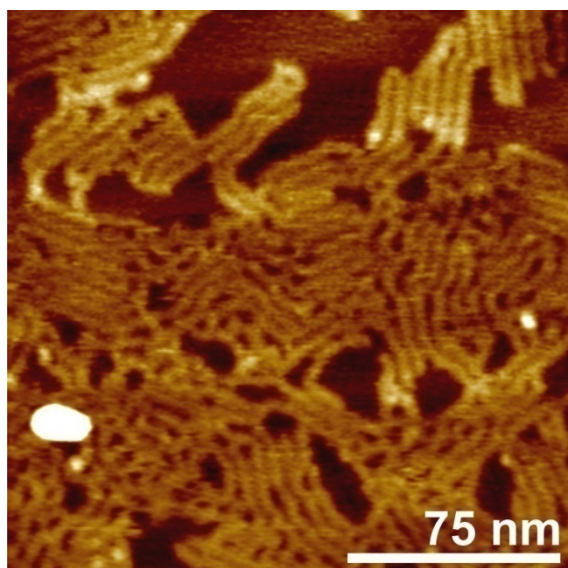
C.8 Supplementary Dynamic Light Scattering Data
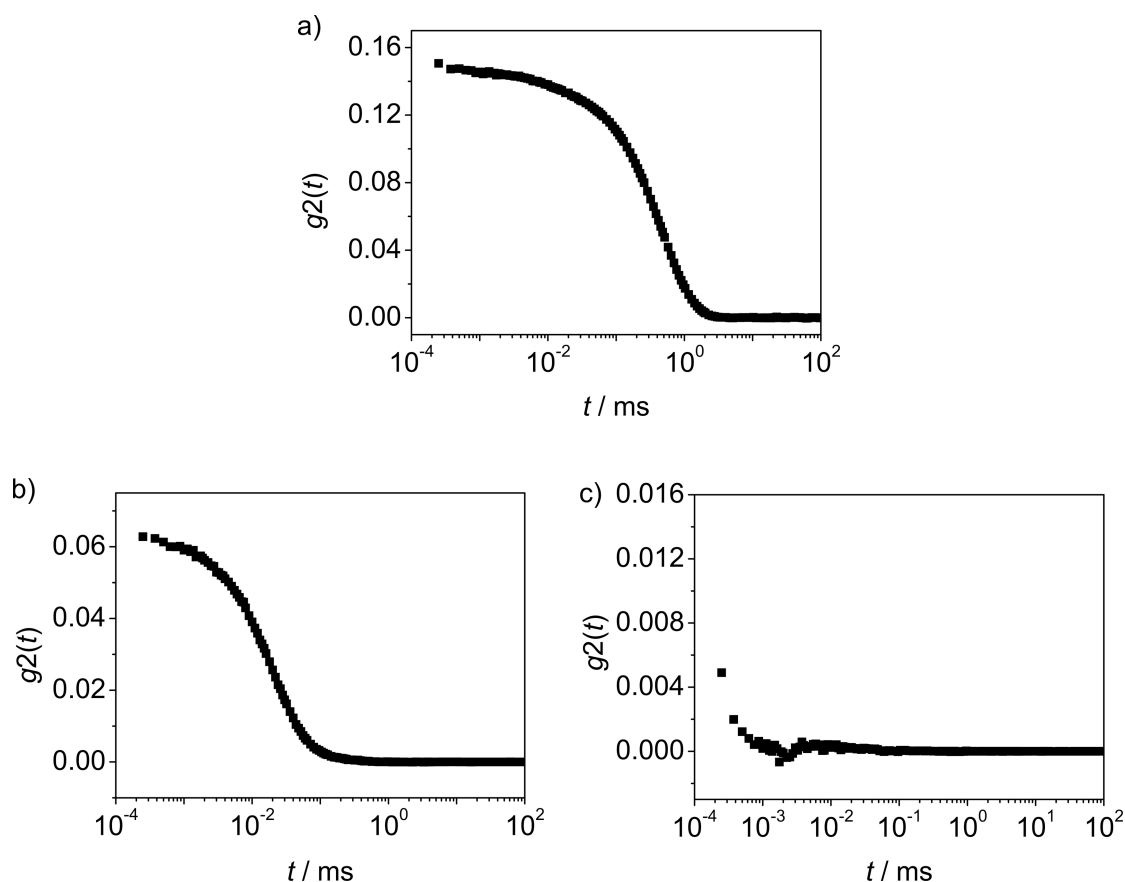
Figure C16. Autocorrelation functions *g2*(*t*) of a) **B** (THF/MCH = 50:50 vol%, *c*(**8**) = 1.0 x 10^{-3} M, 298 K) b) **C** (THF/MCH = 10:90 vol%, *c*(**8**) = 1.0 x 10^{-3} M, 298 K) c) **D** (THF/MCH = 20:80 vol%, *c*(**8**) = 1.0 x 10^{-3} M, 298 K) plotted against the delay time *t* for scattering angles of 90°.

C.9 Titration Experiments

The complex formation by sixfold hydrogen-bonding between Hamilton-receptor-ligated bis(merocyanine) **8** and guest **9** is shown in Scheme C1. Figure 8 in the main text depicts constant host 1:1 UV/Vis titration experiments for **8** and **9** carried out in CHCl$_3$. Owing to the better sensitivity of the barbituric acid dye **9** on hydrogen bond formation, the role of the guest and the host were interchanged. Constant host titrations were carried out by adding **8** (dissolved at high concentrations in a solution of **9**) to solutions of **9** (see Materials and methods section for experimental details). The binding constant was calculated by fitting equation (C4.6a) to the absorption at different wavelengths and averaging over the obtained values.[103] The derivation of this equation is given in the section C.10.

$$A_{obs} = A_A + \frac{A_{AB} - A_A}{2c_A^0}\left(c_A^0 + c_B^0 + \frac{1}{K_{ass}} \pm \sqrt{\left(c_A^0 + c_B^0 + \frac{1}{K_{ass}}\right)^2 - 4c_A^0 c_B^0} \right) \qquad \text{(C4.6a)}$$

Scheme C1. Complex formation between Hamilton-receptor-tethered bis(merocyanine) **8** and barbiturate dye **9**.

Figure C17. a) UV/Vis absorption spectra of **C** ($c(\mathbf{8})$ = 0.8 x 10^{-5} M, THF/MCH = 5:95 vol%) at 298 K without and with 1 equivalent of guest **9** after 2 min and after 3 d. b) Apparent absorption at 541 nm plotted against the time.
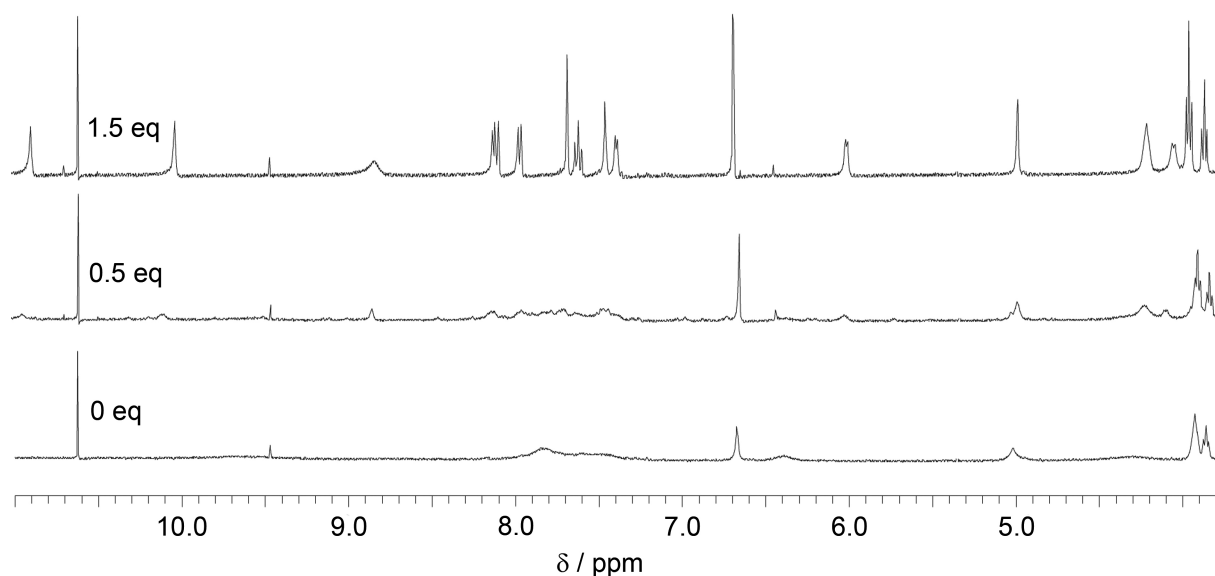
Figure C18. AFM image of a sample 3 d after addition of 1 equivalent of **9** (relating to the total concentration of **8**) to inverted micelles **C**.
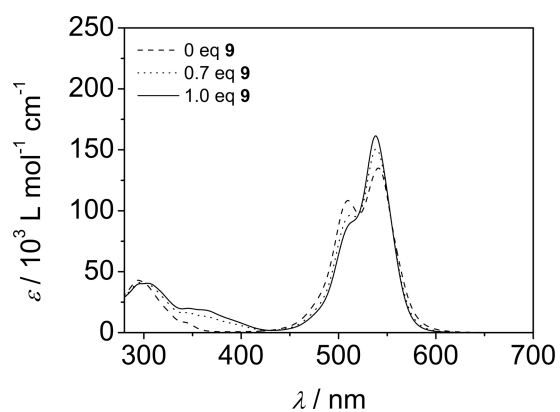
Figure C19. UV/Vis absorption spectra of **B** ($c(\mathbf{8})$ = 1.0 x 10^{-5} M, THF/MCH = 30:70 vol%) at 298 K with different ratios of guest **9**.

Figure C20. Sections of 400 MHz ^{1}H NMR spectra of supramolecular polymers **B** ($c(\mathbf{8})$ = 1.0 x 10^{-3} M, THF/MCH = 50:50 vol%) at 298 K with different ratios of guest **9**.

C.10 Determination of Binding Constants by 1:1 UV/Vis Titration Experiments

The formula described in this section was used to determine binding constants of 1:1 complexes *AB* in cases where the amount of free and bound species are not directly determinable.[103] Bound and unbound species have to exhibit distinct spectral features observable throughout the whole experiment.

Considering an equilibrium between two molecules *A* and *B* capable of binding each other one obtains:
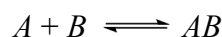
$$A + B \rightleftharpoons AB$$

$$K_{ass} = \frac{[AB]}{[A][B]} \tag{C4.7}$$

A quadratic equation follows for $[AB]$ from the Law of Mass Action:

$$[AB] = K_{ass}[A][B] \tag{C4.8}$$

$$[AB] = K_{ass}(c_A^0 - [AB])(c_B^0 - [AB]) \tag{C4.9}$$

$$[AB] = K_{ass}c_A^0 c_B^0 - K_{ass}(c_A^0 - c_B^0)[AB] + K_{ass}[AB]^2 \tag{C4.10}$$

$$[AB] = \frac{c_A^0 + c_B^0 + \frac{1}{K_{ass}} \pm \sqrt{\left(c_A^0 + c_B^0 + \frac{1}{K_{ass}}\right)^2 - 4c_A^0 c_B^0}}{2} \tag{C4.11}$$

131

while c_A^0 and c_B^0 are the initial concentrations of species A and B. Data from UV/Vis absorption spectroscopy can be evaluated by using either absorbance A or absorption coefficient ε at a distinct wavelength. The fraction of bound species can be expressed by:

$$\frac{[AB]}{c_A^0} = \frac{A_{obs} - A_A}{A_{AB} - A_A} = \frac{\varepsilon_{obs} - \varepsilon_A}{\varepsilon_{AB} - \varepsilon_A} \tag{C4.12}$$

where index *obs* means the value for absorbance A and absorption coefficient ε actually observed for the sample and indices A and AB are the values of the free and the bound species, respectively. Combination of equations (C4.11) and (C4.12) gives the formula used for the nonlinear curve fitting procedure:

$$A_{obs} = A_A + \frac{A_{AB} - A_A}{2c_A^0}\left(c_A^0 + c_B^0 + \frac{1}{K_{ass}} \pm \sqrt{\left(c_A^0 + c_B^0 + \frac{1}{K_{ass}}\right)^2 - 4c_A^0 c_B^0}\right) \tag{C4.6a}$$

$$\varepsilon_{obs} = \varepsilon_A + \frac{\varepsilon_{AB} - \varepsilon_A}{2c_A^0}\left(c_A^0 + c_B^0 + \frac{1}{K_{ass}} \pm \sqrt{\left(c_A^0 + c_B^0 + \frac{1}{K_{ass}}\right)^2 - 4c_A^0 c_B^0}\right) \tag{C4.6b}$$

with K_{ass}, A_A, and A_{AB} or K_{ass}, ε_A, and ε_{AB}, respectively, as fitting parameters. The correct values are obtained for the negative expression.
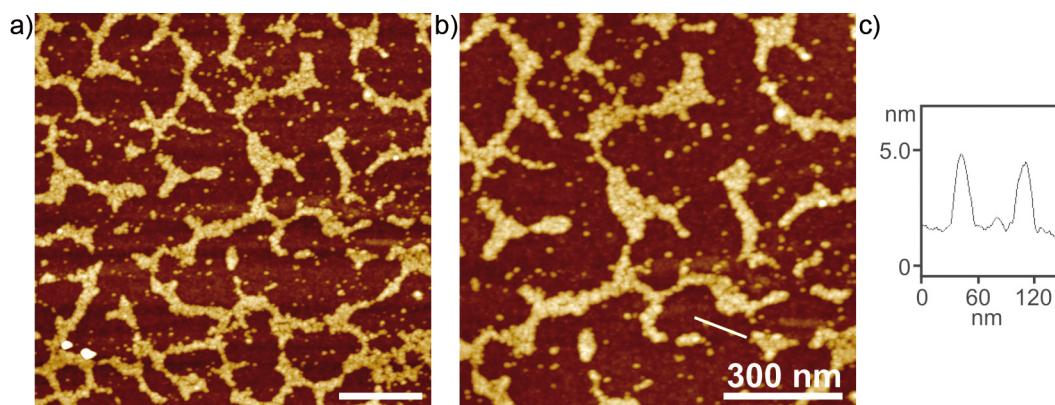
The Levenberg-Marquard algorithm as implemented in the program package Origin 7.5[145] was used for the curve fitting with equations (C4.6a) and (C4.6b).

### *C.11 Supplementary AFM Images*
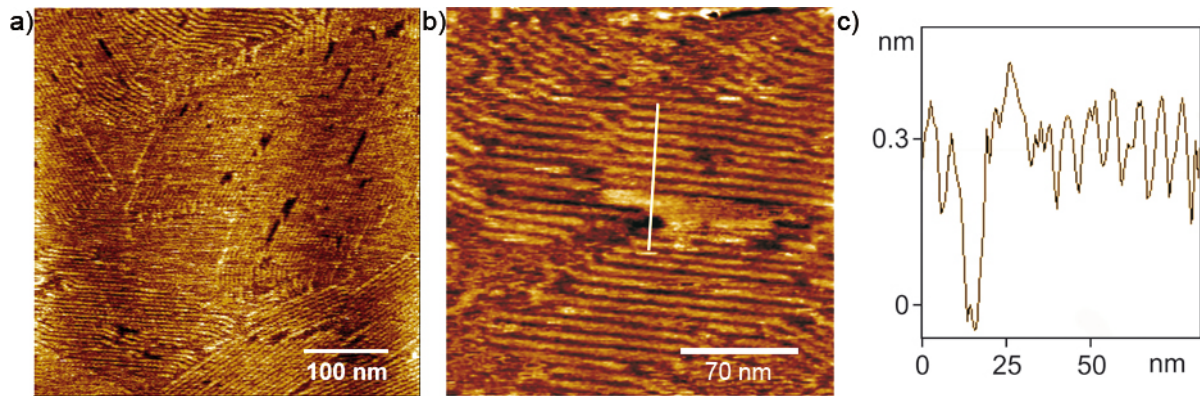
Figure C21. a, b) AFM height images of spin-coated samples of **B** (4000 rpm, $c(\mathbf{8}) = 1.0$ x 10^{-5} M, THF/MCH = 30:70 vol%, 298 K) on HOPG. c) Cross-section along the white line in panel b.

Figure C22. a, b) AFM height images of samples prepared by spin-coating of solutions of Hamilton-receptor-ligated bis(merocyanine) **8** ($c(\mathbf{8})$ = 1.0 x 10^{-5} M, THF/MCH = 5:95 vol%, 298 K) on Si-wafer. c) Cross-section along the white line in panel b.
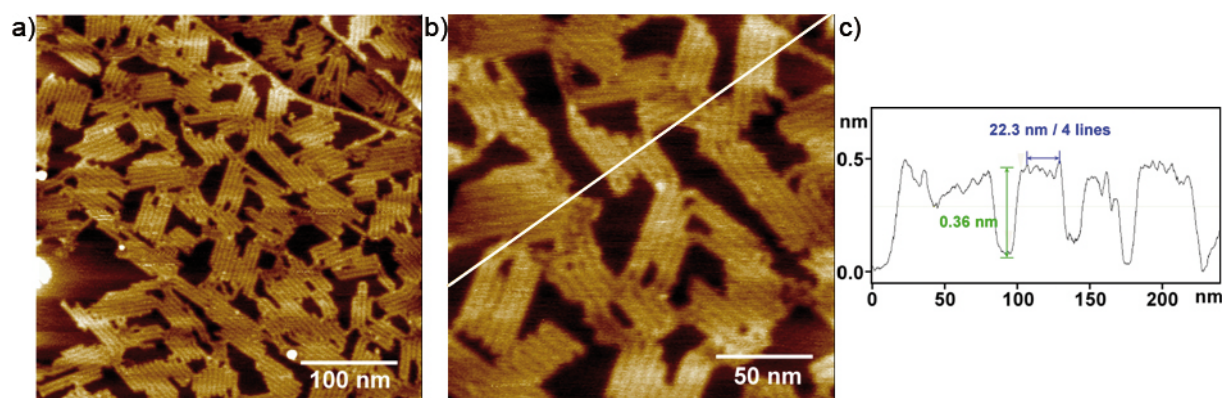
Figure C23. a, b) AFM height images of spin-coated samples of **D** (4000 rpm, $c(\mathbf{8})$ = 1.0 x 10^{-5} M with 1 equivalent of guest **9**, THF/MCH = 5:95 vol%, 298 K) on HOPG. c) Cross-section along the white line in panel b.
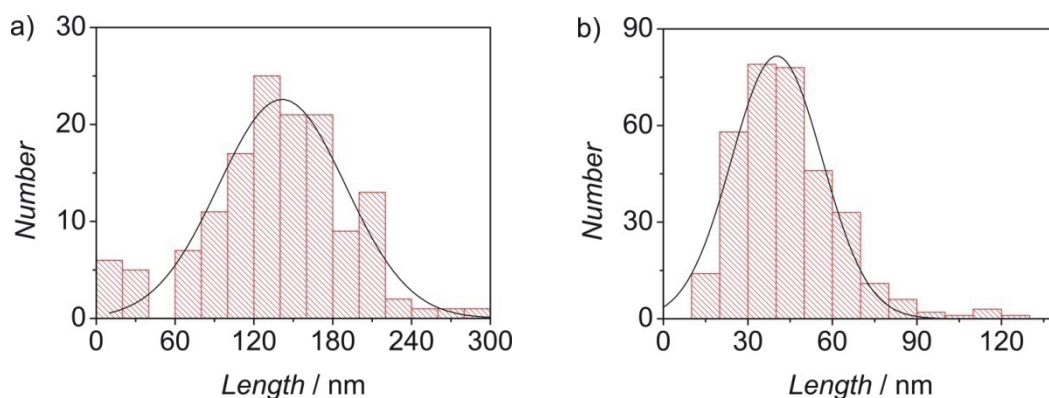
Figure C24. a) Histogram of the lengths of 140 fibrils of **B**. b) Histogram of the lengths of 100 fibrils of **D**. The fits were obtained using the Boltzmann function as implemented in Origin 7.5[145].

C.12 Molecular Modeling

The proposed structures of **B** and **D** optimized on force field level (MM+, HyperChem 8.05[128]) are shown in Figure C25. Comparison of the lateral dimensions with the results obtained from AFM on HOPG suggested monolayers and interpenetration of the peripheral alkyl chains between two chains.
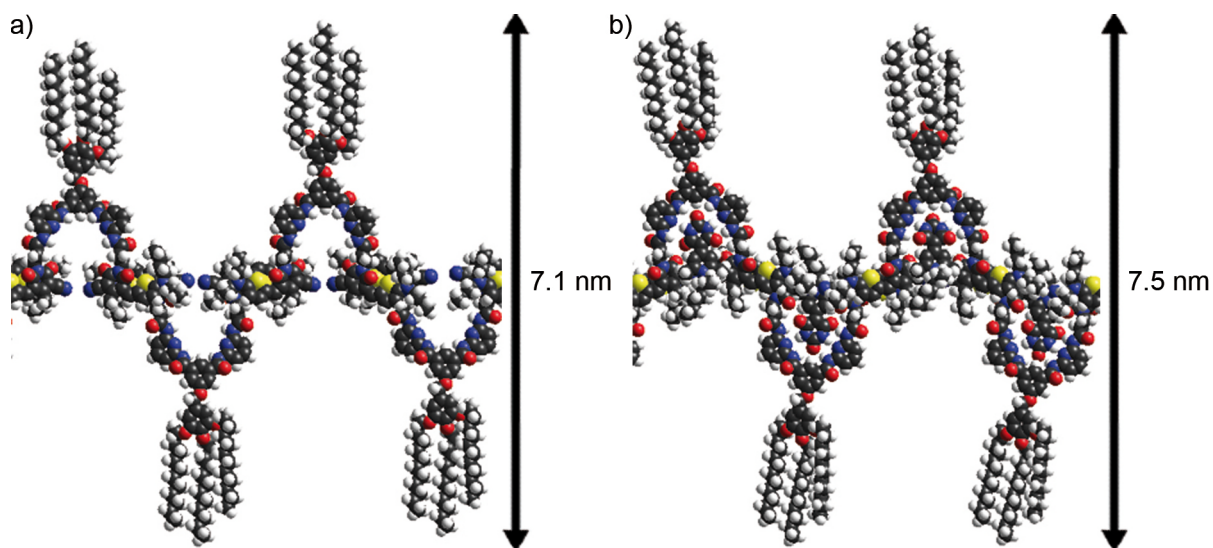
Figure C25. MM+ geometry-optimized model for aggregated species **B** (a) and **D** (b), consisting of four molecules of **8**, or four complexes **8:9**, respectively, held together by dipole-dipole interactions between the merocyanine dye units of **8**.

D Supplement for Chapter 5

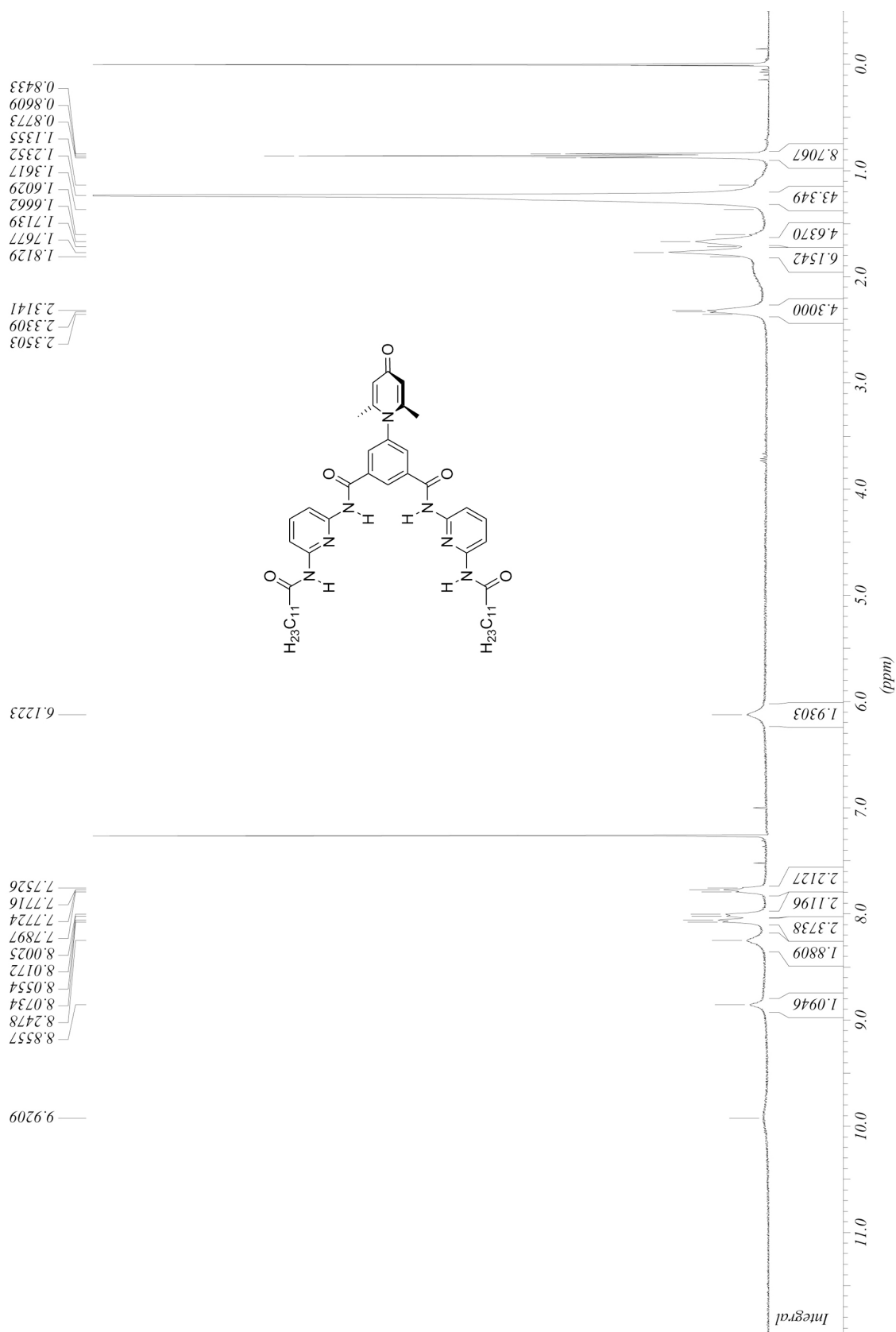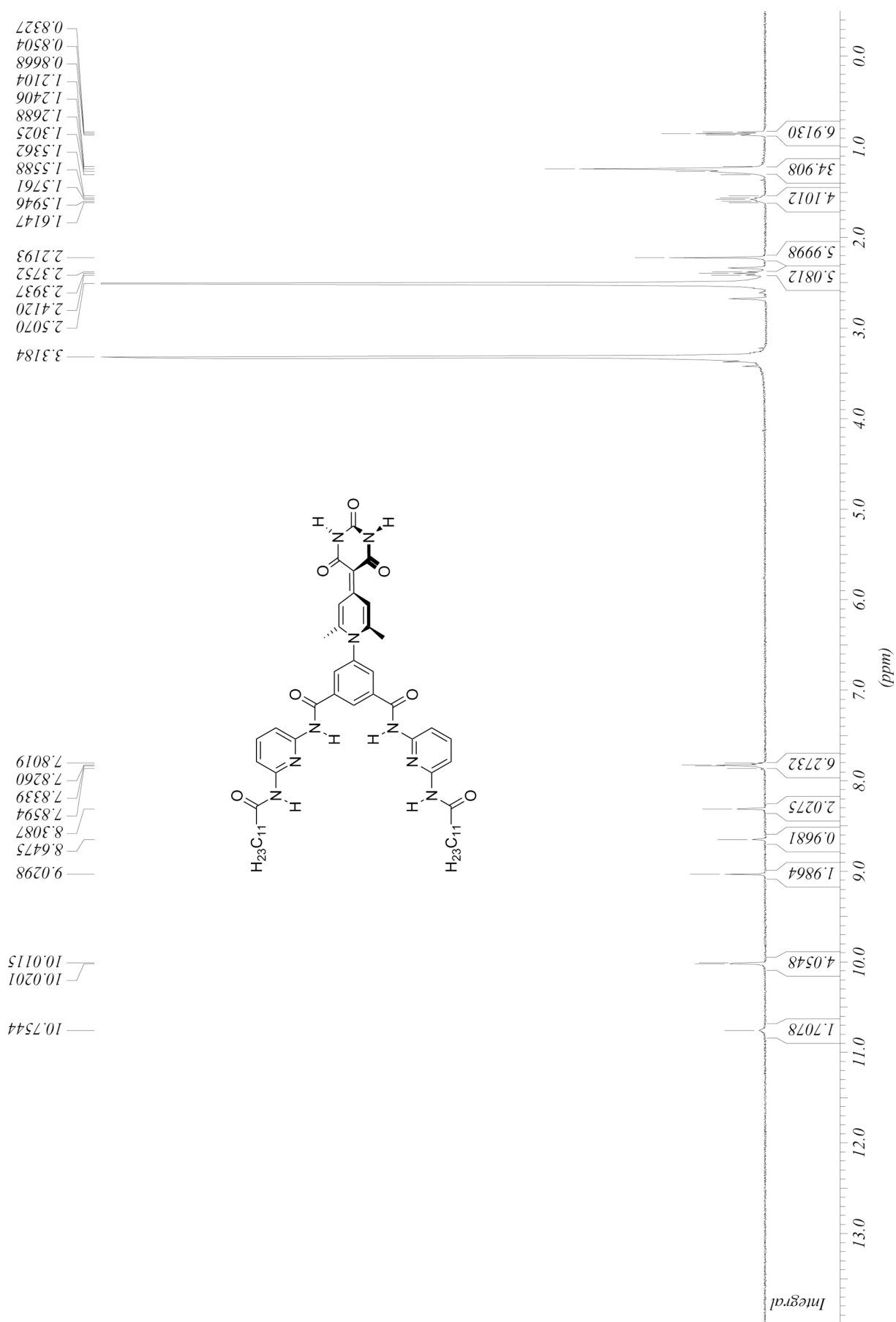## *D.1 Supplementary NMR Spectroscopic Data*

Figure D1. ^{1}H NMR spectrum of pyridone precursor **8** in CDCl$_3$.

Figure D2. ^{1}H NMR spectrum of self-complementary Hamilton-receptor-functionalized merocyanine dye **1** in DMSO-d_6.

Table D1. Complete assignment of the proton signals of Hamilton-receptor-functionalized merocyanine dyes **1** and **12** in $CDCl_3$ and DMSO-d_6.

position	12	1		
	$CDCl_3$	DMSO	$CDCl_3$	
	δ_H (J / Hz)	δ_H (J / Hz)	δ_H (J / Hz)	$\Delta\delta_H$ [b,c]
1, 1'	-	10.75 (s, 2H)	10.78 (s, 2H)	-
1a, 1a'	3.98 (t, 7.7, 4H)	-	-	-
1b, 1b'	1.68 (m, 4H)	-	-	-
1c, 1c'	1.42 (m, 4H)	-	-	-
1d, 1d'	0.96 (t, 7.4, 6H)	-	-	-
2, 2'	9.17 (s, 2H)	9.03 (s, 2H)	9.23[a] (m, 2H)	0.06
3, 3'	2.19 (s, 6H)	2.22 (s, 6H)	2.30 (br s, 6H)	0.11
4, 4'	8.02 (s, 2H)	8.31 (s, 2H)	8.10[a] (m, 2H)	0.08
5	8.69 (s, 1H)	8.65 (s, 1H)	9.08[a] (m, 1H)	0.39
6, 6'	8.52 (s, 2H)	10.02 (s, 2H)	12.12[a] (m, 2H)	3.60
7, 7'	8.00 (d, 8.1, 2H)	7.83 (m, 2H)	7.92 (d, 9.0, 1H)	−0.08
			7.90 (d, 7.8, 1H)	−0.10
8, 8'	7.83 (t, 8.1, 2H)	7.83 (m, 2H)	7.86 (t, 8.1, 2H)	0.03
9, 9'	8.05 (d, 8.0, 2H)	7.83 (m, 2H)	8.25 (d, 7.8, 2H)	0.20
10, 10'	7.60 (s, 2H)	10.02 (s, 2H)	10.82[a] (m, 2H)	3.22
11, 11'	2.39 (t, 7.4, 4H)	2.39 (t, 7.4, 4H)	2.62 (br, 4H)	0.23
12, 12'	1.79 (m, 4H)	1.58 (m, 4H)	1.74 (br, 4H)	−0.05
13, 13'	1.03 (t, 7.4, 6H)	1.24 (br, 32H)	1.36 (br, 4H)	-
14, 14'	-		1.29 (br, 4H)	-
15-20, 15'-20'	-		1.18 (br, 24H	-
21, 21'	-	0.85 (t, 6.8, 6H)	0.81 (t, 7.0, 6H)	−0.22[d]

[a] Estimated value due to partial overlap or broadening of signals. [b] Chemical shift difference $\Delta\delta_H$ of the respective protons of **1** and **12** in $CDCl_3$ (c = 5.0 x 10^{-4} M). [c] The centers of the multiplets for some protons of **1** were used to calculate the shifts. [d] $\Delta\delta_H$ between protons at positions 13 and 21 of **12** and **1**, respectively.

D.2 Mass Spectrometric Studies[i]
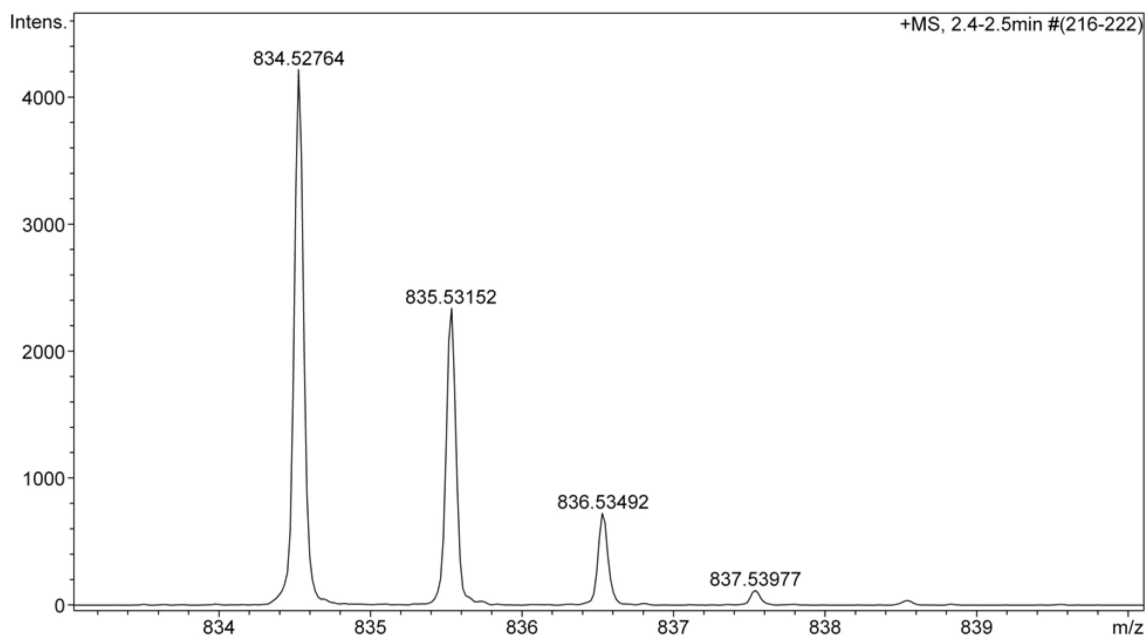
Figure D3. HRMS ESI (positive mode, $CH_3CN/CHCl_3$ = 1:1 vol%) of **8**.
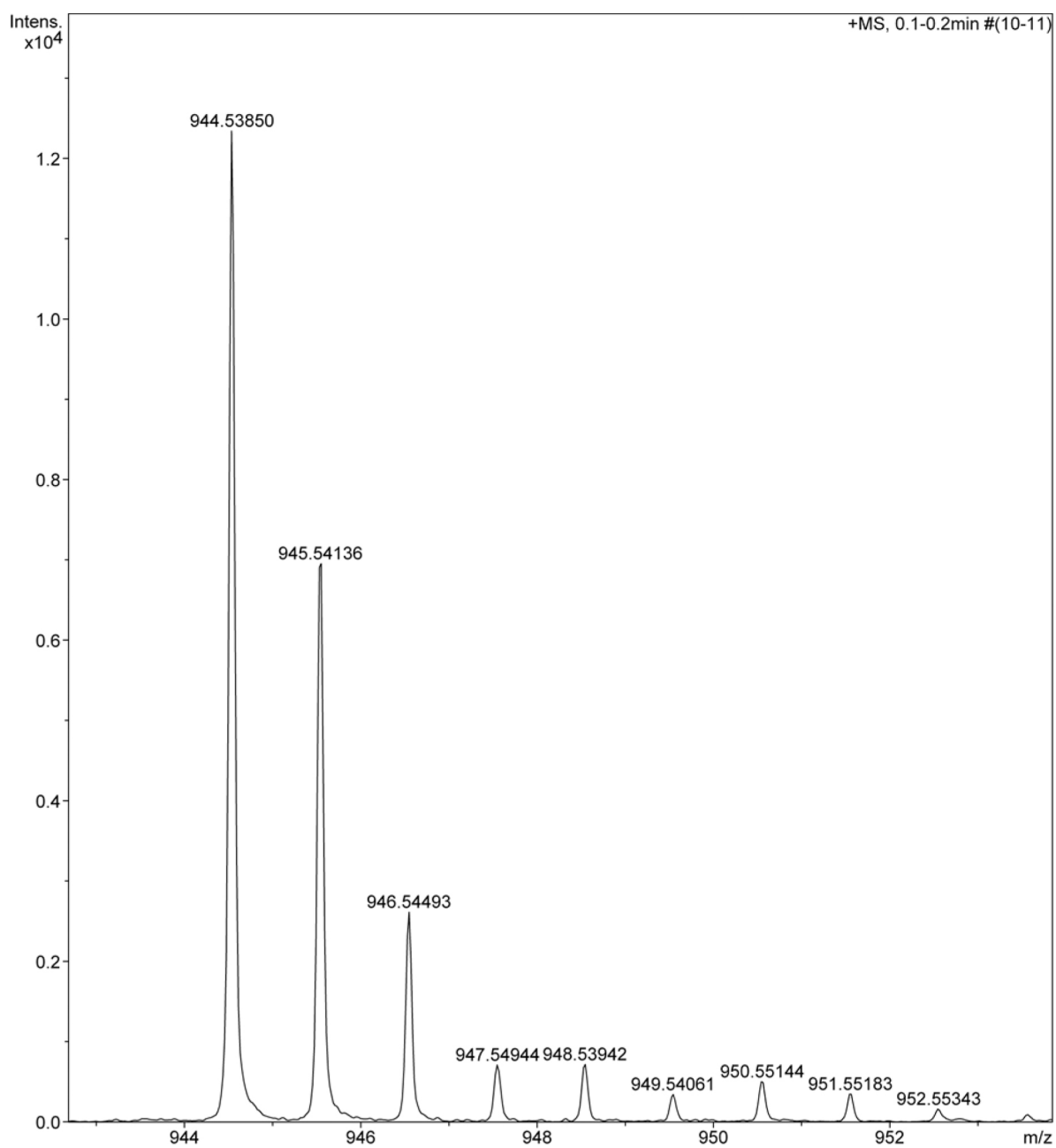

Figure D4. HRMS ESI (positive mode, CHCl$_3$/THF = 1:1 vol%) of **1**.

MALDI-TOF was measured on samples prepared by solvent evaporation from $CHCl_3$ solutions ($c = 1.0 \times 10^{-3}$ M) containing 2-[(2*E*)-3-(4-*tert*-butylphenyl)-2-methylprop-2-enyliden]malononitrile (DCTB) as matrix. Peaks corresponding to the radical cations of monomer and dimer are depicted in Figure D5. The spectrum and the respective calibration were both smoothed using the gauss algorithm (cycles = 1, *m/z* width = 0.5, gauss parameter = 5). Notably, the charged dimer could only be observed with the spectrometer working in linear mode. Solely the radical cation of the monomer was detected in the reflection mode, indicating that the charged assembled species are rather unstable.
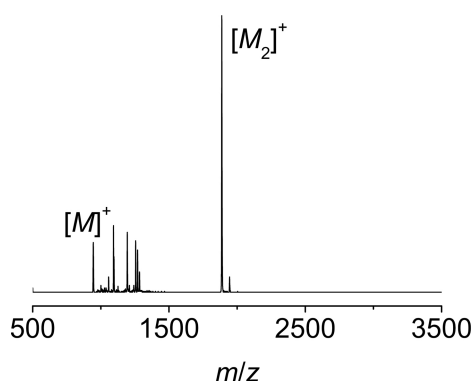
Figure D5. MALDI-TOF spectrum of a sample prepared from a 1.0×10^{-3} M solution of merocyanine dye **1** in $CHCl_3$. The peaks corresponding to the radical cation of monomer and dimer are marked with $[M]^+$ and $[M_2]^+$, respectively.

D.3 Electro-Optical Absorption Spectra
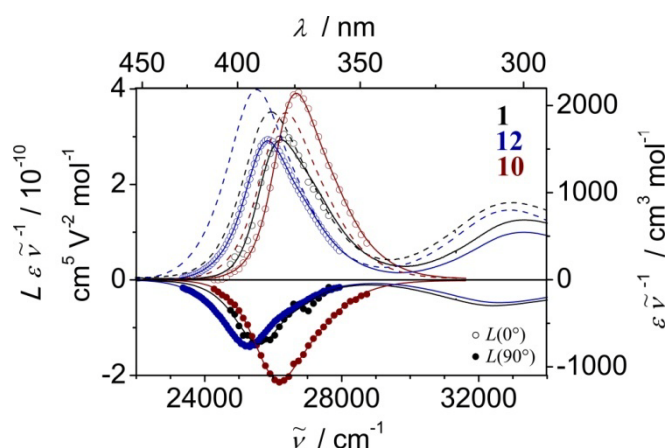
Figure D6. Fitted EOA spectra (solid lines, left scale) at 298 K for merocyanine dyes **1** (black), **12** (blue), and **10** (red) in 1,4-dioxane. Open symbols show the change of absorption for light polarized parallel to the electrical field, filled symbols for light polarized perpendicular to the electrical field. For comparison, the UV/Vis spectra are also shown (dashed lines, right scale).

D.4 Concentration-Dependent Formation of Supramolecular Polymers

Applying the concentration-dependent isodesmic model,[23] the apparent absorption coefficient of the solution $\varepsilon(c_T)$ can be expressed as a function of the total concentration c_T, the equilibrium constant K, and the absorption coefficients of monomer ε_{mon} and aggregate ε_{agg} (see Chapter 2). Equation (D5.1) which was used for the fitting procedure results from a combination of equations (5.1) and (5.2):

$$\varepsilon(c_T) = \frac{2Kc_T + 1 - \sqrt{4Kc_T + 1}}{2K^2 c_T^2}\left(\varepsilon_{mon} - \varepsilon_{agg}\right) + \varepsilon_{agg} \tag{D5.1}$$
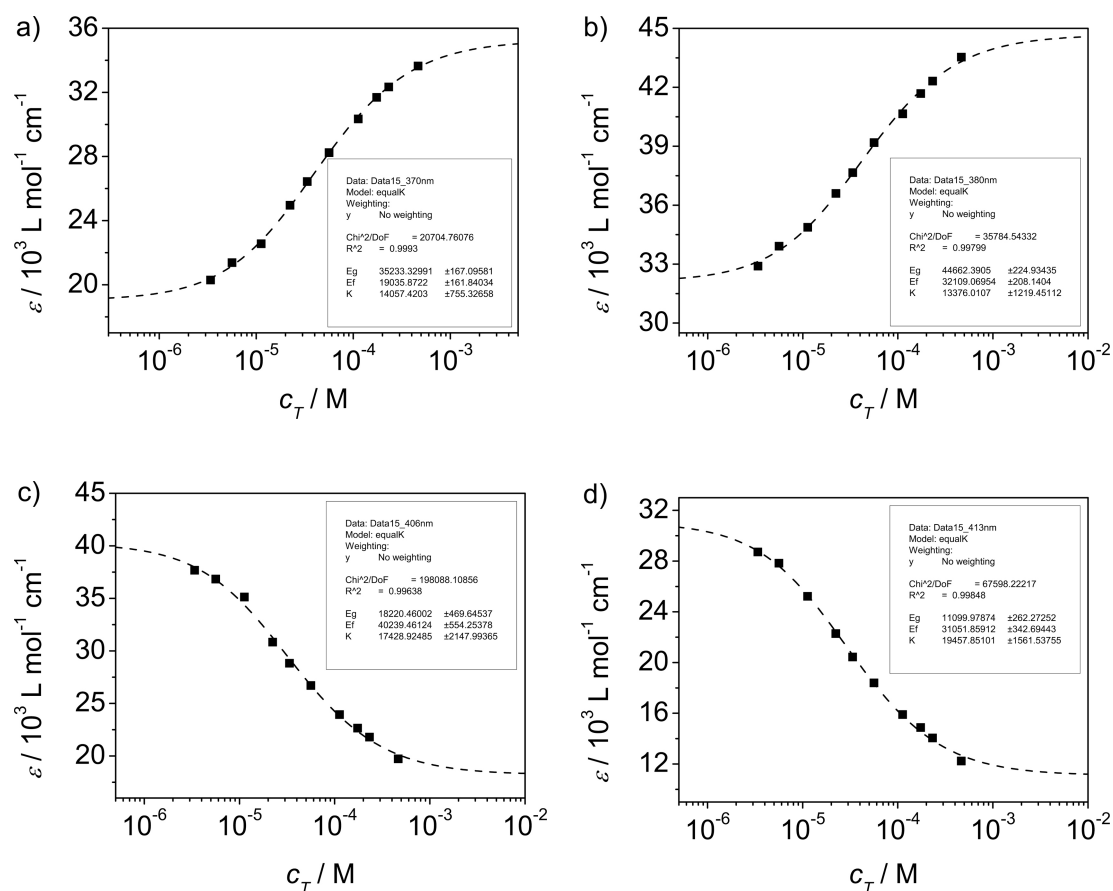
Figure D7. Apparent absorption coefficients of solutions of **1** in THF at 370 nm (a), 380 nm (b), 406 nm (c), and 413 nm (d) plotted against c_T and the corresponding curve obtained by the nonlinear regression analysis based on the isodesmic model.

141
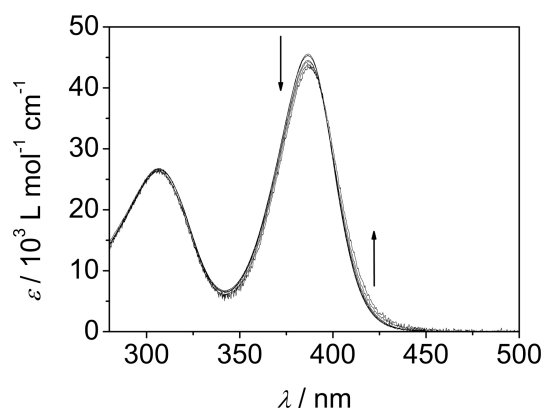
Figure D8. Concentration-dependent UV/Vis spectra of **1** in CHCl$_3$ at 298 K at the concentration range from $c =$ 8.4 x 10^{-5} M to 2.1 x 10^{-6} M. Arrows indicate spectral changes upon dilution.
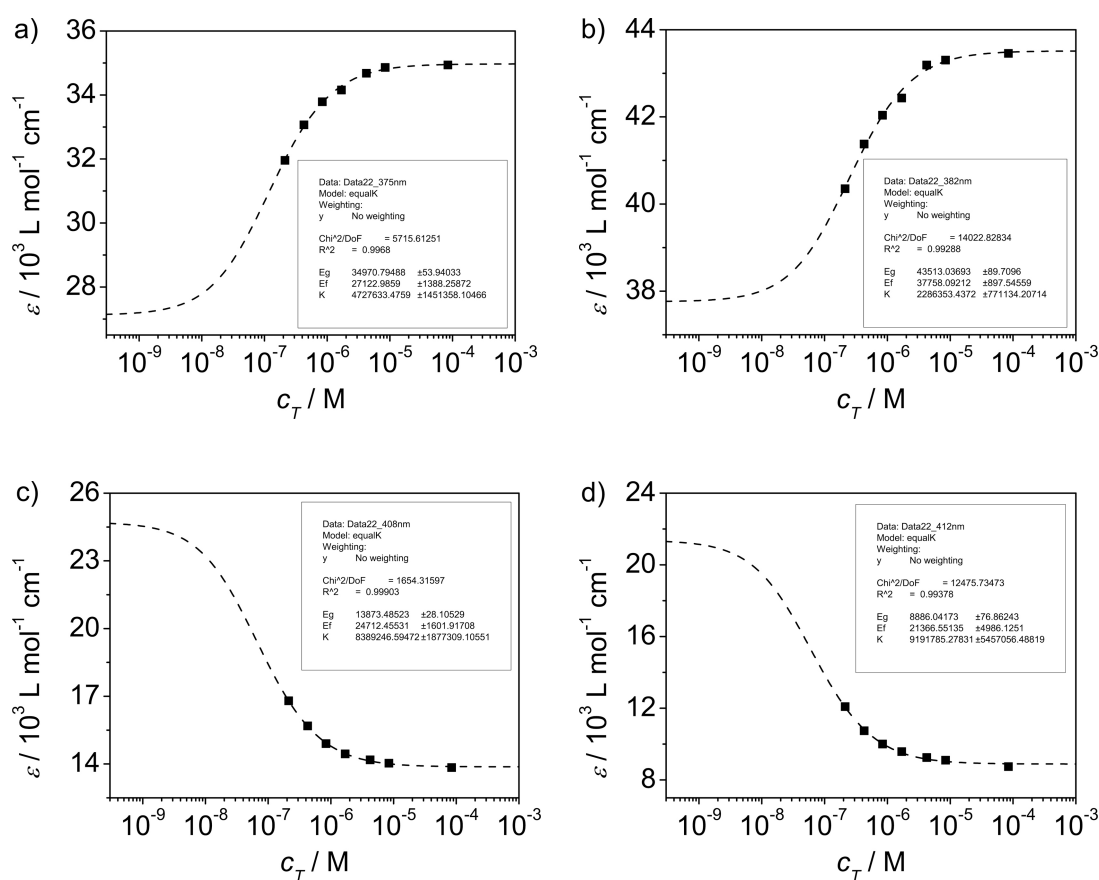
Figure D9. Apparent absorption coefficients of solutions of **1** in CHCl$_3$ at 375 nm (a), 382 nm (b), 408 nm (c), and 412 nm (d) plotted against c_T and the corresponding curve obtained by the nonlinear regression analysis based on the isodesmic model.

D.5 Temperature-Dependent Formation of Supramolecular Polymers

The temperature-dependent isodesmic model expresses the apparent absorption coefficient of the mixture $\varepsilon(T)$ at a certain wavelength as a function of the temperature T, the absorption coefficients of the monomer ε_{mon} and the aggregate ε_{agg}, the melting temperature of the aggregate T_m, and the molar enthalpy of aggregate formation ΔH (see Chapter 2):[23d,28]

$$\varepsilon(T) = \frac{1}{1 + \exp\left(-0.908\Delta H \dfrac{T - T_m}{RT_m^2}\right)}\left(\varepsilon_{agg} - \varepsilon_{mon}\right) + \varepsilon_{mon} \tag{D5.2}$$

The mole fraction of the aggregated species $\alpha_{agg}(T)$ at each temperature could be estimated from absorption spectra according to equation (D5.3):

$$\alpha_{agg}(T) \approx \frac{\varepsilon(T) - \varepsilon_{mon}}{\varepsilon_{agg} - \varepsilon_{mon}} \tag{D5.3}$$

where ε_{mon} and ε_{agg} were extrapolated with equation (D5.2). The number-averaged degree of polymerization $DP_N(T)$, the equilibrium constant K as a function of the temperature, and change of entropy ΔS can be calculated using equations (D5.4)–(D5.6):

$$DP_N(T) = \frac{1}{\sqrt{1 - \alpha_{agg}(T)}} \tag{D5.4}$$

$$DP_N(T) = \frac{1}{2} + \frac{1}{2}\sqrt{4K(T)c_T + 1} \tag{D5.5}$$

$$\Delta G = \Delta H + T\Delta S \tag{D5.6}$$

Figure D10 depicts $\alpha_{agg}(T)$, $DP_N(T)$, and K as functions of the temperature for a 3.5 x 10^{-5} M solution of Hamilton-receptor-functionalized merocyanine dye **1** in THF. Van't Hoff analysis yielded values of $\Delta H = -44.1$ kJ mol^{-1} and $\Delta S = -58.9$ J mol^{-1} K^{-1} (Figure D10d), which were very similar to those calculated from the isodesmic model (see Table D2). This shows that the model is internally consistent.[28]
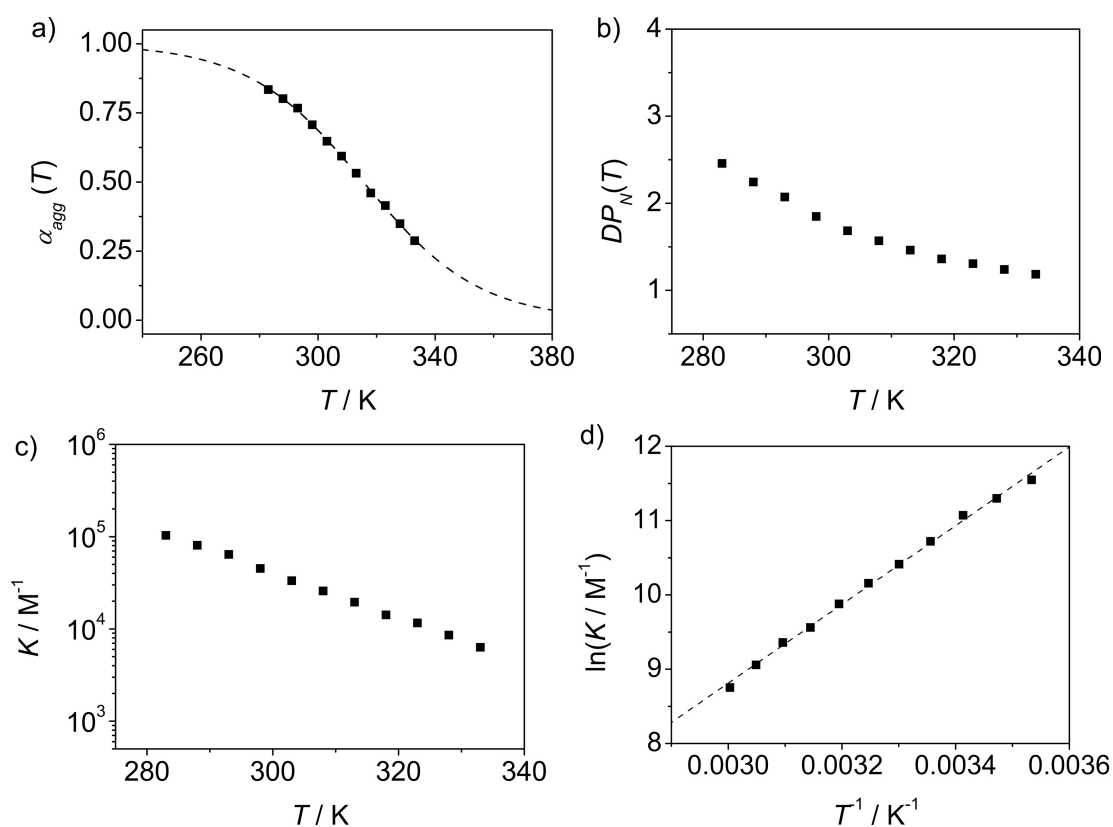
Figure D10. a) Temperature-dependent degree of aggregation $\alpha_{agg}(T)$ calculated from the apparent absorption coefficient at 395 nm of a 3.5 x 10^{-5} M solution of **1** in THF and the corresponding fit based on the isodesmic model. b) Number-averaged degree of polymerization (DP_N) as a function of the temperature. c) Equilibrium constant K as a function of the temperature. d) Van't Hoff plot for the self-assembly of **1** in THF.

Table D2. Thermodynamic parameters T_m (K), ΔH (kJ mol^{-1}), ΔS (J mol^{-1} K^{-1}), and DP_N and DP_W obtained from the temperature-dependent self-assembly of **1** (c = 3.5 x 10^{-5} M, THF) based on the isodesmic model.

T_m	ΔH	ΔS	DP_N[a,b]	DP_W[a,b]
316	−46.2	−65.8	2.7	4.4

[a] Values determined at 298 K. [b] Calculated for c = 1.0 x 10^{-4} M.

D.6 Linear Free Energy Relationship Analysis

LFERs were employed to estimate K for the self-assembly of **1** in n-hexane. An accurate determination of such value was prevented by solubility limitations. With the values given in the literature for the formation of complex **10:12**,[18] a proper estimation of the Gibbs free binding energy is possible (Figure D11, Table D3). The slope of almost unity (equation (D5.7)) is in accordance with the identical binding units and the good fit to the isodesmic model.

$$-\Delta G°(\mathbf{1}) = -(1.01 \text{ x } \Delta G°(\mathbf{10:12})) \qquad r^2 = 0.999 \tag{D5.7}$$
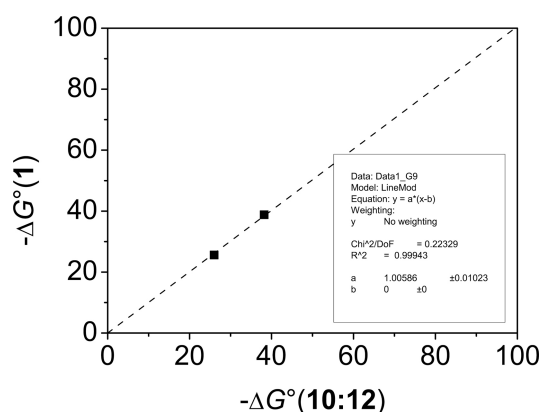
Figure D11. Linear free energy relationship for the solvent-dependent Gibbs free binding energies for bimolecular complex **10:12**[18] and the self-assembly of **1**. The corresponding data are shown in Table D3.

Table D3. Measured and estimated binding constants K (M^{-1}) and Gibbs free binding energies $-\Delta G°$ (kJ mol^{-1}) for complex **10:12** and the self-assembly of **1** at 298 K.

		K	$-\Delta G°$
	THF	$3.6 \text{ x } 10^4$	26.0
10:12	$CHCl_3$	$> 10^6$	$38.2\,^a$
	n-hexane	$2.5 \text{ x } 10^{15\,b}$	$87.8\,^b$
	THF	$3.1 \text{ x } 10^4$	25.6
1	$CHCl_3$	$6.2 \text{ x } 10^6$	38.8
	n-hexane	$3.0 \text{ x } 10^{15\,c}$	$88.3\,^c$

^{a} A K value of $5 \text{ x } 10^6$ M^{-1} was used to calculate $-\Delta G°$. ^{b} This value was estimated by a LFER with a triple hydrogen bonding system.[18] ^{c} Value estimated by a LFER.

D.7 Supplementary Fluorescence Spectra
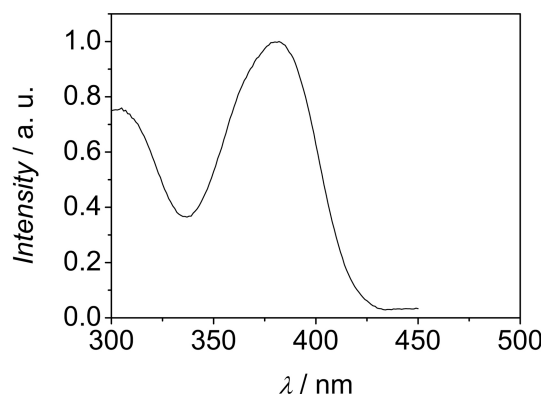
Figure D12. Fluorescence extication spectrum of assemblies of merocyanine dye **1** in $CHCl_3$ ($c = 0.7$ x 10^{-4} M, $\lambda_{em} = 495$ nm).

D.8 Supplementary Dynamic Light Scattering Data
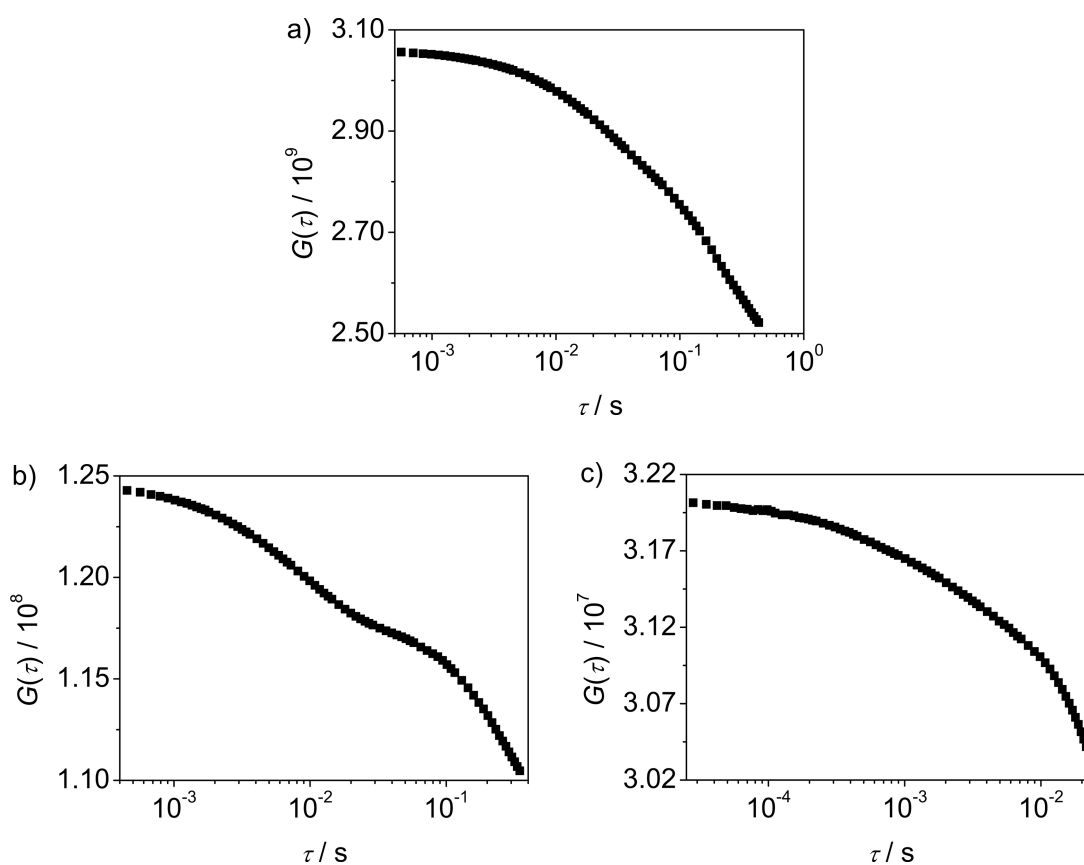
Figure D13. Autocorrelation functions $G(\tau)$ of **1** in $CHCl_3$ solution ($c = 4.5$ x 10^{-4} M, 293 K) plotted against the delay time τ for scattering angles a) 21.1° b) 27.5° c) 64.9°.

D.9 Molecular Modeling
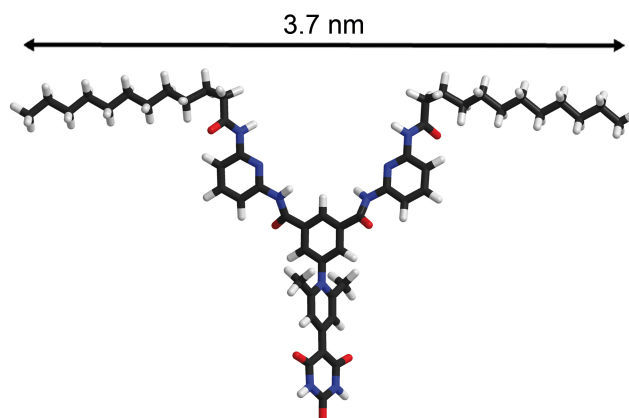
Figure D14. Geometry-optimized (AM1, HyperChem 8.05[128]) structure of a monomer of **1** with fully expanded alkyl substituents.

References and Notes

[1] (a) Dill, K. A. *Biochemistry* **1990**, *29*, 7133–7155. (b) Berg, J. M.; Tymoczko, J. L.; Stryer, L. *Biochemistry*, 6th ed.; W. H. Freeman & Co Ltd: New York, 2006.

[2] (a) Blankenship, R. E.; Olsen, J. M.; Müller, M. *Anoxygenic Photosynthetic Bacteria*; Blankenship, R. E., Madigan, M. T., Bauer, C. E., Eds; Kluver Academic Publishers: Dordrecht, 1995; pp 399–435. (b) Blankenship, R. E.; Matsura, K. *Light Harvesting Antennas in Photosynthesis*; Green, B. R., Parson, W. W., Eds.; Kluwer Academic Publishers: Dordrecht, 2003; pp 195–217. (c) Frigaard, N. U.; Chew, A. G. M.; Li, H.; Maresca, J. A.; Bryant, D. A. *Photosyn. Res.* **2003**, *78*, 93–117. (d) Tamiaki, H. *Photochem. Photobiol. Sci.* **2005**, *4*, 675–680. (e) Balaban, T. S. *Acc. Chem. Res.* **2005**, *38*, 612–623.

[3] (a) McDermott, G.; Prince, S. M.; Freer, A. A.; Hawthornthwaite-Lawless, A. M.; Papiz, M. Z.; Cogdell, R. J.; Isaacs, N. W. *Nature* **1995**, *374*, 517–521. (b) Pullerits, T.; Sundström, V. *Acc. Chem. Res.* **1996**, *29*, 381–389. (c) Hu, X.; Schulten, K. *Physics Today*, **1997**, *50*, 28–34. (d) Scheuring, S.; Sturgis, J. N.; Prima, V.; Bernadac, A.; Lévy, D.; Rigaud, J.-L. *Proc. Natl. Acad. Sci.* **2004**, *101*, 11293–11297. (e) Bahatyrova, S.; Frese, R. N.; Siebert, C. A.; Olsen, J. D.; van der Werf, K. O.; van Grondelle, R.; Niederman, R, A.; Bullough, P. A.; Otto, C.; Hunter, C. N. *Nature* **2004**, *430*, 1058–1062. (f) Scheuring, S. *Curr. Opin. Chem. Biol.* **2006**, *10*, 387–393. (g) Balaban, T. S.; Tamiaki, H.; Holzwarth, A. R. *Supramolecular Dye Chemistry*; Würthner, F., Ed.; Springer: Heidelberg, 2005; pp 1–38.

[4] (a) Vögtle, F. *Supramolecular Chemistry: An Introduction*, 1st ed.; John Wiley & Sons, 1993. (b) Lehn, J.-M. *Supramolecular Chemistry*, 1st ed.; Wiley-VCH: Weinheim, 1995. (c) Steed, J. W.; Atwood, J. L. *Supramolecular Chemistry*, 2nd ed.; John Wiley & Sons, 2009. (d) Lehn, J.-M. *Science* **2002**, *295*, 2400–2403. (e) Reinhoudt, D. N.; Crego-Calama, M. *Science* **2002**, *295*, 2403–2407. (f) Whitesides, G. M.; Grzybowski B. *Science* **2002**, *295*, 2418–2421. (g) Service, R. F. *Science* **2005**, *309*, 95. (h) Schenning, A. P. H. J.; Meijer, E. W. *Chem. Commun.* **2005**, 3245–3258. (i) Uhlenheuer, D. A.; Petkau, K.; Brunsveld, L. *Chem. Soc. Rev.* **2010**, *39*, 2817–2826. (j) Würthner, F.; Meerholz, K. *Chem. Eur. J.* **2010**, *16*, 9366–9373.

[5] (a) Beato, M.; Chávez, S.; Truss, M. *Steroids* **1996**, *61*, 240–251. (b) Hammes, S. R. *Proc. Natl. Acad. Sci. U.S.A.* **2003**, *100*, 2168–2170.

[6] Chakrabartty, A.; Baldwin, R. L. *Adv. Protein Chem.* **1995**, *46*, 141–176.

[7]   (a) Schenck, H. L.; Gellman, S. H. *J. Am. Chem. Soc.* **1998**, *120*, 4869–4870. (b) Kortemme, T.; Ramirez-Alvarado, M.; Serrano, L. *Science* **1998**, *281*, 253–256.

[8]   (a) Chan, H. S.; Bromberg, S.; Dill, K. A. *Phil. Trans. R. Soc. Lond. B* **1995**, *348*, 61–70. (b) Miranker, A. D.; Dobson, C. N. *Curr. Opin. Struct. Biol.* **1996**, *6*, 31–42. (c) Onuchic, J. N.; Wolynes, P. G. *Curr. Opin. Struct. Biol.* **2004**, *14*, 70–75. (d) Shank, E. A.; Cecconi, C.; Dill, J. W.; Marqusee, S.; Bustamante, C. *Nature* **2010**, *465*, 637–641.

[9]   Draper, D. E. *Trends Biochem. Sci.* **1996**, *21*, 145–149.

[10]   Hunter, C. A.; Anderson H. L. *Angew. Chem.* **2009**, *121*, 7624–7636; *Angew. Chem. Int. Ed.* **2009**, *48*, 7488–7499.

[11]   (a) Williams, C.; Brochard, F.; Frisch, H. L. *Ann. Rev. Phys. Chem.* **1981**, *32*, 433–451. (b) Hecht, S. *Mater. Today* **2005**, *8*, 48–55. (c) Foster, E. J.; Berda, E. B.; Meijer, E. W. *J. Am. Chem. Soc.* **2009** *131*, 6964–6966.

[12]   (a) Lee, M.; Cho, B. K.; Zin, W. C. *Chem. Rev.* **2001**, *101*, 3869–3892. (b) Zhang, L.; Eisenberg, A. *Science* **1995**, *268*, 1728–1731. (c) Harada, A.; Kataoka, K. *Science* **1999**, *283*, 65–67. (d) Ouarti, N.; Viville, P.; Lazzaroni, R.; Minatti, E.; Schappacher, M.; Deffieux, A.; Putaux, J.-L.; Borsali, R. *Langmuir* **2005**, *21*, 9085–9090.

[13]   (a) Krische, M. J.; Lehn, J.-M. *Struct. Bonding* **2000**, *96*, 3–29. (b) Scherrington, D. C.; Taskinen, K. A. *Chem. Soc. Rev.* **2001**, *30*, 83–93. (c) Prins, L. J.; Reinhoudt, D. N.; Timmermann, P. *Angew. Chem.* **2001**, *113*, 2446–2492; *Angew. Chem. Int. Ed.* **2001**, *40*, 2382–2426. (d) Brunsveld, L.; Folmer, B. J. B.; Meijer, E. W.; Sijbesma R. P. *Chem. Rev.* **2001**, *101*, 4071–4097. (e) Huc, I. *Eur. J. Org. Chem.* **2004**, 17–29. (f) Sánchez, L.; Martín, N. Guldi, D. M. *Angew. Chem.* **2005**, *117*, 5508–5516; *Angew. Chem. Int. Ed.* **2005**, *44*, 5374–5382.

[14]   (a) Würthner, F.; Yao, S. *Angew. Chem.* **2000**, *112*, 2054–2057; *Angew. Chem. Int. Ed.* **2000**, *39*, 1978–1981. (b) Würthner, F.; Yao, S.; Debaerdemaker, T.; Wortmann, R. *J. Am. Chem. Soc.* **2002**, *124*, 9431–9447.

[15]   (a) Lohr, A.; Grüne, M.; Würthner, F. *Chem. Eur. J.* **2009**, *15*, 3691–3705. (b) Lohr, A.; Uemura, S.; Würthner, F. *Angew. Chem.* **2009**, *121*, 6281–6284; *Angew. Chem. Int. Ed.* **2009**, *48*, 6165–6168.

[16]   (a) Würthner, F.; Yao, S.; Beginn, U. *Angew. Chem.* **2003**, *115*, 3368–3371; *Angew. Chem. Int. Ed.* **2003**, *42*, 3247–3250. (b) Yao, S; Beginn, U.; Gress, T.; Lysetska, M.; Würthner, F. *J. Am. Chem. Soc.* **2004**, *126*, 8336–8348. (c) Lohr, A.; Lysetska, M.; Würthner, F. *Angew. Chem.* **2005**, *117*, 5199–5202; *Angew. Chem. Int. Ed.* **2005**, *44*,

5071–5074. (d) Lohr, A.; Gress, T.; Deppisch, M; Knoll, M; Würthner, F. *Synthesis* **2007**, 3073–3082.

[17]   (a) Würthner, F.; Yao, S.; Heise, B.; Tschierske, C. *Chem. Commun.* **2001**, 2260–2261. (b) Prins, L. J.; Thalacker, C.; Würthner, F.; Timmermann, P.; Reinhoudt, D. N. *Proc. Natl. Acad. Sci. U.S.A.* **2001**, *98*, 10042–10045.

[18]   (a) Würthner, F.; Schmidt, J.; Stolte, M.; Wortmann, R. *Angew. Chem.* **2006**, *118*, 3926–3930; *Angew. Chem. Int. Ed.* **2006**, *45*, 3842–3846. (b) Schmidt, J.; Schmidt, R.; Würthner, F. *J. Org. Chem.* **2008**, *73*, 6355–6362.

[19]   (a) Yagai, S.; Higashi, M.; Karatsu, T.; Kitamura, A. *Chem. Mater.* **2005**, *17*, 4392–4398. (b) Yagai, S.; Higashi, M.; Karatsu, T.; Kitamura, A. *Chem. Commun.* **2006**, 1500–1502 (c) Yagai, S.; Kinoshita, T.; Higashi, M.; Kishikawa, K.; Nakanishi, T.; Karatsu, T.; Kitamura, A. *J. Am. Chem. Soc.* **2007**, *129*, 13277–13287.

[20]   Chang, S.-K.; Hamilton, A. D. *J. Am. Chem. Soc.* **1988**, *110*, 1318–1319.

[21]   Garland, F.; Christian, S. D. *J. Phys. Chem.* **1975**, *79*, 1247–1252.

[22]   (a) Marky, L. A.; Breslauer, K. J. *Biopolymers* **1987**, *26*, 1601–1620. (b) Apperloo, J. J.; Janssen, R. A. J.; Malenfant, P. R. L.; Fréchet, J. M. J. *Macromolecules* **2000**, *33*, 7038–7043.

[23]   (a) Martin, R. B. *Chem Rev.* **1996**, *96*, 3043–3064. (b) Zhao, D.; Moore, J. S. *Org. Biomol. Chem.* **2003**, *1*, 3471–3491. (c) Chen, Z.; Lohr, A.; Saha-Möller, C. R.; Würthner, F. *Chem. Soc. Rev.* **2009**, *38*, 564–584. (d) De Greef, T. F. A.; Smulders, M. M. J.; Wolffs, M.; Schenning, A. P. H. J.; Sijbesma, R. P.; Meijer, E. W. *Chem. Rev.* **2009**, *109*, 5687-5754.

[24]   West, W.; Pearce, S. *J. Phys. Chem.* **1965**, *69*, 1894–1903.

[25]   Yang, Y.-C.; Ward, J. R.; Seiders, R.P. *Inorg. Chem.* **1985**, *24*, 1765–1769.

[26]   Safont-Sempere, M. M.; Osswald, P.; Radacki, K.; Würthner, F. *Chem. Eur. J.* **2010**, *16*, 7380–7384.

[27]   Van der Schoot, P.; Michels, M. A. J.; Brunsveld, L.; Sijbesma, R. P.; Ramzi, A. *Langmuir* **2000**, *16*, 10076–10083.

[28]   (a) Smulders, M. M. J.; Nieuwenhuizen, M. M. L.; de Greef, T. F. A.; van der Schoot, P.; Schenning, A. P. H. J.; Meijer, E. W. *Chem. Eur. J.* **2010**, *16*, 362–367. (b) van der Schoot, P. *Supramolecular Polymers*, 2nd ed.; Ciferri, A., Ed.; CRC Press, Taylor & Francis Group: New York, 2005; pp 77–106.

[29]   (a) Würthner, F.; Thalacker, C.; Diele, S.; Tschierske, C. *Chem. Eur. J.* **2001**, *7*, 2245–2253. (b) Chen, Z.; Stepanenko, V.; Dehm, V.; Prins, P.; Siebbeles, L. D. A.; Seibt, J.; Marquetant, P.; Engel, V.; Würthner, F. *Chem. Eur. J.* **2007**, *13*, 436–449.

[30]   Lahieri, S.; Thompson, L.; Moore, J. S. *J. Am. Chem. Soc.* **2000**, *122*, 11315–11319.

[31]   Kastler, M.; Pisula, W.; Wasserfallen, D.; Pakula, T.; Müllen, K. *J. Am. Chem. Soc.* **2005**, *127*, 4286–4296.

[32]   Sijbesma, R. P.; Beijer, F. H.; Brunsveld, L.; Folmer, B. J. B.; Hirschberg, J. H. K. K.; Lange, R. F. M.; Lowe, J. K. L.; Meijer, E. W. *Science* **1997**, *278*, 1601–1604.

[33]   Berl, V.; Schmutz, M.; Krische, M. J.; Khoury, R. G.; Lehn, J.-M. *Chem. Eur. J.* **2002**, *8*, 1227–1244.

[34]   Castellano, R. K.; Craig, S. L.; Nuckolls, C.; Rebek, J., Jr. *J. Am. Chem. Soc.* **2000**, *122*, 7876–7882.

[35]   Schmuck, C. *Tetrahedron* **2001**, *57*, 3063–3067.

[36]   (a) Oosawa, F.; Asakura, S.; Hotta, K.; Imai, N.; Ooi, T. *J. Polym. Sci.* **1959**, *37*, 323–336. (b) Oosawa, F.; Kasai, M. *J. Mol. Biol.* **1962**, *4*, 10–21. (c) Oosawa, F. *J. Theor. Biol.* **1970**, *27*, 69–86.

[37]   Winklmair, D. *Arch. Biochem. Biophys.* **1971**, *147*, 509–514.

[38]   Jonkheijm, P.; van der Schoot, P.; Schenning, A. P. H. J.; Meijer, E. W. *Science* **2006**, *313*, 80–83.

[39]   Smulders, M. M. J.; Schenning, A. P. H. J., Meijer, E. W. *J. Am. Chem. Soc.* **2008**, *130*, 606–611.

[40]   Goldstein, R. F.; Stryer, L. *Biophys. J.* **1986**, *50*, 583–599.

[41]   Simic, V.; Bouteiller, L.; Jalabert, M. *J. Am. Chem. Soc.* **2003**, *125*, 13148–13154.

[42]   Hirst, A. R.; Coates, I. A.; Boucheteau, T. R.; Miravet, J. F.; Escuder, B. Castelletto, V.; Hamley, I. W.; Smith, D. K. *J. Am. Chem. Soc.* **2008**, *130*, 9113–9121.

[43]   Percec, V.; Dulcey, A. E.; Peterca, M.; Ilies, M.; Ladislaw, J.; Rosen, B. M.; Edlund, U.; Heiney, P. A. *Angew. Chem.* **2005**, *117*, 6674–6679; *Angew. Chem. Int. Ed.* **2005**, *44*, 6516–6521.

[44]   Tobe, Y.; Utsumi, N.; Kawabata, K.; Nagano, A.; Adachi, K.; Araki, S.; Sonoda, M.; Hirose, K.; Naemura, K. *J. Am. Chem. Soc.* **2002**, *124*, 5350–5364.

[45]   Kaiser, T. E.; Stepanenko, V.; Würthner, F. *J. Am. Chem. Soc.* **2009**, *131*, 6719–6732.

[46]   Ueberreiter, K.; Engel, M. *Macromol. Chem.* **1977**, *178*, 2257–2260.

[47]   Metselaar, G. A.; Cornelissen, J. J. L. M.; Rowan, A., E.; Nolte, R. J. M. *Angew. Chem.* **2005**, *117*, 2026–2029; *Angew. Chem. Int. Ed.* **2005**, *44*, 1990–1993.

[48]   Jacobson, H.; Stockmayer, W. H. J. *J. Chem. Phys.* **1950**, *18*, 1600–1606.

[49]   Ercolani, G.; Di Stefano, S. *J. Phys. Chem. B* **2008**, *112*, 4662–4665.

[50]   Stoll, M.; Rouvé, A.; Stoll-Comte, G. *Helv. Chim. Acta* **1934**, *17*, 1289–1308.

[51]   Ciferri, A. *Supramolecular Polymers*, 2nd ed.; CRC Press, Taylor & Francis Group: New York, 2005; pp 29–75.

[52]   Israelachvili, J. N. *Intermolecular and Surface Forces*, 2nd ed.; Academic Press: London, 1992.

[53]   (a) Murphy, K. P.; Privalov, P. L.; Gill, S. J. *Science* **1990**, *247*, 559–561. (b) Breslow, R. *Acc. Chem. Res.* **1991**, *24*, 159–164. (c) Lemieux, R. U. *Acc. Chem. Res.* **1996**, *29*, 373–380. (d) Marmur, A. *J. Am. Chem. Soc.* **2000**, *122*, 2120–2121.

[54]   (a) Hunter, C. A. *Chem. Soc. Rev.* **1994**, *23*, 101–109. (b) Hunter, C. A.; Lawson, K. R.; Perkins, J.; Urch, C. J. *J. Chem. Soc., Perkin Trans. 2* **2001**, 651–669. (c) Grimme, S. *Angew. Chem.* **2008**, *120*, 3478–3483; *Angew. Chem. Int. Ed.* **2008**, *47*, 3430–3434.

[55]   Kollman, P. A.; Allen, L. C. *Chem. Rev.* **1972**, *73*, 283–303.

[56]   Dähne, S. *Science* **1978**, *199*, 1163–1167.

[57]   Atwood, J. L.; Hamada, F.; Robinson, K. D.; Orr, G. W.; Vincent, R. L. *Nature* **1991**, *349*, 683–684.

[58]   Pauling, L. *Proc. Natl. Acad. Sci. U.S.A.* **1928**, *14*, 359–362.

[59]   Iwata, S.; Morokuma, K. *J. Am. Chem. Soc.* **1973**, *95*, 7563–7575.

[60]   Bader, R. F. W. *Atoms in Molecules, A Quantum Theory*; Oxford University Press, Oxford, 1990.

[61]   Gellman, S. H.; Dado, G. P.; Liang, G.-B.; Adams, B. R. *J. Am. Chem. Soc.* **1991**, *113*, 1164–1173.

[62]   (a) R. Taylor, O. Kennard, *Acc. Chem. Res.* **1984**, *17*, 320–326. (b) Legon, A. C.; Millen, D. J. *Acc. Chem. Res.* **1987**, *20*, 39–46. (c) Panunto, T. W.; Urbánczyk-Lipkowska, Z.; Johnson, R.; Etter, M. C. *J. Am. Chem. Soc.* **1987**, *109*, 7786–7797.

[63]   R. J. Gillespie, R. S. Nyholm, *Q. Rev. Chem. Soc.* **1957**, *11*, 339–380.

[64]   (a) R. Taylor, O. Kennard, W. Versichel, *J. Am. Chem. Soc.* **1983**, *105*, 5761–5766. (b) P. Marray-Rust, J. P. Glusker, *J. Am. Chem. Soc.* **1984**, *106*, 1018–1025.

[65]   R. E. Hubbard, *Prog. Biophys. Molec. Biol.* **1984**, *44*, 97–179.

[66]   Anslyn, E. V.; Dougherty, D. A. *Modern Physical Organic Chemistry*; University Science Books; 2006.

[67]   Jeffrey, G. A. *An Introduction to Hydrogen Bonding*; Oxford University Press: New York, 1997.

[68]   Gilli, P.; Pretto, L.; Bertolasi, V.; Gilli, G. *Acc. Chem. Res.* **2009**, *42*, 33–44.

[69]   (a) Searle, M. S.; Williams, D. H. *J. Am. Chem. Soc.* **1992**, *114*, 10690–10697. (b) Searle, M. S.; Williams, D. H.; Gerhard, U. *J. Am. Chem. Soc.* **1992**, *114*, 10697–10704. (c) Bisson, A. P.; Hunter, C. A. *Chem. Commun.* **1996**, 1723–1724.

[70]   (a) Jorgensen, W. L.; Pranata, J. *J. Am. Chem. Soc.* **1990**, *112*, 2008–2010. (b) Pranata, J.; Wierschke, S. G.; Jorgensen, W. L. *J. Am. Chem. Soc.* **1991**, *113*, 2810–2819.

[71]   Sartorius, J.; Schneider, H.-J. *Chem. Eur. J.* **1996**, *2*, 1446–1452.

[72]   (a) Fan, E.; van Araman, S. A.; Kincaid, S.; Hamilton, A. D. *J. Am. Chem. Soc.* **1987**, *115*, 369–370. (b) Wilcox, C. S.; Kim, E.-I.; Romano, D.; Kuo, L. H.; Burt, L. A. Curran, D. P. *Tetrahedron* **1995**, *51*, 621–634.

[73]   Gilli, G.; Bertolasi, V.; Ferretti, V.; Gilli, P. *Acta. Cryst.* **1993**, *B49*, 564–576.

[74]   Hindricks, W.; Saenger, W. *J. Am. Chem. Soc.* **1990**, *112*, 2789–2796.

[75]   (a) Watson, J. D.; Crick, F. H. C. *Nature* **1953**, *171*, 964–967. (b) Douhal, A.; Kim, S. K.; Zewail, A. H. *Nature* **1995**, *378*, 260–263. (c) Robinson, H.; Gao, Y.-G.; Bauer, C.; Roberts, C.; Switzer, C.; Wang, A. H.-J. *Biochemistry* **1998**, *37*, 10897–10905.

[76]   Meyer, H.; Bossert, F.; Horstmann, H. *Liebigs Ann. Chem.* **1978**, 1476–1482.

[77]   Söntjens, S. H. M.; Sijbesma, R. P.; van Genderen, M. H. P.; Meijer, E. W. *J. Am. Chem. Soc.* **2000**, *122*, 7487–7493.

[78]   Beijer, F. H.; Kooijman, H.; Spek, A. L.; Sijbesma, R. P.; Meijer, E. W. *Angew. Chem.* **1998**, *110*, 79–82; *Angew. Chem. Int. Ed.* **1998**, *37*, 75–78.

[79]   Murray, F. J.; Zimmermann, S. C. *Tetrahedron Lett.* **1995**, *36* 7627–7630.

[80]   Würthner, F.; Thalacker, C.; Sautter, A.; Schärtl, W.; Ibach, W.; Hollricher, O. *Chem. Eur. J.* **2000**, *6*, 3871–3886.

[81]   Reichardt, C. *Solvents and Solvent Effects in Organic Chemistry*, 3rd ed.; Wiley-VCH: Weinheim, 2002.

[82]   (a) Schneider, H.-J. *Angew. Chem.* **1991**, *103*, 1419–1439; *Angew. Chem. Int. Ed.* **1991**, *30*, 1417–1436. (b) Reichardt, C. *Chem. Rev.* **1994**, *94*, 2319–2358. (c) Abraham, M. *Chem. Soc. Rev.* **1993**, *22*, 73–83. (d) Cook, J. L.; Hunter, C. A.; Low, C. M. R.; Perez-Velasco, A.; Vinter, J. G. *Angew. Chem.* **2007**, *119*, 3780–3783; *Angew. Chem. Int. Ed.* **2007**, *46*, 3706–3709.

[83]   Würthner, F.; Thalacker, C.; Matschiner, R.; Lukaszuk, K.; Wortmann, R. *Chem. Commun.* **1998**, 1739–1740.

[84]   (a) Gavezzotti, A. *J. Phys. Chem.* **1990**, *94*, 4319–4325. (b) Allen, F. H.; Baalham, C. A.; Lommerse, J. P. M.; Raithby, P. R. *Acta Cryst. B* **1998**, *54*, 320–329. (c) Lee, S.; Mallik, A. B.; Fredrickson, D. C. *Cryst. Growth Des.* **2004**, *4*, 279–290. (d) Paulini, R.; Müller, K.; Diederich, F. *Angew. Chem.* **2005**, *117*, 1820–1839; *Angew. Chem. Int. Ed.* **2005**, *44*, 1788–1805.

[85]   (a) Marder, S. R.; Beratan, D. N.; Cheng, L.-T. *Science* **1991**, *252*, 103–106. (b) Blanchard-Desce, M.; Barzoukas, M. *J. Opt. Soc. Am. B* **1998**, *15*, 302–307. (c) Wolff, J. J.; Wortmann, R. *Adv. Phys. Org. Chem.* **1999**, *32*, 121–217. (d) Meier, H. *Angew. Chem.* **2005**, *117*, 2536–2561; *Angew. Chem. Int. Ed.* **2005**, *44*, 2482–2506.

[86]   Würthner, F.; Wortmann, R.; Meerholz, K. *ChemPhysChem* **2001**, *3*, 17–31.

[87]   Grimme, S.; Schwabe, T.; Mück-Lichtenfeld, C. *Org. Biomol. Chem.* **2007**, *5*, 741–758.

[88]   (a) Morokuma, K. *J. Chem. Phys.* **1971**, *55*, 1236–1244. (b) Kitaura, K.; Morokuma, K. *Int. J. Quantum Chem.* **1976**, *10*, 325–340

[89]   (a) Onsager, L. *J. Am. Chem. Soc.* **1936**, *58*, 1486–1493. (b) Böttcher, C. F. J. *Theory of Electric Polarization*, 2nd ed.; Elsevier Scientific Pub. Co.: Amsterdam, 1973.

[90]   For a review on multiple hydrogen bonding arrays, see: (a) Zimmerman, S. C.; Corbin, P. S. *Struct. Bonding* **2000**, *96*, 63–94. For reviews on spectroscopic studies of hydrogen bonds, see: (b) Murthy, A. S. N.; Rao, C. N. R. *Appl. Spec. Rev.* **1968**, *2*, 69–191. (c) Müller-Dethlefs, K.; Hobza, P. *Chem. Rev.* **2000**, *100*, 143–167. For a review on unorthodox hydrogen bonds, see: (d) Epstein, L. M.; Shubina, E. S. *Coord. Chem. Rev.* **2000**, *231*, 165–181. For a review on halogen acceptors in hydrogen bonding, see: (e) Kovács, A.; Varga, Z. *Coord. Chem. Rev.* **2006**, *250*, 710–727.

[91]   For examples of single hydrogen bonding entities, see: (a) Kyogoku, Y.; Lord, R. C.; Rich, A. *Proc. Natl. Acad. Sci. U.S.A.* **1967**, *57*, 250–257. (b) Hine, J.; Ahn, K. *J. Org.*

Chem. **1987**, *52*, 2083–2086. (c) Rebek, Jr., J.; Askew, B.; Killoran, M.; Nemeth, D.; Lin, F.-T. *J. Am. Chem. Soc.* **1987**, *109*, 2426–2431.

[92] For examples of double hydrogen bonding entities, see: (a) ref. 91a (b) Kyogoku, Y.; Lord, R. C.; Rich, A. *J. Am. Chem. Soc.* **1967**, *89*, 496–504. (c) Hammes, G. G.; Park, A. C. *J. Am. Chem. Soc.* **1969**, *91*, 956–961. (d) Krlkorlan, S. E. *J. Phys. Chem.* **1982**, *86*, 1875–1881. (e) ref. 91c (f) Zimmerman, S. C.; Murray, T. J. *Tetrahedron Lett.* **1994**, *35*, 4077–4080. (g) Satorius, J.; Schneider, H.-J. *Chem. Eur. J.* **1996**, *2*, 1446–1452. (h) Steinke, J. H. G.; Dunkin, I. R.; Sherrington, D. C. *Trends Anal. Chem.* **1999**, *18*, 159–164.

[93] For examples of triple hydrogen bonding entities, see: (a) ref. 91a (b) Kyogoku, Y.; Lord, R. C.; Rich, A. *Biochim. Phys. Acta* **1969**, *179*, 10–17. (c) Hamilton, A. D.; van Engen, D. *J. Am. Chem. Soc.* **1987**, *109*, 5035–5036. (d) Kelly, T. R.; Zhao, C.; Bridger, B. J. *J. Am. Chem. Soc.* **1989**, *111*, 3744–3745. (e) Murray, T. J.; Zimmerman, S. C. *J. Am. Chem. Soc.* **1992**, *114*, 4010–4011. (f) Bell, D. A.; Anslyn, E. V. *Tetrahedron* **1995**, *51* 7161–7172. (g) Beijer, F. H.; Sijbesma, R. P.; Vekemans, J. A. J. M.; Meijer, E. W.; Kooijman, H.; Spek, A. L. *J. Org. Chem.* **1996**, *61*, 6371–6380. (h) ref. 80 (i) Bielejewska, A. G.; Marjo, C. E.; Prins, L. J.; Timmerman, P.; de Jong, F.; Reinhoudt, D. N. *J. Am. Chem. Soc.* **2001**, *123*, 7518–7533. (j) Würthner, F.; Yao, S. *J. Org. Chem.* **2003**, *68*, 8943–8949. (k) Abe, H.; Takase, M.; Doi, Y.; Matsumoto, S.; Furusyo, M.; Inouye, M. *Eur. J. Org. Chem.* **2005**, *14*, 2931–2950. (l) Balaban, T. S.; Berova, N.; Drain, C. M.; Hauschild, R.; Huang, X.; Kalt, H.; Lebedkin, S.; Lehn, J.-M.; Nifaitis, F.; Pescitelli, G.; Prokhorenko, V. I.; Riedel, G.; Smeureanu, G. Zeller, J. *Chem. Eur. J.* **2007**, *13*, 8411–8427.

[94] For a review on quadruple hydrogen bonding systems, see: (a) Sijbesma, R. P.; Meijer, E. W. *Chem. Commun.* **2003**, 5–16. For examples of quadruple hydrogen bonding entities, see: (b) Ducharme, Y.; Wuest, J. D. *J. Org. Chem.* **1988**, *53*, 5789–5791. (c) Lüning, U.; Kühl, C. *Tetrahedron Lett.* **1998**, *39*, 5735–5738. (d) ref. 78 (e) Beijer, F. H.; Sijbesma, R. P.; Kooijman, H.; Spek, A. L.; Meijer, E. W. *J. Am. Chem. Soc.* **1998**, *120*, 6761–6769. (f) Corbin, P. S.; Zimmerman, S. C. *J. Am. Chem. Soc.* **1998**, *120*, 9710–9711. (g) S. H. M. Söntjens, Sijbesma, R. P.; van Genderen, M. H. P.; Meijer, E. W. *J. Am. Chem. Soc.* **2000**, *122*, 7487–7493. (h) Rispens, M. T.; Sánchez, L.; Knol, J.; Hummelen, J. C. *Chem. Commun.* **2001**, 161–162. (i) Corbin, P. S.; Lawless, L. J.; Li, Z.; Ma, Y.; Witmer, M.; Zimmerman, S. C. *Proc. Natl. Acad. Sci. U.S.A.* **2002**, *99*, 5099–5104. (j) Park, T.; Zimmerman, S. C.; Nakashima, S. *J. Am. Chem. Soc.* **2005**, *127*, 6520–6521. (k) Martin, A. M.; Butler, R. S.; Ghiviriga, I.; Giessert, R. E.; Abboud, K. A.; Castellano, R. K. *Chem. Commun.* **2006**, 4413–4415.

(l) Wong, C.-H.; Chow, H.-F.; Hui, S.-K.; Sze, K.-H. *Org. Lett.* **2006**, *8*, 1811–1814. (m) Qu, S.; Li, M. *Tetrahedron* **2008**, *64*, 10890–10895. (n) Hisamatsu, Y.; Shirai, N.; Ikeda, S.-I.; Odashima, K. *Org. Lett.* **2009**, *11*, 4342–4345. (o) Du, P.; Wang, G.-T.; Zhao, X.; Li, G.-Y.; Jiang, X.-K.; Li, Z.-T. *Tetrahedron Lett.* **2010**, *51*, 188–191. (p) Hisamatsu, Y.; Shirai, N.; Ikeda, S.-I.; Odashima, K. *Org. Lett.* **2010**, *12*, 1776–1779.

[95] For examples of sextuple hydrogen bonding entities, see: (a) ref. 20 (b) Chang, S.-K.; van Engen, D.; Fan, E.; Hamilton, A. D. *J. Am. Chem. Soc.* **1991**, *113*, 7640–7645. (c) Corbin, P. S.; Zimmerman, S. C. *J. Am. Chem. Soc.* **2000**, *122*, 3779–3780. (d) Zeng, H.; Miller, R. S.; Flowers II, R. A.; Gong, B. *J. Am. Chem. Soc.* **2000**, *122*, 2635–2644. (e) Zeng, H.; Ickes, H.; Flowers II, R. A.; Gong, B. *J. Org. Chem.* **2001**, *66*, 3574–3583. (f) ref. 93i (g) ref. 33 (h) ref. 18b.

[96] (a) Hof, F.; Scofield D. M.; Schweizer, W. B.; Diederich, F. *Angew. Chem.* **2004**, *116*, 5166–5169; *Angew. Chem. Int. Ed.* **2004**, *43*, 5056–5059. (b) Fischer, F. R.; Schweizer, W. B.; Diederich, F. *Angew. Chem.* **2007**, *119*, 8418–8421; *Angew. Chem. Int. Ed.* **2007**, *46*, 8270–8273.

[97] Fischer, F. R.; Wood, P. A.; Allen, F. H.; Diederich, F. *Proc. Natl. Acad. Sci. U.S.A.* **2008**, *105*, 17290–17294.

[98] (a) Paliwal, S.; Geib, S.; Wilcox, C. S. *J. Am. Chem. Soc.* **1994**, *116*, 4497–4498. (b) Kim, E.-I.; Paliwal, S.; Wilcox, C. S. *J. Am. Chem. Soc.* **1998**, *120*, 11192–11193.

[99] Balagurusamy, V. S. K.; Ungar, G.; Percec, V.; Johansson, G. *J. Am. Chem. Soc.* **1997**, *119*, 1539–1555.

[100] Segal M. (Hoechst AG), PCT EP 0169457 (A1), **2000**.

[101] Prim, D.; Kirsch, G.; Nicoud, J. F. *Synlett.* **1998**, *4*, 383–384.

[102] Würthner, F.; Yao, S.; Schilling, J.; Wortmann, R.; Redi-Abshiro, M.; Mecher, E.; Gallego-Gomez, F.; Meerholz, K. *J. Am. Chem. Soc.* **2001**, *123*, 2810–2824.

[103] (a) Connors, K. A. *Binding Constants*; John Wiley & Sons: New York, 1987. b) Schneider, H.-J.; Yatsimirsky, A. *Principles and Methods in Supramolecular Chemistry*; John Wiley & Sons: Chichester, 2000. For determination of binding constants using NMR, see: c) Macomber, R. S. *J. Chem. Educ.* **1992**, *69*, 375–378. d) Fielding, L. *Tetrahedron* **2000**, *56*, 6151–6170.

[104] For details concerning data evaluation, see the respective Appendix.

[105] Horn, D.; Rieger, J. *Angew. Chem.* **2001**, *113*, 4460–4492; *Angew. Chem. Int. Ed.* **2001**, *40*, 4330–4361.

[106] Schmidt, R.; Uemura, S.; Würthner, F. *Chem. Eur. J.* **2010**, *16*, 13706–13715.

[107] (a) Sherrington, D. C.; Taskinen, K. A. *Chem. Soc. Rev.* **2001**, *30*, 83–93. (b) Brunsveld, L.; Folmer, B. J. B.; Meijer, E. W.; Sijbesma, R. P. *Chem. Rev.* **2001**, *101*, 4071–4097. (c) Hoeben, F. J. M.; Jonkheijm, P.; Meijer, E. W.; Schenning, A. P. H. J. *Chem. Rev.* **2005**, *105*, 1491–1546. (d) Binder, W. H.; Zirbs, R. *Adv. Polym. Sci.* **2007**, *207*, 1–78.

[108] (a) Tecilla, P.; Dixon, R. P.; Slobodkin, G.; Alavi, D. S.; Waldeck, D. H.; Hamilton, A. D. *J. Am. Chem. Soc.* **1990**, *112*, 9408–9410. (b) Dirksen, A.; Hahn, U.; Schwanke, F.; Nieger, M.; Reek, J. N. H.; Vögtle, F.; De Cola, L. *Chem. Eur. J.* **2004**, *10*, 2036–2047. (c) McClenaghan, N. D.; Grote, Z.; Darriet, K.; Zimine, M.; Williams, R. M.; De Cola, L.; Bassani, D. M. *Org. Lett.* **2005**, *7*, 807–810. (d) Molard, Y.; Bassani, D. M.; Desvergne, J.-P.; Horton, P. N.; Hursthouse, M. B.; Tucker, J. H. R. *Angew. Chem.* **2005**, *117*, 1096–1099; *Angew. Chem. Int. Ed.* **2005**, *44*, 1072–1075. (e) Wessendorf, F.; Gnichwitz, J.-F.; Sarova, G. H.; Hager, K.; Hartnagel, U.; Guldi, D. M.; Hirsch, A. *J. Am. Chem. Soc.* **2007**, *129*, 16057–16071. (f) Wessendorf, F.; Grimm, B.; Guldi, D. M.; Hirsch, A. *J. Am. Chem. Soc.* **2010**, *132*, 10786–10795.

[109] (a) Berl, V.; Schmutz, M.; Krische, M. J.; Khoury, R. G.; Lehn, J.-M. *Chem. Eur. J.* **2002**, *17*, 1227–1244. (b) Kolomiets, E.; Buhler, E.; Candau, S. J.; Lehn, J.-M. *Macromolecules* **2006**, *39*, 1173–1181. (c) Binder, W. H.; Petraru, L.; Roth, T.; Groh, P. W.; Pálfi, V.; Keki, S.; Ivan, B. *Adv. Funct. Mater.* **2007**, *17*, 1317–1326.

[110] (a) ref. 108b (b) Franz, A.; Bauer, W.; Hirsch, A. *Angew. Chem.* **2005**, *117*, 1588–1592; *Angew. Chem. Int. Ed.* **2005**, *44*, 1564–1567.

[111] (a) Zhao, X.; Li, Z.-T. *Chem. Commun.* **2010**, *46*, 1601–1616. (b) Berl, V.; Huc, I.; Khoury, R. G.; Krische, M. J.; Lehn, J.-M. *Nature* **2000**, *407*, 720–723. (c) Berl, V.; Krische, M. J.; Huc, I.; Lehn, J.-M.; Schmutz, M. *Chem. Eur. J.* **2000**, *6*, 1938–1946.

[112] (a) Binder, W. H.; Bernstorff, S.; Kluger, C.; Petraru, L.; Kunz, M. *Adv. Mater.* **2005**, *17*, 2824–2828. (b) Burd, C.; Weck, M. *Macromolecules* **2005**, *38*, 7225–7230.

[113] (a) Motesharei, K. Myles, D. C. *J. Am. Chem. Soc.* **1994**, *116*, 7413–7414. (b) Binder, W. H.; Kluger, C.; Josipovic , M.; Straif, C. J.; Friedbacher, G. *Macromolecules* **2006**, *39*, 8092–8101.

[114] Ikeda, M.; Nobori, T.; Schmutz, M.; Lehn, J.-M. *Chem. Eur. J.* **2005**, *11*, 662–668.

[115] (a) Terech, P.; Weiss, R. G. *Chem. Rev.* **1997**, *97*, 3133–3159. (b) van Esch, J. H.; Feringa, B. L. *Angew. Chem.* **2000**, *112*, 2351–2354; *Angew. Chem. Int. Ed.* **2000**, *39*, 2263–2266. (c) Estroff, L. A.; Hamilton, A. D. *Chem. Rev.* **2004**, *104*, 1201–1217. (d)

158

Hirst, A. R.; Smith, D. K. *Chem. Eur. J.* **2005**, *11*, 5496–5508. (e) Hirst, A. R.; Escuder, B.; Miravet, J. F.; Smith, D. K. *Angew. Chem.* **2008**, *120*, 8122–8139; *Angew. Chem. Int. Ed.* **2008**, *47*, 8002–8018. (f) Foster, J. A.; Steed, J. W. *Angew. Chem.* **2010**, *122*, 6868–6874; *Angew. Chem. Int. Ed.* **2010**, *49*, 6718–6724.

[116]   (a) Lewschin, W. L. *Z. Phys.* **1927**, *43*, 230–253. (b) Rabinowitch, E.; Epstein, L. *J. Am. Chem. Soc.* **1941**, *63*, 69–78. (c) Förster, T.; König, E. *Z. Elektrochem.* **1957**, *61*, 344–348. (d) Bergmann, K.; O'Konski, C. T. *Z. Phys. Chem.* **1963**, *67*, 2169–2177. (e) West, W.; Pearce, S. *J. Phys. Chem.* **1965**, *69*, 1894–1903.

[117]   (a) Förster, T. *Z. Naturwissenschaften* **1946**, *33*, 166–175. (b) Kasha, M.; Rawls, H. R.; El-Bayoumi, M. A. *Pure Appl. Chem.* **1965**, *11*, 371–392.

[118]   (a) Rösch, U.; Yao, S.; Wortmann, R.; Würthner, F. *Angew. Chem.* **2006**, *118*, 7184–7188; *Angew. Chem. Int. Ed.* **2006**, *45*, 7026–7030. (b) Yagai, S.; Seki, T.; Karatsu, T.; Kitamura, A.; Würthner, F. *Angew. Chem.* **2008**, *120*, 3415–3419; *Angew. Chem. Int. Ed.* **2008**, *47*, 3367–3371.

[119]   Würthner, F. *Synthesis* **1999**, *12*, 2103-2113.

[120]   Solvent dependent binding studies of reference compounds **10** and **12** revealed slightly lower binding constants in 1,4-dioxane in comparison to THF (see ref. 18). Since concentration-dependent UV/Vis experiments for **1** in THF revealed the predominant existence of monomers at low concentrations, one can safely assume that **1** is present in its monomeric state under the conditions applied in this experiment.

[121]   Würthner, F.; Archetti, G.; Schmidt, R.; Kuball, H.-G. *Angew. Chem.* **2008**, *120*, 4605–4608; *Angew. Chem. Int. Ed.* **2008**, *47*, 4529–4532.

[122]   (a) Liptay, W. *Excited States*; Lim., E. C., Ed.; Academic Press: New York, 1974; Vol. 1, pp 129–229. (b) Beckmann, S.; Etzbach, K.-H.; Krämer, P.; Lukaszuk, K.; Matschiner, R.; Schmidt, A. J.; Schuhmacher, P.; Sens, R.; Seybold, G.; Wortmann, R.; Würthner, F. *Adv. Mater.* **1999**, *11*, 536–541.

[123]   Stolte, M.; Schmidt, J.; Schmidt, R.; Würthner, F.; Kuball, H.-G. *ChemPhysChem*, manuscript in preparation.

[124]   (a) Ephardt, H.; Fromherz, P. *J. Phys. Chem.* **1989**, *93*, 7717–7725. (b) Harriman, A. *J. Photochem. Photobiol. A* **1992**, *65*, 79–93. (c) Khairutdinov, R. F.; Serpone, N. *J. Phys. Chem. B* **1997**, *101*, 2602–2610. (d) Karunakaran, V.; Lustres, J. L. P.; Zhao, L.; Ernsting, N. *J. Am. Chem. Soc.* **2006**, *128*, 2954–2962.

[125]   Pfiffi, D. *FRET-Prozesse in H-Brücken-gebundenen Chromophorassoziaten*; Diploma Thesis; TU Kaiserslautern, **2005**.

159

[126] This value was further confirmed by measuring absolute quantum yields on a C9920-02 from Hamamatsu (Japan). For a 7.1 x 10^{-6} M solution of **1** in CHCl₃ the absolute quantum yield was determined to 0.07.

[127] Strong enhancement of the fluorescence has been reported for merocyanine dyes upon rigidification in frozen solutions, the solid state, organogels, and polymer films. For some examples, see: (a) Würthner, F.; Sens, R.; Etzbach, K.-H.; Seybold, G. *Angew. Chem.* **1999**, *111*, 1753–1757, *Angew. Chem. Int. Ed.* **1999**, *38*, 1649–1652. (b) ref. 19 (c) Bondarev, S. L.; Tikhomirov, S. L.; Knyukshto, V. N.; Turban, A. A.; Ishchenko, A. A.; Kulinich, A. V.; Ledoux, I. *J. Lumin.* **2007**, *124*, 178–186.

[128] *HyperChem* 8.05™; Hypercube Inc.: 1115 NW 4th Street, Gainesville, FL 32601, USA.

[129] (a) Cohen, Y.; Avram, L.; Frish, L. *Angew. Chem.* **2005**, *117*, 524–560; *Angew. Chem. Int. Ed.* **2005**, *44*, 520–554. (b) Chen, Z.; Stepanenko, V.; Dehm, V.; Prins, P.; Siebbeles, L. D. A.; Seibt, J.; Marquetant, P.; Engel, V.; Würthner, F. *Chem. Eur. J.* **2007**, *13*, 436–449.

[130] Perrin, D. D.; Armarego, W. L. F. *Purification of Laboratory Chemicals*; Pergamon Press: Oxford, 1980.

[131] Heller, C. A.; Henry, R. A.; McLaughlin, B. A.; Bliss, D. E. *J. Chem. Engin. Data* **1974**, *19*, 214–219.

[132] Demas, J. N.; Crosby, G. A. *J. Phys. Chem.* **1971**, *65*, 991–1024.

[133] (a) Hwang, T. L.; Shaka, A. J. *J. Am. Chem. Soc.* **1992**, *114*, 3157–3159. (b) Hwang, T. L.; Shaka, A. J. *J. Magn. Reson. B* **1993**, *102*, 155–165.

[134] Wu, D.; Chen, A.; Johnson Jr., C. S. *J. Magn. Reson. A* **1995**, *115*, 260–264.

[135] (a) Lounila, J.; Oikarinen, K.; Ingman, P.; Jokisaari, J.; *J. Magn. Reson. A* **1996**, *118*, 50–54. (b) Esturau, J.; Sánchez-Ferrando, F.; Gavin, J. A.; Roumestand, C.; Delsuc, M. A.; Parella, T. *J. Magn. Reson.* **2001**, *153*, 48–55.

[136] Jerschow, A.; Müller, N. *J. Magn. Reson.* **1997**, *125*, 372–375.

[137] *Low Molecular Mass Gelators* (Topics in Current Chemistry), Vol. 256; F. Fages, Ed.; Springer: Berlin, 2005.

[138] Grimme, S. *J. Comput. Chem.* **2004**, *25*, 1463–1473.

[139] Treutler, O.; Ahlrichs, R. *J. Chem. Phys.* **1995**, *102*, 346–354.

[140] (a) Ahlrichs, R.; Bär, M.; Häser, M.; Horn, H.; Köhmel, C. *Chem. Phys. Lett.* **1989**, *162*, 165–169. (b) Ahlrichs, R.; von Arnim, M. *Methods and Techniques in Computational Chemistry: METECC-95*; Clementi, E.; Corongiu, G., Eds.; Club Européen MOTECC, 1995.

[141] Schäfer, A.; Huber, C.; Ahlrichs, R. *J. Chem. Phys.* **1994**, *100*, 5829–5834.

[142] Fink, R. F.; Seibt, J.; Engel, V.; Renz, M.; Kaupp, M.; Lochbrunner, S.; Zhao, H.-M.; Pfister, J.; Würthner, F.; Engels, B. *J. Am. Chem. Soc.* **2008**, *130*, 12858–12859.

[143] Eichkorn, K.; Weigend, F.; Treutler, O.; Ahlrichs, R. *Theor. Chim. Acta* **1997**, *97*, 119–124.

[144] EDA analysis was performed with the wavels program: Fink, K.; Fink, R. F.; Liu, W.; Jungen, M.; Staemmler, V. *Wavels - a wavefunction based electronic structure program*.

[145] Origin 7.5; OriginLab: Northampton, MA, USA.

List of Publications

- *Solvent Effect on Color, Band Shape, and Charge-Density Distribution for Merocyanine Dyes Close to the Cyanine Limit*

  Würthner, F.; Archetti, G.; Schmidt, R.; Kuball, H.-G. *Angew. Chem.* **2008**, *120*, 4605–4608; *Angew. Chem. Int. Ed.* **2008**, *47*, 4529–4532.

- *Synthesis, Optical Properties, and LFER Analysis of Solvent-Dependent Binding Constants of Hamilton-Receptor-Connected Merocyanine Chromophores*

  Schmidt, J.; Schmidt, R.; Würthner, F. *J. Org. Chem.* **2008**, *73*, 6355–6362.

- *Solvent- and Guest-Responsive Self-Assembly of Hamilton-Receptor-Functionalized Bis(merocyanine) Dyes*

  Schmidt, R.; Uemura, S.; Würthner, F. *Chem. Eur. J.* **2010**, *16*, 13706–13715.

- *Ultrafast Bidirectional Photoswitching of a Spiropyran*

  Buback, J.; Kullmann, M.; Langhojer, F.; Nuernberger, P.; Schmidt, R.; Würthner, F.; Brixner, T. *J. Am. Chem. Soc* **2010**, *132*, 16510–16519.

- *Ring-Closure and Isomerization Capabilities of Spiropyran-Derived Merocyanine Isomers*

  Buback, J.; Nuernberger, P.; Kullmann, M.; Langhojer, F.; Schmidt, R.; Würthner, F.; Brixner, T. *J. Phys. Chem.*, accepted.

Poster Presentations

- VW-Symposium, Complex Materials, Rolduc/The Netherlands, February 18–21, 2007

  Schmidt, R.; Schmidt, J.; Stolte, M.; Kuball, H.-G.; Wortmann, R.; Würthner, F., *"Hydrogen-Bond-Directed Head-to-Tail Orientation of Dipolar Merocyanine Dyes"*

- Chem-SyStM, Würzburg/Germany, December 04, 2007

  Schmidt, R.; Schmidt, J.; Stolte, M.; Kuball, H.-G.; Wortmann, R.; Würthner, F., *"Hydrogen-Bond-Directed Head-to-Tail Orientation of Dipolar Merocyanine Dyes"*

- 3rd EuCheMs Chemistry Congress, Nürnberg/Germany, August 29–September 02, 2010

  Schmidt, R.; Stolte, M.; Stepanenko, V.; Zhang, X.; Würthner, F., *"Self-Assembly of Self-Complementary Hamilton-Receptor-Connected Merocyanine Dyes"*

- Chem-SyStM, Würzburg/Germany, December 07, 2010

  Schmidt, R.; Stolte, M.; Stepanenko, V.; Zhang, X.; Würthner, F., *"Self-Assembly of Self-Complementary Hamilton-Receptor-Connected Merocyanine Dyes"*